Fakultät für Maschinenwesen

Lehrstuhl für Anlagen- und Prozesstechnik

Large-scale hydrogen liquefaction under the aspect of economic viability

Umberto Federico Cardella

Vollständiger Abdruck der von der Fakultät für Maschinenwesen der Technischen Universität München zur Erlangung des akademischen Grades eines

Doktor-Ingenieurs

genehmigten Dissertation.

Vorsitzende(r): Prof. Dr.-Ing. Thomas Sattelmayer

Prüfer der Dissertation:

1. Prof. Dr.-Ing. Harald Klein
2. Prof. Dr.-Ing. Hartmut Spliethoff

Die Dissertation wurde am 17.05.2018 bei der Technischen Universität München eingereicht und durch die Fakultät für Maschinenwesen am 01.10.2018 angenommen.

Parts of the herein presented dissertation have appeared in the following publications:

Cardella, U., et al., Wirtschaftlich umsetzbare Wasserstoff Grossverfluessiger, Deutsche Kaelte-Klima-Tagung, 2015

Cardella, U., et al., Economically viable large-scale hydrogen liquefaction, Materials Science and Engineering, 2017

Cardella, U., et al., Process optimization for large-scale hydrogen liquefaction, International Journal of Hydrogen Energy, 2017

Cardella, U., et al., Roadmap to economically viable hydrogen liquefaction, International Journal of Hydrogen Energy, 2017

Cardella, U., et al., Aspects of hydrogen liquefier scale-up - Process and equipment design, Proceedings of the 14th Cryogenics IIR International Conference, 2017

Acknowledgements

This dissertation is a product of my work as a doctoral researcher at the Institute of Plant and Process Technology of the Technical University Munich and at Linde Kryotechnik AG between the year 2013 and 2017. My gratitude extends to all persons that have supported me during these exciting years.

In particular, I would like to thank my supervising Professor Harald Klein for his precious advice and for guiding me through this dissertation. I have appreciated his always positive and constructive attitude. I could not have wished for a better advisor.

I would like to thank Professor Hartmut Spliethoff for taking the role as second examiner. Also, I would like to thank the chairman of the examining commission Professor Thomas Sattelmayer.

A thank you goes to all the colleagues at the Institute of Plant and Process Technology. In particular, I would like to thank Dr. Sebastian Rehfeldt and Mr. Johannes Sundberg.

A special thanks goes to Mr. Lutz Decker for his role as advisor from industry and for the innumerable technical discussions that we have conducted together. His distinguished expertise in the field of cryogenic engineering and hydrogen technology have been invaluable to me. I want to thank Mr. Klaus Ohlig for the support as well as the colleagues at Linde Kryotechnik AG with which I had the pleasure to work with.

To my parents I want to say “grazie”. I will never forget the love and support that I have received from you from the beginning of my life.

Last but not least, Rebecca, my wife. You are the love of my life. Thank you for your patience and inexhaustible support. Our newborn son Aurelio has filled us with joy and has given to me the last boost to finish this thesis.

Munich, May 17th of 2018 Umberto Cardella

"Yes, my friends, I believe that water will one day be employed as fuel, that hydrogen and oxygen which constitute it, used singly or together, will furnish an inexhaustible source of heat and light, of an intensity of which coal is not capable. Some day the coalrooms of steamers and the tenders of locomotives will, instead of coal, be stored with these two condensed gases, which will burn in the furnaces with enormous calorific power (...). I believe, then, that when the deposits of coal are exhausted we shall heat and warm ourselves with water. Water will be the coal of the future!"

"The Mysterious Island (1874), Jules Verne"

Kurzfassung

Wasserstoff wird als Treibstoff der Zukunft betrachtet. Wasserstoff könnte die Abhängigkeit von fossilen Brennstoffen reduzieren und bietet zugleich Lösungen für die Herausforderungen des Klimawandels sowie der Luftverschmutzung im Energie- und Verkehrssektor. Der Transport und die Lagerung von Wasserstoff wird mit kryogenem Flüssig-Wasserstoff besonders wirtschaftlich. Flüssig-Wasserstoff wird in industriellen Wasserstoffverflüssigungsanlagen produziert. Der Verflüssigungsprozess ist jedoch energie- und kostenintensiv. Die bis heute gebauten industriellen Wasserstoffverflüssigungsanlagen wurden für vergleichsweise geringe Produktionskapazitäten und auf niedrige Investitionskosten ausgelegt. Daher ist der thermodynamische Wirkungsgrad bisheriger Wasserstoffverflüssiger vergleichsweise gering, der spezifische Energiebedarf und die spezifischen Verflüssigungskosten pro Kilogramm Flüssig-Wasserstoff jedoch hoch. Die zukünftig steigende Nachfrage nach Wasserstoff könnte zu einer Hochskalierung der Wasserstoffverflüssigungsanlagen führen. Um die Gesamtkosten für die Lieferung von Wasserstoff an der Tankstelle zu reduzieren, werden daher wirtschaftlich umsetzbare Großwasserstoffverflüssiger benötigt.

Die wirtschaftliche Hochskalierung des Wasserstoffverflüssigungsprozesses erfordert die Suche nach einem Optimum zwischen Investitions- und Betriebskosten. Das Ziel dieser Arbeit ist die Entwicklung von kostenoptimierten Verflüssigungsprozessen für die Produktion von Flüssig-Wasserstoff im großen Maßstab. Es wird ein methodischer Ansatz erarbeitet, um thermodynamisch effiziente und zugleich kostenoptimiete Verflüssigungsprozesse zu entwickeln. Die Verflüssigungsprozesse werden in einem Prozesssimulator modelliert und optimiert. Um die ökonomische Wirtschaftlichkeit der entwickelten Prozesse zu bewerten, wurde ein umfangreiches Modell für die Abschätzung der Investitions- und Betriebskosten implementiert. Im Zuge der Prozessentwicklung wird die technische Umsetzbarkeit der Prozesssysteme und der Apparate bewertet. Es werden Verflüssigungsprozesse mit hohem technologischen Reifegrad entwickelt. Die Verflüssigungsprozesse werden mit den implementierten Prozesssimulations- und Kostenmodellen auf den spezifischen Energiebedarf und die spezifischen Verflüssigungskosten optimiert. Die Optimierung der neuentwickelten Prozesskonzepte wird für verschiedene Prozessverfahren und Verflüssigungskapazitäten durchgeführt.

In dieser Arbeit werden zwei neuartige Verflüssigungsprozesse vorgestellt. Für Verflüssigungskapazitäten bis zu 100 Tonnen pro Tag Wasserstoff wird das Hochdruckverfahren für den Wasserstoff Claude-Kältekreislauf mit einem Gemisch-Kältekreislauf als Vorkühlung bevorzugt. Im Vergleich zu bisherigen Wasserstoffverflüssigern minimiert der entwickelte Verflüssigungsprozess die Verflüssigungskosten bis zu circa 68% auf unter 1 €/kg flüssig Wasserstoff. Gleichzeitig wird der spezifische Energiebedarf für die Verflüssigung um circa 40% reduziert, auf etwa 6 kWh/kg flüssig Wasserstoff. Die in dieser Arbeit vorgestellten Ergebnisse können die Gesamtkosten für die Lieferung von Wasserstoff an der Tankstelle minimieren und könnten somit Wasserstoff als Treibstoff der Zukunft etablieren.

Abstract

Hydrogen is seen as a promising energy carrier to reduce the dependence on fossil fuels. It can solve the challenges related to air pollution and climate change in the energy and transport sector. A cost effective way to store and deliver hydrogen is to bring it in its cryogenic liquid form. Liquid hydrogen in industrial hydrogen liquefiers is produced in energy and capital intensive hydrogen liquefaction processes. At present, industrial hydrogen liquefiers are designed for comparatively small liquefaction capacities and for low capital expenses. The specific energy and the specific costs required to liquefy one kilogram of hydrogen is high. The future demand for hydrogen fuel in clean energy and mobility applications is expected to lead to a scale-up in hydrogen liquefaction plants. To decrease the costs for hydrogen delivery to a hydrogen refilling station, economically viable large-scale hydrogen liquefaction processes are required.

The aim of this work is the development of large-scale hydrogen liquefaction processes that are optimized in the specific liquefaction costs SLC by finding a trade-off between plant capital expenses and operating expenses. For the development of thermodynamic efficient cost-optimized process concepts, a novel methodical approach is presented in this work. Hydrogen liquefaction process concepts with a high level of technological readiness are investigated and developed. The process concepts are modelled and simulated in a comprehensive hydrogen liquefier process simulator model. To evaluate the economic viability, a detailed cost estimation model for the hydrogen liquefaction plant is implemented. The work involves the analysis and design of the main hydrogen liquefier subsystems and the process equipment. The implemented hydrogen liquefier process simulation and cost estimation models are used for the optimization of the hydrogen liquefaction processes for both specific energy consumption SEC and specific liquefaction costs SLC. The process optimization is carried out for different process configurations and liquefaction capacities.

Two novel process concepts for large-scale hydrogen liquefaction are presented within this work. For liquefaction capacities of up to 100 metric tonnes per day of hydrogen the herein developed high-pressure Hydrogen Claude Cycle with Mixed-refrigerant Joule-Thomson Cycle precooling is chosen as preferred process concept. In comparison to built state-of-the-art hydrogen liquefiers, the hydrogen liquefaction process developed in this work reduces the specific liquefaction costs SLC by nearly 68% to below 1 €/kg of liquid hydrogen. The specific energy consumption SEC is reduced by nearly 40% to about 6 kWh/kg. The results presented in this work can substantially reduce the costs for hydrogen delivery to hydrogen refilling stations and enable hydrogen as the fuel of the future.

Contents

Nomenclature

Latin Symbols

A	Heat transfer surface	m^2
a_0	Velocity of sound	$\frac{\mathrm{m}}{\mathrm{s}}$
a_1	Cost coefficient	-
a_{fo}	Reaction rate constant (first-order)	$\frac{\mathrm{m}^3 \cdot \mathrm{s}}{\mathrm{mol}}$
a_v	Specific surface	$\frac{\mathrm{m}^2}{\mathrm{m}^3}$
b_1	Cost coefficient	-
b_{fo}	Reaction rate constant (first-order)	$\frac{\mathrm{m}^3 \cdot \mathrm{s}}{\mathrm{mol}}$
c_{H_2}	Molar concentration of hydrogen	$\frac{\mathrm{mol}}{\mathrm{m}^3}$
c_{el}	Specific electricity costs	$\frac{\mathrm{EUR}}{\mathrm{kWh}}$
c_p	Specific isobaric heat capacity	$\frac{\mathrm{J}}{\mathrm{kg} \cdot \mathrm{K}}$
c_{rfr}	Specific refrigerant costs	$\frac{\mathrm{EUR}}{\mathrm{kg}}$
c_s	Isentropic spouting velocity	$\frac{\mathrm{m}}{\mathrm{s}}$
C	Costs	EUR
CI	Cost index	-
D	Diameter	m
e_d	Cost degression exponent	-
f	Cost factor	-
$\bar{E}_{a,i}$	Molar activation energy	$\frac{\mathrm{J}}{\mathrm{mol}}$
e	Specific exergy	$\frac{\mathrm{J}}{\mathrm{kg}}$
h	Specific enthalpy, height	$\frac{\mathrm{J}}{\mathrm{kg}}$,m
Δh	Specific enthalpy difference	$\frac{\mathrm{J}}{\mathrm{kg}}$
$\Delta \bar{H}_V$	Molar enthalpy of evaporation	$\frac{\mathrm{J}}{\mathrm{mol}}$
$\Delta \bar{H}_R$	Molar enthalpy of reaction	$\frac{\mathrm{J}}{\mathrm{mol}}$
$\Delta \bar{H}_S$	Molar enthalpy of fusion	$\frac{\mathrm{J}}{\mathrm{mol}}$
i	Variable, component	-
I	Interest rate	-
j	Variable	-
k	Reaction rate constant	$\frac{1}{\mathrm{s}}$
K	Equipment base cost parameter	EUR
l	Length	m

m	Mass	kg
$\dot{m}$	Mass flow rate	$\frac{\text{kg}}{\text{s}}$
$\bar{M}$	Molar mass	$\frac{\text{kg}}{\text{kmol}}$
Ma	Mach number	-
N	Number, number of stages	-
n	Rotational speed	$\frac{1}{\text{s}}$
n_s	Specific speed	-
p	Pressure	bar
Δp_d	Pressure drop	bar
P	Power	W
$\dot{Q}$	Heat flow rate	W
r	Reaction rate	$\frac{\text{mol}}{\text{m}^3\cdot\text{s}}$
$\bar{R}$	Universal gas constant	$\frac{\text{J}}{\text{mol}\cdot\text{K}}$
s	Stroke	m
SEC	Specific energy consumption	$\frac{\text{kWh}}{\text{kg}}$
SLC	Specific liquefaction costs	$\frac{\text{EUR}}{\text{kg}}$
SPC	Specific production costs	$\frac{\text{EUR}}{\text{kg}}$
t	Time, thickness	s,m
t_p	Payment period	a
T	Temperature	K
ΔT_{log}	Logarithmic mean temperature difference	K
u_2	Impeller wheel tip velocity	$\frac{\text{m}}{\text{s}}$
U	Heat transfer coefficient	$\frac{\text{W}}{\text{m}^2\cdot\text{K}}$
v	Specific volume	$\frac{\text{m}^3}{\text{kg}}$
V	Volume	m^3
$\bar{V}$	Molar volume	$\frac{\text{m}^3}{\text{kmol}}$
$\dot{V}$	Volumetric flow rate	$\frac{\text{m}^3}{\text{h}}$
w	Specific work, width	$\frac{\text{J}}{\text{kg}}$,m
W	Work	J
x	Optimization variable x, axial coordinate x	-
x_i	Mole fraction component i in liquid phase	-
y_i	Mole fraction component i in gas phase	-
y_o	Mole fraction of ortho-hydrogen	-

y_p	Mole fraction of para-hydrogen	-
Y_a	Yearly plant utilization rate	-
z	Number of components in parallel configuration	-

Greek Symbols

α	Reduced Helmholtz free energy	-
δ	Reduced density	-
$\delta_{S,i}$	Solubility parameter	-
Δ	Difference	-
η	Efficiency	-
κ	Isentropic exponent	-
λ	Thermal conductivity	$\frac{\mathrm{W}}{\mathrm{m \cdot K}}$
μ	Non-dimensional mass flow rate	-
μ_{JT}	Joule-Thomson coefficient	$\frac{\mathrm{K}}{\mathrm{bar}}$
ν	Velocity ratio	-
φ	Flow coefficient	-
π_c	Compression pressure ratio	-
π_e	Expansion pressure ratio	-
Ψ	Pressure (head) coefficient	-
ϱ	Density	$\frac{\mathrm{kg}}{\mathrm{m^3}}$
σ	Standard deviation	-
τ	Reciprocal reduced temperature	-

Superscript

0	Ideal-gas property
eq	Equilibrium
red	Reduced

Subscript

0	Reference condition
1	At the point 1, point in time 1
2	At the point 2, point in time 2
a	Annum
ads	Adsorber
ai	Instrumentation and analysers
amb	Ambient

bd	Buildings
c	Cold, cryogenic
calc	Calculated
CAPEX	Capital expenses
carnot	Carnot
cat	Catalyst
cb	Coldbox shell
cbs	Coldbox system
ce	Cold end
ch	Channel
comp	Compressor, compression
cons	Consumption
conv	Conversion
cooler	Cooler
cps	Capital spare parts
CR	Cost reduction
crit	Critical
cs	Control systems
cst	Construction
cw	Cooling water, cooling water system
del	Delivered
ds	Design
direct	Direct
ecs	Electrical systems and control systems
el	Electrical, electricity
es	Electrical systems
eng	Engineering
ex	Exergy
exp	Expander, expansion
f	Fluid
feed	Feed
fill	Fill
fin	Fin

final	Final
fix	Fixed
flare	Flare system
i	Variable i, component i
ideal	Ideal
in	Inlet
indirect	Indirect
inst	Installed
inv	Inversion
is	Isentropic
ivt	Inventory
l	Liquid
liq	Liquefier
loss	Loss
m	Mean
M	Maintenance
max	Maximum, maximal
mech	Mechanical
melt	Melting point
min	Minimum, minimal
mix	Mixture
net	Net power
N	Normal
off	Offsite
out	Outlet
OM	Operational and maintenance
OPS	Operating personnel and supervision
OPEX	Operating expenses
opt	Optimum, optimal
other	Other
over	Overhead & Administration
p	Pressure
pass	Passage

PC	Precooling
pist	Piston
pump	Pump
prod	Product
PFHX	Plate-fin heat exchanger
pre	Site preparation
pv	Piping and valves
pvt	Piping, valves and transfer lines
RC	Reciprocating piston compressor
recov	Recovery
red	Reduced
res	Residual
rfr	Refrigerant
risk	Risk
rod	Rod
sat	Saturated
spg	Seal and purge gas
s	Stroke
sim	Simulation, simulated
stage	Stage
start	Start-up
str	Structures
sts	Storage tank system
sup	Supplier
T	Temperature
tank	Tank
TC	Turbo compressor
total	Total
tip	Impeller wheel blade tip
tra	Transfer lines
trp	Triple point
TU	Turbine expander
v	Vapour

var	Variable
ve	Vessels
w	Warm
wcs	Warm compression system
wheel	Compressor wheel, Turbine wheel
work	Working
x	Variable of axial location

Abbreviations

ASU	Air separation unit
ATEX	Atmosphères Explosibles
CAPEX	Capital expenses
CGH_2	Compressed hydrogen gas
COMP	Compressor
CO	Cost-optimized
CB	Coldbox
EO	Energy-optimized
EOS	Equation of state
FCEV	Fuel cell electric vehicle
GH_2	Gaseous hydrogen
HP	High pressure
IDEALHY	Integrated design for efficient advanced liquefaction of H_2
JT	Joule-Thomson
LH_2	Liquid hydrogen
$n-H_2$	Normal-hydrogen
$o-H_2$	Ortho-hydrogen
$p-H_2$	Para-hydrogen
LMTD	Logarithmic mean temperature difference
LNG	Liquefied natural gas
LP	Low Pressure
MP	Medium pressure
MR	Mixed-refrigerant
MRC	Mixed-refrigerant cycle
NASA	National Aeronautics and Space Administration

NBP	Normal boiling point
NIST	National Institute of Standards and Technology
O&M	Operation and maintenance
OPEX	Operating expenses
PSA	Pressure swing adsorption
PR	Peng-Robinson
PFHX	Plate-fin heat exchanger
REFPROP	Reference Fluid Thermodynamic and Transport Properties
SLE	Solid-liquid equilibrium
SMR	Methane steam reforming
SRK	Soave-Redlich-Kwong
TCO	Total cost of ownership
TRL	Technological readiness level
USA	United States of America
VLE	Vapour-liquid equilibrium
WE-NET	World Energy NETwork

1 Introduction

The human world population has grown exponentially in the last two centuries. The contemporaneous industrialization has led to the threats of a rising air pollution and global warming due to greenhouse gas emissions such as carbon dioxide CO_2 [Cardella et al. 2017c]. To contain the impact of climate change, national governments and international organizations have recently issued stricter environmental regulations and targets for the reduction of greenhouse gas emissions, for instance within the UNFCC 2015 Paris Climate Agreement.

Hydrogen as energy carrier and fuel cells as an energy conversion device are a promising way forward to reduce the dependence on fossil fuels in the transport and energy sector. Hydrogen fuel cell electric vehicles (FCEV) for hydrogen mobility do not pollute and are capable of overcoming the disadvantages of battery electric vehicles, such as the limited driving range and the high charging times [Ball & Wietschel 2009]. The FCEV generate electricity for an electric motor drive and water by using the hydrogen stored in the tanks as compressed hydrogen gas (CGH_2) with up to 700 bar or as cryogenic fluid [H2 Mobility 2010, Aceves et al. 2010].

In the last decade the installation of hydrogen infrastructure and hydrogen refilling station (HRS) networks has increased substantially with the aid of regional and national initiatives [Ball & Wietschel 2009, Cardella et al. 2017c]. In Germany for example, the installation of up to 400 HRS is planned until the year 2023 [H2 Mobility 2015]. Besides FCEV cars, larger consumers of hydrogen fuel such as buses, trains and ships may soon increase the demand for hydrogen on a large scale. For example, one large ship powered by fuel cells can require up to approximately 10 tonnes per day (tpd) of hydrogen (H_2) fuel [Cardella et al. 2017c].

The hydrogen refuelling costs in the European Union are currently in the range of approximately 9 €/kg H_2 [Stolten 2016]. Based on the refuelling costs of conventional fossil fuels, the long-term target hydrogen refuelling costs are set to approximately $5 - 7$ €/kg H_2 in the European Union or to 4 \$/kg H_2 in the USA [FCH2JU 2014, Stolten 2016].

The main challenge for a hydrogen based mobility is the cost and energy efficient up-scaling of the whole hydrogen supply chain from well-to-wheel, from the hydrogen production to the hydrogen distribution and delivery at the HRS.

Hydrogen gas (GH_2) can be produced from renewable and non-renewable energy sources with a wide range of different industrial processes. The currently most utilized large-scale GH_2 industrial production processes are based on non-renewable fossil fuels as energy source, in example methane steam reforming (SMR), coal gasification and partial oxidation [Haeussinger et al. 2000a]. Additionally, GH_2 is often available as inexpensive by-product of the chemical industry [Ball & Wietschel 2009].

For hydrogen production, one industrial large-scale SMR plant can produce up to approximately 300 tpd GH_2 [Bracha & Decker 2008]. The specific costs for GH_2 that is produced in large-scale non-renewable processes can be lower than 1.5 €/kg GH_2 [Ball & Wietschel 2009].

The hydrogen production processes from renewable energy sources such as biomass, wind and solar power are defined as clean and are becoming increasingly important for their potential for zero greenhouse gas emissions. Electrolysis, the splitting of water with the use of electricity, is the most common of renewable hydrogen production processes. The production and storage of GH_2 with electricity in power-to-gas applications is seen as a potential solution for the utilization of surplus electricity generated from renewable energy sources [FCH2JU 2014]. Depending on the electricity costs, the specific costs for GH_2 produced in large-scale electrolysers are reported between $3.5 - 7.0$ €/kg GH_2 [Ball & Wietschel 2009, Le Duigou et al. 2013].

Liquefying hydrogen is regarded as the cost efficient option to distribute and store hydrogen in large volumes and over long distances, in example in road trailers or ship carriers. In the USA the total costs for liquid hydrogen LH_2 delivery was reported to range $5 - 10$ \$/kg LH_2 [Bromaghim et al. 2010]. Compared to CGH_2, the liquefaction of hydrogen is energy intensive but the additional energy consumption is partially compensated by the higher density and purity of LH_2 as well as by the flexible handling and the lower energy consumption of LH_2 during transportation and at the HRS [Berstad et al. 2010]. Due to the higher density of liquid hydrogen LH_2, up to 3600 kg LH_2 can be transported in one LH_2 trailer compared to a maximum of about 900 kg GH_2 in one CGH_2 trailer [Ball & Wietschel 2009].

Hydrogen was first liquefied by Dewar 1898. Later during the development of nuclear weapons and the space programs in the USA in the 20th century, larger industrial hydrogen liquefaction plants were installed [Barron 1985, Alekseev 2016]. The total installed LH_2 production capacity worldwide is estimated to approximately 400 tpd LH_2 [Krasae-in et al. 2010]. The largest hydrogen liquefaction plants were built in the USA from the 1960s to the 1980s and were designed for hydrogen liquefaction capacities of up to 55 tpd LH_2 [Gardiner 2009]. The largest hydrogen liquefiers in operation today are located in the USA and have a maximum liquefaction capacity in the range of $20 - 35$ tpd LH_2 [Krasae-in et al. 2010, Shigekiyo 2015]. In Europe and Japan, smaller hydrogen liquefiers with a capacity between $5 - 10$ tpd LH_2 are currently in operation [Krasae-in et al. 2010].

Liquid hydrogen LH_2 is produced by the cooling and liquefaction of a hydrogen feed gas stream from ambient temperature to around 20 K. The current state-of-the-art hydrogen liquefaction process is designed with a hydrogen feed gas precooling carried out with a liquid nitrogen LN_2 stream or a nitrogen refrigeration cycle, followed by the further cooling and liquefaction in a cryogenic refrigeration cycle with a Hydrogen Claude Cycle or a Helium Brayton Cycle [Ohlig & Decker 2013].

Prior to the hydrogen liquefaction, the hydrogen feed stream is purified in cryogenic adsorber vessels and is catalytically converted to high fractions of para-hydrogen

within the cryogenic plate-fin heat exchangers [Ohlig & Decker 2013]. This catalytic conversion is a major challenge for industrial large-scale hydrogen liquefaction processes.

The main drawback of hydrogen liquefaction is the small scale of the currently installed hydrogen liquefiers. The specific energy consumption *SEC* and the specific liquefaction costs *SLC* of installed hydrogen liquefiers are comparatively high. Built industrial hydrogen liquefiers were often designed to minimize the initial plant capital expenses while the thermodynamic efficiency of the hydrogen liquefaction process played only a subordinate role [Quack 2001]. The specific energy consumption *SEC* for state-of-the-art hydrogen liquefiers is approximately 10 kWh/kg LH_2 [Cardella et al. 2017c].

The potential future demand for LH_2 from the clean energy sector may soon require efficient large-scale hydrogen liquefaction plants with a hydrogen liquefaction capacity exceeding the current installed hydrogen liquefiers by a factor of 5 to 10 [Cardella et al. 2017d]. To reduce the plant electricity costs, novel large-scale hydrogen liquefaction processes with an increased thermodynamic efficiency are required. A specific energy consumption *SEC* of 6 kWh/kg LH_2 is seen as a benchmark for future large-scale hydrogen liquefaction. This requires a 40 % or higher reduction from the current *SEC*.

Since the late 1970s, a high number of conceptual process design studies for future large-scale hydrogen liquefaction plants with capacities in the range of 50-900 tpd LH_2 were published. In the majority of the published conceptual process design studies the focus was set on maximizing the thermodynamic efficiency of the hydrogen liquefaction process through theoretical simulation [Cardella et al. 2017b].

In industrial process engineering, an optimal process design is a compromise between the thermodynamic efficiency and the plant capital expenses. The electricity costs in gas liquefaction plants represent only a fraction of the total specific liquefaction costs *SLC*. A lower thermodynamic efficiency can be compensated by improved process economics, a lower plant complexity and the use of proven equipment with low technical risks [Cardella et al. 2015a]. These aspects of process design were often underestimated in prior works.

To reach the target costs for LH_2 delivery and hydrogen refuelling, the development of new thermodynamic efficient large-scale hydrogen liquefaction processes should focus on the optimization of the specific liquefaction costs *SLC* by considering both the plant capital and the operating expenses.

2 Objective

The scope of this work is to develop economically viable large-scale hydrogen liquefaction processes with a capacity of up to 100 tpd LH_2 and an improved thermodynamic efficiency. The main objective is to minimize the specific liquefaction costs SLC of hydrogen liquefaction by employing process and equipment technology that is technically ready or that can be qualified as such within the year 2020. The target is to reduce the specific liquefaction costs SLC to about 1 €/kg LH_2 or below. The target for the specific energy consumption SEC is to reach the benchmark value of 6 kWh/kg LH_2.

The thermodynamic principles of hydrogen liquefaction processes are described in the theoretical part of this work in Chapter 3. The state-of-the-art hydrogen liquefaction processes and the equipment are described in Chapter 4.

The simulation of large-scale hydrogen liquefaction processes involve a high number of optimization variables and constraints. A comprehensive hydrogen liquefier process simulation model is developed within this work and described in Chapter 5. For this complex process simulation task, process optimization methods need to be applied to the developed hydrogen liquefier process simulation model. To reach the objectives defined within this work, the specific energy consumption SEC and the specific liquefaction costs SLC of hydrogen liquefaction are used as objective functions for process optimization.

The capacity and performance limitations of process equipment are a major challenge in the development of large-scale hydrogen liquefaction processes. Preliminary equipment design correlations are implemented in the hydrogen liquefier process simulation model and are described in Chapter 6. The optimal design of the catalytic ortho- to para-hydrogen conversion within the hydrogen liquefaction process is complex and requires an accurate kinetic model.

To evaluate the process economics and to optimize the specific liquefaction costs SLC of hydrogen liquefaction processes, a comprehensive cost estimation model is implemented in the hydrogen liquefier process simulation model and is described in Chapter 7.

The process development and optimization of large-scale hydrogen liquefaction processes is described in Chapter 8. For the development of economically viable large-scale hydrogen liquefaction processes, a novel approach is proposed within this work. In order to detect costly components and to identify areas for efficiency improvements, state-of-the-art industrial hydrogen liquefiers and selected conceptual large-scale hydrogen liquefaction processes are evaluated. Subsequently in order to develop novel process concepts for large-scale hydrogen liquefaction, comprehensive process and economic investigations of the hydrogen liquefier systems are carried out. Process optimization and sensitivity analyses are undertaken to further improve and evaluate the developed process concepts. In the final Chapter 9, one preferred cost-optimized large-scale hydrogen liquefaction process concept is selected for a final process optimization.

3 Theoretical Background

This chapter describes the theoretical part of this work. The fundamental thermodynamic principles of hydrogen liquefaction are described in Section 3.1. The physical properties of the hydrogen allotropes and the relevant technical aspects of the ortho- to para-hydrogen conversion are described in Section 3.2. The thermodynamic fluid property estimation methods used for the hydrogen liquefaction process simulation in this work are described in section 3.3.

3.1 Thermodynamic principles of hydrogen liquefaction

The fundamental thermodynamic principles of cryogenic refrigeration and liquefaction processes are described within this section.

3.1.1 Fundamentals

The fundamental principles of cryogenic refrigeration and gas liquefaction are described in literature [Hausen & Linde 1985, Timmerhaus & Flynn 1989]. The thermodynamic modelling of refrigeration and liquefaction processes is based on the balance equations for mass, energy and entropy as well as on the equations of state (EOS) for fluids [Stephan et al. 2007].

By assuming a steady-state open flow process system with a constant mass flow rate $\dot{m} = \dot{m}_{in} = \dot{m}_{out}$, the First Law of Thermodynamics can be expressed as:

$$\dot{Q} + P = \dot{m} \cdot (h_{out} - h_{in}) \ , \tag{3.1}$$

with the specific enthalpy of the inlet stream h_{in}, the specific enthalpy of the outlet stream h_{out} and the heat flow rate $\dot{Q}$ [Stephan et al. 2007]. In Equation (3.1), the variation of both the kinetic energy and the potential energy across the system is assumed to be negligible [Stephan et al. 2007].

In cryogenic process engineering, a hydrogen liquefier is a device that produces refrigeration for the cooling and liquefaction of a hydrogen gas stream. The major difference between a hydrogen refrigerator and a hydrogen liquefier is that a hydrogen liquefier requires cooling throughout a wide range of different temperatures T rather than at a constant temperature T_0 [Hausen & Linde 1985]. A schematic drawing of an ideal reversible process cycle for the cooling and liquefaction of a hydrogen (H_2) stream from the inlet temperature T_{in} to the outlet temperature T_{out} is illustrated in Figure 3.1.

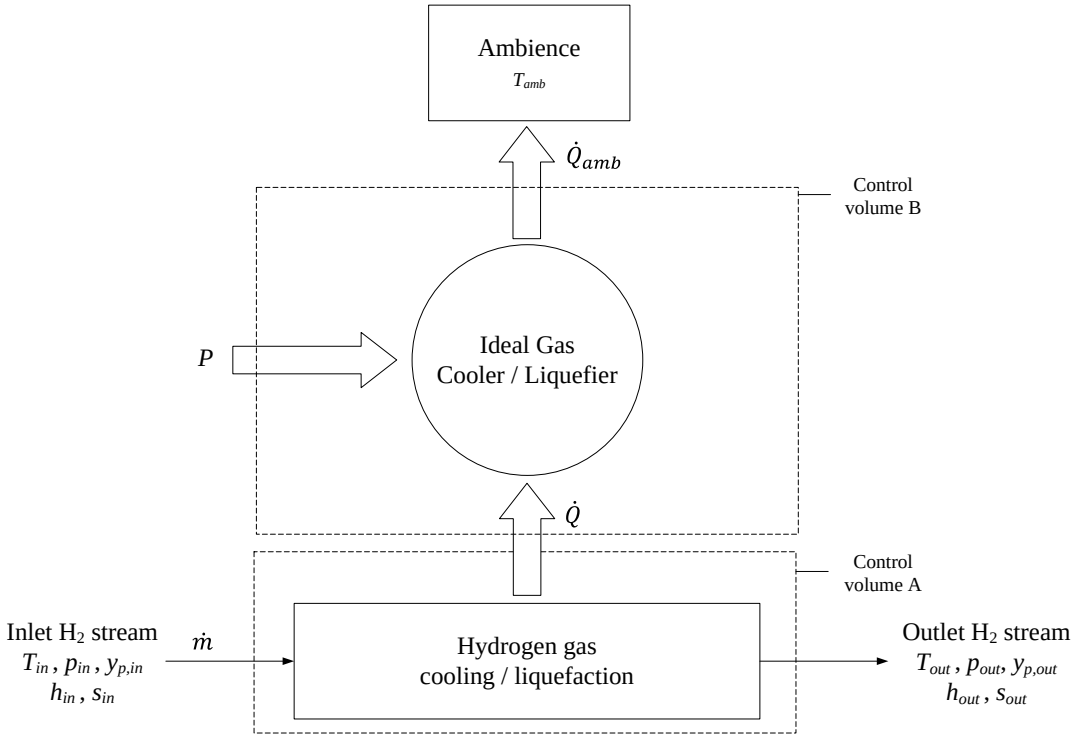

Figure 3.1: Schematic drawing of an ideal cooling process for a hydrogen stream

The First Law of Thermodynamics in the form of the energy balance in Equation (3.1) applied to the cooling of the hydrogen stream in Figure 3.1 (control volume A) is:

$$\dot{Q} = \dot{m} \cdot (h_{in} - h_{out}) \; . \tag{3.2}$$

The heat flow rate $\dot{Q}$ removed from the hydrogen stream is added to the ideal reversible process cycle that rejects the heat flow rate $\dot{Q}_{amb}$ to the ambience [Stephan et al. 2007, Venkatarathnam & Timmerhaus 2008]. The First Law of Thermodynamics in the form of the energy balance in Equation (3.1) can be applied to the ideal reversible process cycle in Figure 3.1 (control volume B):

$$\dot{Q} + P = \dot{Q}_{amb} \, . \tag{3.3}$$

The combination of Equation (3.3) with Equation (3.2) yields:

$$\dot{m} \cdot (h_{in} - h_{out}) + P = \dot{Q}_{amb} \, . \tag{3.4}$$

The cooling and liquefaction of a hydrogen gas stream requires the power input $P > 0$ to perform the work W:

$$P = \frac{dW}{dt} \, . \tag{3.5}$$

3.1.2 Ideal work and efficiency

The Carnot equation can be used to determine the minimum work w_{ideal} that is required for an ideal reversible refrigerator that provides refrigeration over a constant temperature T_0. The Carnot equation for an ideal refrigerator working in steady-state in an ideal reversed Carnot cycle to provide the refrigeration to remove the heat flow rate $\dot{Q}_0$ to cool a hydrogen stream at a constant temperature T_0 can be formulated from the First Law and the Second Law of Thermodynamics [Baehr & Kabelac 2012]:

$$P_{ideal} = \dot{Q}_0 \cdot \frac{T_{amb} - T_0}{T_0} \,. \tag{3.6}$$

The ideal refrigerator rejects the heat at the ambient temperature T_{amb} and requires the minimum (ideal) power input P_{ideal} [Hausen & Linde 1985].

Real hydrogen liquefaction processes are not reversible and produce irreversibilities. Furthermore, in a hydrogen liquefaction process, the refrigeration to remove the heat flow rate $\dot{Q}_0$ that is required to cool and liquefy a hydrogen stream is provided over a wide range of temperatures T. The exergy efficiency η_{ex} [Stephan et al. 2007] is used to evaluate the thermodynamic performance of hydrogen liquefaction processes. The exergy efficiency η_{ex} of a hydrogen liquefaction process is defined in Equation (3.7) as the ratio between the minimum specific work w_{ideal} required for an ideal hydrogen liquefaction process and the actual specific work required by the hydrogen liquefaction process w_{net} [Cardella et al. 2017d]:

$$\eta_{ex} = \frac{w_{ideal}}{w_{net}} \,. \tag{3.7}$$

The minimum specific work w_{ideal} required for an ideal hydrogen liquefaction process represents the minimum theoretical work that is required by an ideal reversible cycle to cool and liquefy a hydrogen gas stream from the inlet conditions to the outlet liquid state. It can be determined by applying the First Law of Thermodynamics in the form of the energy balance in Equation (3.1) and the Second Law of Thermodynamics to the hydrogen stream shown in Figure 3.1:

$$w_{ideal} = \Delta e = e_{out} - e_{in} = (h_{out} - h_{in}) - T_{amb} \cdot (s_{out} - s_{in}) \,. \tag{3.8}$$

The specific exergy difference Δe [Baehr & Kabelac 2012] between the inlet hydrogen gas stream and the outlet liquid hydrogen (LH_2) stream is determined with the specific enthalpy difference $\Delta h = h_{out} - h_{in}$ and the specific entropy difference $\Delta s = s_{out} - s_{in}$.

In this work, the actual specific work w_{net} that is required by the hydrogen liquefaction process is defined as the specific energy consumption *SEC*. To decrease the specific energy consumption *SEC* and the electricity costs of the hydrogen liquefaction process, a high exergy efficiency η_{ex} is desired [Cardella et al. 2017c].

3.1.3 Thermodynamics of process components

In order to understand the basic cryogenic refrigeration cycles used in hydrogen liquefaction processes, the relevant thermodynamic models for the process components are explained within this section.

Compression

Compressors are used for the compression of gases from a lower inlet pressure level p_{in} to a higher outlet pressure level p_{out}. The First Law of Thermodynamics in the form of the energy balance in Equation (3.1) for steady-state open flow systems can be applied to the compressor system illustrated in Figure 3.2:

$$P_{comp} = \dot{m} \cdot \Delta h = \dot{m} \cdot (h_{out} - h_{in}) \ , \tag{3.9}$$

assuming an adiabatic compressor $\dot{Q} = 0$ and neglecting the variations in the kinetic and potential energy [Stephan et al. 2007]. For a compressor the specific enthalpy difference Δh across the compressor corresponds to the required specific compression work and is positive ($\Delta h > 0$). A power input $P_{comp} > 0$ at the shaft is required to drive the compressors in cryogenic refrigeration and liquefaction processes.

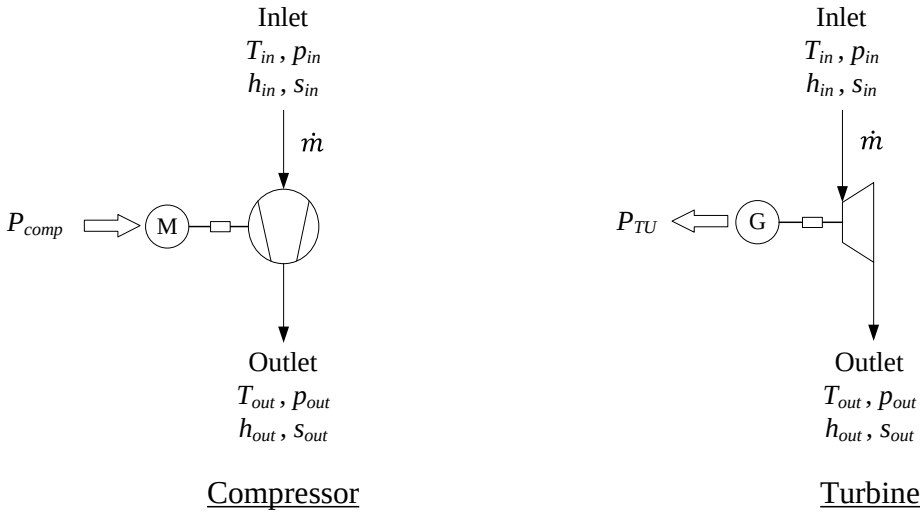

Figure 3.2: Schematic drawing of a compressor system (left) and turbine system (right)

For the calculation of the actual compressor power P_{comp}, it is common to assume an isentropic compression which corresponds to an ideal reversible adiabatic compression with no friction losses [Stephan et al. 2007]. In an isentropic compression, the specific entropy of the inlet stream s_{in} is equal to the specific entropy of the outlet stream s_{out}. In this case, the specific isentropic enthalpy difference $\Delta h_{is} = h_{out,is} - h_{in}$ across the compressor is calculated with the specific isentropic enthalpy of the outlet stream $h_{out,is}$ with the condition $s_{in} = s_{out}$. In real compressors, the specific entropy

difference $\Delta s = s_{out} - s_{in}$ across the compressor increases ($\Delta s > 0$). The actual specific enthalpy difference Δh is calculated with the isentropic efficiency η_{is} [Stephan et al. 2007]:

$$\eta_{is} = \frac{h_{out,is} - h_{in}}{h_{out} - h_{in}} . \tag{3.10}$$

The actual compressor power P_{comp} can be determined from the isentropic efficiency η_{is} of the compressor with the following equation:

$$P_{comp} = \dot{m} \cdot \frac{1}{\eta_{is}} \cdot (h_{out,is} - h_{in}) . \tag{3.11}$$

In real compressors, further mechanical losses of the compressor and other compressor parts, e.g. bearings, seals, gear-box, need to be considered and are typically included in the mechanical efficiency η_{mech} [Campbell 2014]. For the conversion of electrical energy to the mechanical energy, an electrical motor efficiency η_{el} is assumed.

Expansion without work

The refrigeration in cryogenic refrigeration and liquefaction processes is produced by the expansion of a fluid. The expansion of a fluid through a throttle valve, the Joule-Thomson (JT) valve, is the most simple and inexpensive option for this task. The JT expansion is based on the JT effect: the expansion of a fluid stream from a higher pressure (HP) level p_{HP} to a lower pressure (LP) level p_{LP} through a JT valve causes a temperature difference ΔT across the JT valve [Hausen & Linde 1985].

According to the First Law of Thermodynamics in the form of the energy balance described in Equation (3.1), a throttling process carried out without any flow of heat $\dot{Q} = 0$ or mechanical power $P = 0$ leads to an isenthalpic process in which the specific enthalpy difference Δh across the JT valve is $\Delta h = 0$.

The JT coefficient μ_{JT} of a fluid is an important parameter for the design of cryogenic refrigeration and liquefaction processes. The JT coefficient μ_{JT} defines the behaviour of a fluid in a JT expansion and is dependent on both temperature T and pressure p [Maytal & Pfotenhauer 2012]:

$$\mu_{JT} = \left(\frac{dT}{dp} \right)_h . \tag{3.12}$$

In a temperature-pressure diagram, the curve at which the JT coefficient is $\mu_{JT} = 0$ is defined as the inversion curve and the respective temperature is defined as the inversion temperature T_{inv} [Hausen & Linde 1985]. Below the inversion temperature T_{inv}, a fluid throttled in a JT valve cools down ($\mu_{JT} > 0$) while it warms up ($\mu_{JT} < 0$) when it is expanded above T_{inv}.

The JT coefficients μ_{JT} for helium, hydrogen and neon as a function of temperature T are plotted in Figure A.1 in the Appendix A.

Expansion with work

The expansion of a gas from p_{HP} to p_{LP} in a turbine expander is a more efficient option for refrigeration. In a turbine expander, work is extracted from the expanding fluid and is converted to mechanical work at the turbine shaft [Stephan et al. 2007].

The turbine power P_{TU} resulting from the fluid expansion can be determined by applying the First Law of Thermodynamics to the turbine system in Figure 3.2:

$$P_{TU} = \dot{m} \cdot (h_{in} - h_{out}) \ , \tag{3.13}$$

with the identical assumptions made for Equation (3.9). The isentropic efficiency η_{is} of the turbine expander is defined as [Stephan et al. 2007]:

$$\eta_{is} = \frac{h_{out} - h_{in}}{h_{out,is} - h_{in}} \, . \tag{3.14}$$

The isentropic efficiency η_{is} is used for the calculation of the turbine power P_{TU}:

$$P_{TU} = \eta_{is} \cdot \dot{m} \cdot (h_{in} - h_{out,is}) \ . \tag{3.15}$$

For the expanded fluid with $p_{out} < p_{in}$, the specific enthalpy at the turbine outlet h_{out} is lower than the specific enthalpy at the turbine inlet ($h_{out} < h_{in}$). Consequently, also the temperature at the turbine outlet T_{out} is lower than the temperature at the turbine inlet T_{in}. For a turbine power $P_{TU} > 0$, the expansion in a turbine always leads to a temperature decrease $\Delta T < 0$.

Heat transfer

Heat exchangers transfer the heat between different fluid streams and are a core component of thermodynamic refrigeration and liquefaction processes. A schematic drawing of a heat exchanger is shown in Figure 3.3 with the heat flow rate $\dot{Q}$ that is transferred from the warm stream (w) to the cold stream (c).

The total heat flow rate $\dot{Q}$ that is transferred in the steady-state heat exchanger in Figure 3.3 can be determined by applying the energy balances on both the fluid streams from the inlet to the outlet of the heat exchanger:

$$\dot{Q} = \dot{m}_w \cdot (h_{w,in} - h_{w,out}) = \dot{m}_c \cdot (h_{c,out} - h_{c,in}) \ , \tag{3.16}$$

assuming that there is no heat inleak from the environment to the heat exchanger as well as neglecting the variation in the kinetic and potential energy [Baehr & Stephan 2004].

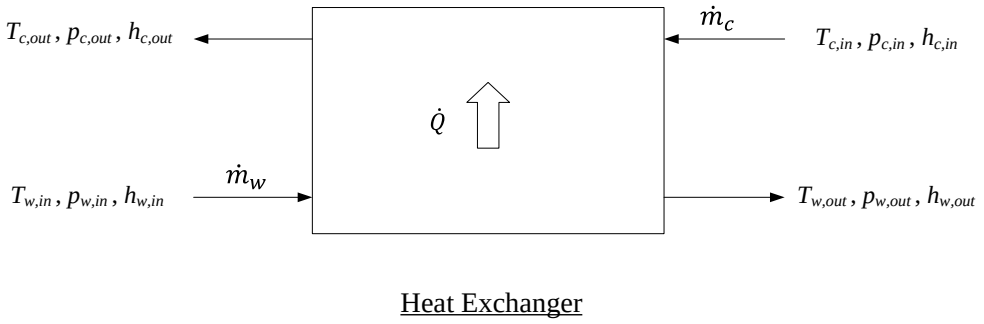

Figure 3.3: Schematic drawing of a counter-current heat exchanger transferring the heat from a warm stream (w) to a cold stream (c)

A further correlation between the temperature difference ΔT of the fluid streams and the total transferred heat flow rate $\dot{Q}$ is given by the following equation:

$$\dot{Q} = U \cdot A \cdot \Delta T_{log} \,. \tag{3.17}$$

The heat flow rate $\dot{Q}$ in Equation (3.17) is calculated with the heat transfer coefficient U, the heat transfer surface A and the logarihtmic mean temperature difference (LMTD) ΔT_{log} between the streams [Polifke & Kopitz 2005].

3.1.4 Refrigeration cycles

The basic thermodynamic refrigeration cycles used in hydrogen liquefaction processes are described within this section. The refrigeration cycles are based on the following successive process steps in which the refrigerant stream undergoes a:

1.) **Compression** in a compressor close to ambient temperature T_{amb}.

2.) **Precooling** in a heat exchanger to an intermediate precooling temperature.

3.) **Expansion** in a JT valve or in an expander.

4.) **Warming-up** in a heat exchanger to remove the heat from warm streams.

The Joule-Thomson (JT) Cycle, the Reversed Brayton Cycle and the Claude Cycle [Timmerhaus & Flynn 1989, Flynn 2004] are the main thermodynamic refrigeration cycles employed in the hydrogen liquefaction processes within this work.

Joule-Thomson Cycle

A schematic drawing of a simplified Joule-Thomson (JT) Cycle is shown in Figure 3.4 for the cooling of a hydrogen (H_2) stream with the mass flow rate $\dot{m}$. The main advantage of the JT Cycle is that it is simple: it requires only a JT valve to expand the refrigerant stream and produce cold. The JT Cycles are implemented with pure refrigerant fluids or with fluid mixtures.

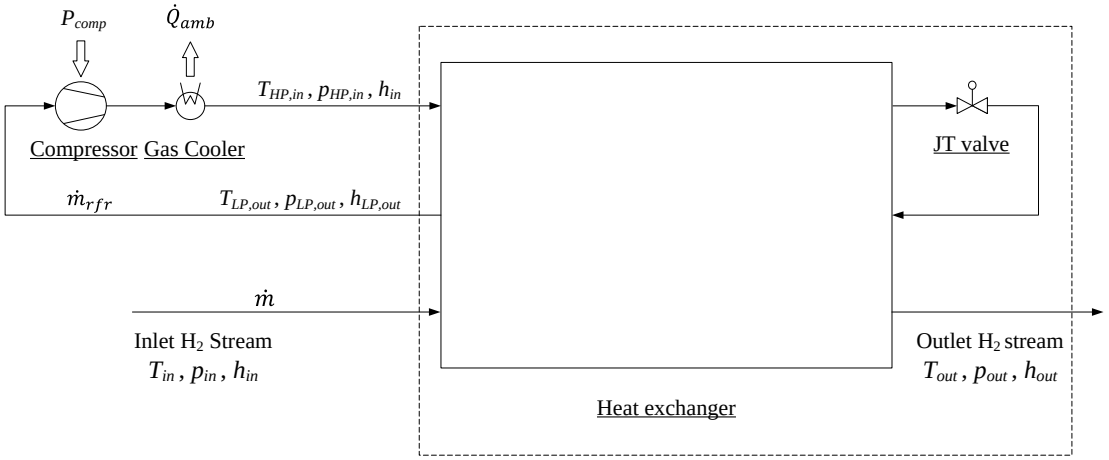

Figure 3.4: Schematic drawing of a simplified Joule-Thomson (JT) refrigeration cycle with a JT valve

The main drawback of the JT Cycle is that the refrigeration is limited by the JT coefficient μ_{JT}. The cooling temperature that can be achieved at the outlet of the JT valve is limited by the inversion temperature T_{inv} of the refrigerant as well as by the temperature at which the refrigerant solidifies.

The expansion in the JT valve of the JT cycle can produce a temperature decrease only if the expansion of the used refrigerant fluid is carried out below its inversion temperature T_{inv}. Refrigerant fluids with inversion temperatures T_{inv} that are below ambient temperature $T_{inv} < T_{amb}$ need to be precooled to a temperature $T < T_{inv}$ before an expansion with temperature reduction can take place across the JT valve. In hydrogen liquefaction processes, the expansion in JT valves is typically employed for the expansion into the two-phase region at temperatures below their critical temperature T_{crit} [Ohlig & Decker 2013]. At the outlet of the JT valve, the JT cycle can thus produce liquid that can be evaporated with high heat transfer coefficients U [Alekseev 2014].

Reverse Brayton cycle

A schematic drawing of a simplified Reverse Brayton Cycle is illustrated in Figure 3.5. In a Reverse Brayton Cycle, the expansion of the refrigerant stream is carried out only by turbine expanders. Henceforth in this work the abbreviated term “Brayton Cycle” refers to the Reversed Brayton Cycle.

Compared to the JT Cycle, the Brayton Cycle can produce refrigeration through the turbine expander power P_{TU}. The minimum operating temperature T_{min} that can be achieved in a Brayton Cycle is limited by the temperature at which the used refrigerants solidify. A further practical limit to T_{min} is given by the turbine design. A two-phase flow in the turbine is technically challenging and is typically avoided [Ohlig & Decker 2013]. Therefore, Brayton Cycles are often operated only in the gas phase.

Claude Cycle

A schematic drawing of a simplified Claude Cycle is illustrated in Figure 3.6. The Claude Cycle can be considered as a combination of the JT Cycle and the Brayton Cycle. The refrigerant stream is split into a first refrigerant stream which is expanded in a turbine expander (Brayton part) and a second refrigerant stream which is further cooled before being expanded in a JT valve (JT part) at the cold end [Ohlig & Decker 2013]. Within the Claude Cycle, the turbine expansion is used for the precooling of the JT stream and to reduce the inlet temperature to the JT valve below the inversion temperature T_{inv} [Alekseev 2014].

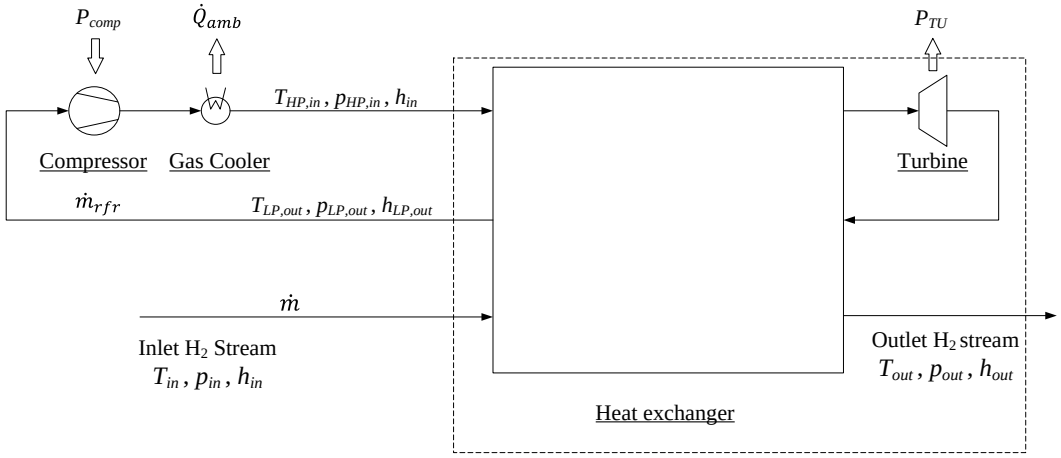

Figure 3.5: Schematic drawing of a simplified Reverse Brayton Cycle

3.2 Hydrogen allotropes and ortho-para conversion

Hydrogen is by far the most abundant element in the observable universe [Lauermann et al. 2013]. The diatomic hydrogen molecule has a molar mass $\bar{M} = 2.0159\,\mathrm{kg/kmol}$. In order to be liquefied, hydrogen needs to be cooled to low cryogenic temperatures. The normal boiling point (NBP) temperature is $T_{sat} = 20.4\,\mathrm{K}$.

A challenge in hydrogen liquefaction processes are the existing different forms of the hydrogen allotropes. The difference in the thermodynamic and physical properties of the different hydrogen allotropes is significant and have an important impact on the hydrogen liquefaction process design [Lipman et al. 1963].

Parts of this section are published in Donaubauer et al. 2018.

3.2.1 Allotropic forms of hydrogen

The two allotropic forms of the hydrogen molecule are ortho-hydrogen o$-H_2$ and para-hydrogen p$-H_2$. The two hydrogen allotropes differ in their atomic nuclei spins,

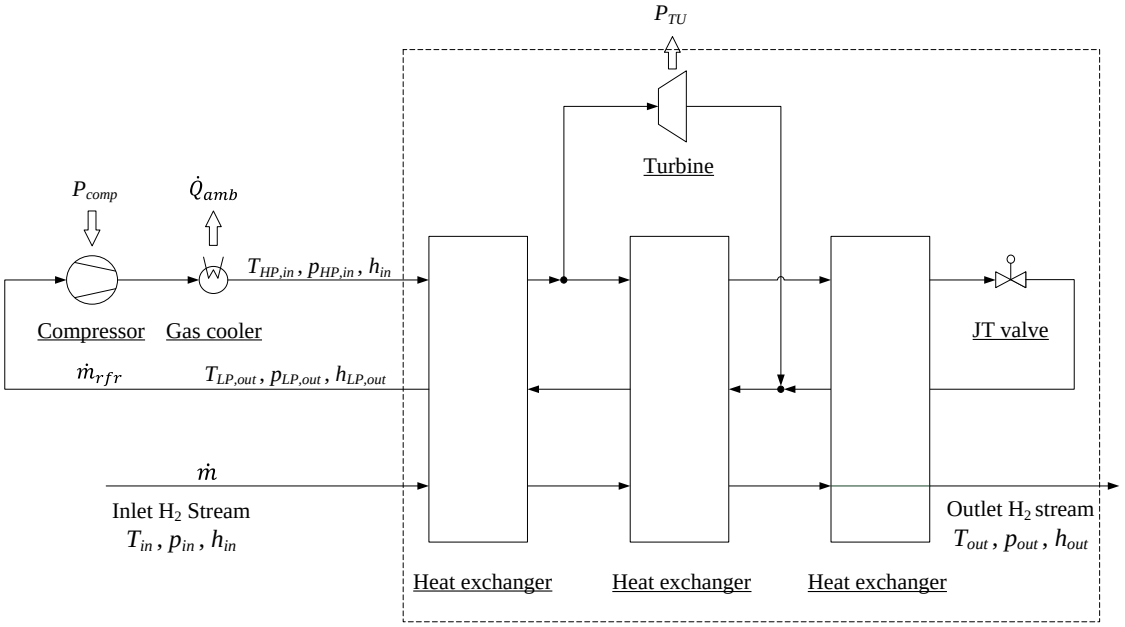

Figure 3.6: Schematic drawing of a simplified Claude Cycle with a turbine expander and a Joule-Thomson valve

as illustrated in Figure 3.7. Ortho-hydrogen o$-H_2$ is defined as the hydrogen allotrope in which the nuclei rotate in the identical direction (symmetric nuclei spin) while para-hydrogen p$-H_2$ is defined as the hydrogen allotrope in which the nuclei rotate in the opposite direction (anti-symmetric) [Bonhoeffer & Harteck 1929].

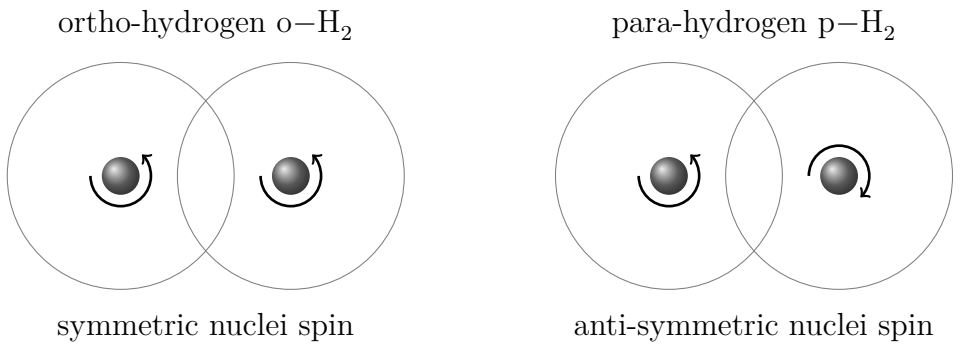

Figure 3.7: Nuclei spins of ortho-hydrogen o$-H_2$ (symmetric) and para-hydrogen p$-H_2$ (anti-symmetric). Adapted from Donaubauer 2015 and Cardella et al. 2015b

Besides the two allotropic forms of hydrogen, equilibrium-hydrogen e$-H_2$ and normal-hydrogen n$-H_2$ are commonly defined mixture compositions of ortho-hydrogen o$-H_2$ and para-hydrogen p$-H_2$ [Lauermann et al. 2013]. Equilibrium hydrogen e$-H_2$ corresponds to the temperature T dependent equilibrium mixture composition of ortho-hydrogen o$-H_2$ and para-hydrogen p$-H_2$ [Leachman et al. 2009]. At ambient temperatures, the hydrogen allotropes reach an equilibrium distribution ratio of

3:1 with a mole fraction of ortho-hydrogen $y_o = 0.75$ and a mole fraction of para-hydrogen $y_p = 0.25$ [Leachman et al. 2009]. This particular composition is referred to as normal-hydrogen n$-H_2$. Henceforth in this work the term "hydrogen" refers to normal-hydrogen.

3.2.2 Ortho- to para-hydrogen conversion

The ortho- to para-hydrogen conversion of the hydrogen feed stream is a major process step that is required in hydrogen liquefaction processes.

A summary of the theoretical background and technical aspects of the ortho- to para-hydrogen conversion is given in the work of Essler 2013.

Equilibrium composition and enthalpy of reaction

The ortho- to para-hydrogen conversion at the temperature T can be carried out only up to the corresponding equilibrium ortho-para hydrogen mixture composition. Due to the lower energy state of para-hydrogen compared to ortho-hydrogen, the ortho- to para-hydrogen conversion is exothermic and is connected with the release of the molar enthalpy of reaction $\Delta\bar{H}_R$ [Leachman et al. 2009]. The equilibrium ortho-para hydrogen mixture composition and the molar enthalpy of reaction $\Delta\bar{H}_R$ are both dependent on temperature [Lauermann et al. 2013]. In Figure 3.8 the equilibrium mole fraction of para-hydrogen y_p^{eq} (left axis) and the molar enthalpy of reaction $\Delta\bar{H}_R$ (right axis) are plotted as a function of temperature.

The equilibrium mole fraction of para-hydrogen y_p^{eq} at ambient temperatures corresponds to normal-hydrogen $y_p = 0.25$. At lower temperatures, the equilibrium ortho-para hydrogen mixture composition shifts towards a higher mole fraction of para-hydrogen y_p. For instance, the equilibrium mole fraction of para-hydrogen p$-H_2$ at a cryogenic temperature $T = 80\,\mathrm{K}$ is about $y_p^{eq} = 0.5$ while it is $y_p^{eq} = 0.998$ close to the normal boiling point (NBP) temperature $T_{sat} = 20.4\,\mathrm{K}$ [Farkas 1935, Leachman et al. 2009]. At decreasing hydrogen temperatures T, the equilibrium ortho-para hydrogen mixture composition shifts from normal-hydrogen to higher mole fractions of para-hydrogen while the exothermic enthalpy of reaction $\Delta\bar{H}_R$ is released. The value of the molar enthalpy of reaction $\Delta\bar{H}_R$ is higher at lower cryogenic temperatures.

The ortho- to para-hydrogen conversion has an important impact on hydrogen liquefaction processes. Unless the reaction rate of the ortho- to para-hydrogen conversion is increased by the use of catalyst materials or by applying magnetic fields [Lauermann et al. 2013, Essler 2013], the natural spontaneous change towards the equilibrium ortho-para hydrogen mixture composition with temperature is slow [Milenko et al. 1997].

In a liquid hydrogen (LH_2) storage tank, liquefied non-catalysed normal-hydrogen n$-H_2$ would slowly convert from the initial mole fraction of para-hydrogen of $y_p = 0.25$ towards the higher equilibrium mole fraction of para-hydrogen y_p^{eq} at the corresponding

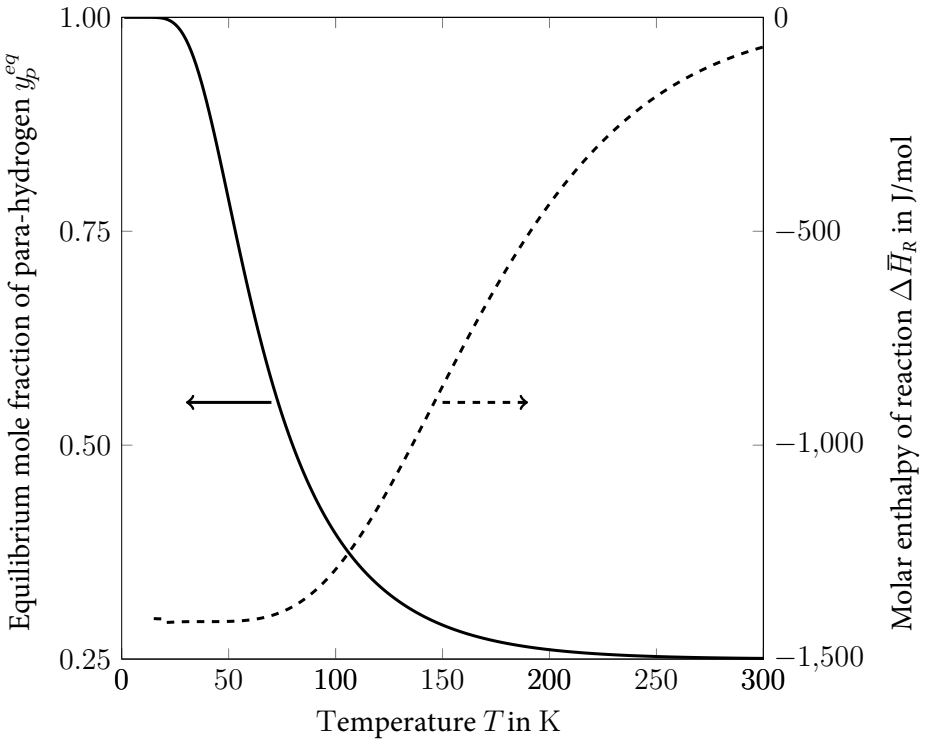

Figure 3.8: Temperature dependency of the equilibrium mole fraction of para-hydrogen y_p^{eq} (left axis) and the molar enthalpy of reaction $\Delta\bar{H}_R$ (right axis) [Cardella et al. 2015b, Cardella et al. 2015b, Donaubauer et al. 2018]

LH_2 storage temperature T_{LH_2}. The released molar enthalpy of reaction $\Delta\bar{H}_R$ is higher than the heat of evaporation $\Delta\bar{H}_V$ of normal-hydrogen n$-H_2$ at the NBP temperature $T_{sat} = 20.4\,K$ [Ohlig & Decker 2013]. The exothermic ortho- to para-hydrogen conversion of liquefied normal-hydrogen n$-H_2$ would evaporate the stored LH_2 product over a short period of time. The higher the inlet mole fraction of para-hydrogen y_p in the storage tank is, the slower are the boil-off losses of LH_2 product with time [Essler 2013]. Therefore, to minimize the LH_2 boil-off losses during storage and transport, a catalytic ortho- to para-hydrogen conversion is required in the hydrogen liquefaction process [Ohlig & Decker 2013].

The heat generated by the released molar enthalpy of reaction $\Delta\bar{H}_R$ from the catalytic ortho- to para-hydrogen conversion has to be removed by additional refrigeration in the hydrogen liquefaction process [Ohlig & Decker 2013]. As described by the Carnot equation (3.6), a heat removal at higher temperatures T is thermodynamically more efficient. In addition to this, the value of the molar enthalpy of reaction $\Delta\bar{H}_R$ is lower at higher temperatures, as illustrated in Figure 3.8 [Cardella et al. 2015b, Donaubauer 2015, Donaubauer et al. 2018]. Therefore, to maximize the exergy efficiency η_{ex} of the hydrogen liquefaction process, the ortho- to para-hydrogen conversion should be performed continuously as the hydrogen is cooled along the equilibrium ortho-para hydrogen mixture curve [Lipman et al. 1963, Ohlig & Decker 2013]. However, in real kinetic reactors, the catalytic ortho- to para-hydrogen conversion does not reach the theoretical equilibrium conversion. The outlet mole fraction of para-hydrogen y_p is

always below the theoretically feasible equilibrium mole fraction of para-hydrogen y_p^{eq}.

Reaction kinetics

Understanding the reaction kinetics for the catalytic ortho- to para-hydrogen conversion is of importance for the thermodynamic efficient and economically viable design of hydrogen liquefaction processes [Lipman et al. 1963].

Paramagnetic catalyst materials can change the direction of the nuclei spins and catalyse the ortho- to para-hydrogen conversion [Essler 2013]. This was first discovered by Farkas & Sachsse 1933 and was later studied by Wigner 1933. Several solid catalyst materials for the ortho- to para-hydrogen conversion were studied and kinetic investigations were published in literature, for instance by [Weitzel et al. 1960b, Buyanov 1960, Barrick et al. 1965, Ilisca 1992]. For the catalytic ortho- to para-hydrogen conversion, solid catalyst materials based on iron oxide or chromium oxide are the most commonly used [Ohlig & Decker 2013]. Due to the inexpensive manufacturing hydrous ferric oxide $Fe(OH)_3$ is employed in the majority of industrial hydrogen liquefaction processes. The effectiveness of hydrous ferric oxide as an ortho- to para-hydrogen conversion catalyst was demonstrated by Weitzel et al. 1960b and Barrick et al. 1965.

The heterogeneous catalysis for the ortho- to para-hydrogen conversion on a catalyst surface is divided into seven steps [Weitzel et al. 1960a]:

1.) Diffusion of ortho-hydrogen from the main fluid stream to the surface.

2.) Diffusion of ortho-hydrogen through the catalyst pores.

3.) Adsorption of ortho-hydrogen on surface.

4.) Reversible ortho-para-hydrogen surface reaction.

5.) Desorption of the para-hydrogen.

6.) Diffusion of para-hydrogen through the catalyst pores to the surface of the catalyst.

7.) Diffusion of para-hydrogen into the main fluid stream.

The kinetic model approach is essential to determine the reaction rate r for the catalytic ortho- to para-hydrogen conversion. The influence of the four diffusion steps of ortho-hydrogen and para-hydrogen on the overall reaction rate r was shown to be negligible for hydrous ferric oxide catalyst [Weitzel et al. 1960a].

In the majority of the previously published works, a first-order kinetic approach was chosen to describe the reaction kinetics of the catalytic ortho- to para-hydrogen conversion [Donaubauer 2015, Donaubauer et al. 2018]. The first-order kinetic approach assumes that the reaction adsorption and desorption steps can be neglected [Weitzel et al. 1960a].

For the overall reaction rate r, the first-order kinetic approach considers only the catalyst surface reaction step. The first-order kinetic approach for the reaction rate r can thus be expressed with the reaction rate constant k as a function of the molar

concentration c_{H_2} [Cardella et al. 2015b, Donaubauer 2015, Donaubauer et al. 2018]:

$$r = k_{fo} \cdot c_{H_2} \cdot (y_o - y_o^{eq}) \ , \tag{3.18}$$

with the difference between the fraction of ortho-hydrogen y_o and the equilibrium fraction of ortho-hydrogen y_o^{eq}. In contrast to the simple first-order kinetic approach, a Langmuir-Hinshelwood kinetic approach that considers the ortho-hydrogen y_o adsorption and the para-hydrogen y_p desorption processes in the overall reaction rate r was studied by Hutchinson 1966.

3.3 Thermodynamic property estimation

The accurate estimation of thermodynamic fluid properties with equations of state (EOS) is essential for the modelling and simulation of hydrogen liquefaction processes. The theory and models for the thermodynamic property estimation of pure fluids and fluid mixtures are described in literature, for instance by Poling et al. 2001 and Leachman et al. 2017.

The hydrogen liquefaction processes require the use of fluids that can be employed as refrigerants below the critical point temperature T_{crit} of hydrogen without solidifying. These refrigerants fluids are restricted to hydrogen, helium (He) and neon (Ne) as well as to fluid mixtures of helium-hydrogen-neon.

For the hydrogen precooling above the critical point temperature T_{crit} of hydrogen, several additional fluids can be employed as refrigerants without the risk of solidification. For instance, oxygen (O_2) with the triple point temperature $T_{trp} = 54.36\,\mathrm{K}$ and nitrogen (N_2) with $T_{trp} = 63.15\,\mathrm{K}$ [Lemmon et al. 2013] can be employed as refrigerants for the hydrogen precooling below the temperature $T < 80\,\mathrm{K}$. Due to the risk of explosive mixtures with hydrogen, oxygen can not be considered as viable refrigerant in hydrogen liquefaction processes.

The different forms of EOS models for the fluids relevant in this work are described in the following sections with reference to published literature.

3.3.1 Equations of state for hydrogen

For an accurate process simulation and design, the differences in the thermophysical properties of hydrogen allotropes need to be considered in equations of state (EOS) [Leachman & Richardson 2012].

A literature review on different forms of EOS available for hydrogen, ranging from simple cubic EOS like Soave-Redlich-Kwong (SRK) [Soave 1972] and Peng-Robinson (PR) [Peng & Robinson 1976] to more advanced EOS, is given by Essler 2013. The EOS for para-hydrogen developed by Younglove 1982 and the EOS for ortho-, para-,

normal- and equilibrium-hydrogen implemented in the fluid property package software GASPAK© [Arp et al. 1999] are empirical equations with coefficients that were fitted with experimental data [Leachman et al. 2009, Essler 2013]. Both the models of Younglove 1982 and Arp et al. 1999 consider only the differences in the ideal gas specific isobaric heat capacity c_p^0 between the hydrogen allotropes [Essler 2013]. The state-of-the-art fundamental EOS for ortho-, para- and normal-hydrogen developed by Leachman et al. 2009 are implemented in the Reference Fluid Thermodynamic and Transport Properties software REFPROP [Lemmon et al. 2013] of the National Institute of Standards and Technology (NIST). Compared to the EOS of Younglove 1982 and Arp et al. 1999, the EOS of Leachman et al. 2009 are able to predict the properties of hydrogen allotropes with a higher accuracy, particularly at cryogenic temperatures near the critical point.

The triple point, the critical point and the normal boiling point of ortho-hydrogen and para-hydrogen as given by Leachman et al. 2009 are listed in Table 3.1.

Table 3.1: The critical point, the triple point and the normal boiling point (NBP) of ortho-hydrogen (o$-H_2$) and para-hydrogen (p$-H_2$) [Leachman et al. 2009]

Fluid	Critical point		Triple point	NBP, 1.01 bar
	T_{crit} in K	p_{crit} in bar	T_{trp} in K	T_{sat} in K
Ortho-hydrogen	33.22	13.11	14.01	20.38
Para-hydrogen	32.94	12.86	13.80	20.27

The EOS of Leachman et al. 2009 are in the form of the dimensionless reduced Helmholtz free energy α:

$$\alpha(\tau,\delta) = \alpha^0(\tau,\delta) + \alpha^{res}(\tau,\delta) \,, \tag{3.19}$$

with the ideal-gas contribution α^0 and a residual contribution α^{res} [Leachman et al. 2009]. The reduced Helmholtz free energy α is dependent on temperature T and density ϱ through the reciprocal reduced temperature τ [Leachman et al. 2009]:

$$\tau = \frac{T_{crit}}{T} \,, \tag{3.20}$$

and the reduced density δ [Leachman et al. 2009]:

$$\delta = \frac{\varrho_{crit}}{\varrho} \,. \tag{3.21}$$

For the hydrogen allotropes, the EOS of Leachman et al. 2009 implemented in REFPROP [Lemmon et al. 2013] in the form given in Equation 3.19 are employed in this work for the calculation of relevant thermodynamic properties such as the specific enthalpy h and the specific entropy s.

Substantial differences are found in the thermodynamic properties between the different hydrogen allotropes, as for instance in the specific isobaric heat capacity c_p, the specific enthalpy h and the specific entropy s [Leachman et al. 2009]. The specific isobaric heat capacity c_p of normal- and para-hydrogen is plotted as a function of temperature T in Figure A.2 in the Appendix A.

The differences in most of the transport properties between different hydrogen allotropes are minor [Leachman et al. 2007, Essler 2013]. For instance, the viscosity is almost independent on the ortho- and para-hydrogen mixture composition [Essler 2013]. In contrast the thermal conductivity λ is strongly dependent on the ortho- and para-hydrogen mixture composition [Roder 1984].

Ortho- and para-hydrogen mixture compositions

The detailed engineering of hydrogen liquefaction processes with ortho- to para-hydrogen conversion requires the estimation of hydrogen properties at arbitrary ortho- and para-hydrogen mixture compositions [Essler 2013]. In particular, the specific enthalpy h is required in process simulation to determine the required refrigeration [Essler 2013].

At present, the state-of-the-art fundamental EOS of Leachman et al. 2009 in REFPROP [Lemmon et al. 2013] can be used only for the estimation of ortho-, para- and normal-hydrogen properties. Based on the fundamental EOS of Leachman et al. 2009, a new hybrid EOS using statistical thermodynamics for the accurate estimation of hydrogen properties at all ortho- and para-hydrogen mixture compositions by Leachman & Richardson 2012 may be implemented in REFPROP [Lemmon et al. 2013] in the future.

An option for the estimation of thermodynamic properties at all ortho- and para-hydrogen mixture compositions is to assume an ideal mixture of ortho- and para-hydrogen and use ideal mixture equations [Hust & Stewart 1965, Arp et al. 1999]. In this case, the specific enthalpy h and the specific entropy s of an ideal ortho- and para-hydrogen mixture can be determined as a function of the temperature T, pressure p and the mole fraction of para-hydrogen fraction y_p by using the EOS available for normal- and para-hydrogen [Essler 2013]. An equilibrium-hydrogen model adapting the ideal gas specific isobaric heat capacity c_p^0 of para-hydrogen to the c_p^0 of equilibrium-hydrogen as described by Woolley et al. 1948 and Le Roy et al. 1990 is proposed in literature [Valenti et al. 2012].

3.3.2 Equations of state for helium, neon and nitrogen

Helium (He), hydrogen (H_2), neon (Ne) and nitrogen (N_2) are used as refrigerant fluids for the hydrogen liquefaction processes within this work. Relevant fluid properties are given in Table 3.2.

Nitrogen is limited by a triple point temperature of $T_{trp} = 63.15\,\mathrm{K}$ [Lemmon et al. 2013] and is used as cryogenic refrigerant fluid at temperatures near the normal boiling

point (NBP). Besides hydrogen, helium and neon are the only fluids with a triple point temperature T_{trp} that is below the critical point temperature of hydrogen T_{crit}.

Table 3.2: Relevant physical properties of helium, normal-hydrogen, neon and nitrogen, as given in REFPROP [Lemmon et al. 2013]

Fluid	Molar mass	Critical point		Triple point	NBP, 1.01 bar
	$\bar{M}$ in kg/kmol	T_{crit} in K	p_{crit} in bar	T_{trp} in K	T_{sat} in K
Helium	4.00	5.20	2.28	2.18	4.22
Hydrogen	2.02	33.15	12.96	13.96	20.37
Neon	20.18	44.49	26.79	24.56	27.10
Nitrogen	28.01	126.19	33.96	63.15	77.36

The state-of-the-art equations of state (EOS) for the thermodynamic property estimation of helium, neon and nitrogen are in the form of the fundamental Equation 3.19 for the dimensionless reduced Helmholtz free energy α [Jacobsen et al. 1997, Leachman et al. 2017]. For the thermodynamic property estimation within this work, the EOS implemented as standard models in REFPROP [Lemmon et al. 2013] and developed by Vega 2013 for helium-4, by Katti et al. 1986 for neon and by Span et al. 2000 for nitrogen are employed.

3.3.3 Equations of state for fluid mixtures

The fluid mixtures considered as refrigerants within this work are binary fluid mixtures of neon with helium or hydrogen and multi-component fluid mixtures of nitrogen with hydrocarbons.

The cubic equations of state (EOS) of Soave-Redlich-Kwong (SRK) [Soave 1972] and Peng-Robinson (PR) [Peng & Robinson 1976] are widely used for fluid mixtures composed of common light gases with hydrocarbons [Poling et al. 2001]. Modern mixture EOS are based on the fundamental equation for the reduced mixture Helmholtz free energy $\alpha_{mix}(\delta,\tau,y)$ [Jacobsen et al. 1997] that is dependent on reduced density δ, the reciprocal reduced temperature τ and the mole fractions of the mixture composition y [Jacobsen et al. 1997, Kunz et al. 2007].

Mixtures of neon with helium and hydrogen

For thermodynamic property estimation of cryogenic binary mixtures of neon with helium or hydrogen, accurate mixture equations of state (EOS) in the form of the reduced mixture Helmholtz free energy $\alpha_{mix}(\delta,\tau,y)$ are in the development [Richardson et al. 2015].

Mixtures of nitrogen with hydrocarbons

The fluids with a triple point temperature above the triple point temperature of nitrogen $T_{trp} = 63.15\,\mathrm{K}$ that are used in refrigerant mixtures within this work are listed with relevant properties in Table A.1 in the Appendix A.

Mixed refrigerant (MR) fluids composed of nitrogen and hydrocarbons are widely used as cryogenic refrigerants for the liquefaction of natural gas at around 120 K and are also considered in this work.

The cubic EOS of Soave-Redlich-Kwong (SRK) [Soave 1972] and the cubic EOS of Peng-Robinson (PR) [Peng & Robinson 1976] are the commonly used equations for the estimation of fluid mixture properties composed of nitrogen and hydrocarbons [Khan & Lee 2013]. Compared to common cubic EOS, the more recent GERG-2008 wide range fundamental EOS for natural gas and mixtures [Kunz & Wagner 2012] is claimed to achieve a higher accuracy [Kunz et al. 2007, Dauber 2011].

3.3.4 Solid-liquid equilibria

The freezing of refrigerants can cause severe damages to process equipment and operating personnel [Maytal & Pfotenhauer 2012]. Therefore, the cryogenic fluids used in hydrogen liquefaction processes are operated at temperatures in which a solidification of the fluid is avoided.

A fluid mixture with higher boiling refrigerant fluids can increase the thermodynamic efficiency of a cryogenic refrigeration processes [Maytal & Pfotenhauer 2012]. The efficient refrigeration at low cryogenic temperatures is limited by the mixture melting point temperature $T_{melt,mix}$. For pure fluids, the triple point temperature T_{trp} represents a theoretical operating temperature limit. To avoid the risk of refrigerant freezing, the knowledge of the solid-liquid equilibrium (SLE) of fluid mixtures is essential. The SLE of binary mixtures such as hydrogen-neon [Brouwer et al. 1970] and nitrogen-ethane [Brouwer et al. 1970] as a function of the molar composition is available from experimental measurements in literature. The experimental SLE data for fluid mixtures of three or more refrigerant components is scarce.

The mixture melting point is particularly relevant for the fluid mixtures of nitrogen and hydrocarbons considered within this work. A simple conservative approach to estimate $T_{melt,mix}$ of a fluid mixture is given by Maytal & Pfotenhauer 2012:

$$T_{mix,melt} = \sum_i y_i \cdot T_{melt,i}\,, \tag{3.22}$$

with the mole fraction y_i and melting point $T_{melt,i}$ of the pure fluid component i in the fluid mixture. A further theoretical approach to estimate the SLE of cryogenic mixtures is given by Robinson 1995 and considers the molar enthalpy of fusion $\Delta\bar{H}_{S,i}$, the molar volume $\bar{V}$ and the solubility parameter $\delta_{S,i}$ of the fluid component i.

3.4 Ideal work of hydrogen liquefaction

The hydrogen liquefaction process is energy intensive. The minimum specific work w_{ideal} required for an ideal hydrogen liquefaction process can be calculated with Equation (3.8) at the inlet and outlet conditions of the hydrogen feed stream and the liquid hydrogen (LH_2) product. The minimum specific work w_{ideal} required for an ideal hydrogen liquefaction process with an inlet hydrogen pressure $p_{in} = 1.01\,\text{bar}$, an inlet temperature $T_{in} = 303\,\text{K}$ and the mole fraction of para-hydrogen $y_p = 0.25$ (normal-hydrogen) is approximately $w_{ideal} = 3.8\,\text{kWh/kg}\ LH_2$ at a LH_2 product storage pressure $p_{LH_2} = 1.01\,\text{bar}$ and the respective final equilibrium mole fraction of para-hydrogen $y_p = 0.998$.

4 Hydrogen liquefaction processes

The principles of hydrogen liquefaction processes are described in numerous publications in literature [Barron 1985, Ohlig & Decker 2013]. Liquid hydrogen LH_2 is produced in a hydrogen liquefaction process by the cooling and the liquefaction of a gaseous hydrogen stream GH_2 from ambient temperature at about $T_{amb} \approx 300\,\mathrm{K}$ to the saturated LH_2 temperature $T_{sat,l} = 20.3\,\mathrm{K}$ at the normal pressure. Hydrogen was first liquefied by Dewar 1898. In the following century, more efficient and larger industrial hydrogen liquefaction processes were implemented.

A simplified block diagram for the hydrogen liquefaction process is illustrated in Figure 4.1. The hydrogen feed gas stream GH_2 produced in a hydrogen production plant is purified and is then fed to the hydrogen liquefier coldbox with a feed pressure p_{feed} between typically $p_{feed} = 15 - 30\,\mathrm{bar}$ [Haeussinger et al. 2000a]. The hydrogen feed pressure p_{feed} and the hydrogen feed purity are dependant on the GH_2 production and purification processes upstream of the hydrogen liquefier. For example the GH_2 produced in methane steam reforming (SMR) plants is typically purified by a pressure swing adsorption (PSA) unit and is then fed to the hydrogen liquefier coldbox with a purity of approximately 99.999 mole-% with 10 ppm of residual impurities [Ohlig & Decker 2013].

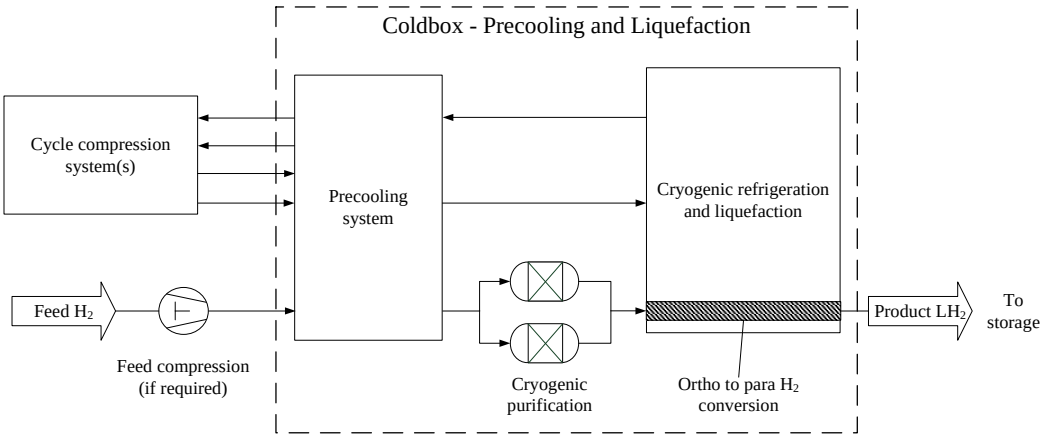

Figure 4.1: Simplified process flow diagram for hydrogen liquefaction [Cardella et al. 2017d]

The hydrogen liquefaction process can be subdivided into different process steps. The cooling and liquefaction of hydrogen is typically carried out with the aid of two or more refrigerant systems at different temperature levels. In a first step prior to the hydrogen liquefaction, the hydrogen feed stream is cooled down to an intermediate precooling temperature T_{PC} by a precooling refrigerant stream or a precooling cycle.

After the precooling, the hydrogen feed stream is conducted through an additional cryogenic purification unit in adsorber vessels. The hydrogen feed gas is subsequently cooled further and catalytically converted from normal-hydrogen with a fraction of para-hydrogen $y_p = 0.25$ to a higher final fraction of para-hydrogen $y_p \geq 0.98$ [Ohlig & Decker 2013].

The cooling capacity below the precooling temperature T_{PC} is provided by a cryogenic refrigeration cycle. The hydrogen feed stream is then expanded from the feed pressure level p_{feed} to the final LH_2 product storage pressure p_{LH_2} and is then liquefied. The final LH_2 product storage pressure is typically in the range $p_{LH_2} = 1.2 - 2.5\,\text{bar}$ and the final LH_2 purity is typically above 99.99999 mole-% [Bracha & Decker 2008].

Downstream of the hydrogen liquefaction process, the LH_2 product is stored in cylindrical or spherical LH_2 storage tanks [Taylor et al. 1986]. From the storage tanks, the LH_2 product is filled into trailers or ship carriers at the filling stations for the distribution to the customers [Bracha & Decker 2008].

A high number of different hydrogen liquefaction process configurations were implemented in built hydrogen liquefiers or were proposed as conceptual process designs for future large-scale hydrogen liquefiers. As illustrated in Figure 4.2, hydrogen liquefaction processes in this work are categorized by the type of precooling and by the type of cryogenic refrigeration cycle used.

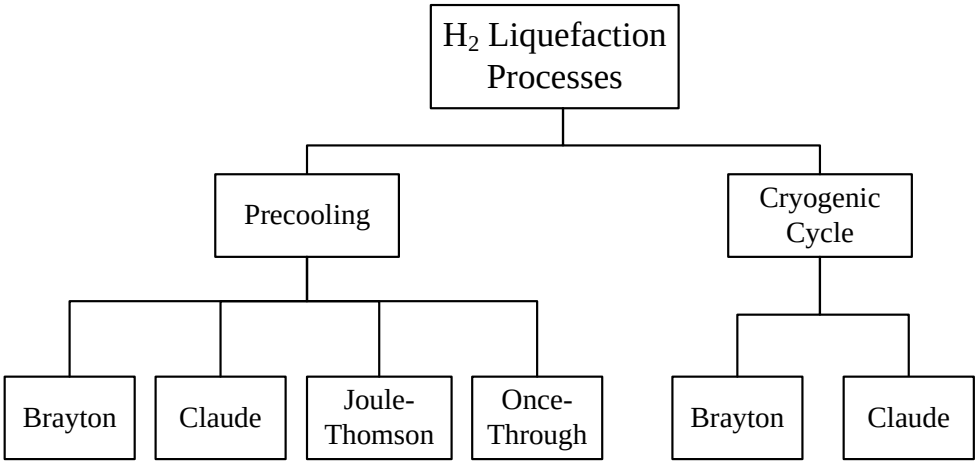

Figure 4.2: Categorization of hydrogen liquefaction processes by type of precooling and cryogenic refrigeration cycle

The hydrogen liquefaction process can be designed also without a precooling refrigerant. In this case, the entire refrigeration capacity is provided by the cryogenic refrigeration cycle. The thermodynamic efficiency of the hydrogen liquefaction process increases by including an additional precooling step. This is mainly due to the possibility of using refrigerants with a higher boiling point than helium and hydrogen at higher temperatures. Based on either pure fluids or fluid mixtures as refrigerants, a large

range of precooling processes can be adopted. The simplest precooling is performed by "once-through" warming up of a precooling refrigerant stream in a heat exchanger without a recirculation. Alternatively as illustrated in Figure 4.2, different closed-loop precooling cycles can be implemented.

The cryogenic refrigeration cycle provides the refrigeration for the cooling and liquefaction of the hydrogen feed stream as well as for the removal of the additional heat that is released by the exothermic ortho- to para-hydrogen conversion. The cryogenic refrigeration is provided at very low temperatures below the critical temperature T_{crit} of hydrogen [Bracha & Decker 2008]. Because of the risks of freezing, the refrigerant fluids available for the cryogenic refrigeration cycle of hydrogen liquefiers are restricted to hydrogen, helium and neon as well as a mixtures of these fluids.

4.1 Built processes

Parts of this section are published in Cardella et al. 2017c.

An overview on built industrial hydrogen liquefiers is given by Krasae-in et al. 2010 and in IDEALHY 2012. Most of the recently installed hydrogen liquefiers are sized for hydrogen liquefaction capacities of up to approximately 10 tpd LH_2 and are installed in the European Union, Japan and USA. In the USA, larger hydrogen liquefiers with a hydrogen liquefaction capacity between 20 tpd and 35 tpd LH_2 are in operation today [Shigekiyo 2015].

The cryogenic refrigeration cycle in built hydrogen liquefaction processes is based either on a Helium Brayton cycle or a Hydrogen Claude cycle [Ohlig & Decker 2013]. The process design is chosen depending on the hydrogen liquefaction capacity, project specific engineering requirements as well as site dependent boundary conditions such as the utility costs for electricity and refrigerants.

In built hydrogen liquefiers, the hydrogen feed stream and the refrigerant streams are typically precooled to an intermediate precooling temperature $T_{PC} \approx 80\,\mathrm{K}$ by a "once-through" liquid nitrogen LN_2 stream [Ohlig & Decker 2013]. Additionally also a closed-loop Nitrogen Claude Cycle (N_2 Claude Cycle) or Brayton Cycle (N_2 Brayton Cycle) can be implemented for hydrogen precooling [Gallarda 2001, Ohlig & Decker 2014].

Because of the low investment costs and simple operation, the precooling with LN_2 is implemented in the majority of the installed hydrogen liquefiers. With this process design, a LN_2 stream is supplied to the hydrogen liquefier coldbox from nearby air separation units (ASU) via vacuum insulated pipes or by trailers [Bracha & Decker 2008]. The LN_2 supply for the hydrogen liquefier is cost effective because the LN_2 is produced in large cost-optimized and thermodynamic efficient ASUs that are built for a high number of customers [Alekseev 2014]. The LN_2 is typically expanded in a JT valve and is then evaporated at a temperature of about 79 K, the boiling point of LN_2 at a pressure of 1.2 bar, and superheated against the streams that are cooling down in a

counter-current plate-fin heat exchanger (PFHX). The warmed up gaseous nitrogen GN_2 is often released to atmosphere or recirculated. No additional expensive equipment such as compressors and turbines is required for LN_2 precooling.

A thermodynamically less efficient precooling design option is to replace the LN_2 precooling with one or more additional cryogenic turbine expander stages operating at a higher temperature within the cryogenic refrigeration cycle [Alekseev 2014]. This process configuration is used particularly in Helium Brayton Cycles in which the electricity costs are comparatively low and the hydrogen liquefier is built in a remote location in which an economic LN_2 supply is not available or expensive. The process configuration without a separate precooling requires the installation of additional cryogenic turbine expanders.

Downstream of the hydrogen precooling, the hydrogen feed stream is conducted through cryogenic adsorber vessels that are installed in parallel configuration for adsorption and regeneration. The cryogenic adsorbers operated at an inlet adsorber temperature $T_{ads} \approx 80\,\mathrm{K}$ are required to remove the residual impurities in the hydrogen feed stream that could freeze at the process temperatures below 80 K [Bracha & Decker 2008].

In recently built industrial hydrogen liquefiers, the required catalytic ortho- to para-hydrogen conversion of the hydrogen feed stream is carried out downstream of the cryogenic adsorber vessels with hydrous ferric oxide $Fe(OH)_3$ catalyst that is filled in the passages of the PFHX [Lipman et al. 1963, Bracha & Decker 2008]. In this manner, a continuous cooling and catalytic ortho- to para-hydrogen conversion is achieved. A thermodynamically less efficient process design option is to perform the catalytic ortho- to para-hydrogen conversion stepwise in adiabatic or isothermal reactor vessels placed at different temperature levels within the hydrogen liquefaction process.

In the cryogenic refrigeration cycle, the refrigeration capacity is provided by the expansion of the helium or hydrogen refrigerant streams in Joule-Thomson (JT) valves or in turbine expanders. The expanded refrigerants are warmed up against the streams that are cooled down in counter-current PFHX.

For the final cooling and liquefaction, the hydrogen feed stream is expanded from the supercritical feed pressure level $p_{feed} > 13\,\mathrm{bar}$ to the LH_2 product storage pressure p_{LH_2} by an isenthalpic expansion in a JT valve [Ohlig & Decker 2013].

As shown in Figure 4.4, the JT expansion can be carried out in an ejector which uses the hydrogen feed stream to compress a flow of hydrogen boil-off gas from the storage tank [Ohlig & Decker 2013]. The hydrogen feed stream which was expanded into the two-phase region in the JT valve is fully liquefied, subcooled and converted to the required fraction of para-hydrogen y_p in the last PFHX [Bracha & Decker 2008].

4.1.1 Helium Brayton Cycle

The state-of-the-art Helium Brayton Cycle is shown in Figure 4.3. In the Helium Brayton Cycle helium is used as refrigerant fluid for the cryogenic refrigeration cycle. The helium refrigerant is compressed from the low pressure (LP) to a high pressure (HP) level of about $p_{HP} = 15 - 20\,\text{bar}$ in an oil-injected helium rotary screw compressor [Ohlig & Decker 2013]. The Helium Brayton Cycle requires an additional oil removal system downstream of the oil-injected rotary screw compressor that is not depicted in Figure 4.3.

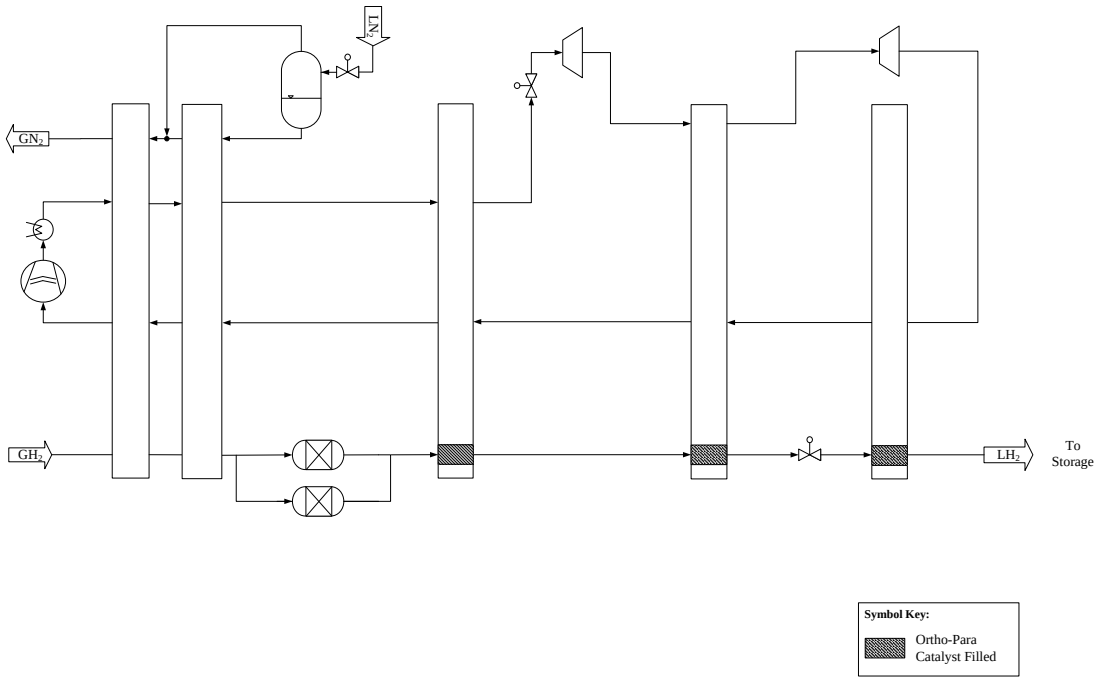

Figure 4.3: State-of-the-art Helium Brayton Cycle with LN_2 precooling. Adapted from [Ohlig & Decker 2013]

The HP helium refrigerant stream is typically precooled by liquid nitrogen LN_2 and is then expanded in the oil or gas bearing helium turbine expanders from the HP to LP level. The LP helium stream is warmed up with the cooled down streams in the counter-current PFHX before being routed to the suction side of the oil-injected helium rotary screw compressor.

The Helium Brayon Cycle is often employed as cryogenic refrigeration cycle for smaller hydrogen liquefiers with a hydrogen liquefaction capacity of up to approximately 3 tpd LH_2 [Ohlig & Decker 2014]. This is mainly due to the relatively low plant capital expenses (CAPEX) required for a Helium Brayton Cycle resulting from the use of cost efficient standardized helium rotary screw compressors [Ohlig & Decker 2013]. Because of the comparatively low thermodynamic efficiency of oil-injected helium rotary screw compressors, the specific energy consumption *SEC* and hence the operating

expenses (OPEX) of hydrogen liquefiers equipped with a Helium Brayton Cycle are relatively high [Ohlig & Decker 2013].

4.1.2 Hydrogen Claude Cycle

For larger hydrogen liquefaction capacities, the electricity costs and thus the specific operating expenses (OPEX) become increasingly important for the process economics of the hydrogen liquefier. Therefore, as stated by Ohlig & Decker 2014, hydrogen liquefiers with a hydrogen liquefaction capacity above approximately 2 tpd LH_2 are typically designed with the Hydrogen Claude Cycle. Compared to the Helium Brayton Cycle, the Hydrogen Claude Cycle is characterized by a higher thermodynamic efficiency and lower OPEX [Ohlig & Decker 2013]. This is mainly due to the lower specific energy consumption *SEC* of the Hydrogen Claude Cycle as well as the lower yearly refrigerant make-up costs required for the hydrogen refrigerant.

The process flow diagram for a state-of-the-art hydrogen liquefier with LN_2 precooling and a Hydrogen Claude Cycle is shown in Figure 4.4. This state-of-the-art hydrogen liquefaction process is based on the 5.5 tpd LH_2 industrial hydrogen liquefier that was built by the Linde AG in Leuna and which is in operation since the year 2007 [Bracha & Decker 2008].

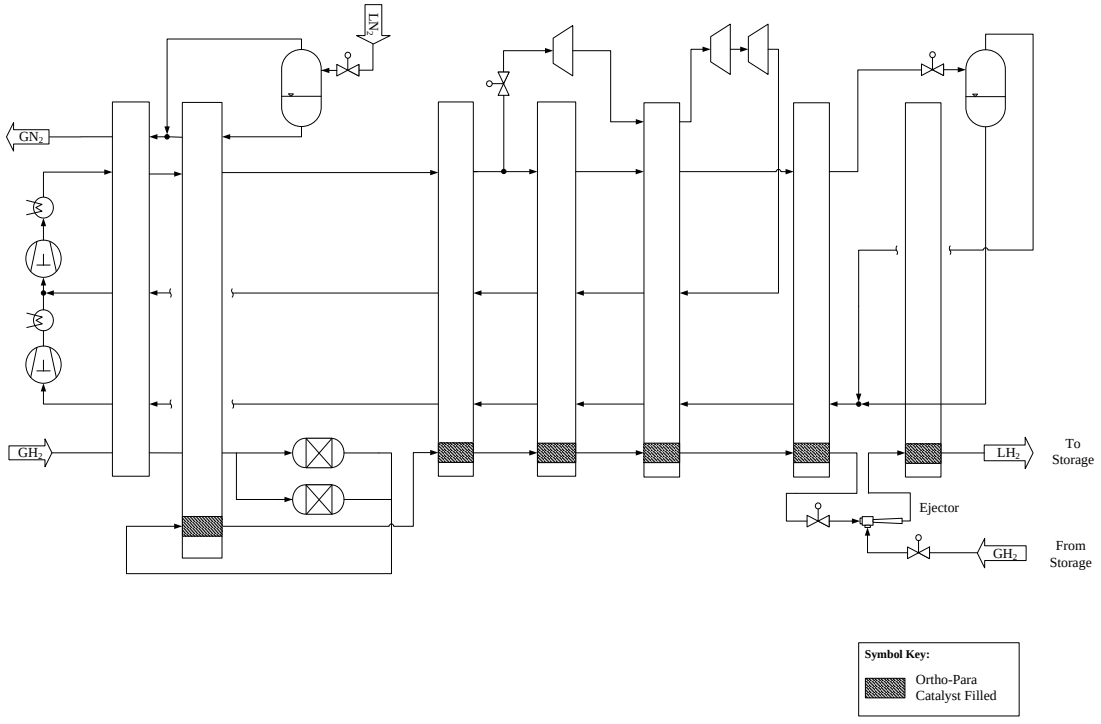

Figure 4.4: State-of-the-art Hydrogen Claude Cycle with LN_2 precooling based on the Leuna hydrogen liquefier. Adapted from [Bracha & Decker 2008]

For the hydrogen compression in the Hydrogen Claude Cycle, the efficient but more expensive reciprocating piston compressors are employed [Ohlig & Decker 2013]. As described by Bracha & Decker 2008 for the hydrogen liquefier in Leuna, the hydrogen refrigerant stream is compressed in two dry-running oil-free reciprocating compressors with inter-cooling. A downstream oil removal system is not required. The Hydrogen Claude Cycle described by Bracha & Decker 2008 includes three cryogenic turbine expanders that are placed in series to subsequently expand the hydrogen refrigerant stream from the HP level of about $p_{HP} = 20\,\text{bar}$ to a medium pressure (MP) level close to $p_{MP} = 5\,\text{bar}$.

As illustrated in Figure 4.4, the hydrogen feed stream and the HP refrigerant streams are precooled by LN_2 in the first counter-current plate-fin heat exchanger (PFHX). Downstream of the precooling, the HP refrigerant stream is split into two hydrogen streams. The first HP refrigerant stream is routed to the cryogenic turbine string for an expansion to the MP level. Before the expansion, the second HP refrigerant stream is cooled further below the critical temperature T_{crit} of hydrogen to a cold end temperature T_{ce} of about $T_{ce} \approx 30\,\text{K}$ [Bracha & Decker 2008].

This HP hydrogen refrigerant stream is expanded in a Joule-Thomson (JT) valve from HP to the low pressure (LP) level into a phase separator. In the Leuna hydrogen liquefier, a LP level of $p_{LP} = 1.2\,\text{bar}$ was chosen for the liquefaction of the hydrogen feed stream at the required LH_2 product storage pressure $p_{LH_2} = 1.3\,\text{bar}$ and product temperature $T_{LH_2} = 21\,\text{K}$ [Bracha & Decker 2008]. An ejector is used to expand the hydrogen feed stream and to re-liquefy the boil-off gas generated in the LH_2 storage tank [Bracha & Decker 2008].

The LP hydrogen refrigerant stream is warmed up close to ambient temperature and is then routed to the suction side of the LP cycle compressor at the outlet of the coldbox. In the LP compressor, the hydrogen refrigerant stream is pressurized from LP to MP pressure. At the LP compressor discharge, the compressed LP hydrogen refrigerant stream is mixed to the main MP hydrogen refrigerant coming from the coldbox and is then compressed in the large MP compressor to the HP level.

As illustrated in Figure 4.5, the Hydrogen Claude Cycle with a thermodynamically improved process can be designed with additional hydrogen turbine strings that provide refrigeration at different temperature levels within the cryogenic refrigeration cycle [Drnevich 2003, Ohlig & Decker 2014].

For the hydrogen liquefier precooling at plant locations in which a LN_2 supply is economically not convenient, a closed-loop nitrogen refrigeration cycle (N_2 cycle) can be installed [Gallarda 2001, Ohlig & Decker 2014].

Additionally to improve the thermodynamic efficiency of the hydrogen liquefier, an external refrigeration unit (chiller) can be installed for the hydrogen feed stream precooling to an intermediate temperature level $T_{PC,int}$ above the precooling temperature T_{PC}, as described for an enhanced Hydrogen Claude Cycle in [Gallarda 2001, Drnevich 2003].

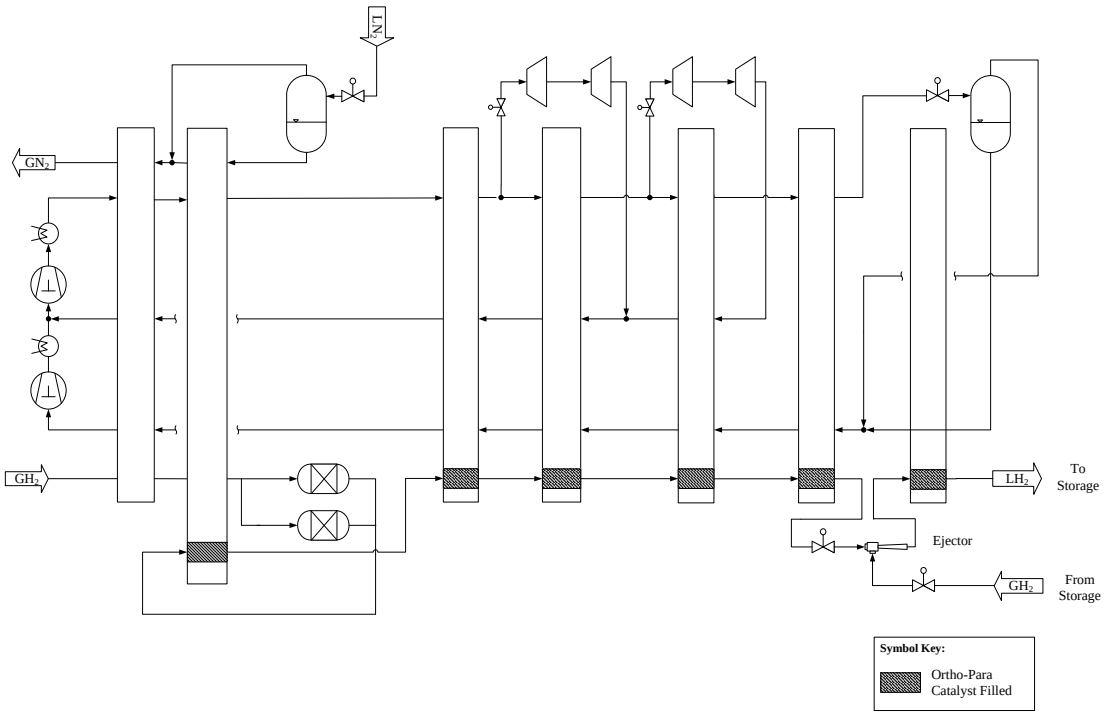

Figure 4.5: Improved Hydrogen Claude Cycle with LN_2 precooling. Adapted from [Drnevich 2003, Ohlig & Decker 2014]

For example the 2.3 tpd LH_2 hydrogen liquefier installed by the company Air Liquide in French Guayana was designed with a chiller unit for an intermediate precooling to $T_{PC,int} = 230\,\mathrm{K}$ and a N_2 cycle consisting of a N_2 screw compressor and a N_2 turbine for the precooling to $T_{PC} = 80\,\mathrm{K}$ [Gallarda 2001, Leon 2008].

4.1.3 Reported specific energy consumption

The current technology for built industrial hydrogen liquefiers is summarized in Table 4.1. The performance data for built industrial hydrogen liquefiers in literature is scarce [Cardella et al. 2017c]. Only limited information can be found on the specific energy consumption *SEC* as well as on the respective process design, the liquefaction capacity and the boundary conditions of built hydrogen liquefiers.

There is a discrepancy in the reported *SEC* between different sources in literature. For hydrogen liquefiers installed in the USA, Drnevich 2003 reported a specific energy consumption *SEC* between $SEC = 12.5 - 15\,\mathrm{kWh/kg\ LH_2}$ without giving further information on the respective process design and boundary conditions. For industrial hydrogen liquefiers, a *SEC* between approximately $SEC = 8 - 13.5\,\mathrm{kWh/kg\ LH_2}$ is reported by Ohlig & Decker 2013. The *SEC* for hydrogen liquefiers built with a hydrogen liquefaction capacity ≤ 3 tpd LH_2 with a Helium Brayton Cycle and LN_2 precooling is reported to range between approximately $SEC = 12 - 13.5\,\mathrm{kWh/kg\ LH_2}$ [Ohlig & Decker 2013]. The *SEC* for hydrogen liquefiers built with a hydrogen

liquefaction capacity ≤ 15 tpd LH_2 with a Hydrogen Claude Cycle and LN_2 precooling range between approximately $SEC = 11 - 13\,\mathrm{kWh/kg\ LH_2}$ [Ohlig & Decker 2014].

Table 4.1: Summary of the process design features of state-of-the-art industrial hydrogen liquefiers. Adapted from Ohlig & Decker 2014

Cryogenic refrigeration	Helium Brayton Cycle	Hydrogen Claude Cycle
Compressors	Rotary screw	Reciprocating piston
Turbine-expanders	Gas or oil bearing	Gas or oil bearing
Precooling	LN_2 once-through	LN_2 once-through or N_2 cycle
Reported *SEC*	12–13.5 kWh/kg LH_2	8–13 kWh/kg LH_2

The exergy efficiency η_{ex} of built hydrogen liquefaction processes is estimated between approximately $\eta_{ex} = 20 - 30\%$. However, a consistent evaluation of the exergy efficiency η_{ex} of built hydrogen liquefiers is challenging and should be carried out with identical boundary conditions [Berstad et al. 2009]. For instance the hydrogen feed pressure p_{feed} available at the inlet of the hydrogen liquefier has a major influence on the required *SEC* and the calculated exergy efficiency η_{ex}.

More performance data as well as information on the process design and boundary conditions is available for the decommissioned 4.4 tpd LH_2 hydrogen liquefier in Ingolstadt [Gross et al. 1994, Bracha et al. 1994] and for the 5.5 tpd LH_2 hydrogen liquefier in Leuna [Bracha & Decker 2008]. Both hydrogen liquefiers were designed with a Hydrogen Claude Cycle with LN_2 precooling. The *SEC* for the hydrogen liquefier in Leuna was reported to approximately $SEC = 11.9\,\mathrm{kWh/kg\ LH_2}$. This figure includes an assumed specific energy consumption of 0.4 kWh/l LN_2 [Bracha & Decker 2008] for the production of LN_2 from a nearby air separation unit (ASU).

4.2 Prior conceptual processes

Built industrial hydrogen liquefiers were often designed to minimize the plant initial capital expenses (CAPEX) while the exergy efficiency η_{ex} of the hydrogen liquefaction process played only a subordinate role [Quack 2001]. Therefore, the potential to improve the hydrogen liquefaction process and thus reduce the specific energy consumption *SEC* for large-scale hydrogen liquefiers is large. Since the late 1970s and particularly in the last two decades, a high number of conceptual design studies on future highly efficient large-scale hydrogen liquefaction processes was published in literature. A literature review of large-scale hydrogen liquefaction processes ranging from about 50 tpd LH_2 to 860 tpd LH_2 is presented in [Krasae-in et al. 2010, IDEALHY 2012].

A summary of conceptual large-scale hydrogen liquefaction processes relevant to this work is presented hereafter. The conceptual hydrogen liquefaction processes are categorized

by the type of cryogenic refrigeration cycle. Parts of this section are published in Cardella et al. 2017c.

4.2.1 Hydrogen Claude Cycle

One of the first conceptual studies on large-scale liquefaction processes was carried out by Baker & Shaner 1978. The authors investigated a hydrogen liquefaction process for 250 tpd LH_2 based on a Hydrogen Claude Cycle with nitrogen (N_2) precooling. The hydrogen liquefaction process is comparable to the state-of-the-art Hydrogen Claude Cycle of built hydrogen liquefiers. The precooling is carried out with a liquid nitrogen LN_2 stream and a cold gaseous nitrogen GN_2 stream which are supplied by a N_2 refrigerator and re-liquefaction plant. In contrast to modern industrial hydrogen liquefiers, the catalytic ortho- to para-hydrogen conversion in this concept is not continuous but is performed stepwise in two reactor vessels that are placed at the temperature level of LN_2 and LH_2 [Baker & Shaner 1978]. For a hydrogen feed pressure $p_{feed} = 1.01$ bar and a product storage pressure $p_{LH_2} = 9.3$ bar, a specific energy consumption $SEC = 10.9$ kWh/kg LH_2 was estimated by Baker & Shaner 1978.

The World Energy NETwork (WE-NET) study in Japan evaluated different process concepts in a study for a 300 tpd LH_2 large-scale hydrogen liquefier [Ohira 2004]. For the hydrogen precooling, a N_2 liquefaction cycle was designed to produce the LN_2 [Matsuda & Nagami 1997]. Five different cryogenic refrigeration cycle processes were investigated: a Hydrogen Claude Cycle, a Helium Brayton Cycle, a Neon Brayton Cycle, a Fluid Mixture Cycle consisting of hydrogen and hydrocarbons and a "Nelium" Fluid Mixture Cycle consisting of helium and neon [Iwamoto 1996, Matsuda & Nagami 1997, Fukano et al. 2000, Ohira 2004]. Based on a technical-economic evaluation, the Hydrogen Claude Cycle was selected as preferred process configuration [Fukano et al. 2000, Ohira 2004].

The final WE-NET process included hydrogen turbines with turbine energy recovery as well as hydrogen turbo compressors that are not available on the market and would require a major technological development [Ohira 2004]. A continuous catalytic ortho- to para-hydrogen conversion was considered. The *SEC* was estimated to $SEC = 8.5 - 8.8$ kWh/kg LH_2 and included the hydrogen feed compression from an inlet hydrogen feed pressure of $p_{feed,1} = 1.06$ bar to about $p_{feed,2} = 30$ bar [Matsuda & Nagami 1997, Ohira 2004]. The final WE-NET process was re-calculated by Berstad et al. 2009 with a higher inlet hydrogen feed pressure $p_{feed,1} = 21$ bar with an estimated $SEC = 7.0$ kWh/kg LH_2.

In a conceptual study for large-scale hydrogen liquefaction, Kuendig et al. 2006 investigated a Hydrogen Claude Cycle precooled by a liquefied natural gas (LNG) stream. The concept is based on the assumption that a LNG stream is re-gasified at a LNG import terminal and the energy required for the LNG evaporation is used for the precooling of a 50 tpd LH_2 hydrogen liquefier [Kuendig et al. 2006]. It was estimated that a LNG stream as precooling can reduce the specific energy consumption

to values close to $SEC = 3.5\,\text{kWh/kg LH}_2$ [Kuendig et al. 2006]. For a similar hydrogen liquefaction process with a Hydrogen Claude Cycle and LNG precooling, Shigekiyo 2015 estimated a reduction in the specific energy consumption from $SEC = 11\,\text{kWh/kg LH}_2$ to $SEC = 3.2\,\text{kWh/kg LH}_2$. The hydrogen liquefaction process concepts proposed by Kuendig et al. 2006 and Shigekiyo 2015 are dependent on the on-site availability of a LNG facility as well as on the assumption that a LNG stream can be used at no additional costs without considering the energy consumption required for the liquefaction of natural gas.

As an improvement to built hydrogen liquefaction processes, a process concept with an improved Hydrogen Claude Cycle was proposed by the Linde AG for a 50 tpd LH_2 hydrogen liquefier [Froeschle & Kederer 2010, Ohlig & Decker 2014]. The hereinafter defined Linde-2010 process concept focused on the up-scaling of the state-of-the-art hydrogen liquefaction process with simple process improvements that would require comparatively low additional capital expenses (CAPEX) and short industrial qualification procedures [Ohlig & Decker 2014]. The LN_2 precooling is replaced by chiller units and a closed-loop Nitrogen Claude Cycle [Ohlig & Decker 2014]. Compared to the hydrogen liquefaction process implemented in Leuna, the Hydrogen Claude Cycle is improved by including three turbine strings. A hydrogen turbine energy recovery is considered to improve the *SEC* [Ohlig & Decker 2014]. Based on an assumed inlet feed pressure $p_{feed} = 25\,\text{bar}$ with continuous catalytic ortho- to para-hydrogen conversion, a $SEC = 7.5 - 8.0\,\text{kWh/kg LH}_2$ was estimated [Froeschle & Kederer 2010, Ohlig & Decker 2014].

4.2.2 Helium Brayton Cycle

In the WE-NET project a LN_2 and GN_2 precooled Helium Brayton Cycle for 300 tpd LH_2 was investigated [Matsuda & Nagami 1997, Fukano et al. 2000, Ohira 2004]. Based on an inlet hydrogen feed pressure $p_{feed} = 1.06\,\text{bar}$, the specific energy consumption was estimated to $SEC = 8.7\,\text{kWh/kg LH}_2$ [Matsuda & Nagami 1997, Ohira 2004].

Later on Valenti & Macchi 2008 proposed a hydrogen liquefaction process for a very large-scale hydrogen liquefaction capacity of approximately 860 tpd LH_2. The process concept is based on a Helium Brayton Cycle that is designed to provide the refrigeration for the entire hydrogen liquefaction process without any separate precooling system. Four helium turbines with turbine energy recovery and a helium axial-flow turbo compressor with 15 compressor stages were considered [Valenti & Macchi 2008]. High isentropic efficiencies $\eta_{is} > 90\%$ were assumed for the turbines and compressors [Valenti & Macchi 2008]. The hydrogen feed stream is liquefied by an expansion from 60 bar to 1 bar in a LH_2 expander [Valenti & Macchi 2008]. The specific energy consumption was estimated to $SEC = 5.0\,\text{kWh/kg LH}_2$ assuming that the hydrogen feed stream is available at an inlet hydrogen feed pressure $p_{feed} = 60\,\text{bar}$ [Valenti & Macchi 2008]. Due to the absence of a separate hydrogen liquefier precooling, Krasae-in et al. 2010 questioned the high thermodynamic efficiency estimated in the original publication. The additional specific energy consumption required for the

compression of the hydrogen feed stream from $p_{feed,1} = 1\,\text{bar}$ to $p_{feed,2} = 60\,\text{bar}$ would increase the total SEC to approximately $SEC = 7\,\text{kWh/kg LH}_2$.

A 50 tpd LH_2 hydrogen liquefaction process concept with a Helium Brayton Cycle consisting of four helium turbine strings placed at different temperature levels was proposed by Staats 2008 and Shimko & Gardiner 2008. Similar to the hydrogen liquefaction process of Valenti & Macchi 2008, no additional precooling system was considered. In the process concept, the hydrogen feed stream and the helium refrigerant are compressed by reciprocating piston compressors [Staats 2008]. The hydrogen feed stream is expanded in a LH_2 piston expander from $p_{feed} = 21\,\text{bar}$ to the LH_2 product storage pressure $p_{LH_2} = 1.0\,\text{bar}$ [Staats 2008]. The catalytic ortho- to para-hydrogen conversion is carried out in 4 reactor vessels at different temperatures [Staats 2008]. The SEC for this process was estimated to $SEC = 8.7\,\text{kWh/kg LH}_2$ including the hydrogen feed compression and approximately $SEC = 7.4\,\text{kWh/kg LH}_2$ excluding the hydrogen feed compression [Staats 2008, Shimko & Gardiner 2008].

4.2.3 Neon Brayton cycle

The use of neon as refrigerant for hydrogen liquefaction was demonstrated in 1952 with a laboratory hydrogen liquefier that used liquid neon to liquefy hydrogen at about $p_{LH_2} = 6.7\,\text{bar}$ [Hood & Grilly 1952]. Later on, conceptual hydrogen liquefaction processes employing pure neon refrigerant in the cryogenic refrigeration cycle of hydrogen liquefiers were proposed as an alternative to the conventional Hydrogen Claude Cycles and Helium Brayton Cycles.

A hydrogen liquefaction process with a Neon Brayton Cycle using LN_2 and cold GN_2 streams for precooling was proposed by Gaumer et al. 1988. The Neon Brayton Cycle is designed with a neon turbo compressor and neon turbines [Gaumer et al. 1988]. The Neon Brayton Cycle is used to cool the hydrogen feed stream to a cold end temperature $T_{ce} \approx 30\,\text{K}$ [Gaumer et al. 1988]. The hydrogen feed stream is compressed to $p_{feed} = 45\,\text{bar}$ in a reciprocating piston compressor and is expanded for liquefaction in a dense fluid piston expander [Gaumer et al. 1988]. For a 33 tpd LH_2 hydrogen liquefier a specific energy consumption $SEC > 9\,\text{kWh/kg LH}_2$ was estimated [Gaumer et al. 1988].

Two conceptual hydrogen liquefaction processes with a Neon Brayton Cycle with turbine energy recovery and nitrogen precooling were proposed for a 300 tpd LH_2 hydrogen liquefier within the WE-NET project [Ohira 2004]. Based on an inlet hydrogen feed pressure $p_{feed} = 1.06\,\text{bar}$, a $SEC = 8.4 - 8.6\,\text{kWh/kg LH}_2$ was estimated [Matsuda & Nagami 1997, Fukano et al. 2000, Ohira 2004].

4.2.4 Helium-Neon Mixture Brayton Cycle

A helium-neon "nelium" refrigerant fluid mixture for the cryogenic refrigeration cycle was studied within the WE-NET project by Fukano et al. 2000. A process concept with

a Helium-Neon Mixture Brayton Cycle and propane (C_3H_8) precooling was proposed also by Quack 2002.

In the hydrogen liquefaction process proposed by Quack 2002, the hydrogen feed stream is compressed from $p_{feed,1} = 1\,\text{bar}$ to $p_{feed,2} = 80\,\text{bar}$ by the means of a reciprocating piston compressor that is cooled by cooling water and by C_3H_8. The hydrogen feed gas is precooled to a precooling temperature of about $T_{PC,int} = 220\,\text{K}$ with a C_3H_8 vapour compression refrigerator [Quack 2002]. At this temperature, the C_3H_8 refrigerator would have to be operated at a sub-atmospheric pressure which is not recommended for explosive refrigerants [Berstad et al. 2009]. For the cryogenic refrigeration cycle, Quack 2002 proposed a Helium-Neon Mixture Brayton Cycle with a helium mole fraction $y_{\text{He}} = 0.8$ and a neon mole fraction $y_{\text{Ne}} = 0.2$. The helium-neon refrigerant mixture was proposed to increase the molar mass $\bar{M}$ of the refrigerant fluid mixture to use turbo compressors. In the process concept of Quack 2002, the helium-neon refrigerant mixture is compressed in a turbo compressor with $8 - 16$ compressor stages. For turbine energy recovery, Quack 2002 included additional 6 compressor stages driven by an identical number of cryogenic turbine expanders. The hydrogen feed stream is expanded from $p_{feed,2} = 80\,\text{bar}$ to $p_{\text{LH}_2} = 1\,\text{bar}$ in a dense fluid expander with the generated hydrogen flash gas being compressed in an additional hydrogen cold compressor and expanded in a JT valve for re-liquefaction [Quack 2002]. Based on an inlet hydrogen feed pressure $p_{feed,1} = 1\,\text{bar}$, Quack 2002 estimated a specific energy consumption SEC of approximately $SEC = 6.9\,\text{kWh/kg LH}_2$, including an assumed specific energy consumption of $0.4\,\text{kWh/kg LH}_2$ for pressure drops and auxiliary power consumers e.g. cooling water pumps and fans. For the 173 tpd LH_2 process concept, a $SEC = 7.5 - 7.8\,\text{kWh/kg LH}_2$ is estimated with the equipment performance data provided by industry in the original publication [Quack 2002].

For the process concept of Quack 2002, Berstad et al. 2009 estimated a specific energy consumption $SEC = 5.5\,\text{kWh/kg LH}_2$ based on an assumed inlet hydrogen feed pressure $p_{feed,1} = 21\,\text{bar}$ with the compression to $p_{feed,2} = 80\,\text{bar}$ proposed by Quack 2002.

Later, Berstad et al. 2010 proposed a 86.4 tpd LH_2 process concept that was based on the process concept of Quack 2002. For the hydrogen precooling, in contrast to Quack 2002, Berstad et al. 2010 implemented a Mixed-refrigerant Cycle (MRC) as proposed by Stang et al. 2006. The refrigerant fluid mixture proposed by Berstad et al. 2010 consists of 9 refrigerant components: nitrogen (N_2), neon (Ne), R14 (CF_4), methane (CH_4), ethane (C_2H_6), ethylene (C_2H_4), propane (C_3H_8), n-butane (n-C_4H_{10}) and n-pentane (n-C_5H_{12}). The MRC is assumed to be operated down to a temperature below 73 K [Berstad et al. 2010] which can be regarded as a risk due to the potential freezing of refrigerant components. Depending on the use of either Joule-Thomson (JT) valves or liquid MR expanders in the MRC, $a = 6.2 - 6.5\,\text{kWh/kg LH}_2$ including turbine energy recovery in the Helium-Neon Mixture Brayton Cycle was estimated by Berstad et al. 2010. The estimated SEC would increase to approximately $SEC = 6.6 - 6.9\,\text{kWh/kg LH}_2$ without turbine energy recovery and would increase by approximately $1.5\,\text{kWh/kg LH}_2$ if the hydrogen feed compression from $p_{feed,1} = 1\,\text{bar}$ to $p_{feed,2} = 21\,\text{bar}$ is included.

The IDEALHY study [IDEALHY 2011] focused on the development of a conceptual large-scale hydrogen liquefaction process for 50 tpd LH_2. The process design of the IDEALHY study was based on the process features proposed by the aforementioned Quack 2002 and Berstad et al. 2010: a MRC precooling and a Helium-Neon Mixture Brayton Cycle [Stolzenburg et al. 2013]. In the IDEALHY study, the hydrogen feed pressure is assumed at $p_{feed,1} = 20\,\text{bar}$ and is compressed to $p_{feed,2} = 82\,\text{bar}$ in a reciprocating piston compressor [Stolzenburg & Mubbala 2013]. The catalytic ortho- to para-hydrogen conversion is carried out in 4 adiabatic reactors placed at different temperatures from 130 K to 85 K and in the heat exchangers below 85 K [Berstad et al. 2013]. Chiller units are included for an intermediate precooling to $T_{PC,int} = 279\,\text{K}$ [Berstad et al. 2013]. The MRC precooling is designed for a precooling temperature $T_{PC} = 130\,\text{K}$ and the fluid mixture consists of 5 refrigerant components: N_2, CH_4, C_2H_6, C_3H_8 and n-C_4H_{10} [Berstad et al. 2013]. The Helium-Neon Mixture Brayton Cycle consists of a mixture with a helium mole fraction $y_{\text{He}} = 75\,\text{mol} - \%$ and a neon mole fraction $y_{\text{Ne}} = 25\,\text{mol} - \%$ [Berstad et al. 2013]. The Helium-Neon Mixture Brayton Cycle is designed with 6 cryogenic turbine expanders that are coupled to an identical number of turbo compressor stages while the main compression of the helium-neon mixture is performed in three multi-stage hermetically-sealed turbo compressors [Berstad et al. 2013]. At the cold end, the hydrogen feed stream is expanded from about 80 bar to 2 bar into the two-phase region [Berstad et al. 2013]. As in Quack 2002, a hydrogen JT cycle with an additional hydrogen reciprocating piston compressor is required for the liquefaction of the generated hydrogen flash gas [Berstad et al. 2013]. The specific energy consumption *SEC* of the IDEALHY study was estimated to $SEC = 6.4\,\text{kWh/kg}\ LH_2$ or to approximately $SEC = 6.8\,\text{kWh/kg}\ LH_2$ by assuming an additional specific energy consumption of approximately $SEC = 0.4\,\text{kWh/kg}\ LH_2$ for auxiliary electrical power consumers [Stolzenburg & Mubbala 2013]. The estimated *SEC* increases to approximately $SEC = 7.8 - 8.2\,\text{kWh/kg}\ LH_2$ if the hydrogen feed compression from 1 bar to $p_{feed,1} = 20\,\text{bar}$ is considered.

4.2.5 Other cycles

Based on the process concept of Berstad et al. 2010, Krasae-in 2013 proposed a process concept for 100 tpd LH_2 with a 5-component or 10-component Mixed-refrigerant Cycle (MRC) precooling and 4 Hydrogen Brayton Cycles with 4 hydrogen compressors and 4 turbine expanders with turbine energy recovery. In Krasae-in 2013, the coldest Hydrogen Brayton Cycle is designed to operate at a typically undesired subatmopheric pressure levels below 0.5 bar. For the hydrogen precooling to $T_{PC} = 75\,\text{K}$, the MRC is designed with three turbine expanders with turbine energy recovery [Krasae-in 2013]. The low operation temperature ($< 72\,\text{K}$) chosen for the MRC precooling in Krasae-in 2013 is a major risk due to the potential freezing of the refrigerant components with a higher melting point. At an assumed inlet hydrogen feed pressure $p_{feed} = 21\,\text{bar}$, Krasae-in 2013 estimated a $SEC = 6.3\,\text{kWh/kg}\ LH_2$ with optimistic assumptions for the compressor efficiencies and including pressure drops in the heat exchangers. The

estimated SEC would increase to approximately $SEC = 7.8\,\text{kWh/kg LH}_2$ if the hydrogen feed compression from 1 bar to $p_{feed} = 21\,\text{bar}$ is considered. Due to the unfavourable process conditions and the high number of refrigeration cycles, the technical and economic viability of the process concept of Krasae-in 2013 for industrial applications is considered to be low.

4.3 Equipment for hydrogen liquefaction

This section describes the main technical design aspects of the process equipment in hydrogen liquefaction processes with the focus on the equipment capacity and performance limitations. The core process equipment of industrial hydrogen liquefaction processes are:

- Turbine expanders,
- Compressors and
- Plate-fin heat exchangers (PFHX).

The cold and cryogenic equipment of the hydrogen liquefier is installed within one or several cryogenic coldbox vessels [Bracha & Decker 2008]. The hydrogen liquefier is connected to a downstream liquid hydrogen LH_2 storage tank system through vacuum-insulated transfer lines [Bracha & Decker 2008].

The compressors and other warm equipment operated at temperatures close to ambient temperature $T_{amb} = 300\,\text{K}$ are installed outside the cryogenic coldbox vessels. Further standard process equipment of industrial process plants that are not described herein include, among others, pumps, coolers, chillers, phase separator vessels, drums, piping, valves, instrumentation, analysers and measuring devices.

Parts of this section are published in Cardella et al. 2017a.

4.3.1 Coldbox

The coldbox (CB) in hydrogen liquefiers are cylindrical or rectangular shaped vessels that are installed in a horizontal or vertical configuration. For larger industrial liquefiers, vertical-standing site-erected coldbox vessels are often installed and the equipment is often split into two or more coldbox vessels [Kerry 2007, IDEALHY 2012].

The equipment operating in the precooling part of the hydrogen liquefier at temperatures above the precooling temperature T_{PC} is typically installed in a cylindrical or rectangular shaped precooling coldbox and can be insulated with perlite material as in air separation units (ASU) [Kerry 2007]. The colder equipment operating in the liquefier part of the hydrogen liquefier at a temperature below the precooling temperature T_{PC} is installed in a cylindrical cryogenic coldbox. To minimize the heat inleak from warmer to colder equipment and achieve vacuum levels $< 10^{-5}\,\text{mbar}$, the cryogenic coldbox is typically a

vacuum-insulated coldbox vessel with multilayer superinsulation (MLI) [Timmerhaus & Flynn 1989].

The coldbox (CB) vessels generally include the following equipment of the hydrogen liquefaction process [Bracha & Decker 2008]:

- Plate-fin heat exchangers (PFHX),
- Turbine expanders,
- Adsorber vessels,
- Phase separator vessels,
- Catalytic reactor vessels,
- Piping, valves and instrumentation and
- Vacuum system.

While large perlite-insulated coldbox vessels can be field erected without major limitations, the vacuum-insulated coldbox vessels are normally pre-fabricated in the shop because of the high quality requirements for the manufacturing [Kerry 2007]. The pre-fabricated coldbox need to be transported from the manufacturer to the hydrogen liquefier construction site. The maximum geometrical dimensions of the pre-fabricated vacuum-insulated coldbox vessels that can be manufactured and transported economically are limited by the manufacturing capabilities of the supplier and by the maximum feasible transport dimensions. The maximum feasible transport dimensions for road or ship transport limit the maximum feasible dimensions for pre-fabricated coldbox vessels to maximum coldbox diameters $4.0 - 5.5\,\mathrm{m}$ [IDEALHY 2012] and maximum coldbox lengths $20 - 40\,\mathrm{m}$. For large-scale hydrogen liquefaction, the maximum feasible coldbox size is thus a limitation that needs to be considered.

4.3.2 Expanders

The cryogenic turbine expanders in the hydrogen liquefaction process are employed to expand fluids for refrigeration. During the expansion, the turbines produce mechanical power that is dissipated or recovered. In this work, cryogenic radial-flow turbo-expanders are considered.

The design of radial-flow turbine expanders is described in literature [Whitfield & Baines 1990, Bloch & Soares 2001, Grote & Feldhusen 2007]. The turbine expanders in industrial cryogenic refrigeration processes can be distinguished by the type of bearing system and by the type of turbine brake. The turbine expanders can be further distinguished by the type of fluid phase flow at the turbine outlet into single-phase (dry) expanders and two-phase (wet or dense fluid) expanders.

Bearing system

The state-of-the-art bearing systems for cryogenic turbine expanders use oil bearing, gas bearing or magnetic bearing technology [Ohlig & Decker 2014]. In contrast to the oil bearing turbines, turbine designs with gas bearings or magnetic bearings do not require an additional oil supply system [Bischoff & Decker 2010]. Oil bearing and gas bearing turbines are the state-of-the-art in industrial hydrogen liquefiers. Figure 4.6 shows a schematic drawing of the state-of-the-art oil bearing turbine and gas bearing turbine systems used in industrial helium and hydrogen liquefiers [Alekseev 2015].

The gas bearing turbines can be further distinguished into dynamic gas bearing turbines and static gas bearing turbines [Bischoff & Decker 2010]. The main difference between static and dynamic gas bearing turbines is that the static gas bearings require an external supply of process gas to the bearing [Bischoff & Decker 2010]. Dynamic gas bearing turbines can achieve higher efficiencies [Ohlig & Decker 2014].

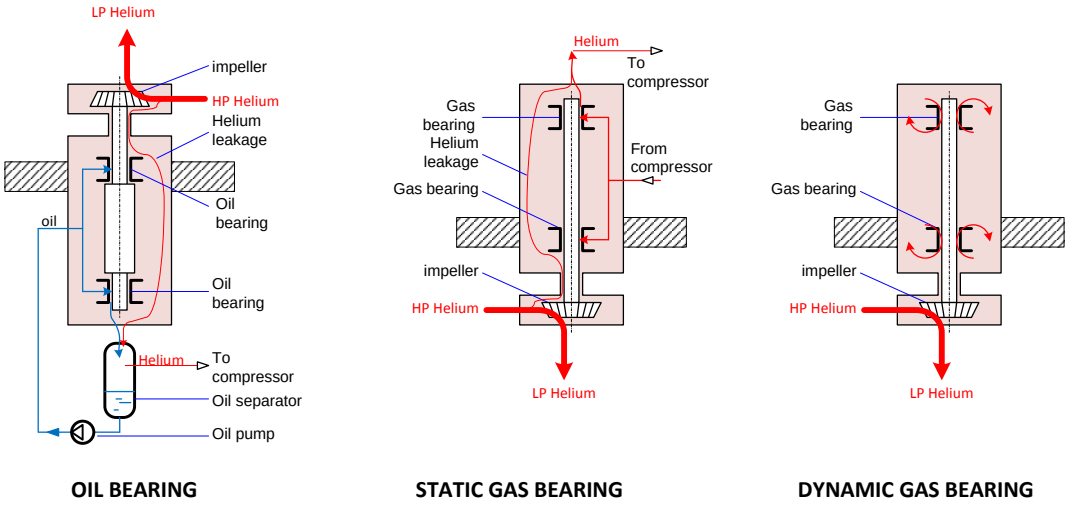

Figure 4.6: State-of-the-art bearing systems for cryogenic turbine expanders as used in helium and hydrogen liquefiers. With the permission of the author Alexander Alekseev, Linde AG

Gas bearing turbines use a gas film in the bearings to eliminate the risk of an oil contamination of the process gas [Ohlig & Bischoff 2012, Alekseev 2014]. Further advantages of gas bearing turbines include higher turbine isentropic efficiencies η_{is}, reduced space requirements and higher turbine reliability [Bischoff & Decker 2010, Ohlig & Bischoff 2012]. Therefore, modern hydrogen liquefiers are often equipped with either static or dynamic gas bearing turbine technology [Ohlig & Decker 2014].

Efficiency

The turbine isentropic efficiency η_{is} has a significant impact on the exergy efficiency η_{ex} of the hydrogen liquefaction process. The isentropic efficiency η_{is} of cryogenic turbines is typically in the range $\eta_{is} = 0.7 - 0.9$ [Bloch & Soares 2001].

The turbine isentropic efficiency η_{is} can be determined with efficiency diagrams as a function of non-dimensional design parameters such as the turbine velocity ratio ν, the specific speed n_s and the specific diameter d_s [Balje 1981, Bloch & Soares 2001]. The turbine isentropic efficiency $\eta_{is,TU}$ can also be expressed as a function of the isentropic specific enthalpy difference Δh_{is} or the expansion pressure ratio π_{TU} across the turbine [Bischoff & Decker 2010, IDEALHY 2012]. The higher the deviation from the optimal rotational speed $n_{TU,opt}$ is, the lower is the feasible turbine isentropic efficiency $\eta_{is,TU}$ [Jumonville 2010, IDEALHY 2012].

Capacity

A major challenge in the up-scaling of hydrogen liquefaction processes are the capacity limitations of the current state-of-the-art turbine designs. The currently available capacities of cryogenic turbines are plotted qualitatively in Figure 4.7 as a function of the turbine power P_{TU} [Cardella et al. 2017a]. The turbine power P_{TU} can be correlated with the turbine size through the turbine impeller wheel diameter D_{wheel}.

At the lower capacity limit, cryogenic gas bearing turbines can be manufactured for turbine powers $P_{TU} < 1\,\text{kW}$ with turbine impeller wheel diameters below $D_{wheel} = 0.02\,\text{m}$ [Cretegny et al. 2003, Bischoff & Decker 2010].

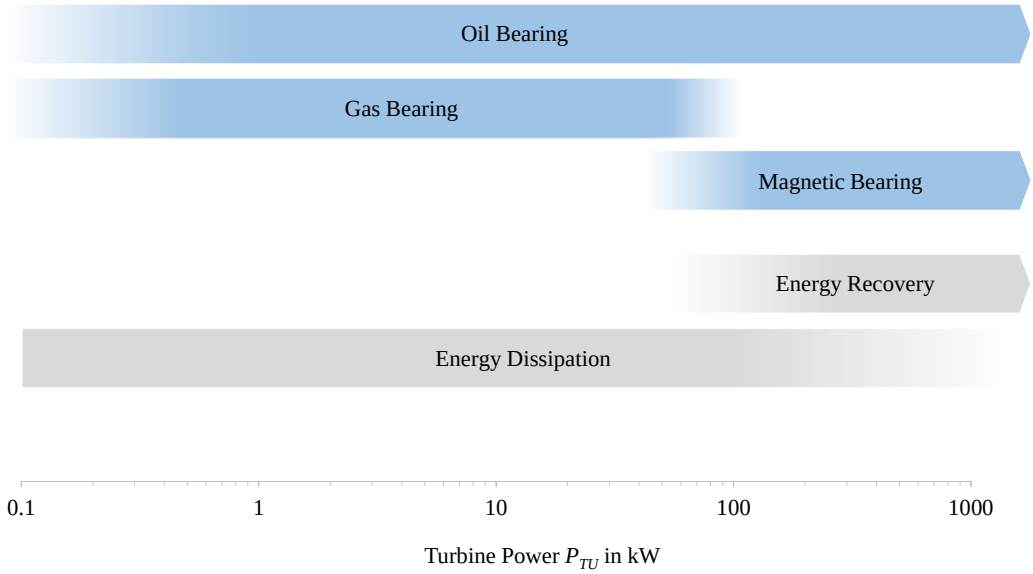

Figure 4.7: Qualitative plot of the turbine power P_{TU} for state-of-the-art turbine expanders categorized by the type of bearing system and the type of brake system [Cardella et al. 2017a]

At the upper capacity limit, dynamic gas bearing turbines are currently installed with a maximum turbine power $P_{TU} \leq 50\,\text{kW}$ [Bischoff & Decker 2010]. The maximum capacity of existing gas bearing turbines in built hydrogen liquefiers is thus smaller compared to the turbine size that is required for future large-scale hydrogen liquefaction processes [Cardella et al. 2017c, Cardella et al. 2017a].

Larger sized oil bearing turbines or magnetic bearing turbines with a turbine power P_{TU} ranging from a few kilowatts to several megawatts are employed in other as state-of-the-art industrial cryogenic processes, for example in air separation units (ASU) [General Electric n.d., Cryostar n.d.(b)]. For these larger turbines, turbine impeller wheel diameters $D_{wheel} > 1.0\,\text{m}$ can be implemented [Bloch & Soares 2001, Cryostar n.d.(a)]. However, the current design of these very large oil bearing turbines and magnetic bearing turbines is currently not proven for the use with the cryogenic fluids and the operating conditions required in the cryogenic refrigeration cycle of hydrogen liquefiers, e.g. low molar mass of hydrogen $\bar{M}_{\text{H}_2}$ and helium $\bar{M}_{\text{He}}$, high-speed operation, low cryogenic temperatures, special materials and insulation [Cardella et al. 2017a].

Further technology development and industrial qualification procedures are needed before these turbine design modifications can be applied to hydrogen liquefaction processes with low risks. The current limitations in feasible turbine capacity and size can be overcome with minor modifications in the turbine design [Cardella et al. 2017c].

Speed

The expansion pressure ratio π_{TU} that can be achieved across a turbine in the refrigeration cycle is dependent on the fluid and the turbine rotational speed n_{TU}. Fluids with a low molar mass $\bar{M}$ like hydrogen and helium require higher impeller wheel tip velocities u_2 and higher turbine rotational speeds n_{TU} compared to heavier fluids with a higher molar mass $\bar{M}$ e.g. neon and nitrogen. The expansion pressure ratio π_{TU} across one turbine expander is typically $\pi_{TU} < 10$ for helium and $\pi_{TU} < 3$ for hydrogen [Bloch & Soares 2001, Bischoff & Decker 2010]. In the hydrogen liquefier in Leuna for instance, three hydrogen oil bearing turbines are operated in series and achieve a total expansion pressure ratio of about $\pi_{TU} = 4$ with rotational speeds of up to $n_{TU} = 102000\,\text{rpm}$ [Bracha & Decker 2008].

The turbine rotational speed n_{TU} and the impeller wheel tip velocity u_2 are thus key turbine design parameters for the hydrogen liquefaction process. The maximum feasible turbine rotational speed $n_{TU,max}$ is mainly dependent on the turbine size, the bearing technology and the maximum allowed impeller wheel tip velocity $u_{2,max}$. Depending on the turbine wheel blade material, the maximum allowed impeller wheel tip velocity $u_{2,max}$ is currently limited to approximately $u_{2,max} = 400 - 500\,\text{m/s}$ [Bloch & Soares 2001]. Higher impeller wheel tip velocities $u_2 > 550\,\text{m/s}$ can be achieved with titanium wheels [Bloch & Soares 2001].

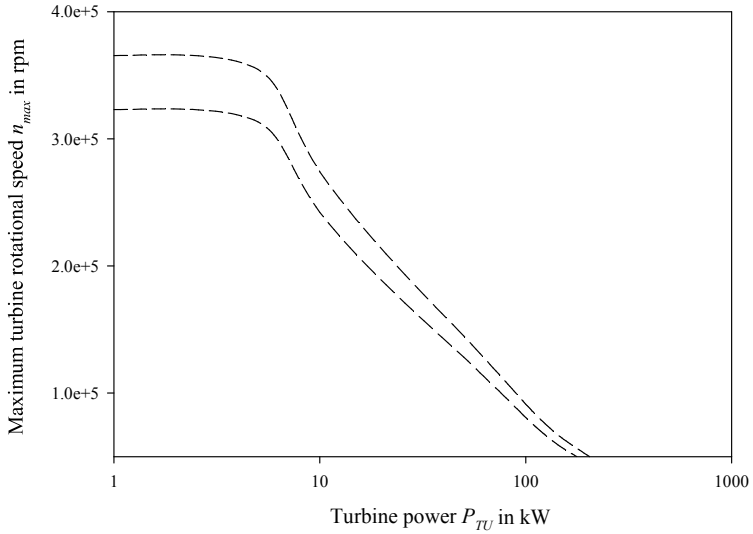

Figure 4.8: Qualitative plot of the maximum rotational speed $n_{TU,max}$ feasible for state-of-the-art turbine expanders as a function of the turbine power P_{TU}

Figure 4.8 shows a qualitative plot of the maximum feasible rotational speed $n_{TU,max}$ as a function of the turbine power P_{TU}. Due to the increasing mechanical forces on the turbine impeller wheel and bearings, the maximum allowed rotational speed $n_{TU,max}$ decreases at increasing turbine capacity and size.

State-of-the-art dynamic gas bearing turbines for turbine powers $P_{TU} = 1 - 50\,\text{kW}$ achieve maximum rotational speeds between approximately $n_{TU,max} = 100000 - 350000\,\text{rpm}$ [Bischoff & Decker 2010, Ohlig 2014]. Large oil bearing or magnetic bearing turbine expanders for turbine powers $P_{\text{TU}} > 100\,\text{kW}$ are restricted by lower feasible maximum rotational speeds $n_{TU,max} < 100000\,\text{rpm}$ [Jumonville 2010].

Brake system

By expanding the process gas from a high pressure (HP) level at the turbine inlet to a lower pressure (LP) level at the turbine outlet, turbine expanders produce mechanical energy. Due to the additional capital expenses (CAPEX) that are required for a turbine energy recovery system, a turbine energy recovery becomes economically convenient only for higher electricity costs and for larger turbine powers $P_{TU} > 100\,\text{kW}$ [General Electric n.d., Kerry 2007]. For small-scale turbines with a low turbine power $P_{TU} < 100\,\text{kW}$, the produced mechanical energy is typically dissipated to the ambience by the means of a turbine brake system that is coupled to the turbine shaft [Alekseev 2014].

In built hydrogen liquefiers, the mechanical energy produced in the cryogenic turbines is currently dissipated [Ohlig & Decker 2014]. The exergy efficiency η_{ex} of the hydrogen liquefaction process can be increased by recovering the turbine energy [Ohlig & Decker 2014]. The two existing technologies for turbine energy recovery are turbine-generator units and turbine-compressor units [Kerry 2007]. These turbine energy recovery technologies are state-of-the-art for large oil bearing turbines and magnetic bearing

turbines used in ASU as well as natural gas processing plants [General Electric n.d., Cryostar n.d.(b)].

A turbine-generator unit consists of an electric generator which is coupled to the turbine to convert mechanical energy into electrical energy to generate electricity. The electricity is used to power an electric motor drive or is fed to the electrical grid.

In a turbine-compressor unit, a process gas stream is compressed in a turbo compressor which is coupled to the turbine shaft and is driven by the turbine wheel [Kerry 2007]. A process design with turbine-compressors units is more complex: it requires an optimum matching of the process and the machine design on both the turbine and the compressor side [Kerry 2007]. The constraints imposed by the mechanical coupling of the turbine and the compressor can have a negative impact on the performance of the refrigeration process.

The transfer of the turbine energy recovery technologies to the cryogenic refrigeration cycle in hydrogen liquefiers is feasible within the medium-term but is technically challenging. The main technical challenges are restricted to the special materials and design required for the high-speed turbine operation with helium and hydrogen gas [Cardella et al. 2017a].

4.3.3 Compressors

The work input required to provide refrigeration to the hydrogen liquefaction process is carried out by the compressors. As illustrated in Figure 4.9, industrial compressors can be categorized by their principle of operation in positive displacement compressors and turbo compressors [Bloch & Godse 2006, Grote & Feldhusen 2007]. The most common compressors in industrial cryogenic refrigeration processes plants are reciprocating piston compressors, rotary screw compressors and turbo compressors. In built hydrogen liquefiers, reciprocating piston compressors or rotary screw compressors are typically used [Ohlig & Decker 2013].

The compressors are restricted in the maximum feasible capacity. The choice of the compressor type is dependent on the process design and vice versa the process design is dependent on the available compressors. The refrigerant fluid to be compressed, the required compressor capacity and the required compression pressure ratio π_{comp} are the main compressor selection criteria. For the up-scaling of hydrogen liquefaction processes, the maximum feasible compressor inlet volumetric flow rate $\dot{V}_{in,max}$ and the feasible compression pressure ratio $\pi_{comp,max}$ are the compressor design limiting parameters that need to be considered [Cardella et al. 2017a].

Figure 4.10 shows the typical range of application of different compressor types for industrial cryogenic refrigeration processes as a function of the compressor capacity, which is expressed with the inlet volumetric flow $\dot{V}_{in}$. Rotary screw compressors and reciprocating piston compressors are typically applied for lower compressor inlet volumetric flows $\dot{V}_{in}$ and for higher total compressor pressure ratios $\pi_{comp,total}$ [Grote

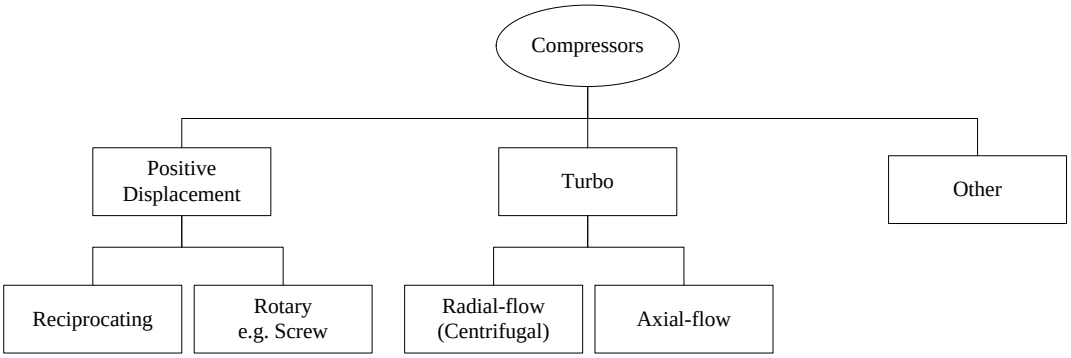

Figure 4.9: Categorization of typical industrial process compressors for industrial cryogenic refrigeration processes by the principle of operation

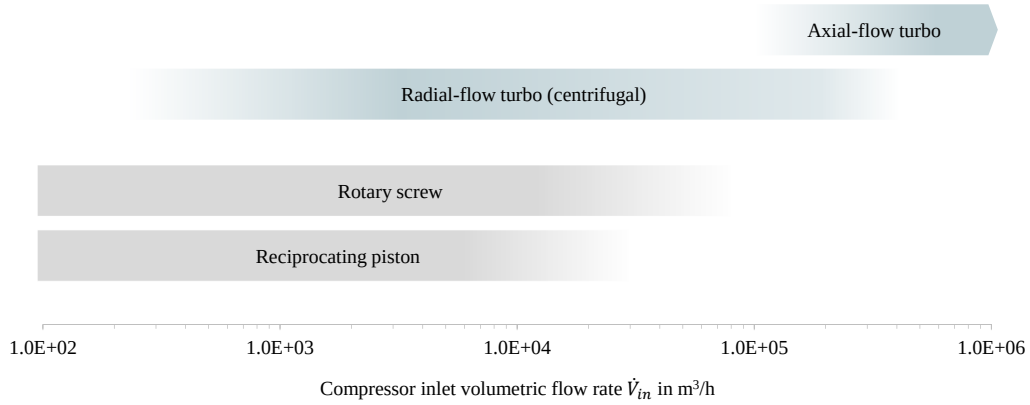

Figure 4.10: The typical application ranges of different compressor types for industrial cryogenic refrigeration processes as a function of the compressor inlet volumetric flow $\dot{V}_{in}$. Adapted from [General Electric 2005a, Grote & Feldhusen 2007, Alekseev 2014]

& Feldhusen 2007, Alekseev 2014]. Turbo compressors are typically implemented in industrial processes requiring higher compressor inlet volumetric flows $\dot{V}_{in}$.

To remove the heat generated by the compression, reciprocating piston compressors and turbo compressors are often designed as multi-stage compressors with inter-cooling. A higher number N_{stage} of compressor stages with inter-cooling is thermodynamically more efficient as it decreases the inlet temperature to the next compressor stage thus reducing the required compressor power consumption P_{comp}. A higher number N_{stage} of compressor stages is connected with higher capital expenses (CAPEX) and higher pressure drops Δp_d.

The compressor power consumption P_{comp} accounts for more than 90% of the total power consumption of the hydrogen liquefaction process. The compressor efficiency thus has a significant impact on the exergy efficiency η_{ex} of the hydrogen liquefaction process. The compressor efficiency is mainly dependent on the compressor type as well as the compressor capacity and design. The compressor isentropic efficiency η_{is} for large compressors is in the range $\eta_{is} = 0.65 - 0.92$ while mechanical efficiencies $\eta_{mech} > 0.96$ are feasible [Campbell 2014]. Electric motors are typically employed as compressor drives in hydrogen liquefiers. Large electric motor drives can achieve electrical efficiencies $\eta_{el} > 0.97$ [Gonen 2011, McCoy & Douglass 2014].

Rotary screw compressors

Oil-injected rotary screw compressors are the state-of-the-art compressors for the helium Brayton cycle in built hydrogen liquefiers [Ohlig & Decker 2013]. The oil-injected rotary screw compressors require an additional oil removal system but are standardized machines that can be installed at comparatively low capital expenses (CAPEX) and achieve high compression pressure ratios $\pi_{comp} \geq 10$ per stage [Belloni et al. 2008].

Compared to reciprocating piston compressors and turbo compressors, the isentropic efficiency η_{is} of rotary screw compressors is low in the range of approximately $\eta_{is} = 0.65 - 0.75$ [Alekseev 2014, Campbell 2014]. Therefore, the use of oil-injected helium rotary screw compressors in built hydrogen liquefiers is limited to hydrogen liquefaction capacities below approximately 3 tpd LH_2 [Ohlig & Decker 2014]. For this reason only reciprocating piston compressors and turbo compressors are considered for the large-scale hydrogen liquefaction processes developed in this work.

Reciprocating piston compressors

Reciprocating piston compressors use pistons in one or multiple cylinders to displace a gas volume with each stroke [Eifler et al. 2009]. In hydrogen liquefiers, reciprocating piston compressors are the state-of-the-art for the compression of the hydrogen feed gas stream and the hydrogen in the cryogenic refrigeration cycle.

Large reciprocating piston compressors can achieve high isentropic efficiencies in the range of $\eta_{is} = 0.75 - 0.92$ [Campbell 2014, Cardella et al. 2017d]. A further advantage of reciprocating piston compressors are the high compression pressure

ratios π_{comp} that are feasible per stage, even for fluids with a low molar mass $\bar{M}$ like hydrogen and helium.

The compression pressure ratio π_{comp} is mainly limited by the maximum allowed outlet temperature $T_{out,max}$ after each compressor stage, which is typically limited to values between $T_{out,max} = 410 - 430\,\mathrm{K}$ [Eifler et al. 2009]. For hydrogen compression, pressure ratios between $\pi_{comp} = 2 - 3$ can be implemented. Multi-stage reciprocating piston compressors with up to 4 compressor stages with inter-cooling are typically installed [Grote & Feldhusen 2007].

Lubricated reciprocating piston compressors can be installed in hydrogen liquefaction plants but require an additional oil removal system [Quack 2002]. In built hydrogen liquefiers, dry-running oil-free hydrogen reciprocating piston compressors are typically installed to eliminate the oil removal system and avoid the risk of oil contamination into the cryogenic refrigeration cycle [Ohlig & Decker 2013]. Compared to turbo compressors, the required service frequency for reciprocating piston compressors is higher.

Due to the limited mechanical forces that can be tolerated, the piston stroke s, the piston stroke volume V_s per cylinder as well as the maximum allowed piston diameter D_{pist} and the piston rod diameter D_{rod} can be regarded as limiting design parameters for the capacity of reciprocating piston compressors [Eifler et al. 2009]. The piston diameter is typically limited to $D_{pist,max} \leq 1.0\,\mathrm{m}$.

The reciprocating piston compressors can be installed vertically or horizontally and can be designed with single-acting or double-acting pistons [Bloch & Godse 2006]. The maximum capacity is achieved with horizontally installed reciprocating piston compressors. Depending on the compressor manufacturer, very large reciprocating piston compressors with compressor inlet volumetric flows up to about $\dot{V}_{in,max} = 25000\,\frac{\mathrm{m}^3}{\mathrm{h}}$ and a maximum compressor power of about $P_{max} = 40\,\mathrm{MW}$ can be installed [Burkhardt Compression 2015, General Electric 2005b].

Turbo compressors

Turbo compressors can be further categorized into radial-flow turbo compressors and axial-flow turbo compressors [Grote & Feldhusen 2007]. The radial-flow turbo compressors are typically employed for operating pressures $p \leq 100\,\mathrm{bar}$ and for a compressor inlet volumetric flow between approximately $\dot{V}_{in} = 1000 - 200000\,\frac{\mathrm{m}^3}{\mathrm{h}}$ [General Electric 2005a, Grote & Feldhusen 2007]. Radial-flow turbo compressors with a compressor inlet volumetric flow $\dot{V}_{in} < 1000\,\frac{\mathrm{m}^3}{\mathrm{h}}$ are feasible but the capacity is assumed to be outside the typical range of application which is considered to be economic.

The axial-flow turbo compressors are typically employed for low operating pressures $p \leq 20\,\mathrm{bar}$ and for very large compressor inlet volumetric flows $\dot{V}_{in} > 100000\,\frac{\mathrm{m}^3}{\mathrm{h}}$ [General Electric 2005a, Grote & Feldhusen 2007].

The isentropic efficiency η_{is} of turbo compressors is in the range $\eta_{is} = 0.70 - 0.88$ [Campbell 2014, Cardella et al. 2017d]. Compared to reciprocating piston compressors, turbo compressors can be operated for a longer time without requiring service.

The main technical challenge for the use of turbo compressors in hydrogen liquefiers is the low compression pressure ratio π_{comp} that is feasible per stage. Due to the low molar mass $\bar{M}$ of hydrogen and helium, an ambient temperature compression in turbo compressors is limited by the maximum compression pressure ratio $\pi_{comp,max}$ feasible per stage and by the maximum number of compressor stages N_{max} that can be implemented in one compressor unit [Cardella et al. 2017a].

The feasible compression stage pressure ratio is dependent on the maximum allowed impeller wheel tip velocity $u_{2,max}$. The maximum impeller wheel tip velocity $u_{2,max}$ of state-of-the-art turbo compressors is limited to $u_{2,max} = 400 - 500\,\mathrm{m/s}$ [Kerry 2007, Cardella et al. 2017a]. For instance up to $N_{stage} = 16$ compressor stages would be required for the compression of hydrogen with a total compression pressure ratio $\pi_{comp} = 4$ as required in the Hydrogen Claude Cycle in Leuna plant [Bracha & Decker 2008], [Di Bella & Osborne 2014, Cardella et al. 2017a]. In the long-term, the technical development of advanced high-speed turbo compressors with titanium or high strength alloys may lead to higher feasible impeller wheel tip velocities $u_2 > 550\,\mathrm{m/s}$ and thus stage compression pressure ratios $\pi_{comp} > 1.2$ for hydrogen and helium [Di Bella & Osborne 2014, Cardella et al. 2017a].

Multi-stage turbo compressors are further distinguished into single-shaft and multi-shaft integrally-geared turbo compressors [Grote & Feldhusen 2007]. While the single-shaft turbo compressors run at one rotational speed n_{TC}, integrally-geared turbo compressors allow to optimize the rotational speed n_{TC} for each impeller wheel [Grote & Feldhusen 2007] and are thus more efficient.

Due to the comparatively high efficiencies and low specific capital expenses (CAPEX) at the required compressor capacity, integrally-geared turbo compressors are particularly interesting for the application in industrial cryogenic refrigeration processes. For integrally-geared turbo compressors, the maximum number of impeller stages is typically limited to $N_{max} = 8 - 10$ [Grote & Feldhusen 2007, MAN n.d.].

The impeller wheel diameter D_{wheel} of integrally-geared turbo compressors ranges between $D_{wheel} = 0.1 - 1.5\,\mathrm{m}$ [MAN n.d.]. For impeller wheel diameters $D_{wheel} > 0.1\,\mathrm{m}$, the maximum rotational speed is limited to $n_{TU,max} = 50000\,\mathrm{rpm}$ [MAN n.d.].

The turbo compressors require a seal system to minimize the refrigerant make-up costs from the continuous loss of refrigerant through the compressor. Nitrogen turbo compressors typically use carbon ring seals with relatively high refrigerant loss rates of about 0.2% of the compressor flow [Kohler et al. 2014]. Dry gas seals require a higher compressor CAPEX but are used to minimize the refrigerant leakage losses for explosive or expensive refrigerants e.g. mixed-refrigerants in liquefied natural gas (LNG) plants [Kohler et al. 2014]. The refrigerant loss rates with dry gas seals are nearly independent from the compressor flow [Kohler et al. 2014]. Hermetically-sealed compressors can be installed to achieve theoretically zero refrigerant losses during the compressor operation.

However, compared to carbon-ring or dry gas sealed compressors hermetically-sealed compressors require significantly higher CAPEX, are currently limited in the maximum feasible capacity and achieve lower efficiencies [Cardella et al. 2017b]. Therefore, Kohler et al. 2014 stated that hermetically-sealed compressors are economically not convenient for small-scale LNG plants.

4.3.4 Heat exchangers

In industrial hydrogen liquefiers, multi-stream aluminium brazed plate-fin heat exchangers (PFHX) in counter-current flow configuration are used to transfer the heat between the streams that warm up (cold streams) and the streams that cool down (warm streams). The main advantages of PFHX are the compatibility with the cryogenic process conditions and fluids in hydrogen liquefiers, the high specific surface $a_v = 500 - 1800\,\mathrm{m^2/m^3}$ [Linde AG n.d.], the low pressure drops Δp as well as the small temperature differences ΔT that are feasible between warm and cold streams [Belloni et al. 2008].

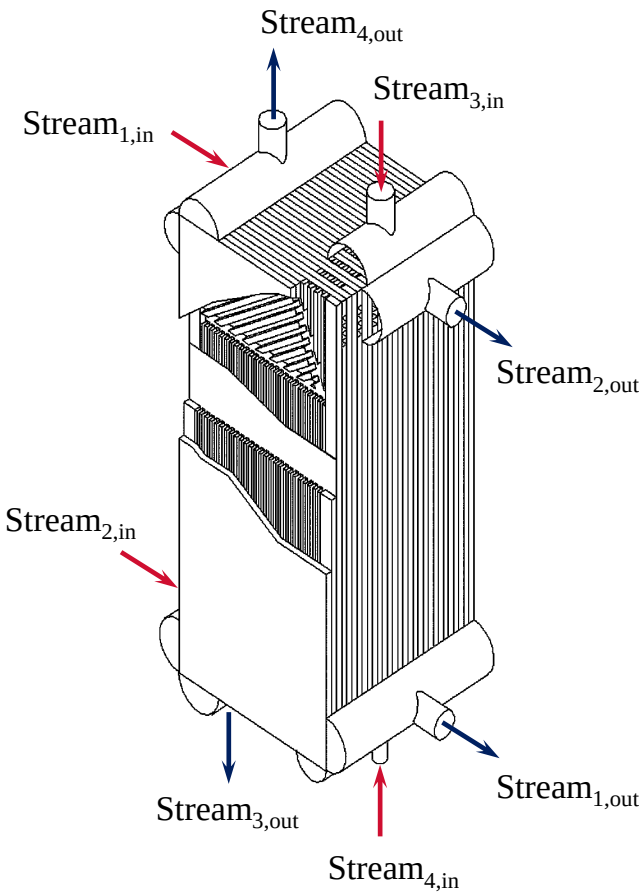

Figure 4.11: Schematic drawing of an aluminium brazed plate-fin heat exchanger from the manufacturer Linde AG. Adapted from [Linde AG n.d.]

A schematic drawing of a PFHX by the manufacturer Linde AG is illustrated in Figure 4.11 [Linde AG n.d.]. The process streams enter and exit the PFHX via nozzles and headers. The warm and the cold streams flow through a high number of different channels $N_{ch} \leq 200$ and passages [Belloni et al. 2008].

The PFHX can transfer the heat between up to 8 different streams. Due to the theoretically higher thermodynamic efficiencies, the temperature differences ΔT between streams in the heat exchangers should be minimized, particularly at lower temperatures. Additionally, thermal and mechanical stresses caused by large and rapid temperature differences ΔT in the PFHX have to be avoided. Therefore, the maximum temperature differences ΔT_{max} between streams in the PFHX are limited to values $\Delta T_{max} < 30\,\mathrm{K}$ [ALPEMA 2000].

Depending on the process design, different types of fins are used for the heat transfer: plain, perforated or serrated fins [Linde AG n.d.]. The practicable fin height h_{fin} varies between approximately $h_{fin} = 4 - 10\,\mathrm{mm}$ and the fin thickness t_{fin} varies between approximately $t_{fin} = 0.2 - 0.6\,\mathrm{mm}$ [Linde AG n.d., Belloni et al. 2008].

The size and the performance of PFHX have an important impact on the design and exergy efficiency η_{ex} of the hydrogen liquefaction process. A larger PFHX heat transfer surface A_{PFHX} and volume V_{PFHX} is linked to a higher exergy efficiency η_{ex} but also with higher plant capital expenses (CAPEX). However, the PFHX are limited in the maximum geometrical dimensions that can be manufactured and installed within the hydrogen liquefier coldbox.

The maximal geometrical dimensions of a PFHX that can be manufactured are dependent on the manufacturer and are reported to $l_{max} \times h_{max} \times w_{max} = 8.2 \times 3.0 \times 1.5$ m by Linde AG n.d. The PFHX are manufactured as cores with a maximum PFHX volume $V_{PFHX,max}$ between approximately $V_{PFHX,max} = 15 - 30\,\mathrm{m}^3$ [Fischer 2008, Belloni et al. 2008]. In practice, the PFHX dimensions that can be implemented are further restricted by the process design, the number of streams, the design pressure p_{ds} and the space available in hydrogen liquefier cold box [Cardella et al. 2017a]. The size and the number of the PFHX cores that can be installed in the coldbox is thus limited. The maximum feasible geometrical dimensions are thus a limitation to an efficient up-scaling of the hydrogen liquefaction process. Typical design limitations and ranges of application for PFHX are summarized in Table 4.2.

4.3.5 Ortho- to para-hydrogen conversion reactors

A challenge for industrial hydrogen liquefaction processes is the design of catalytic ortho- to para-hydrogen conversion reactors. The first industrial hydrogen liquefiers were built with isothermal or adiabatic reactor vessels that were placed at different temperature levels in the hydrogen feed gas stream [Lipman et al. 1963]. In the hydrogen liquefier in Ingolstadt [Gross et al. 1994], two adiabatic reactor vessels as well as two isothermal reactor vessels cooled by a LN_2 bath and LH_2 bath were installed.

Table 4.2: Typical design limitations and ranges of application for plate-fin heat exchangers. Adapted from [Linde AG n.d., Alekseev 2014]

Parameter	Value
Specific surface a_v in $\frac{m^2}{m^3}$	$500 - 1600$
Maximum volume per core $V_{PFHX,max}$ in m^3	$15 - 30$
Maximum number of streams	8
Maximum design pressure $p_{ds,max}$ in bar	120
Design temperature T_{ds} in K	$4 - 350$

In recently installed hydrogen liquefiers, the catalytic ortho- to para-hydrogen conversion is carried out with the catalyst filled inside the channels of the plate-fin heat exchangers (PFHX) [Lipman et al. 1963, Bracha & Decker 2008]. Due to the cooling and continuous catalytic conversion of the hydrogen feed gas stream in the PFHX, a thermodynamically more efficient conversion close to the equilibrium is achieved. Hydrous ferric oxide $Fe(OH)_3$ is the commonly used catalyst material [Weitzel et al. 1960b, Bracha & Decker 2008]. For an improved distribution of the catalyst, perforated fins are used in the reacting hydrogen feed gas stream passages of the PFHX [Donaubauer et al. 2018]. The PFHX design with catalytic ortho- to para-hydrogen conversion is complex but the impact of the ortho- to para-hydrogen conversion reactor design on the efficiency and costs of the hydrogen liquefaction process is significant [Cardella et al. 2017a].

4.3.6 Cryogenic adsorbers

The typical purity of the hydrogen feed gas stream at the inlet of the cryogenic adsorber vessels is $\geq 99.999\%$ with ≤ 10 ppm of residual impurities, mainly nitrogen as well as traces of other air gases and hydrocarbons [Ohlig & Decker 2013]. To remove these impurities and reduce their concentration below approximately 1 ppm, cryogenic adsorber vessels are installed in the hydrogen feed stream downstream of the precooling temperature level $T_{LN_2} \approx 80$ K [Bracha & Decker 2008, Ohlig & Decker 2013]. This additional purification in cryogenic adsorber vessels is required to eliminate the risk of damages to the hydrogen liquefier equipment due to the potential freezing of impurities at low cryogenic temperatures [Ohlig & Decker 2013].

The cryogenic adsorber vessels are filled with charcoal or molecular sieve adsorbent material which is regenerated with a stream of warm pure hydrogen gas [Haeussinger et al. 2000b, Ohlig & Decker 2013]. The installed cryogenic adsorbers enable to achieve high LH_2 product purities above 99.99999 mole-% [Bracha & Decker 2008] that are important for applications requiring high hydrogen purities e.g. the superconductor industry.

The size of the adsorber vessels depends on the concentration and type of impurities, the adsorbent material as well as the maximum pressure drop $\Delta p_{d,ads}$ that is allowed across the adsorber vessels [Bathen & Breitbach 2001]. The required adsorber diameter D_{ads} and the bed height h_{ads} are mainly dependent on the hydrogen inlet volumetric flow $\dot{V}_{in,ads}$, the adsorption temperature $T_{in,ads}$ and pressure p_{ads}. The adsorption capacity of the adsorbent decreases for higher adsorption temperatures T_{ads} and for lower pressure p_{ads}, thus requiring larger adsorber vessels [Bathen & Breitbach 2001].

The cryogenic adsorber vessels are installed in parallel configuration for adsorption and regeneration [Haeussinger et al. 2000b, Ohlig & Decker 2013]. The maximum number and size of adsorber vessels that can be installed is limited by the space available in the hydrogen liquefier coldbox and the additional capital expenses (CAPEX).

4.3.7 Liquid hydrogen storage tank

Downstream of the hydrogen liquefaction process, the LH_2 product is fed to the LH_2 storage tank system via vacuum-insulated transfer lines [Bracha & Decker 2008]. The LH_2 storage tanks are used to store the LH_2 product at temperatures close to $T_{tank} = 20\,\mathrm{K}$ with double-walled vacuum-insulated vessels [Taylor et al. 1986]. The typical LH_2 storage pressures are $p_{tank} = 1.2 - 2.5\,\mathrm{bar}$ [Bracha & Decker 2008]. Filling stations are required for the LH_2 trailers or ships. The capital expenses (CAPEX) for the LH_2 storage tank system are among the highest in a hydrogen liquefaction plant.

Cylindrical vacuum-insulated LH_2 storage tanks are installed for LH_2 storage volumes of up to approximately $V_{tank} = 400\,\mathrm{m^3}$ [Yurum 1995, Bracha & Decker 2008]. For larger storage capacities, spherical vacuum-insulated LH_2 storage tanks are installed. Up to date, the National Aeronautics and Space Administration (NASA) installed the largest spherical LH_2 storage tanks with a diameter $D_{tank} \approx 20\,\mathrm{m}$ and a LH_2 storage volume of approximately $V_{tank} = 4000\,\mathrm{m^3}$ [Taylor et al. 1986]. Large LH_2 storage tanks for storage volumes $V_{tank} = 2500 - 4000\,\mathrm{m^3}$ are currently in the development for the future LH_2 transportation in ships [Yurum 1995, Ball & Wietschel 2009]. Similar to the spherical tanks in LNG plants, the construction of larger spherical LH_2 storage tanks for storage volumes $V_{tank} > 10000\,\mathrm{m^3}$ may be feasible in the long-term [Taylor et al. 1986, Yurum 1995].

The LH_2 storage tanks generate a certain amount of cold hydrogen boil-off that is either burned and lost in the flare system or is recirculated and re-liquefied within the hydrogen liquefaction process e.g. with an ejector [Bracha & Decker 2008]. In large LH_2 spherical storage tanks, the LH_2 boil-off losses due to heat inleak can be kept low, with feasible boil-off rates below 0.2 % per day [Taylor et al. 1986, Yurum 1995].

5 Process Modelling and Optimization

The models implemented in this work for the simulation and optimization of large-scale hydrogen liquefaction processes are described within this chapter.

5.1 Liquefier process simulator model

Parts of this section are published in Cardella et al. 2017b and Cardella et al. 2017d. The hydrogen liquefaction processes are modelled in the steady-state process simulator UniSim Design® [UniSim Design 2015]. For the development and optimization of hydrogen liquefaction processes, a comprehensive hydrogen liquefier process simulation model is implemented in UniSim Design®. The hydrogen liquefier process simulation model employs different fluid property packages with equations of state (EOS). For process simulation, built-in unit operation models are used for the calculation of process components such as heat exchangers, compressors and expanders.

The process simulation model is built into different subflowsheets in UniSim Design® according to the process systems in a hydrogen liquefier: the refrigerant compression systems, the precooling part as well as the cryogenic refrigeration and liquefaction part. The different subflowsheets are connected into one hydrogen liquefier process simulation model by material streams. Figure 5.1 shows an exemplary process flowsheet of the hydrogen liquefier precooling part of the hydrogen liquefier process simulator model. Figure 5.2 shows an exemplary process flowsheet of the cryogenic refrigeration and the liquefaction part of the hydrogen liquefier process simulator model.

To perform detailed side calculations, spreadsheets programmed within the subflowsheets of the hydrogen liquefier process simulator model are linked to relevant process parameters that are calculated by the process simulator. The spreadsheets are used for a preliminary equipment design as well as for the estimation of the specific energy consumption SEC and the specific liquefaction costs SLC.

5.1.1 Fluid properties

The basis for the hydrogen liquefier process simulation model is the fluid property estimation with the equations of state (EOS) described in Section 3.3. The hydrogen liquefier process simulation model is implemented with the fluid property estimation methods that are either built into the UniSim Design® fluid packages [UniSim Design 2015] or that are available in REFPROP of NIST [Lemmon et al. 2013]. The fluid property estimation methods available in REFPROP are coupled to the process simulator UniSim Design® with the property package software REFPROP CAPE-OPEN [AmsterCHEM 2010].

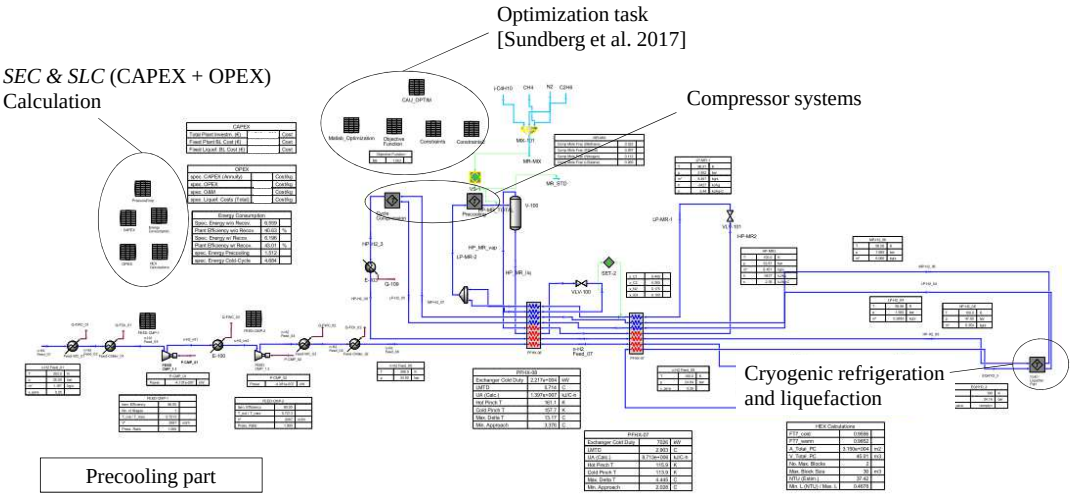

Figure 5.1: Exemplary process flowsheet of the precooling part of the hydrogen liquefier process simulator model in UniSim Design 2015

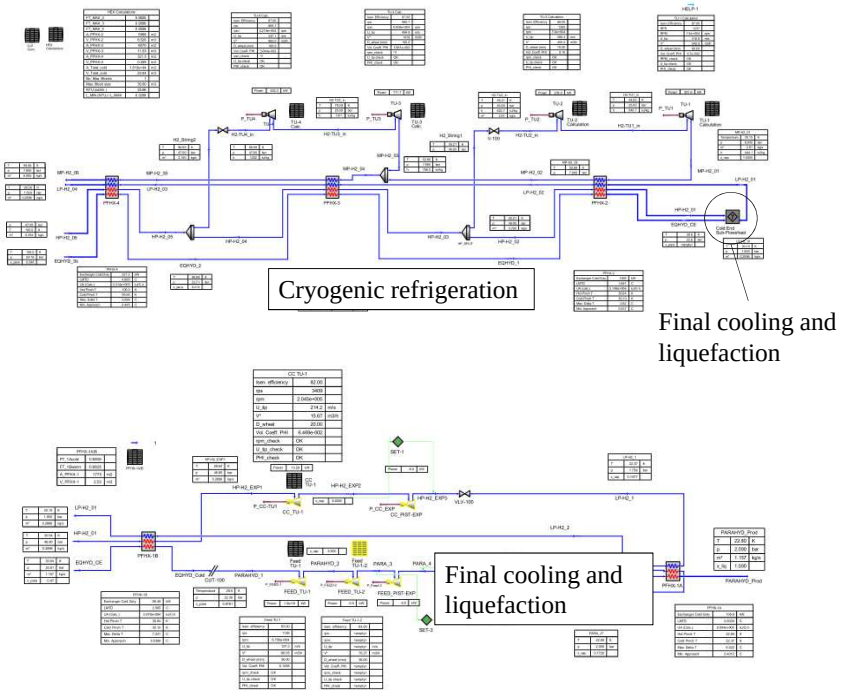

Figure 5.2: Exemplary process flowsheet of the cryogenic refrigeration (upper flowsheet) and the liquefaction part (lower flowsheet) of the hydrogen liquefier process simulator model in UniSim Design 2015

Hydrogen allotropes and ortho- to para-hydrogen conversion

The properties of the hydrogen allotropes in the hydrogen liquefier process simulation model are calculated with the EOS of Leachman et al. 2009 from REFPROP [Lemmon et al. 2013]. The hydrogen streams in the hydrogen liquefaction process that are not subject to the catalytic ortho- to para-hydrogen conversion are simulated with the fluid properties and the EOS for normal-hydrogen by Leachman et al. 2009 in REFPROP. The hydrogen feed stream that is cooled in the heat exchangers with continuous catalytic ortho- to para-hydrogen conversion is simulated by assuming equilibrium-hydrogen. The equilibrium-hydrogen model for REFPROP of Valenti et al. 2012 is based on the fundamental EOS of Leachman et al. 2009 for para-hydrogen and is a regression of the ideal gas specific isobaric heat capacity c_p^0 of para-hydrogen from Leachman et al. 2009 with the ideal gas specific isobaric heat capacity c_p^0 of equilibrium-hydrogen from the quantum theory [Woolley et al. 1948, Le Roy et al. 1990]. A similar model assumption was made by Berstad et al. 2010.

In this work, equilibrium-hydrogen is assumed down to a temperature of 28 K and the respective equilibrium mole fraction of para-hydrogen $y_p^{eq} \geq 0.98$. The assumption of continuous equilibrium-hydrogen conversion in the process simulator was found to be sufficiently accurate for the optimization and comparison of different conceptual hydrogen liquefaction processes within this work. At the cold end, the hydrogen feed stream expansion as well as the final cooling and liquefaction below the temperature $T = 28\,\mathrm{K}$ are simulated with the fluid properties and the EOS of para-hydrogen [Leachman et al. 2009] from REFPROP.

Helium, neon and nitrogen

The thermodynamic fluid properties of all pure refrigerant fluids used in this work are calculated with the standard EOS models implemented in REFPROP: the EOS of Vega 2013 for helium, the EOS of Katti et al. 1986 for neon and the EOS of Span et al. 2000 for nitrogen.

Mixtures of nitrogen and hydrocarbons

In this work, fluid mixtures composed of nitrogen and hydrocarbons with up to five fluid components are simulated in the precooling cycle of the hydrogen liquefaction process. The fluid mixture components are given in Table A.1 in the Appendix A.

In this work, the estimation of the fluid mixture properties were evaluated using the cubic EOS of Peng-Robinson (PR) [Peng & Robinson 1976] and the EOS of GERG-2008 [Kunz & Wagner 2012] available in the process simulator UniSim Design®. The difference in the total compressor power P_{comp} calculated for a standard hydrogen precooling process using the EOS of Peng & Robinson 1976 (PR) and the EOS of Kunz & Wagner 2012 (GERG-2008) in UniSim Design® was low. Compared to the GERG-2008, the EOS of PR requires a lower computation time during process optimization in UniSim Design®. The fluid mixtures composed of nitrogen and

hydrocarbons are thus calculated with the EOS of PR with the binary interaction coefficients available in UniSim Design® [UniSim Design 2015].

Mixtures of neon with helium and hydrogen

Binary fluid mixtures composed of neon with helium or hydrogen are simulated in the cryogenic refrigeration cycle of the hydrogen liquefaction process. For helium-neon mixtures, a preliminary mixture model with mixing parameters for helium and neon was provided by Dr. Eric Lemmon of NIST for the EOS of Kunz & Wagner 2012 in REFPROP [Lemmon et al. 2013]. For the hydrogen-neon mixture, mixing parameters for the EOS of GERG-2008 [Kunz & Wagner 2012] and the EOS of PR [Peng & Robinson 1976] were not available in UniSim Design®. In this work, the hydrogen-neon mixtures in the cryogenic refrigerant cycle are simulated only in the gas phase with the fitted EOS of PR. Therefore, the binary interaction coefficients of the cubic EOS of SRK and PR were fitted in the fluid phase regression environment in UniSim Design® to experimental vapor-liquid-equilibrium (VLE) p-x-$y(T)$ data published by Streett & Jones 1965 and Heck & Barrick 1966 for hydrogen-neon mixtures. The VLE calculations with the fitted EOS showed a good match with the available VLE data from Streett & Jones 1965 and Heck & Barrick 1966. It was shown that the difference in the calculated total specific energy consumption SEC between simulation cases with PR and SRK was below 1% and thus negligible.

5.1.2 Simulation of the unit operations

In this work, the hydrogen liquefaction process simulation is carried out with process equipment such as heat exchangers, compressors, expanders, valves and phase separators that are simulated with the built-in unit operation models that are available in the process simulator UniSim Design®.

The preliminary equipment design and performance correlations described in Chapter 6 are implemented in the spreadsheets of the hydrogen liquefier process simulator model and are coupled to core process parameters calculated during process simulation.

For the calculation of multi-stream counter-current plate-fin heat exchangers (PFHX) in the hydrogen liquefier process simulation model, the LNG heat exchanger model in UniSim Design® [UniSim Design 2015] is used. In order to consider economically and technically viable industrial PFHX designs, the PFHX design constraints described in Section 6.3 are applied to the hydrogen liquefier process simulation model.

The turbine expanders, the reciprocating piston compressors and the turbo compressors in the hydrogen liquefier process simulation model are calculated with the respective unit operation model in UniSim Design® [UniSim Design 2015]. The compressors are simulated as multi-stage compressors with inter-stage and after-stage cooling with coolers. The turbine and compressor design constraints described in Section 6.1 and 6.2 are applied to the respective unit operations in the hydrogen liquefier process simulation

model. Figure 5.3 shows an exemplary process flowsheet of the compression systems in the hydrogen liquefier process simulator model.

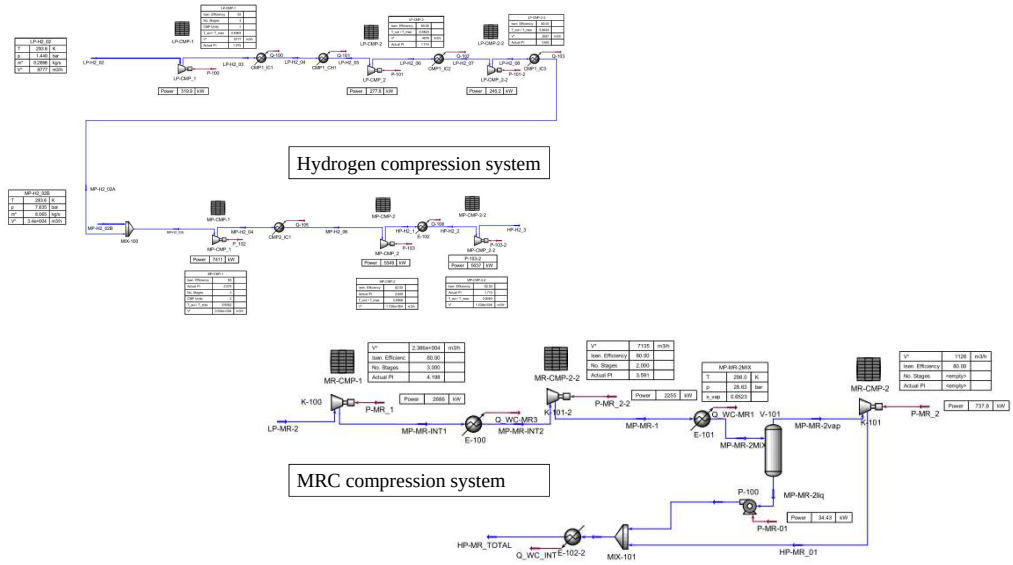

Figure 5.3: Exemplary process flowsheet of the compression systems in the hydrogen liquefier process simulator model in UniSim Design 2015

The isentropic efficiencies η_{is} required for the compressor and turbine power calculation, P_{comp} and P_{TU}, in UniSim Design® are computed as a function of the inlet volumetric flow $\dot{V}_{in}$ in the hydrogen liquefier process simulation model.

For the compressor power calculation within this work, a combined mechanical-electrical efficiency $\eta_{mech,el} = 0.95$ is assumed as the product of the compressor mechanical efficiency η_{mech} and the electrical motor efficiency η_{el}:

$$\eta_{mech,el} = \eta_{mech} \cdot \eta_{el} \,. \tag{5.1}$$

The turbine expanders in the hydrogen liquefier process simulation model are calculated either with energy dissipation via a brake system or with turbine energy recovery via a turbine-generator unit for the production of electricity. The turbine energy recovery with turbo-generators is considered in the simulation cases in which the turbine power is $P_{TU} \geq 50\,\text{kW}$. For the turbine power recovery P_{recov}, the total energy conversion from mechanical energy to electrical energy is assumed with a turbine energy recovery efficiency $\eta_{recov} = 0.80$. For the turbine expanders with a turbine power $P_{TU} < 50\,\text{kW}$, no turbine energy recovery is considered in the process simulation.

5.1.3 Specific energy consumption

The specific energy consumption *SEC* of hydrogen liquefaction processes is calculated in the spreadsheets of the hydrogen liquefier process simulation model. In this work, the specific energy consumption *SEC* is defined as

$$SEC = w_{net} = \frac{P_{net}}{\dot{m}_{\mathrm{LH_2}}} = \frac{\sum_i P_{cons,i} - \sum_j P_{recov,j}}{\dot{m}_{\mathrm{LH_2}}}, \tag{5.2}$$

with the total net power consumption P_{net} of the hydrogen liquefier and the liquid hydrogen (LH_2) mass flow rate $\dot{m}_{\mathrm{LH_2}}$. The net power consumption P_{net} is defined as the difference between the sum of the electrical power consumption $P_{cons,i}$ of the electrical consumers i and the turbine power recovered $P_{recov,j}$ by the turbine expanders j with turbine energy recovery.

Besides the compressors, the auxiliary electrical power consumption for the cooling water pumps and fans are included in the *SEC* calculation with an assumed percentage factor of 0.03 on the total compressor cooling power.

For hydrogen liquefaction processes with liquid nitrogen (LN_2) precooling, a specific energy consumption of 0.5 kWh/kg LN_2 is assumed in the total *SEC* calculation based on the LN_2 production from an air separation unit (ASU) [Bracha & Decker 2008, EIGA 2010]. The value assumed for the specific energy consumption of LN_2 production is considered only as a penalty for the comparison of the *SEC* of simulated hydrogen liquefaction processes. For the estimation of the specific liquefaction costs *SLC* as described in Chapter 7, only the operating expenses (OPEX) associated with a LN_2 supply price in €/kg LN_2 are considered.

5.1.4 Specific liquefaction costs

The detailed cost estimation model described in Chapter 7 is implemented in the hydrogen liquefier process simulator model in UniSim Design® and is used to compute the specific liquefaction costs *SLC* from the plant capital expenses (CAPEX) and operating expenses (OPEX).

5.2 Process optimization

The design of hydrogen liquefaction processes with state-of-the-art equipment is complex. It requires an optimization task in which a high number of optimization variables is manipulated to optimize an objective function while satisfying all optimization constraints defined for the process and equipment design. Process optimization is used in this work to find optimal process design solutions with the hydrogen liquefier process simulator.

Parts of this section are published in Cardella et al. 2017d.

5.2.1 Optimization method

The hydrogen liquefaction process represents a non-linear optimization problem. A non-linear optimization problem can be described with the vector x of optimization variables that are manipulated in order to minimize the objective function $f(x)$ while considering the inequality constraints $g(x) \leq 0$ [Sundberg et al. 2017]. The dimension of the optimization problem is given by the number N of optimization variables $x = x_1...x_N$.

In this work a mathematical optimization method developed by Sundberg et al. 2017 in the software Matlab® is used to perform the optimization task. Figure 5.4 depicts the used process optimization approach for the hydrogen liquefier. The hydrogen liquefier process simulation model implemented in the process simulator UniSim Design® is coupled to the external optimization platform in Matlab® via an ActiveX connection [Cardella et al. 2017d]. For this hybrid approach to process optimization, Sundberg et al. 2017 developed a software tool with optimization algorithms that are implemented in Matlab®. The optimization task is defined in spreadsheets within the UniSim Design® process simulation environment.

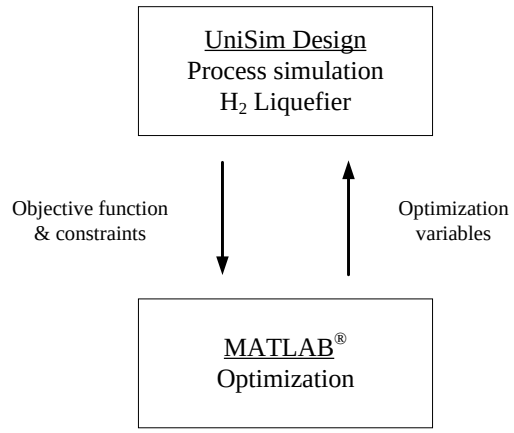

Figure 5.4: Schematic illustration of the implemented hydrogen liquefier process optimization approach. Adapted from Sundberg et al. 2017

The objective function $f(x)$ is minimized by manipulating the vector x of optimization variables with the defined upper and lower bounds while satisfying the inequality constraints $g(x)$ [Cardella et al. 2017d]. The optimization task is solved using the gradient-based nonlinear solver *fmincon* with the sequential quadratic programming algorithm *sqp* in Matlab® [Cardella et al. 2017d].

5.2.2 Optimization variables and constrains

Process parameters calculated in the hydrogen liquefier process simulation model are used as optimization variables and constraints. In this work, up to about $N = 18$ optimization variables x are optimized simultaneously with upper and lower limits that are defined in the process simulator [Cardella et al. 2017d]. Typical optimization variables used for the hydrogen liquefaction process optimization include the mole fractions y_i of refrigerant mixtures as well as pressure and temperature levels within the refrigeration cycles [Cardella et al. 2017d].

Up to 22 nonlinear inequality constraints $g(x)$ are defined to represent realistic boundary conditions for the process and equipment design [Cardella et al. 2017d]. The constraints are chosen based on process and equipment design data that is available from industrial manufacturers or from literature. Typical inequality constraints $g(x)$ used for the hydrogen liquefaction process optimization include the maximum compressor inlet volumetric flow $\dot{V}_{max}$, the maximum heat exchanger $U \cdot A$ value as well as minimum temperature differences ΔT_{min} and maximum temperature differences ΔT_{max} calculated at any point in the heat exchanger unit operation model [Cardella et al. 2017d].

The optimization variables and constraints used for the process optimization cases of the hydrogen liquefaction processes are described in Chapter 8.

5.2.3 Objective functions

The optimization method described in Section 5.2.1 is applied to the hydrogen liquefier process simulation to minimize the objective function $f(x)$.

For the hydrogen liquefaction process optimization within this work, both the specific energy consumption *SEC* in kWh/kg LH_2 and the specific liquefaction costs *SLC* in €/kg LH_2 are used as objective function $f(x)$ [Cardella et al. 2017b]. For each optimized hydrogen liquefaction process design, this results in an energy-optimized case (EO) and a cost-optimized case (CO).

5.3 Liquefier spreadsheet model

Parts of this section are published in Cardella et al. 2015a.

In addition to the hydrogen liquefier process simulator model in UniSim Design®, a thermodynamic hydrogen liquefier spreadsheet model was implemented in Microsoft Excel®. The hydrogen liquefier spreadsheet model is used to perform process calculations with the preliminary equipment design described in Chapter 6 and the cost estimation model described in Chapter 7.

The liquefier spreadsheet model calculates step-by-step the thermodynamic state of all points in the hydrogen liquefaction process from the cold end to the warm end. The thermodynamic fluid properties described in Section 5.1.1 are calculated in the spreadsheet with Visual-Basic cell functions available for REFPROP [Lemmon et al. 2013] and GASPAK [Arp et al. 1999].

The energy and mass balances for the thermodynamic process components implemented in the liquefier spreadsheet model are calculated with the iterative solver method integrated in Microsoft Excel®. In the liquefier spreadsheet model, the thermodynamic process conditions of multi-stream heat exchangers are calculated only at the warm end and at the cold end. A temperature cross between the warm streams and cold streams inside the heat exchangers can not be excluded [Alabdulkarem et al. 2011].

5.4 Kinetic ortho- to para-hydrogen conversion model

In order to predict the catalytic ortho- to para-hydrogen conversion in adiabatic or isothermal ortho- to para-hydrogen reactor vessels and in plate-fin heat exchangers (PFHX), a theoretical model coupling reaction kinetics with heat transfer was developed by Donaubauer 2015 in Matlab ® in the frame of this work.

Parts of this section are published in Donaubauer 2015 and Donaubauer et al. 2018.

5.4.1 Reaction kinetics

Based on the three available experimental data sets published by Weitzel et al. 1960b and Hutchinson 1966, the reaction kinetics of the catalytic ortho- to para-hydrogen conversion on hydrous ferric oxide $Fe(OH)_3$ catalyst was investigated by Donaubauer 2015. The determined reaction kinetics were applied by Donaubauer 2015 to both the Langmuir-Hinshelwood kinetic approach and the first-order kinetic approach. A Langmuir-Hinshelwood kinetic model (a) and a first-order kinetic model (b) with temperature and pressure dependent reaction rate constants k_i were evaluated by Donaubauer 2015.

The first-order kinetic model (b) was selected as reliable kinetic model by Donaubauer 2015 and is used also in this work. The determined first-order rate constant k_{fo} for the first-order kinetic model (b) is described in the following equation:

$$k_{fo} = \frac{\exp\left(\frac{\bar{E}_a}{\bar{R}\cdot T}\right)}{a_{fo}\cdot c_{\mathrm{H_2}} + b_{fo}} \cdot \frac{1}{1 - y_o^{eq}}\,, \tag{5.3}$$

with the molar activation energy $\bar{E}_a$ and the reaction rate constants a_{fo} and b_{fo} fitted with experimental data points [Donaubauer 2015, Cardella et al. 2015b, Donaubauer et al. 2018]. The accuracy of the determined first-order kinetic model against the available experimental data is represented in Donaubauer 2015, Cardella et al. 2015b and Donaubauer et al. 2018.

5.4.2 Plate-fin heat exchanger model

The kinetic model of a two stream counter-current plate-fin heat exchanger (PFHX) in Matlab® was implemented by Donaubauer 2015. The model combines reaction kinetics with heat, mass and momentum transfer correlations in a steady-state one-dimensional pseudohomogeneous reactor model [Donaubauer 2015, Cardella et al. 2015b, Donaubauer et al. 2018]. The PFHX model is based on the equation of state (EOS) for hydrogen allotropes by Leachman et al. 2009 in REFPROP. The thermodynamic properties for arbitrary ortho-para hydrogen mixtures are calculated with the assumption of ideal mixture equations [Hust & Stewart 1965]. Figure 5.5 shows a schematic drawing of a PFHX with ortho- to para-hydrogen conversion in the warm (w) hydrogen feed stream [Donaubauer 2015].

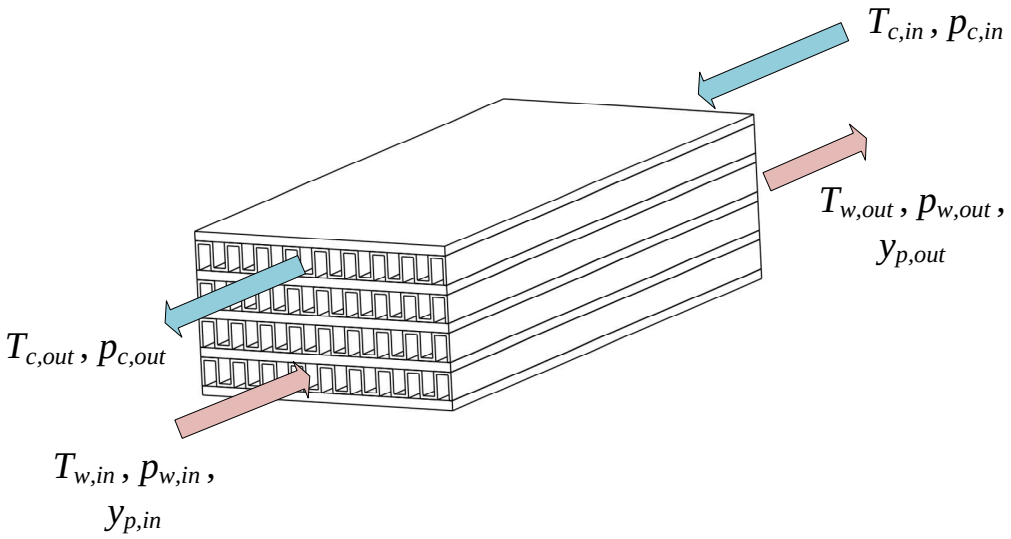

Figure 5.5: Plate-fin heat exchanger with ortho- to para-hydrogen conversion in the warm (w) hydrogen feed stream. Adapted from Cardella et al. 2015b

The thermodynamic and transport properties as well as the correlations for heat transfer and flow friction implemented in the PFHX model are described in Donaubauer 2015. The geometrical dimensions of the PFHX in the model are based on the industrial design of Linde AG [Linde AG n.d.] with perforated fins assumed in the hydrogen feed stream passages filled with catalyst and rectangular offset strip fins in the refrigerant stream [Donaubauer 2015, Donaubauer et al. 2018]. The fin dimensions are assumed to be dependent on the PFHX design pressure p_{ds} [Donaubauer 2015, Donaubauer et al. 2018].

The kinetic PFHX model is used to calculate the temperature profiles of the hydrogen feed and refrigerant streams as well as the mole fraction of para-hydrogen y_p as a function of the PFHX axial length coordinate x. The kinetic PFHX model is used to calculate the required catalyst volume V_{cat} and the geometrical dimensions of the PFHX.

6 Equipment design

A major technical and economic challenge in the up-scaling of hydrogen liquefaction processes is the design of larger, more efficient and cost-optimized process equipment. The estimation of the dimensions and performance of process equipment provides the input for the calculation of the specific energy consumption *SEC* and the specific liquefaction costs *SLC* of the hydrogen liquefier.

This chapter describes the preliminary sizing calculations and the performance estimation methods used for the core process equipment in this work:

- Turbine expanders,
- Compressors and
- Plate-fin heat exchangers (PFHX).

Due to the maximum feasible transport dimensions described in Section 4.3.1, the cold process equipment of large-scale hydrogen liquefaction processes is assumed to be installed in two cryogenic coldbox vessels: a precooling coldbox and a liquefier coldbox.

The herein described preliminary equipment estimation methods are implemented in the hydrogen liquefier process simulation models described in Chapter 5 and are used for the process development and process optimization in Chapter 8. The preliminary equipment design is used as an input for more detailed equipment design calculations that are carried out with proprietary software of manufacturers.

Parts of this chapter are published in Cardella et al. 2017d and in Cardella et al. 2017a.

6.1 Turbine expanders

Figure 6.1 describes the preliminary sizing and performance estimation method implemented for radial-flow turbine expanders within this work. The radial-flow turbine expanders are hereinafter referred to as turbines.

The turbine dimensioning starts with the thermodynamic parameters that are available from the process calculation in the hydrogen liquefier process simulation model, for instance the mass flow rate $\dot{m}_{TU}$ through the turbine, the turbine outlet temperature $T_{TU,out}$ and outlet pressure $p_{TU,out}$ as well as the required expansion pressure ratio π_{TU}. The expansion pressure ratio π_{TU} is defined as:

$$\pi_{TU} = \frac{p_{TU,in}}{p_{TU,out}} \,. \tag{6.1}$$

The turbine rotational speed n_{TU} is calculated in Equation (6.2) with the impeller wheel tip velocity u_2 at the turbine wheel outside diameter u_2 and the outlet wheel diameter D_{wheel} [Seume & Mailach 2014]:

$$n_{TU} = \frac{u_2}{3.1416 \cdot D_{wheel}} \,. \tag{6.2}$$

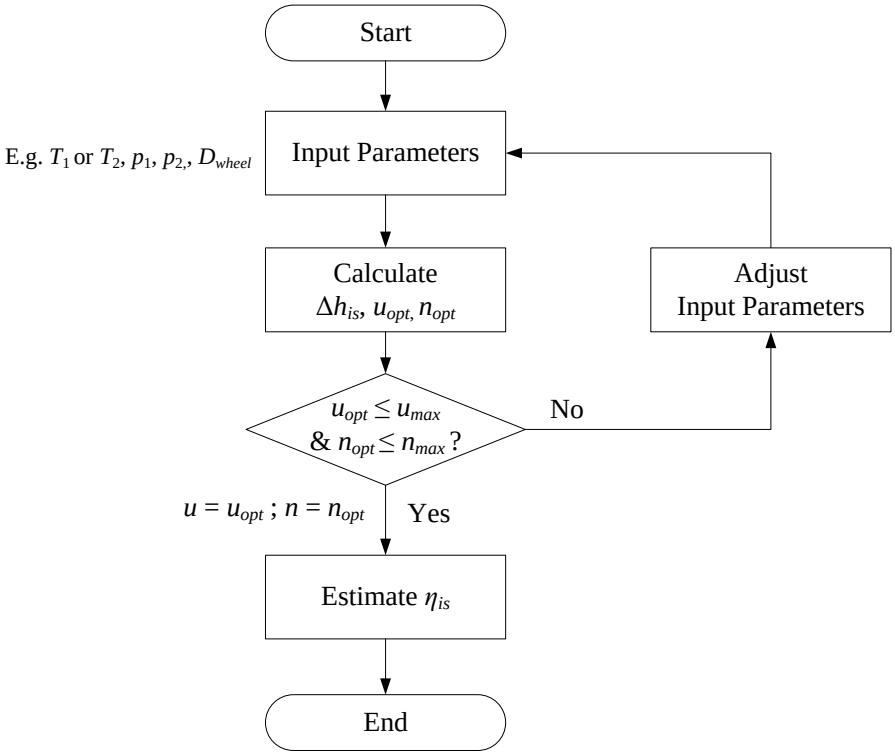

Figure 6.1: Schematic calculation method for the preliminary sizing and performance estimation of turbines in this work

In this work, the wheel diameter D_{wheel} is assumed as an input parameter that is available from standard wheel sizes of turbine manufacturers.

The turbine velocity ratio ν can be used for the preliminary turbine dimensioning. The impeller wheel tip velocity u_2 is calculated from the velocity ratio ν with the isentropic spouting velocity c_s [Bloch & Soares 2001]:

$$\nu = \frac{u_2}{c_s} \,. \tag{6.3}$$

The isentropic specific enthalpy difference Δh_{is} across the turbine is expressed as [Dixon & Hall 2013]:

$$\Delta h_{is} = \frac{1}{2} \cdot c_s^2 \,. \tag{6.4}$$

The maximum turbine isentropic efficiency η_{is} for an ideal turbine is achieved at a turbine velocity ratio $\nu_{opt} = \frac{1}{\sqrt{2}} = 0.707$ [Jumonville 2010, Dixon & Hall 2013]. In this case, the optimum impeller wheel tip velocity $u_{2,opt}$ is calculated as a function of the isentropic enthalpy difference Δh_{is} across the turbine by combining Equation (6.3) with Equation (6.4) as

$$u_{2,opt} = \sqrt{\Delta h_{is}}\,. \tag{6.5}$$

For non-ideal turbines, the optimal turbine velocity ratio ν_{opt} to achieve the maximum turbine isentropic efficiency η_{is} is typically found at turbine velocity ratios $\nu_{opt} \approx 0.7$. The optimum impeller wheel tip velocity $u_{2,opt}$ can then be calculated with [Dixon & Hall 2013]:

$$u_{2,opt} = 0.7 \cdot \sqrt{2 \cdot \Delta h_{is}}\,. \tag{6.6}$$

To ensure the mechanical integrity of the turbine, the thermodynamic and geometrical input parameters are modified until both the rotational speed n_{TU} and the impeller wheel tip velocity u_2 are below the respective allowed maximum $n_{TU} \leq n_{TU,max}$ and $u_2 \leq u_{2,max}$. For a given turbine design and size, the maximum rotational speed $n_{TU,max}$ is assumed to be known from the turbine manufacturers and is assumed based on Figure 4.8. The maximum impeller wheel tip velocity $u_{2,max}$ is assumed to $u_{2,max} = 500\,\mathrm{m/s}$. As explained in Figure 6.1, if the optimal impeller wheel tip velocity $u_{2,opt}$ calculated with Δh_{is} from Equation (6.6) is $u_{2,opt} > u_{2,max}$ or if the optimal rotational speed $n_{TU,opt} > n_{TU,max}$, the turbine impeller wheel tip velocity u_2 or the rotational speed n_{TU} is lowered.

For the process simulation and optimization carried out within this work, the turbine isentropic efficiency $\eta_{is,TU} = 0.75 - 0.88$ [Cardella et al. 2017d] is estimated with a simple correlation as a function of the turbine inlet volumetric flow $\dot{V}_{in}$:

$$\eta_{is,TU} = f(\dot{V}_{TU,in})\,. \tag{6.7}$$

The correlation is based on a comprehensive analysis of the turbine isentropic efficiencies $\eta_{is,TU}$ for H_2, He, Ne and N_2 turbines that was carried out with the aid of design software of turbine manufacturers for different mass flow rates and at varying temperature and pressure conditions. The correlation for the turbine isentropic efficiencies $\eta_{is,TU}$ is implemented in the hydrogen liquefier process simulation model. It is assumed that the turbine isentropic efficiency $\eta_{is,TU}$ from Equation (6.7) corresponds to the turbine efficiency at the optimal rotational speed $n_{TU,opt}$. Additionally, an efficiency reduction factor $\frac{\eta_{is,red}}{\eta_{is,opt}} = 0.98$ is assumed for turbines with $\frac{u_{2,max}}{u_{2,opt}} < 0.9$.

The main turbine design assumptions used in this work are summarized in Table 6.1. For the hydrogen liquefaction processes considered within this work, gas bearing turbines are assumed for turbine powers $P_{TU} \leq 150\,\mathrm{kW}$ while oil bearing or magnetic bearing turbines are assumed to be installed for larger turbine powers $P_{TU} > 150\,\mathrm{kW}$.

Table 6.1: Main design assumptions for the preliminary sizing and performance estimation of the cryogenic turbines. Adapted from [CARDELLA et al. 2017d]

Turbine parameter	Value (Range)
Power capacity P_{TU}	$1 - 15000\,\mathrm{kW}$
Isentropic efficiency η_{is}	$0.75 - 0.88$
Energy recovery efficiency η_{recov}	0.80
Max. wheel tip velocity $u_{2,max}$	$500\,\mathrm{m/s}$
Max. rotational speed n_{max}	$40000 - 350000\,\mathrm{rpm}$
	between 1 kW and 500 kW

As an alternative a maximum number of $z = 3$ gas bearing turbines are assumed to be operable in parallel configuration in the large-scale hydrogen liquefaction processes.

As described in Section 5.1.2, a turbine energy recovery efficiency $\eta_{recov} = 0.80$ is assumed for the cryogenic turbine expanders simulated with a turbine energy recovery via an electric generator.

6.2 Compressors

For the hydrogen liquefaction process simulation and optimization within this work, reciprocating piston and radial-flow turbo compressors are considered. The compressor inlet volumetric flow rate $\dot{V}_{in}$ is assumed as capacity limiting parameter. The design and performance limitations assumed for reciprocating piston and radial-flow turbo compressors are summarized in Table 6.2.

Table 6.2: The maximum number of compressor stages N_{max}, the minimum compressor inlet volumetric flow $\dot{V}_{in,min}$, the maximum compressor inlet volumetric flow $\dot{V}_{in,max}$, and the isentropic efficiency η_{is} range assumed for process development and optimization

Parameter	Reciprocating piston	Radial-flow Turbo
Max. number of stages N_{max}	4	6
Min. volumetric flow $\dot{V}_{in,min}$ in $\frac{m^3}{h}$	1	1000
Max. volumetric flow $\dot{V}_{in,max}$ in $\frac{m^3}{h}$	18000	200000
Isentropic efficiency η_{is}	0.75 - 0.86	0.75 - 0.85
Mechanical-electrical efficiency $\eta_{mech,el}$	0.95	0.95

Based on available data from industrial compressor manufacturers, a comprehensive evaluation of the efficiency of actual reciprocating piston compressors and radial-flow turbo compressors operated with H_2, He, Ne, N_2 and fluid mixtures was carried for different compressor inlet volumetric flow rates $\dot{V}_{in}$. For reciprocating piston compressors

and radial-flow turbo compressors, averaged compressor isentropic efficiencies $\eta_{is,comp}$ were determined as a function of the compressor inlet volumetric flow $\dot{V}_{in}$. Compared to radial-flow turbo compressors, reciprocating piston compressors achieve higher isentropic efficiencies $\eta_{is,comp}$ at smaller compressor inlet volumetric flows $\dot{V}_{in}$.

For the hydrogen liquefier process simulation model described in Chapter 5, the compressor isentropic efficiencies $\eta_{is,comp}$ are computed as a function of the compressor inlet volumetric flow $\dot{V}_{in}$. The assumed compressor isentropic efficiencies $\eta_{is,comp}$ are listed in Table 6.2 and are considered to be conservative.

For the calculation of the compressor power consumption P_{comp}, the mechanical-electrical efficiency $\eta_{mech,el}$ described in Equation 5.1 in Section 5.1.2 is assumed to $\eta_{mech,el} = 0.95$.

6.2.1 Reciprocating compressors

In this work, the hydrogen reciprocating piston compressors used for the large-scale hydrogen liquefaction processes are assumed to be dry-running oil-free multi-stage reciprocating piston compressors with double-acting pistons.

To limit the skid size of reciprocating piston compressors to viable geometrical dimensions, a maximum compressor inlet volumetric flow $\dot{V}_{in,max} = 18000\,\frac{\mathrm{m}^3}{\mathrm{h}}$ per unit is assumed [Cardella et al. 2017d]. For the hydrogen liquefaction processes calculated with a total compressor inlet volumetric flow $\dot{V}_{in,total} > \dot{V}_{in,max}$, a number of z reciprocating piston compressor units are assumed to be installed in parallel configuration. The total compressor inlet volumetric flow $\dot{V}_{in,total}$ is then split among z units:

$$\dot{V}_{in} = \frac{\dot{V}_{in,total}}{z}\,. \tag{6.8}$$

A maximum number of $z_{max} = 3$ reciprocating piston compressor units are assumed to be viable in parallel configuration.

The number of required compressor stages N_{RC} is estimated with the required total compression pressure ratio $\pi_{RC,total}$:

$$\pi_{RC,total} = \frac{p_{out}}{p_{in}} \tag{6.9}$$

and the maximum compression pressure ratio $\pi_{RC,max}$ feasible per stage:

$$N_{RC} = \frac{\log \pi_{RC,total}}{\log \pi_{RC,max}}\,. \tag{6.10}$$

The calculated number of required compressor stages N_{RC} is rounded up to the next higher integer number. Figure 6.2 shows an exemplary process flow diagram of a compressor with $N_{RC} = 3$ compressor stages. The maximum number of compressor stages $N_{RC,max}$ that can be implemented in one reciprocating piston compressor unit

is assumed to $N_{RC,max} = 4$, with a maximum of three inter-stage coolers and one after-stage cooler that are cooled with cooling water. A pressure drop Δp_{cw} is assumed across each cooler.

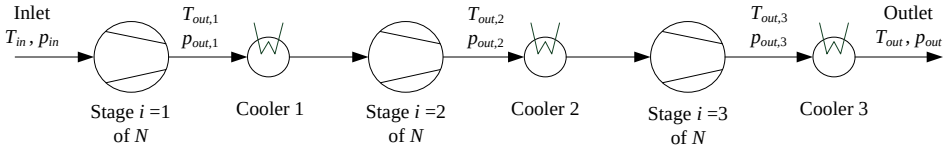

Figure 6.2: Process flow diagram of a compressor with $N_{RC} = 3$ compressor stages

The maximum compression pressure ratio $\pi_{RC,max}$ feasible per stage is assumed to be dependent on the calculated compressor outlet temperature $T_{out,i} \leq T_{out,max}$ after each compressor stage i. The maximum allowed compressor outlet temperature $T_{out,max}$ is assumed to $T_{out,max} = 413\,\mathrm{K}$. For hydrogen compression, this results in a maximum compression pressure ratio in the range $\pi_{RC,max} = 2.2 - 2.5$ per stage.

The stage pressure ratio $\pi_{comp,i}$ is calculated with [Grote & Feldhusen 2007]:

$$\pi_{RC,i} = \pi_{RC,total}^{\frac{1}{N_{RC}}} . \tag{6.11}$$

The compressor outlet pressure $p_{out,i}$ after the compressor stage i is calculated with:

$$p_{out,i} = p_{in,i} \cdot \left(\frac{p_{out}}{p_{in,i}} \right)^{\frac{1}{N_{RC}-i+1}} + \Delta p_{cw} . \tag{6.12}$$

In this work, the compressor inlet volumetric flow rate $\dot{V}_{in}$ is used as main design parameter for the hydrogen reciprocating compressors. The compressor stroke s, the stroke volume V_s as well as the piston diameter D_{pist} and piston rod diameter D_{rod} are calculated based on the procedure for the preliminary design of reciprocating piston compressors described in [Eifler et al. 2009]. The stroke volume V_s is calculated as a function of the total compressor inlet volumetric flow $\dot{V}_{in,tot}$, the rotational speed n_{RC} and the number of cylinders implemented per stage. A maximum of 4 cylinders is assumed to be feasible per reciprocating compressor stage. The piston diameter D_{pist} is calculated as a function of the stroke s and the stroke volume V_s.

The maximum feasible piston diameter is assumed to $D_{pist,max} = 1.0\,\mathrm{m}$ while the maximum piston rod diameter is assumed to be limited to $D_{rod,max} = 0.15\,\mathrm{m}$. The stroke s is calculated with the average piston velocity and the rotational speed $n_{RC} = 200 - 700\,\mathrm{rpm}$. The maximum feasible stroke is assumed to be limited to $s_{max} = 400\,\mathrm{mm}$ [General Electric 2005b].

6.2.2 Turbo compressors

The compressors for the large-scale hydrogen liquefaction processes in this work require compressor inlet volumetric flows $\dot{V}_{in} < 100000\,\frac{\mathrm{m}^3}{\mathrm{h}}$ that are outside the optimal range of application of axial-flow turbo compressors. Therefore, only the design of radial-flow turbo compressors is considered in this work. The radial-flow turbo compressors are hereinafter referred to as turbo compressors.

For the preliminary design of a single turbo compressor stage, the impeller wheel diameter D_{wheel} and the pressure (head) coefficient Ψ are used to calculate the impeller wheel tip velocity u_2, the rotational speed n_{TC} and further non-dimensional design parameters [Grote & Feldhusen 2007]. In this work the aforementioned parameters allow to evaluate the feasibility of the turbo compressor design simultaneously to the process simulation in the hydrogen liquefier process simulation model.

For the preliminary estimation of the compressor main geometrical dimensions, the rotational speed n_{TC} and the number N_{TC} of required turbo compressor impeller stages are calculated. From the ratio between the total isentropic specific enthalpy difference $\Delta h_{is,total}$ across the turbo compressor and the maximum isentropic specific enthalpy difference $\Delta h_{is,max}$ that is feasible per stage, N_{TC} can be estimated [Grote & Feldhusen 2007].

The isentropic specific enthalpy difference Δh_{is} across the turbo compressor stage i is calculated in the hydrogen liquefier process simulator model with the given thermodynamic process parameters e.g. the compressor inlet temperature $T_{in,i}$, the inlet pressure $p_{in,i}$ and the compression stage pressure ratio π_{TC}. The number of required turbo compressor impeller stages N_{TC} is estimated with the ratio between the total compression pressure ratio $\pi_{TC,total}$ required across the compressor and the maximum compression pressure ratio $\pi_{TC,max}$ feasible per stage. For the integrally-geared turbo compressors considered within this work, a maximum number of $N_{TC,max} = 8$ turbo compressor stages are assumed to be feasible.

To achieve the maximum compressor efficiency, the optimal impeller wheel tip velocity $u_{2,opt}$ of a turbo compressor stage is calculated with the isentropic enthalpy difference Δh_{is} and a pressure coefficient of about $\Psi \approx 0.50$ [Casey et al. 2013]:

$$u_{2,opt} = \sqrt{\frac{\Delta h_{is}}{\Psi}}\,. \tag{6.13}$$

The calculated optimal impeller wheel tip velocity $u_{2,opt}$ must satisfy the condition $u_{2,opt} \leq u_{max}$. For state-of-the-art turbo compressors, the maximum feasible impeller wheel tip velocity $u_{2,max}$ is assumed to be limited by the aerodynamic constraints imposed by the machine Mach number Ma and the velocity of sound a_0 [Grote & Feldhusen 2007]:

$$Ma = \frac{u_{2,opt}}{a_0} < 0.9\,. \tag{6.14}$$

The maximum feasible impeller wheel tip velocity is further limited by mechanical constraints and is assumed to $u_{2,max} = 500\,\mathrm{m/s}$.

The maximum feasible compression pressure ratio $\pi_{TC,max}$ per stage is dependent on the fluid and on the maximum feasible impeller wheel tip velocity $u_{2,max}$. The maximum feasible compression pressure ratio $\pi_{TC,max}$ per stage can be calculated with the maximum feasible isentropic enthalpy difference $\Delta h_{is,max}$ per stage and the thermodynamic process parameters that are available from the process simulation. With Equation (6.13) and the assumed $u_{2,max} = 500\,\mathrm{m/s}$, the calculated maximum isentropic specific enthalpy difference $\Delta h_{is,max}$ that is feasible per stage is approximately $\Delta h_{is,max} = 125\,\mathrm{kJ/kg}$.

The rotational speed n_{TC} is calculated with the optimal impeller wheel tip velocity $u_{2,opt}$, which is calculated with Equation (6.13):

$$n_{TC} = \frac{u_2}{3.1416 \cdot D_{wheel}}\,. \tag{6.15}$$

The impeller wheel diameter D_{wheel} is assumed as geometrical input parameter with the condition $n_{TC} \leq n_{TC,max}$. In this work, the maximum feasible rotational speed n_{max} is dependent on the impeller wheel diameter D_{wheel} and is assumed to $n_{max} = 50000\,\mathrm{rpm}$.

The allowed non-dimensional flow coefficient φ:

$$\varphi = \frac{4 \cdot \dot{V}_{in}}{3.1416 \cdot D_{wheel}^2 \cdot u_2} \tag{6.16}$$

is assumed to be in the range $0.02 \leq \varphi \leq 0.16$ [Grote & Feldhusen 2007] and is used to evaluate the feasibility of the impeller wheel design during process simulation.

6.3 Plate-fin heat exchangers

During the process simulation and optimization in the hydrogen liquefier process simulation model, a preliminary dimensioning of the multi-stream aluminium brazed plate-fin heat exchangers (PFHX) is performed.

The preliminary geometrical dimensions of the PFHX are estimated with the aid of the basic thermodynamic heat transfer correlations described in Section 3.1.3. As described in Equation (3.17), the product of the overall heat transfer coefficient U and the total PFHX surface area A is calculated with the total heat flow rate $\dot{Q}$ of the heat exchanger and the mean temperature difference ΔT_m between the cold and warm streams:

$$U \cdot A = \frac{\dot{Q}}{\Delta T_m}\,. \tag{6.17}$$

The product of the overall heat transfer coefficient U and the heat transfer surface A is calculated in the process simulator as $(U \cdot A)_{sim}$ value from the composite curves of the warm and the cold streams.

The total PFHX heat transfer surface A_{PFHX} is estimated with the $(U \cdot A)_{sim}$ value calculated in the process simulator and an assumed overall heat transfer coefficient U_{PFHX} [ALPEMA 2000, Belloni et al. 2008]:

$$A_{PFHX} = \frac{(U \cdot A)_{sim}}{U_{PFHX}} . \tag{6.18}$$

The overall heat transfer coefficient U_{PFHX} is assumed to $U_{PFHX} = 0.1\,\mathrm{kW/m^2 \cdot K}$ for the PFHX in the hydrogen liquefier coldbox and to $U_{PFHX} = 0.2\,\mathrm{kW/m^2 \cdot K}$ for the PFHX in the precooling coldbox [Belloni et al. 2008].

The required PFHX volume V_{PFHX} is estimated from the calculated PFHX heat transfer surface A_{PFHX} with the specific surface a_v for PFHX assumed to $a_v = 500 - 700\,\mathrm{m^2/m^3}$ [ALPEMA 2000, Belloni et al. 2008]:

$$V_{PFHX} = \frac{A_{PFHX}}{a_v} . \tag{6.19}$$

The maximum feasible PFHX volume $V_{PFHX,max}$ is assumed to be dependent on the maximum operating pressure p_{max} of the PFHX streams. The higher the maximum operating pressure p_{max}, the lower the maximum feasible PFHX volume $V_{PFHX,max}$ per core. The maximal PFHX geometrical dimensions per core that are assumed to be manufacturable for the hydrogen liquefaction processes within this work are $l_{max} \times h_{max} \times w_{max} = 8.2 \times 2.5 \times 1.5\mathrm{m}$ [Linde AG n.d., Belloni et al. 2008]. The maximum feasible PFHX volume is assumed to be between $V_{PFHX,max} = 15 - 30\,\mathrm{m^3}$ per core [Linde AG n.d., Alekseev 2014].

If a larger PFHX volume V_{PFHX} is calculated in the hydrogen liquefier process simulation, multiple PFHX cores are assumed to be installed in parallel configuration within the coldbox. The number of required PFHX cores z_{PFHX} in parallel configuration is estimated from the ratio between the PFHX volume V_{PFHX} calculated with Equation (6.19) and the assumed maximum feasible PFHX volume $V_{PFHX,max}$ per core:

$$z_{PFHX} = \frac{V_{PFHX}}{V_{PFHX,max}} . \tag{6.20}$$

The size of the precooling coldbox and liquefier coldbox that can be installed is limited. Therefore for the hydrogen liquefaction capacities considered in this work, the feasible total PFHX volume V_{PFHX} is assumed to be limited by a maximum number of $z_{PFHX,max} = 2$ cores installed in parallel configuration.

The minimum allowed temperature difference ΔT_{min} and the maximum allowed temperature difference ΔT_{max} between the warm streams and the cold streams are assumed for each PFHX. In this work, the minimum allowed temperature difference ΔT_{min} calculated at any point in the PFHX is assumed to be $\Delta T_{min} = 0.5 - 2.5$ dependent on the operating temperature and the type of fluid, e.g. single-phase or two-phase flow or pure fluid or fluid mixture [Cardella et al. 2017d]. To avoid thermal stresses, the

maximum allowed temperature difference ΔT_{max} calculated at any point in the PFHX is assumed to $\Delta T_{max} = 25\,\mathrm{K}$ in this work.

Depending on the type of fluid, a fixed pressure drop Δp is assumed for each fluid stream in the PFHX, e.g. for single-phase or two-phase flow and for passages with or without catalyst.

6.3.1 PFHX with ortho- to para-hydrogen conversion

The plate-fin heat echangers (PFHX) with ortho- to para-hydrogen conversion catalyst are calculated in MATLAB® with the kinetic model for PFHX developed by DONAUBAUER 2015 and described in Section 5.4.

The inlet temperature T_{in}, the inlet pressure p_{in} and the inlet mole fraction of para-hydrogen $y_{p,in}$ of the hydrogen feed stream are the input parameters to the kinetic model for PFHX in MATLAB®.The kinetic model for PFHX in MATLAB® is used to determine the outlet temperature T_{out}, the outlet pressure p_{out} as well as the outlet mole fraction of para-hydrogen $y_{p,out}$ and the required geometrical dimensions of the PFHX as a result of the catalytic ortho- to para-hydrogen conversion in the hydrogen feed stream in the PFHX.

Based on the results of the kinetic model, the required volume of catalyst V_{cat} and the required PFHX volume V_{PFHX} are calculated. In order to evaluate the impact of the catalytic ortho- to para-hydrogen conversion on the required volume of catalyst V_{cat} and the PFHX volume V_{PFHX}, the non-dimensional ortho- to para-hydrogen conversion factor η_{conv} is defined as

$$\eta_{conv} = \frac{y_{p,out} - y_{p,in}}{y_{p,out}^{eq} - y_{p,in}}\,, \tag{6.21}$$

with the inlet mole fraction of para-hydrogen $y_{p,in}$ and the outlet mole fraction of para-hydrogen $y_{p,out}$ calculated in the kinetic model in MATLAB® [CARDELLA et al. 2017a]. The conversion factor η_{conv} is used as a performance indicator for the degree to which the ortho- to para-hydrogen conversion is carried out within the PFHX reactor. A high conversion factor η_{conv} represents a thermodynamic efficient catalytic ortho- to para-hydrogen conversion close to the equilibrium mole fraction of para-hydrogen y_p^{eq}.

7 Process economics

For the development of hydrogen liquefaction processes, both the plant capital expenses (CAPEX) and the operating expenses (OPEX) need to be considered. A hydrogen liquefier cost estimation model was developed within this work to methodically evaluate and optimize the process economics for large-scale hydrogen liquefaction processes.

A schematic procedure for the implemented cost estimation model is outlined in Figure 7.1.

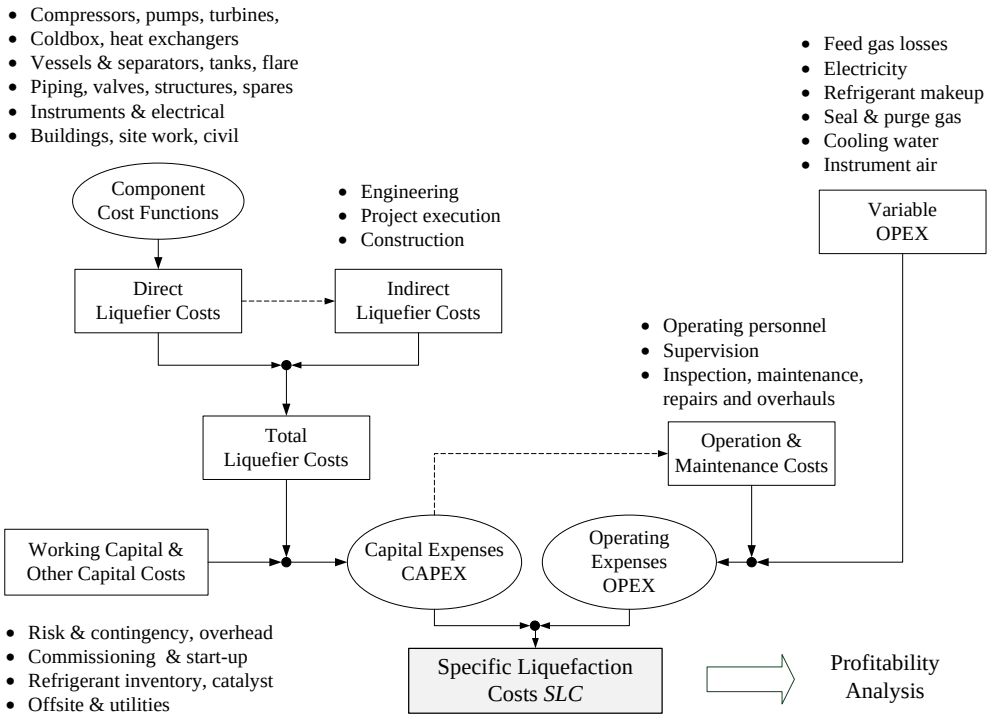

Figure 7.1: Schematic procedure for the estimation of the specific liquefaction costs *SLC* of hydrogen liquefiers [Cardella et al. 2017d]

The total plant CAPEX and OPEX are used to calculate and optimize the specific liquefaction costs *SLC* for different hydrogen liquefaction process concepts. The *SLC* in €/kg LH_2 represent the total costs of ownership (TCO) of a hydrogen liquefaction plant and are equal to the costs for producing one kg of liquid hydrogen LH_2. Furthermore, the hydrogen liquefier costs estimated by the model can be used as a basis to perform profitability analyses and to assess the whole liquid hydrogen supply chain from well-to-wheel.

The cost estimation model is based on equipment cost functions and cost factors which were developed and modified within this work from cost functions published in literature. Another source were equipment cost functions and cost factors which were developed

and validated within this work with cost data available from industrial equipment manufacturers. Cost indexes are employed in order to relate the available cost data to present costs.

The hydrogen liquefier cost estimation model is implemented in the hydrogen liquefier process simulation model described in Chapter 5 and is coupled directly to process and equipment parameters that are calculated during process simulation.

A detailed description of the hydrogen liquefier cost estimated model is given in the following sections of this chapter. Parts of this chapter are described in Cardella et al. 2017b, Cardella et al. 2017d.

7.1 Specific liquefaction costs

In this work the process economics of large-scale hydrogen liquefaction processes are evaluated with the specific liquefaction costs *SLC*. The *SLC* are mainly dependent on the hydrogen liquefaction capacity, the selected process design and the plant location.

The implemented calculation method for the *SLC* is described in Figure 7.1. The *SLC* are calculated in €/kg LH_2 with Equation (7.1) in the hydrogen liquefier process simulation models and are used as the objective function for process optimization:

$$SLC = \frac{C_{CAPEX,a} + C_{OPEX,var} + C_{OM}}{\dot{m}_{\mathrm{LH_2},a}} \,. \tag{7.1}$$

The *SLC* include an assumed fixed annuity payment $C_{CAPEX,a}$ in €/a resulting from the total plant capital expenses (CAPEX) $C_{CAPEX,total}$, the yearly variable operating expenses (OPEX) $C_{OPEX,var}$ in €/a as well as the operational and maintenance (O&M) expenses C_{OM} in €/a. The variable OPEX $C_{OPEX,var}$ include yearly OPEX such as the electricity costs C_{el}, the refrigerant make-up costs $C_{OPEX,rfr}$ and other utility costs.

The sum of the total CAPEX and OPEX is divided by the yearly LH_2 production capacity $\dot{m}_{\mathrm{LH_2},a}$ in tonnes per annum (tpa). The yearly LH_2 production capacity $\dot{m}_{\mathrm{LH_2},a}$ is calculated with the yearly plant utilization rate Y_a and the hydrogen liquefaction capacity $\dot{m}_{\mathrm{LH_2}}$ in kg/s:

$$\dot{m}_{\mathrm{LH_2},a} = Y_a \cdot 8760\,\mathrm{h/a} \cdot 3600\,\mathrm{s/h} \cdot \dot{m}_{\mathrm{LH_2}} \,. \tag{7.2}$$

The yearly plant utilization rate Y_a is assumed at $Y_a = 0.95$ which is equivalent to approximately 8322 h/a and is in line with the availability required for large cryogenic refrigeration plants [Serio et al. 2015].

The calculation of the total plant CAPEX $C_{CAPEX,total}$, the variable OPEX $C_{OPEX,var}$ and the operational and maintenance (O&M) expenses C_{OM} is described in detail in the following sections.

7.2 Capital expenses

The total plant capital expenses (CAPEX) $C_{CAPEX,total}$ are required for the engineering, procurement and construction as well as the commissioning and start-up of hydrogen liquefaction plants. The total plant CAPEX $C_{CAPEX,total}$ of hydrogen liquefiers is dependent on the selected process design, the hydrogen liquefaction capacity and the plant location [Syed et al. 1998].

Different CAPEX estimation methods for industrial process plants are published in literature ranging from simple order-of-magnitude estimates to firm price cost estimates [Sinnott 1993]. To evaluate different hydrogen liquefaction process concepts, the plant CAPEX estimation method implemented in this work is based on a level of accuracy comparable to that of preliminary feasibility studies [Couper 2003]. It is assumed that the hydrogen liquefaction plant is erected within an existing industrial complex in which major utilities and facilities are available from outside the boundaries (battery limits) of the hydrogen liquefier [Sinnott 1993].

For the specific liquefaction costs SLC calculated within this work, the total plant CAPEX $C_{CAPEX,total}$ is assumed as a fixed annuity payment $C_{CAPEX,a}$ with the following relation:

$$C_{CAPEX,a} = C_{CAPEX,total} \cdot \frac{I_{fix} \cdot (1 + I_{fix})^{t_p}}{(1 + I_{fix})^{t_p} - 1} \,. \tag{7.3}$$

This amount $C_{CAPEX,a}$ has to be paid yearly at a fixed annual interest rate I_{fix} over an assumed payment period $t_p = 20\,\text{a}$ [Syed et al. 1998]. The higher the assumed fixed annual interest rate I_{fix}, the higher is the impact of the plant CAPEX $C_{CAPEX,total}$ on the total SLC. Fixed annual interest rates in the range $I_{fix} = 0.07 - 0.11$ [Syed et al. 1998, Langguth 2015] are common and thus $I_{fix} = 0.07$ is assumed within this work.

The total plant CAPEX $C_{CAPEX,total}$ is calculated with the relation

$$C_{CAPEX,total} = C_{CAPEX,liq} + C_{CAPEX,work} + C_{CAPEX,off} + C_{CAPEX,other} \tag{7.4}$$

as the sum of the hydrogen liquefier CAPEX $C_{CAPEX,liq}$, the working CAPEX $C_{CAPEX,work}$, the offsite CAPEX $C_{CAPEX,off}$ and other CAPEX $C_{CAPEX,other}$ [Syed et al. 1998].

The hydrogen liquefier CAPEX $C_{CAPEX,liq}$ include the CAPEX for the engineering, procurement and construction tasks that are required to make the hydrogen liquefaction plant ready for commissioning and start-up [Sinnott 1993]. As illustrated in Figure 7.1, the hydrogen liquefier CAPEX $C_{CAPEX,liq}$ in this work is calculated as the sum of the hydrogen liquefier direct CAPEX $C_{CAPEX,direct}$ and the indirect CAPEX $C_{CAPEX,indirect}$ [Sinnott 1993, Couper 2003]:

$$C_{CAPEX,liq} = C_{CAPEX,direct} + C_{CAPEX,indirect} \,. \tag{7.5}$$

The estimation of the hydrogen liquefier CAPEX $C_{CAPEX,liq}$ is described in the following sections.

7.2.1 Direct liquefier costs

The cost estimation accuracy is increased by splitting the hydrogen liquefaction process into different process modules [Guthrie 1969]. The equipment costs C_i are subdivided into warm equipment $C_{i,w}$ and cold equipment costs $C_{i,c}$ as well as into relevant cost modules according to their function within the hydrogen liquefier.

As illustrated in Figure 7.1, the hydrogen liquefier direct CAPEX $C_{CAPEX,direct}$ include the capital expenses for the purchase, delivery and installation [Couper 2003] of the following hydrogen liquefier equipment:

- Coldbox system C_{cbs} as described in Section 4.3.1,
- Warm compression system C_{wcs}: compressors C_{comp} and liquid pumps C_{pump} including motor drives and coolers; warm vessels $C_{ve,w}$,
- LH_2 storage tank system C_{sts}: LH_2 storage tank C_{tank}, flare system C_{flare} and filling station C_{fill},
- Piping and valves C_{pv} including vacuum-insulated transfer lines C_{tra},
- Structures C_{str},
- Analysers and instrumentation C_{ai},
- Electrical systems C_{es} and control systems C_{cs},
- Capital spare parts C_{csp} and
- Construction buildings C_{bd} and site preparation C_{pre}.

The cost estimation method for the hydrogen liquefier direct CAPEX $C_{CAPEX,direct}$ is summarized in Table 7.1. The capital cost estimation model implemented within this work is based on equipment cost functions and percentage cost factors that were either adapted from literature [Walas 1988, Syed et al. 1998, Couper 2003] or that were developed and fitted specifically for the estimation of hydrogen liquefier equipment costs. For the development and validation of the equipment cost functions, available cost data from equipment manufacturers and industrial hydrogen liquefiers was used.

To correlate the hydrogen liquefaction capacity and the process design with the plant CAPEX, the equipment cost functions are calculated as a function of equipment capacity parameters [Walas 1988]. Additional cost factors for materials, fluid type, temperature, pressure and design are introduced in this work. In the cost model implemented in the hydrogen liquefier process simulation model, the equipment cost functions are calculated during process simulation and optimization.

The implemented cost functions estimate the costs for the hydrogen liquefier equipment i either as purchased costs at the supplier manufacturing location $C_{sup,i}$ or as installed equipment costs $C_{inst,i}$ [Walas 1988, Couper 2003]:

$$C_{inst,i} = f_{inst} \cdot C_{del,i} = f_{inst} \cdot f_{del} \cdot C_{sup,i} \,. \tag{7.6}$$

Table 7.1: Estimation of the hydrogen liquefier direct capital expenses (CAPEX) $C_{CAPEX,direct}$

Direct liquefier costs	Cost estimation
Warm compression system	$C_{wcs} = \sum C_{comp} + \sum C_{pump} + \sum C_{ve,w}$
Coldbox system	$C_{cbs} = \sum C_{cb} + \sum C_{TU} + \sum C_{PFHX} + \sum C_{ve,c}$
Piping and valves	$C_{pvt} = C_{pv,w} + C_{pv,c} + C_{tra}$
Structural	$C_{str} = f_{str} \cdot C_{wcs,del}$
Analysers & Instrumentation	$C_{ai} = C_{ai,w} + C_{ai,c}$
Electrical & control system	$C_{ecs} = C_{es,w} + C_{es,w} + C_{cs,w} + C_{cs,c}$
LH_2 storage system	$C_{sts} = C_{tank} + C_{flare} + C_{fill}$
Capital spare parts	C_{csp}
Construction buildings	$C_{bd} = f_{bd} \cdot (C_{cbs,del} + C_{wcs,del} + C_{sts} + C_{csp})$
Site preparation	$C_{pre} = f_{pre} \cdot (C_{cbs,del} + C_{wcs,del} + C_{sts} + C_{csp})$
Total direct CAPEX	$C_{CAPEX,direct} = C_{wcs} + C_{cbs} + C_{pvt} + C_{str}$ $+C_{ai} + C_{ecs} + C_{sts} + C_{csp} + C_{bd} + C_{pre}$

To calculate equipment delivered costs $C_{del,i}$ to the hydrogen liquefier construction site, a delivery cost factor $f_{del} = 1.05$ [Couper 2003] is assumed. To calculate the equipment installed costs $C_{inst,i}$, an installed cost factor f_{inst} is applied.

The available cost data for the hydrogen liquefier equipment is related to a specific year in the past. In this work, the *Chemical Engineering Plant Cost Index* (CEPCI) [Chemical Engineering n.d.] is used to relate the equipment costs from a past year $C_{a,1}$ to the present year $C_{a,2}$ with cost indexes CI:

$$C_{a,2} = C_{a,1} \cdot \frac{CI_{a,2}}{CI_{a,1}}. \tag{7.7}$$

The equipment cost functions for the coldbox vessels costs C_{cb}, the warm vessels costs $C_{ve,w}$ and cold vessels costs $C_{ve,c}$ are based on simple cost-capacity correlations [Williams 1947, Peters et al. 1991] that are fitted with equipment base cost parameters K_i developed in this work.

For the coldbox vessels costs C_{cb}, the plate-fin heat exchanger (PFHX) costs C_{PFHX} are used as capacity parameter. The warm vessels and cold vessels costs, $C_{ve,w}$ and $C_{ve,c}$, include the costs for the refrigerant storage vessels, phase separator vessels, adsorber vessels and ortho- to para-hydrogen reactor vessels implemented in the hydrogen liquefaction processes. The volume V_i in m^3, the inlet volumetric flow rate $\dot{V}_{in}$ in m^3/h or the mass flow rate $\dot{m}_i$ in kg/s are used as capacity parameters for $C_{ve,w}$ and $C_{ve,c}$. The cost degression exponents $e_{d,i}$ for vessels are taken from literature [Walas 1988, Couper 2003].

The LH_2 storage tank costs C_{tank} are calculated with equipment costs functions for shop-fabricated and field-erected storage tanks from literature [Walas 1988, Couper 2003]. In this work, the base cost parameter K_{tank} is fitted for double-walled vacuum-insulated cryogenic LH_2 tanks. The LH_2 product storage volume V_{LH_2} is used as capacity parameter for the LH_2 storage tank costs C_{tank}.

The equipment cost functions developed in this work for the compressors C_{comp}, the turbine expanders C_{TU} and the plate-fin heat exchangers (PFHX) C_{PFHX} are presented in the following paragraphs. Further equipment costs that are included in the hydrogen liquefier direct CAPEX $C_{CAPEX,direct}$ are assumed as fixed costs or are calculated by applying percentage cost factors on subtotal or total cost items.

Compressor costs

The compressor cost function used in this work for reciprocating piston compressors $C_{comp,RC}$ and for turbo compressors $C_{comp,TC}$ is calculated with the cost degression exponents $e_{d,RC}$ and $e_{d,TC}$ from literature [Walas 1988]. The compressor cost function for reciprocating piston compressors $C_{comp,RC}$ is calculated with the following relation:

$$C_{comp,RC} = f_{f,RC} \cdot f_{T,RC} \cdot K_{comp,RC} \cdot (P_{comp})^{e_{d,RC}} . \tag{7.8}$$

The compressor cost function for turbo compressors $C_{comp,TC}$ is calculated with the following relation:

$$C_{comp,TC} = f_{f,TC} \cdot f_{T,TC} \cdot K_{comp,TC} \cdot (P_{comp})^{e_{d,TC}} . \tag{7.9}$$

The compressor power consumption P_{comp} in kW is used as compressor capacity parameter [Walas 1988]. In this work, the base cost parameters for reciprocating piston compressors $K_{comp,RC}$ and for turbo compressors $K_{comp,TC}$ from Walas 1988, Syed et al. 1998 and Couper 2003 were converted from USD ($) to EUR (€) currency at a fixed conversion rate and were updated to the year 2014 with cost indexes CI. The implemented compressor cost functions $C_{comp,RC}$ and $C_{comp,TC}$ are assumed to calculate the compressor installed costs including the costs for electric motor drives and coolers.

To match the common compressor applications in hydrogen liquefiers, the compressor cost functions $C_{comp,RC}$ and $C_{comp,TC}$ were further developed and adapted within this work. To distinguish between compressors operating at warm or cryogenic compressor inlet temperatures, the temperature cost factor f_T is introduced. To take into account the impact of the process fluid on the compressors costs, the fluid cost factor f_f is introduced, e.g. to distinguish between explosive gases that require ATEX certification and inert gases. To take into the account potential cost savings in the engineering and installation of identical compressor units operating in parallel configuration, a cost reduction factor $f_{CR} = 0.8$ is assumed.

Turbine expander costs

Two different turbine cost functions $C_{TU,i}$ for hydrogen liquefiers are implemented within this work. The turbine shaft power P_{TU} in kW is used as capacity parameter for the turbine expander cost estimation [Walas 1988].

For a turbine shaft power $P_{TU} \leq 150\,\text{kW}$, high-speed cryogenic turbine expanders with gas bearing technology are assumed and the turbine cost function $C_{TU,1}$ is defined as follows:

$$C_{TU,1} = f_{ds,TU,1} \cdot f_{f,TU,1} \cdot f_{T,TU,1} \cdot K_{TU,1} \cdot (P_{TU})^{e_{d,TU,1}} . \tag{7.10}$$

The base cost parameter $K_{TU,1}$ and the degression exponent $e_{d,TU,1}$ were fitted in this work with available cost data from industrial turbine manufacturers. To account for the impact of different process fluids and the fluid molar mass $\bar{M}$ on turbine equipment costs, the fluid cost factor $f_{f,TU,1}$ is introduced. To account for additional costs for the design with turbine energy recovery and to differentiate between turbines with more complex designs, the design cost factor $f_{ds,TU,1}$ is introduced e.g. for subatmospheric or two-phase flow operation at the turbine outlet. To take into account the special turbine design for lower cryogenic temperatures, the temperature cost factor $f_{T,TU,1}$ is introduced.

For larger turbines with a turbine shaft power $P_{TU} > 150\,\text{kW}$, a second turbine cost function $C_{TU,2}$ is employed within this work:

$$C_{TU,2} = f_{ds,TU,2} \cdot f_{f,TU,2} \cdot f_{T,TU,2} \cdot K_{TU,2} \cdot (P_{TU})^{e_{d,TU,2}} . \tag{7.11}$$

The cost degression exponent $e_{d,TU,2}$ and base cost parameter $K_{TU,2}$ are taken from literature [Walas 1988, Syed et al. 1998, Couper 2003]. The base cost parameter $K_{TU,2}$ given in literature is modified in this work with turbine cost data available from cryogenic turbine manufacturers. The turbine cost factors for temperature $f_{T,TU,2}$, fluid type $f_{f,TU,2}$ and design type $f_{ds,TU,2}$ are used also for the turbine cost function $C_{TU,2}$.

For both turbine cost functions $C_{TU,1}$ and $C_{TU,2}$, the base cost parameters K_{TU} are converted to EUR (€) currency and are updated to the year 2014 with cost indexes CI.

Plate-fin heat exchanger costs

The plate-fin heat exchanger (PFHX) heat transfer surface A_{PFHX} has an important impact on the OPEX and the CAPEX of the hydrogen liquefaction process. Therefore, the PFHX costs C_{PFHX} are often calculated as a function of the PFHX heat transfer surface A_{PFHX} or the PFHX volume V_{PFHX} [Walas 1988, VDI 2013].

In this work, both A_{PFHX} and V_{PFHX} are used as capacity parameters for the PFHX costs C_{PFHX} and are calculated, as described in Section 6.3, in the process simulator with the $(U \cdot A)_{sim}$ value, the product of the overall heat transfer coefficient U and the total PFHX surface area A.

The PFHX cost function C_{PFHX} developed in this work is expressed in form of a simple cost-capacity correlation [Williams 1947, Peters et al. 1991] that relates the calculated PFHX volume V_{PFHX} to a base PFHX volume $V_{PFHX,0}$ with the corresponding base PFHX cost parameter $K_{PFHX,0}$:

$$C_{PFHX} = f_{p,PFHX} \cdot f_{ds,PFHX} \cdot K_{PFHX,0} \cdot \left(\frac{V_{PFHX}}{V_{PFHX,0}} \right)^{e_{d,PFHX}} . \tag{7.12}$$

The PFHX costs C_{PFHX} are also dependent on the process design and PFHX design. To account for the increasing manufacturing costs of PFHX at higher design pressures p_{ds}, a PFHX design pressure cost factor f_p and a PFHX design cost factor f_{ds} are introduced in this work. The design pressure cost factor f_p is based on a pressure cost factor defined in literature for shell and tube heat exchangers and is calculated as a function of the heat transfer surface A for different pressures [Walas 1988, Couper 2003]:

$$f_{p,PFHX} = a_1 \cdot \ln\left(A_{PFHX}\right) + b_1 . \tag{7.13}$$

Table 7.2: Heat exchanger pressure cost factor coefficients as a function of the design pressure p_{ds}. Adapted from [Walas 1988, Couper 2003]

Design pressure p_{ds}	a_1	b_1
$< 21\,\text{bar}$	0.78	0.05
$21 - 41\,\text{bar}$	1.03	0.07
$41 - 62\,\text{bar}$	1.14	0.12
$> 62\,\text{bar}$	1.37	0.15

The coefficients a_1 and b_1 are dependent on the heat exchanger design pressure p_{ds} [Walas 1988, Couper 2003]. In this work, the coefficients a_1 and b_1 from literature [Walas 1988, Couper 2003] are applied to the PFHX and are adapted to include also a pressure cost factor f_p for design pressures $p_{ds} > 62\,\text{bar}$, as shown in Table 7.2. The PFHX costs C_{PFHX} increase for higher design pressures p_{ds} and for larger PFHX heat transfer surfaces A_{PFHX}.

Other direct costs

Other hydrogen liquefier direct costs $C_{direct,other}$ listed in Table 7.1 include additional equipment and facilities required for the construction and operation of the hydrogen liquefier. In this work, the costs for construction buildings C_{bd} such as compressor and coldbox buildings, warehouses, shelters, office and control rooms are included in the CAPEX estimation. The hydrogen liquefier costs associated with the site preparation C_{pre} are considered in this work, including the expenses for the cleaning, piling and paving of the construction site as well as the excavations required for equipment foundations and buildings [Couper 2003]. The costs for construction land are not considered.

7.2.2 Indirect liquefier costs

The hydrogen liquefier indirect CAPEX $C_{CAPEX,indirect}$ include all the costs related to the engineering, the design and the construction of the hydrogen liquefaction plant as well as the costs associated with the execution and the supervision of the project [Peters et al. 1991, Sinnott 1993].

In this work, the hydrogen liquefier indirect CAPEX $C_{CAPEX,indirect}$ are calculated by applying percentage cost factors on subtotal or total cost items of the total direct hydrogen liquefier CAPEX $C_{CAPEX,direct}$, as indicated by the dashed line in Figure 7.1. The cost estimation method for the hydrogen liquefier indirect CAPEX $C_{CAPEX,indirect}$ is summarized in Table 7.3.

Table 7.3: Estimation of the hydrogen liquefier indirect capital expenses (CAPEX) $C_{CAPEX,indirect}$

Indirect liquefier costs	Cost estimation
Engineering & Project Execution	$C_{eng,c} = f_{eng,c} \cdot C_{cb,del}$
	$C_{eng,w} = f_{eng,w} \cdot C_{eng,c}$
	$C_{eng} = C_{eng,c} + C_{eng,w}$
Construction & Supervision	$C_{cst} = f_{cst} \cdot (C_{CAPEX,direct} + C_{eng})$
Total Indirect Liquefier Costs	$C_{CAPEX,indirect} = C_{eng} + C_{cst}$

The engineering costs C_{eng} of the hydrogen liquefier depend on the hydrogen liquefaction process and on the project complexity [Syed et al. 1998]. In this work, the estimation of the total engineering costs C_{eng} is divided into the engineering costs required for the cold equipment in the cryogenic coldbox systems $C_{eng,c}$ and the engineering costs required for the warm equipment of the plant $C_{eng,w}$. The engineering costs C_{eng} are estimated with the cost factors $f_{eng,c}$ and $f_{eng,w}$ that are based on literature [Peters et al. 1991] and are fitted in this work for industrial hydrogen liquefiers.

In this work, the construction costs C_{cst} are assumed to include, amongst others, the costs for concrete and civil works, foundations, materials and tools, permits as well as other miscellaneous construction costs. The construction costs C_{cst} of the hydrogen liquefier are dependent on the plant location and are difficult to quantify with preliminary cost estimation methods. Therefore, a conservative approach for the estimation of the construction costs C_{cst} is implemented. A part of the hydrogen liquefier construction costs are assumed to be included in the equipment installed costs $C_{inst,i}$ as well as in the construction buildings costs C_{bd} and the site preparation costs C_{pre}. Additionally, the construction costs C_{cst} are estimated by applying the cost factor f_{cst} on the hydrogen liquefier direct CAPEX $C_{CAPEX,direct}$ and on the engineering costs C_{eng}.

7.2.3 Overhead and contingencies

The capital expenses (CAPEX) for overhead and administration C_{over} as well as the contingencies for uncertainty and risks C_{risk} [Syed et al. 1998] in the applied hydrogen liquefaction process and equipment technology are included in the herein described cost model and are described in Table 7.4.

Table 7.4: Estimation of the hydrogen liquefier capital expenses (CAPEX) for overhead and administration C_{over}, working CAPEX $C_{CAPEX,work}$ and offsite CAPEX C_{off}

Other capital expenses	Cost estimation
Contingencies & Risks	$C_{risk} = f_{risk} \cdot (C_{cbs,del} + C_{wcs,del})$
Overhead & Administration	$C_{over} = f_{over} \cdot (C_{cbs,del} + C_{wcs,del} + C_{sts} + C_{csp})$
Commissioning & Start-up	$C_{start} = f_{start} \cdot (C_{CAPEX,direct} + C_{eng})$
Working capital	$C_{CAPEX,work} = C_{start} + C_{ivt} + C_{cat}$
Offsite Capital	$C_{CAPEX,off}$

7.2.4 Working capital and offsite capital

Further capital expenses (CAPEX) considered in the total plant CAPEX $C_{CAPEX,total}$ of hydrogen liquefiers are the working CAPEX $C_{CAPEX,work}$ and the offsite CAPEX $C_{CAPEX,off}$. The cost estimation method for the working CAPEX $C_{CAPEX,work}$ and the offsite CAPEX C_{off} is described in Table 7.4.

The working CAPEX $C_{CAPEX,work}$ is required for the commissioning and start-up of the hydrogen liquefaction plant [Sinnott 1993]. Within the herein implemented hydrogen liquefier cost model, the working CAPEX $C_{CAPEX,work}$ includes the commissioning and start-up CAPEX C_{start} as well as the expenses for initial refrigerant inventories C_{ivt} and ortho- to para-hydrogen catalyst material C_{cat}. For the estimation of the capital expenses for plant commissioning and start-up C_{start}, a percentage cost factor between $8 - 10\%$ on the fixed CAPEX is recommended in literature [Peters et al. 1991]. In this work, a percentage cost factor f_{start} is applied on the sum of the direct CAPEX $C_{CAPEX,direct}$ and the total engineering CAPEX C_{eng}.

The offsite CAPEX $C_{CAPEX,off}$ includes the CAPEX for auxiliary equipment and utilities that are not directly associated with the plant [Sinnott 1993]. Depending on the hydrogen liquefaction process design, the following cost items are included in the offsite CAPEX $C_{CAPEX,off}$:

- Refrigerant storage tanks including make-up system,
- Liquid nitrogen LN_2 storage tank system,
- Cooling water system with cooling towers, pumps, water treatment, make-up system and potable water,

- Chiller units and
- Instrument air system.

7.3 Operating expenses

Besides the total plant capital expenses (CAPEX) $C_{CAPEX,total}$, the specific liquefaction costs SLC include also the variable operating expenses (OPEX) $C_{OPEX,var}$ and the fixed or semi-variable operational and maintenance (O&M) expenses C_{OM}.

7.3.1 Variable Operating costs

The variable operating expenses (OPEX) $C_{OPEX,var}$ are directly dependent on the hydrogen liquefaction capacity $\dot{m}_{\mathrm{LH_2}}$. As described in Table 7.5, the variable OPEX $C_{OPEX,var}$ in the herein described hydrogen liquefier cost estimation model include the yearly variable OPEX for utilities: the electricity costs C_{el}, the costs for hydrogen feed gas losses C_{feed}, the make-up costs for refrigerants C_{rfr} and cooling water C_{cw}. It is assumed that the yearly OPEX for seal and purge gas C_{spg} include the yearly OPEX for seal gas, purge gas and dry instrument gas.

Table 7.5: Estimation of the hydrogen liquefier yearly variable operating expenses $C_{OPEX,var}$

Variable OPEX $C_{OPEX,var}$	Cost estimation
Electricity	$C_{el} = c_{el} \cdot \dot{m}_{\mathrm{LH_2},a} \cdot SEC$
Hydrogen feed gas losses	$C_{feed} = SPC \cdot f_{feed} \cdot \dot{m}_{\mathrm{LH_2},a}$
Liquid nitrogen $\mathrm{LN_2}$	$C_{\mathrm{LN_2}} = c_{\mathrm{LN_2}} \cdot \dot{m}_{\mathrm{LN_2},a}$
Refrigerant make-up	$C_{rfr} = c_{rfr} \cdot \dot{m}_{loss,a}$
Cooling water make-up	C_{cw}
Seal and purge gas	$C_{spg} = c_{spg} \cdot N_{comp,stage} \cdot \dot{m}_{spg,a}$

Electricity

The electricity costs C_{el} are calculated directly from the specific energy consumption SEC computed in the hydrogen liquefier process simulation model. The specific electricity costs c_{el} for large industrial consumers typically vary between 0.05–0.10 €/kWh dependent on the plant location, local tax regulations and the total energy consumption [Grave et al. 2015, Cardella et al. 2017d]. The specific electricity costs c_{el} are lower for large industrial consumers with a large annual energy consumption. In this work, the base specific electricity costs c_{el} for the large-scale hydrogen liquefiers are assumed with 0.05 €/kWh and a sensitivity c_{el} =0.05-0.10 €/kWh is considered.

Hydrogen feed gas losses

Further yearly OPEX are generated from continuous losses of the hydrogen feed gas and LH_2 product C_{feed}. These costs are estimated in Table 7.5 with the assumed specific production costs SPC for hydrogen gas GH_2 and with a percentage factor f_{feed} on the yearly hydrogen liquefaction capacity $\dot{m}_{LH_2,a}$ [Stolzenburg et al. 2013].

Refrigerant make-up

The yearly refrigerant make-up OPEX C_{rfr} due to refrigerant leakage losses have an impact on the specific liquefaction costs SLC. The refrigerant costs C_{rfr} are dependent on the hydrogen liquefaction process design and are estimated in Table 7.5 with the specific refrigerant costs c_{rfr} and the respective refrigerant loss rate $\dot{m}_{loss}$.

The refrigerant make-up OPEX C_{rfr} increase with a higher number of refrigeration cycles and are dependent on the refrigerant fluid as well as on the compressor seal system [Kohler et al. 2014]. The specific refrigerant costs c_{rfr} for neon and helium can be one or two order-of-magnitudes higher than for hydrogen. Due to the availability of comparatively inexpensive GH_2 from the hydrogen feed stream, the hydrogen refrigerant make-up costs are assumed to be included in C_{feed}.

7.3.2 Operating and Maintenance costs

The operational and maintenance (O&M) expenses C_{OM} are part of the specific liquefaction costs SLC. A higher number of compressors and expanders typically increases the yearly O&M expenses and decreases the yearly plant utilization rate Y_a. The yearly O&M expenses C_{OM} include the expenses for plant maintenance C_M as well as for operating personnel and supervision C_{OPS}. The cost estimation method used for the O&M expenses C_{OM} is shown in Table 7.6. The plant maintenance costs C_M are the yearly expenses for the plant operation, inspection, maintenance, repair and overhaul [Syed et al. 1998, Bloch & Geitner 2006]. As indicated by the dashed line in Figure 7.1, the plant maintenance costs C_M are estimated as a fixed percentage f_M of the total plant CAPEX $C_{CAPEX,total}$ per year [Syed et al. 1998, Stolzenburg & Mubbala 2013]. For the operating personnel and supervision, a fixed yearly expense C_{OPS} is assumed.

Table 7.6: Estimation of the hydrogen liquefier yearly O&M expenses C_{OM}

O&M expenses C_{OM}	Cost estimation
Personnel for operation and supervision	C_{OPS}
Plant maintenance	$C_M = f_M \cdot C_{CAPEX,total}$
Total operation and maintenance (O&M)	$C_{OM} = C_{OPS} + C_M$

8 Process development and optimization

Parts of this chapter are published in Cardella et al. 2017b, Cardella et al. 2017d, Cardella et al. 2017c.

The main objective of this work is to develop highly efficient large-scale hydrogen liquefaction processes which are optimized in the total specific liquefaction costs *SLC*. The process development approach implemented for economically viable large-scale hydrogen liquefaction processes is illustrated schematically in Figure 8.1.

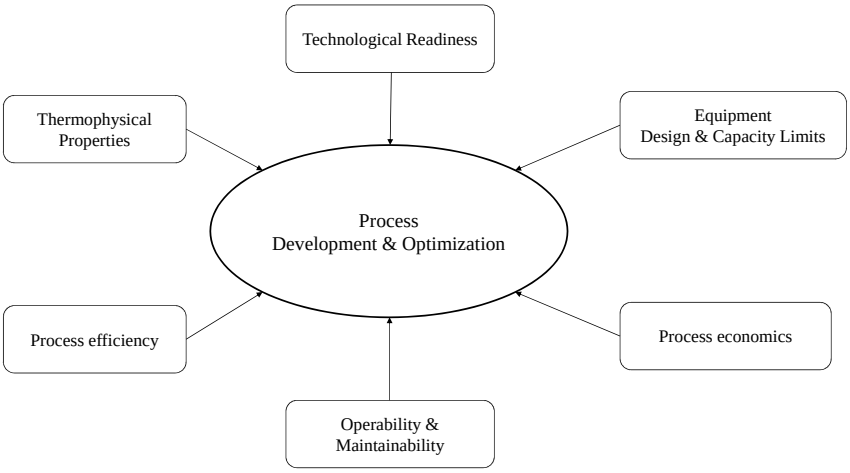

Figure 8.1: Key design factors considered in the development and optimization of large-scale hydrogen liquefaction processes. Adapted from Cardella et al. 2015a

The process and economic boundary conditions used for process simulation and optimization cases in this work are defined in the basis of design in Section 8.1. To identify the key drivers for the cost and efficiency optimization, an evaluation of a state-of-the-art built hydrogen liquefaction process and two selected conceptual large-scale hydrogen liquefaction processes is undertaken in Section 8.2.

The development of economically viable large-scale hydrogen liquefaction processes is carried out by considering both the specific energy consumption *SEC* and the specific liquefaction costs *SLC*. For this purpose, detailed process-economic studies are carried out in the hydrogen liquefier process simulator and cost estimation model. During process development, the feasibility of the equipment design is evaluated with data from industrial equipment manufacturers. Further aspects which are considered for the process development are the process complexity, the technological maturity and risks as well as the plant operability and maintainability.

8.1 Basis of design

The main process and economic boundary conditions are defined as basis of design and simulation within this section. The development objectives for the large-scale hydrogen liquefaction processes are summarized in Table 8.1. The target is to increase the hydrogen liquefaction capacity from the installed hydrogen liquefiers with 5–25 tpd LH_2 to 100 tpd LH_2. The large-scale hydrogen liquefaction processes developed within this chapter shall have a high technological readiness and shall minimize the specific liquefaction costs *SLC* to approximately 1 €/kg LH_2 or below while reducing the specific energy consumption *SEC* to values close to 6 kWh/kg LH_2.

Table 8.1: Objectives for the large-scale hydrogen liquefaction processes developed within this work. Adapted from Cardella et al. 2017c

Parameter	Target
Technological readiness	Medium-term, year 2020
Capacity in tpd LH_2	100
SEC in kWh/kg LH_2	6.0
SLC in €/kg LH_2	≤ 1.0

8.1.1 Process boundary conditions

The specific energy consumption *SEC* and the specific liquefaction costs *SLC* of hydrogen liquefaction processes are dependent on process boundary conditions.

The main process boundary conditions used for the process simulation throughout this work are given in Table 8.2. For process simulation, the purity of the hydrogen feed stream is assumed to be 100%. In the hydrogen liquefier process simulation, the liquid hydrogen LH_2 product is assumed as saturated liquid. As a simplification for process comparison, the heat inleak from warmer components and the ambience into the hydrogen liquefaction process and the LH_2 storage tank is considered to be zero. Therefore, it is assumed that no LH_2 boil-off is generated in the storage tank and no boil-off re-liquefaction is required. The re-liquefaction of cold hydrogen gas from the rising level in the storage tank is not considered.

In this work, an inlet hydrogen feed gas pressure $p_{feed,in} = 25$ bar is assumed. The LH_2 product storage pressure is assumed at $p_{LH_2} = 2.0$ bar. The minimum specific work for an ideal hydrogen liquefaction process with the boundary conditions defined in Table 8.2 is calculated to approximately $w_{ideal} = 2.7$ kWh/kg LH_2.

Table 8.2: Basis of simulation: main process boundary conditions. Adapted from Cardella et al. 2017b, Cardella et al. 2017d

Ambience conditions	
Ambient temperature T_{amb} in K	293
Ambient pressure p_{amb} in bar	1.013
Cooling water temperature T_{cw} in K	293
Hydrogen feed stream (inlet)	**Value**
Capacity $\dot{m}_{\mathrm{LH_2}}$ in tpd LH_2	100
Feed Pressure $p_{feed,in}$ in bar	25
Feed Temperature $T_{feed,in}$ in K	303
Mole fraction of para-H_2 $y_{p,in}$	0.25
LH_2 product stream	
Pressure $p_{\mathrm{LH_2}}$ in bar	2
Temperature (saturated) $T_{\mathrm{LH_2}}$ in K	22.8
Mole fraction of para-H_2 $y_{p,final}$	≥ 0.98

Table 8.3: Main assumptions for the hydrogen liquefier cost model. Adapted from Cardella et al. 2017b, Cardella et al. 2017d

Cost model assumptions	Value
Plant location	Germany
Plant utilization rate Y_a	0.95
Plant operation period t_p in years	20
Yearly interest rate I_{fix}	0.07
Base electricity costs c_{el} in €/kWh	0.05

8.1.2 Economic boundary conditions

The main economic boundary conditions used for the cost estimation model in the hydrogen liquefier process simulation are summarized in Table 8.3.

8.1.3 Equipment simulation basis

For the process development, only process equipment and systems with a technological readiness level (TRL) [U.S. Department of Energy 2011] above TRL 7 are considered in this work [Cardella et al. 2017c]. The main equipment assumptions used for the simulation of the unit operations in the hydrogen liquefier simulator model are summarized in Table 8.4 [Cardella et al. 2017d]. Based on the unit operations,

the preliminary equipment design correlations described in Chapter 6 are implemented in the hydrogen liquefier process simulator model.

Table 8.4: Main assumptions for the simulation of the unit operations in the hydrogen liquefier simulator model. Adapted from Cardella et al. 2017d

Compressors	Parameter	Value (Range)
Reciprocating piston	Isentropic efficiency η_{is}	$0.78 - 0.86$
	Inlet volumetric flow $\dot{V}_{in}$ in m^3/h	18000
Centrifugal turbo	Isentropic efficiency η_{is}	$0.76 - 0.85$
Energy conversion	Mechanical-electrical efficiency $\eta_{mech,el}$	0.95
Expanders	**Parameter**	**Value (Range)**
Turbine expander	Isentropic efficiency η_{is}	$0.78 - 0.88$
Generator brake	Energy recovery efficiency η_{recov}	0.80
Heat Exchangers	**Parameter**	**Value (Range)**
Plate-fin heat exchanger	Min. temperature difference ΔT_{min} in K	$0.5 - 2.5$
	Max. temperature difference ΔT_{max} in K	25
Coolers	Temperature difference ΔT_{min} in K	5

8.2 Evaluation of prior processes

Based on the boundary conditions described in the previous section, a state-of-the-art built hydrogen liquefier process and two conceptual large-scale hydrogen liquefaction processes from literature are re-calculated in the hydrogen liquefier process simulator model and evaluated.

8.2.1 Reference process

The state-of-the-art 5 tpd LH_2 hydrogen liquefaction process with liquid nitrogen (LN_2) precooling at 80 K and Hydrogen Claude Cycle shown in Figure 4.5 is used as reference process within this work. The reference process is implemented in both the hydrogen liquefier process simulator model in UniSim Design® and in the spreadsheet model in Microsoft Excel®.

The reference 5 tpd LH_2 process is calculated with fixed non-optimized process conditions based on a hydrogen liquefier process design by the company Linde Kryotechnik AG. The process conditions of the LN_2 precooling stream and in the Hydrogen Claude Cycle are similar to the Leuna hydrogen liquefier [Bracha & Decker 2008]. In both hydrogen liquefier process simulation models, the specific energy consumption of the non-optimized

reference 5 tpd LH_2 process is calculated to approximately $SEC = 9.9$ kWh/kg LH_2 [Cardella et al. 2015a]. By assuming a specific energy consumption of 0.5 kWh/kg LN_2 for the LN_2 production, more than 40% of the total *SEC* are required for the LN_2 precooling.

8.2.2 Comparison of existing process concepts

Two large-scale hydrogen liquefaction process concepts from literature described in Chapter 4 are selected as benchmarks for process evaluation. The 50 tpd LH_2 Linde-2010 process concept [Froeschle & Kederer 2010, Ohlig & Decker 2014] is selected as a benchmark process for a high technical maturity and low plant capital expenses (CAPEX). The 50 tpd LH_2 IDEALHY process concept [Stolzenburg et al. 2013] is selected as benchmark for the specific energy consumption *SEC*. As described in Section 4.2.4, the technical maturity of the IDEALHY process concept is lower compared to the Linde-2010 process concept. The main process features of the selected process concepts are summarized in Table 8.5.

Table 8.5: Main features of the 50 tpd LH_2 process concepts Linde-2010 [Froeschle & Kederer 2010, Ohlig & Decker 2014] and IDEALHY [Stolzenburg et al. 2013]

Parameter	Linde-2010	IDEALHY
Feed pressure p_{feed} in bar	25	82
Precooling	N_2 Claude Cycle	MRC
	Chiller	Chiller
Cryogenic refrigeration	H_2 Claude Cycle	He-Ne Brayton Cycle
		H_2 JT Cycle
Reported *SEC* in kWh/kg LH_2	7.5-8.0	6.4-6.8

Based on the boundary conditions defined in Section 8.1.1, the 50 tpd LH_2 Linde-2010 and the IDEALHY process concepts are re-calculated with the hydrogen liquefier spreadsheet model and the cost estimation model. The simulation results for the specific energy consumption *SEC* and the specific liquefaction costs *SLC* for the reference 5 tpd LH_2 process as well as the 50 tpd LH_2 Linde-2010 and IDEALHY process concepts are shown in Figure 8.2 [Cardella et al. 2017c].

The specific energy consumption for the re-calculated 50 tpd LH_2 Linde-2010 process concept is $SEC = 7.4$ kWh/kg LH_2 with an exergy efficiency of approximately $\eta_{ex} = 0.36$. The *SEC* for the re-calculated 50 tpd LH_2 IDEALHY process concept is $SEC = 6.4$ kWh/kg LH_2 ($\eta_{ex} = 0.42$), approximately 14% lower compared to the Linde-2010 process concept. The simulation results for the Linde-2010 and IDEALHY proces concepts show a good match with the *SEC* estimation reported in the original publications.

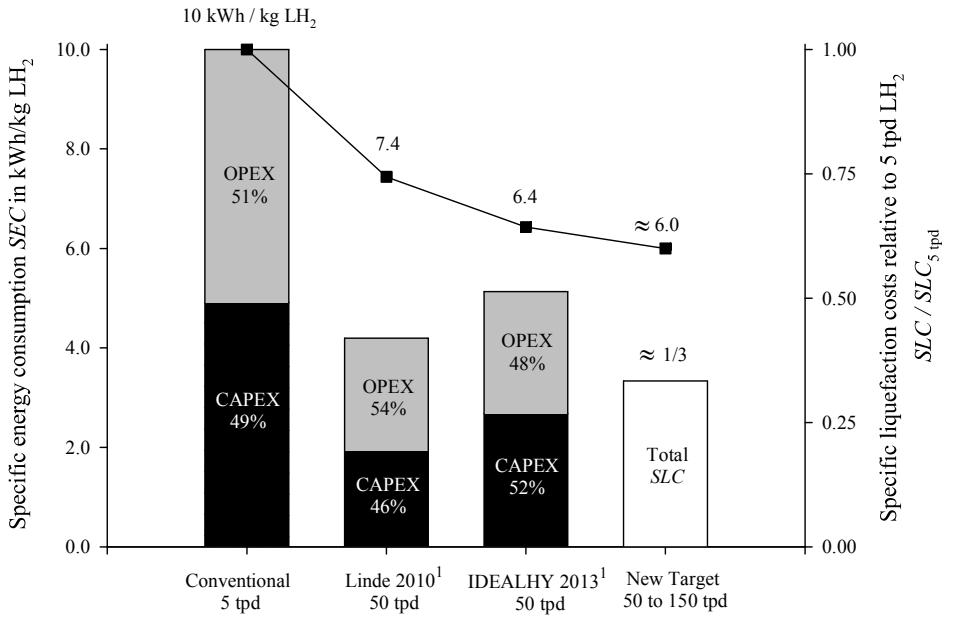

[1]The process and cost calculation was adapted from the original publication

Figure 8.2: Specific energy consumption *SEC* and specific liquefaction costs *SLC* relative to the $SLC_{5\text{tpd}}$ for the reference 5 tpd LH_2 process, the 50 tpd LH_2 Linde-2010 and IDEALHY process concepts re-calculated at electricity costs $c_{el} = 0.05$ €/kWh with the hydrogen liquefier spreadsheet model [Cardella et al. 2017c]

The lower *SEC* of the IDEALHY process concept is mainly due to the lower power consumption required for the precooling with Mixed-refrigerant Joule-Thomson Cycle (MRC) compared to the Nitrogen Claude Cycle in the Linde-2010 process concept. Additionally, the hydrogen feed stream in the IDEALHY process concept is compressed to a higher feed pressure from $p_{feed,in} = 25$ bar to $p_{feed} = 82$ bar, which reduces the *SEC*.

It is noteworthy that the total plant CAPEX $C_{CAPEX,total}$ estimated for the IDEALHY process concept take up more than 50% of the total *SLC* even for the large-scale hydrogen liquefaction capacity of 50 tpd LH_2. The main reason is the capital intensive design of the IDEALHY process concept with a high number of rotating and static equipment. Compared to conventional reciprocating piston and turbo compressors, the hermetically-sealed turbo compressors required for the Helium-Neon (He-Ne) Mixture Brayton Cycle in the IDEALHY process concept [Berstad et al. 2013] are expensive and lead to a substantially higher CAPEX. Additionally, the IDEALHY process concept includes two hydrogen reciprocating piston compressors, the mixed-refrigerant turbo compressor, chiller units as well as a high number of turbine-compressor units and vessels [Berstad et al. 2013].

The operating expenses (OPEX) in Figure 8.2 include both the variable OPEX $C_{OPEX,var}$ and the operational and maintenance (O&M) expenses C_{OM}. The simulation results for

both 50 tpd LH_2 process concepts show that the variable OPEX $C_{OPEX,var}$ represent less than one-third of the total *SLC*.

The bar charts for the calculated specific liquefaction costs *SLC* in Figure 8.2 are plotted relative to the $SLC_{5\text{tpd}}$ calculated for the reference 5 tpd LH_2 process. For the LN_2 supply costs, averaged specific refrigerant costs c_{LN_2} for Germany are assumed.

For the specific electricity costs c_{el} of 0.05 €/kWh, specific liquefaction costs *SLC* of 1.38 €/kg LH_2 are estimated in the original publication [Stolzenburg et al. 2013]. The *SLC* calculated in this work for the 50 tpd LH_2 IDEALHY process concept are higher compared to the *SLC* estimated in the original publication. The total plant capital expenses (CAPEX) $C_{CAPEX,total}$ and the *SLC* for the IDEALHY process concept appear to be underestimated in the original publication of Stolzenburg et al. 2013. Furthermore, the yearly refrigerant make-up costs $C_{OPEX,rfr}$ for the MRC and the Helium-Neon Mixture Brayton Cycle are not included in Stolzenburg et al. 2013. The *SLC* calculated in this work for the 50 tpd LH_2 Linde-2010 process concept are estimated to be more than 50% lower compared to the $SLC_{5\text{tpd}}$ of the reference 5 tpd LH_2 process. The *SLC* for the re-calculated IDEALHY process concept are calculated to be approximately 20% higher compared to the Linde-2010 process concept [Cardella et al. 2015a]. The simulation results thus indicate that the simple and thermodynamically less efficient Linde-2010 process concept is the economically more viable design while the IDEALHY process concept with the higher exergy efficiency η_{ex} requires substantially higher specific liquefaction costs *SLC*.

8.3 Analysis of liquefier process systems

The comparison of the existing process concepts indicated that a hydrogen liquefaction process designed only for specific energy consumption *SEC* minimization can lead to process designs with high capital expenses (CAPEX) that are economically not viable. The optimal process concept is dependent on plant location, liquefaction capacity, operator requirements as well as boundary conditions such as the specific electricity costs c_{el} and the specific refrigerant costs c_{rfr}. In order to reach the herein defined targets, a further process development and optimization is required with the specific liquefaction costs *SLC* as main objective function.

For process development, the hydrogen liquefaction process systems are investigated with process-economic analyses that are carried out in the hydrogen liquefier process simulator model in UniSim Design®. The main hydrogen liquefier process systems are the cryogenic refrigeration cycle and the precooling. The process optimization task is carried out iteratively between the hydrogen liquefier process systems [Cardella et al. 2017d]. The process variables defined for the hydrogen feed stream, such as the feed pressure p_{feed} and the precooling temperature T_{PC}, have a major impact on the process optimization of the hydrogen liquefier process systems.

The process optimization is started with the optimization of the process variables in the liquefier part ($T < T_{PC}$) of the hydrogen liquefier process simulator model while the precooling part ($T \geq T_{PC}$) is simulated with fixed non-optimized process variables. Then, the optimization of the process variables in the precooling part is carried out while the liquefier part is simulated with fixed non-optimized process variables. The optimization is continued until no considerable improvement in the objective function is achieved [Cardella et al. 2017d]. The optimal stand-alone solutions for the hydrogen liquefier process systems are combined into large-scale hydrogen liquefaction process concepts that are further optimized and evaluated.

8.3.1 Investigation of the hydrogen feed stream

The hydrogen feed stream from the inlet of the hydrogen liquefier coldbox to the liquefied hydrogen product is investigated in this section for the hydrogen liquefaction capacity of 100 tpd LH_2.

Precooling temperature

The precooling temperature T_{PC} has a substantial impact on the overall hydrogen liquefaction process. It affects both the precooling system and the cryogenic refrigeration cycle. Generally, a lower precooling temperature T_{PC} results in a higher refrigeration power and a higher compressor power consumption P_{comp} in the precooling system while a higher precooling temperature T_{PC} results in a higher compressor power consumption P_{comp} in the cryogenic refrigeration cycle. Thermodynamically it is convenient to shift a large portion of the refrigeration power to the hydrogen liquefier process system operating at higher temperature and at a higher thermodynamic efficiency.

In the hydrogen liquefier process simulation, the precooling temperature T_{PC} is assumed to be equal to the adsorption temperature T_{ads} and the temperature at which the catalytic ortho- to para-hydrogen conversion is started. A higher thermodynamic efficiency is achieved if the catalytic ortho- to para-conversion is started at a higher temperature. However, the nitrogen adsorption capacity decreases substantially at higher adsorption temperatures T_{ads}. This results in larger adsorber vessels in the coldbox and thus higher costs. Adsorption temperatures above $T_{ads} > 100$ K are thus avoided.

Feed pressure

The specific isobaric heat capacity c_p of normal-hydrogen is plotted in Figure 8.3 as a function of temperature T and pressure p in the region close to the critical temperature T_{crit}. There is a high peak in the specific isobaric heat capacity c_p of hydrogen close to T_{crit}. The c_p variation makes it challenging to keep small temperature differences ΔT between the warm hydrogen feed stream and the cold refrigerant streams inside the plate-fin heat exchangers (PFHX). The non-optimal cooling of the hydrogen feed stream causes inefficiencies that need to be balanced by larger temperature differences ΔT in the PFHX and a higher refrigeration power. As suggested by Lipman et al. 1963, a feed pressure p_{feed} above the critical pressure p_{crit} reduces this high peak in the c_p close to T_{crit}. Smaller temperature differences ΔT in the PFHX can be achieved with a higher hydrogen feed pressure p_{feed}.

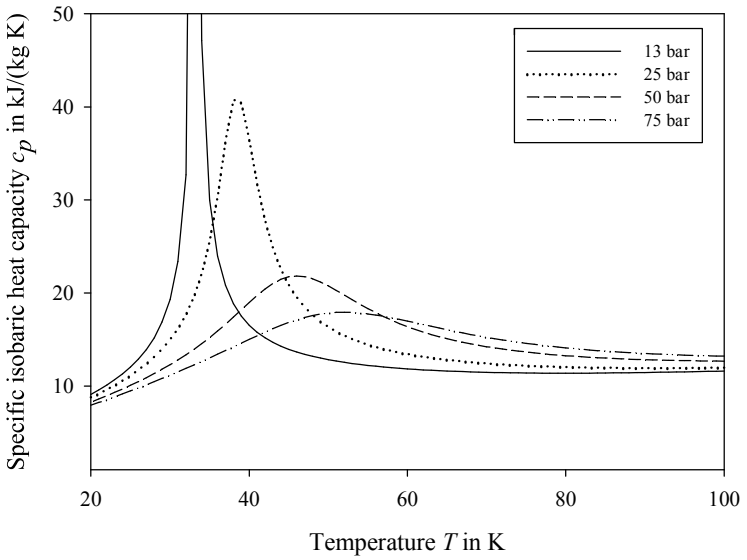

Figure 8.3: Specific isobaric heat capacity c_p of n$-H_2$ as a function of temperature T for different pressures p, computed with REFPROP [Lemmon et al. 2013]

The hydrogen feed stream cooling is thus carried out with an inlet feed pressure above the critical pressure p_{crit}. In this work, the feed pressure is assumed at $p_{feed} = 25\,\text{bar}$. The minimum specific work w_{ideal} required for an ideal hydrogen liquefaction process decreases with higher inlet feed pressures p_{feed}. However, the value of w_{ideal} gives only a qualitative indication for the influence of the feed pressure $p_{feed,in}$ on the specific energy consumption *SEC*. For non-ideal hydrogen liquefaction processes, the *SEC* decreases only slightly with higher inlet feed pressures p_{feed}. A feed pressure $p_{feed} > 25\,\text{bar}$ requires a feed compression with an additional reciprocating piston compressor at higher capital expenses (CAPEX). The additional feed compression power P_{comp} and compressor costs $C_{comp,RC}$ are considered in the *SEC* and in the *SLC*. A higher feed pressure p_{feed} reduces the volumetric flow rates $\dot{V}$ and equipment dimensions but leads also to higher design pressures p_{ds} which are associate with higher costs. The maximum PFHX volume $V_{PFHX,max}$ that can be manufactured per core decreases with higher p_{ds}. Therefore, the maximum feed pressure is limited to $p_{feed,max} = 80\,\text{bar}$ in this work.

The influence of the feed pressure p_{feed} on the non-ideal hydrogen liquefaction process is also dependent on the type of hydrogen feed expansion at the cold end. The feed expansion is carried out at a temperature below T_{crit}. In this work, the reference hydrogen liquefaction process with Hydrogen Claude Cycle and liquid nitrogen (LN_2) precooling is calculated at three different feed pressure levels $p_{feed} = 25 - 75\,\text{bar}$ for 100 tpd LH_2 in the hydrogen liquefier process simulation model. A single-stage reciprocating piston compressor is required for $p_{feed} = 50\,\text{bar}$ and a two-stage reciprocating piston compressor is required for $p_{feed} = 75\,\text{bar}$. Each feed pressure level is simulated with two different feed options for the feed expansion to the LH_2 product storage pressure p_{LH_2}. The two feed options 1 and 2 are illustrated in Figure 8.4. The feed option 1 is designed with a feed expansion via the Joule-Thomson (JT) valve VLV-01. The feed option 2 is designed with a feed expansion in the JT valve VLV-01 and in an upstream JT turbine TU-1. As a modification of the feed option 2 shown in Figure 8.4, the feed stream expanded in the JT turbine TU-1 can be further cooled in PFHX-1B and catalytically converted prior to the final expansion in the JT valve VLV-01.

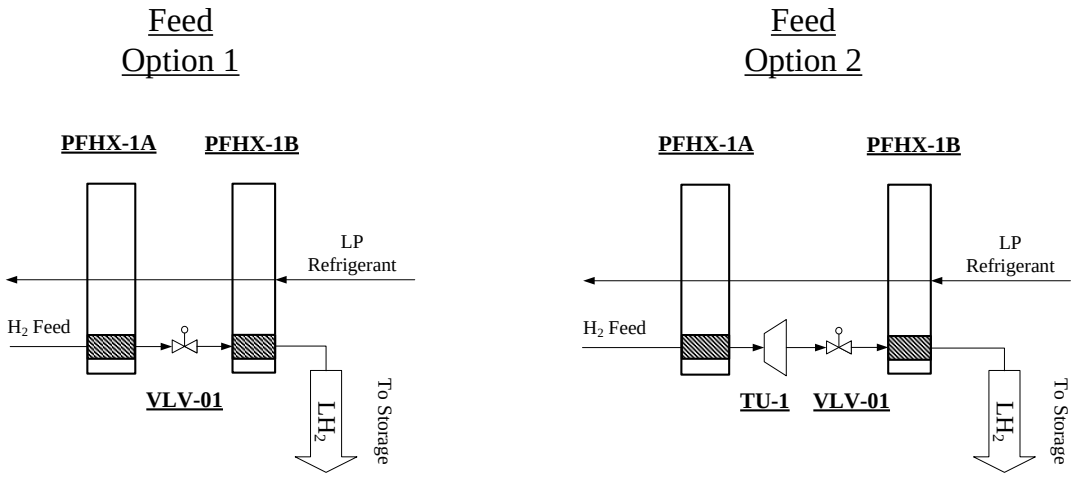

Figure 8.4: Feed options for the feed stream expansion and liquefaction at the cold end

The plot in Figure 8.5 shows the calculated specific energy consumption *SEC* for the feed option 1 and 2 as a function of p_{feed}. For feed option 1 with only JT valve, the *SEC* and specific liquefaction costs *SLC* are higher in the simulation cases with a higher feed pressure p_{feed}. The higher pressure ratio between p_{feed} and p_{LH_2} across the JT valve results in a two-phase flow with a higher vapour fraction y_{vap}. The higher the vapour fraction y_{vap} at the outlet of the JT valve, the higher the required refrigeration power and the higher *SEC*. Compared to the base simulation case with $p_{feed} = 25\,\text{bar}$, the *SEC* with feed option 1 increases by about 5% and the *SLC* increase by about 6% at $p_{feed} = 75\,\text{bar}$. The vapour fraction y_{vap} downstream of JT valve VLV-01 can be reduced by a lower inlet temperature T and smaller pressure ratios across the JT valve VLV-01. This can be achieved in feed option 2 with the upstream JT turbine.

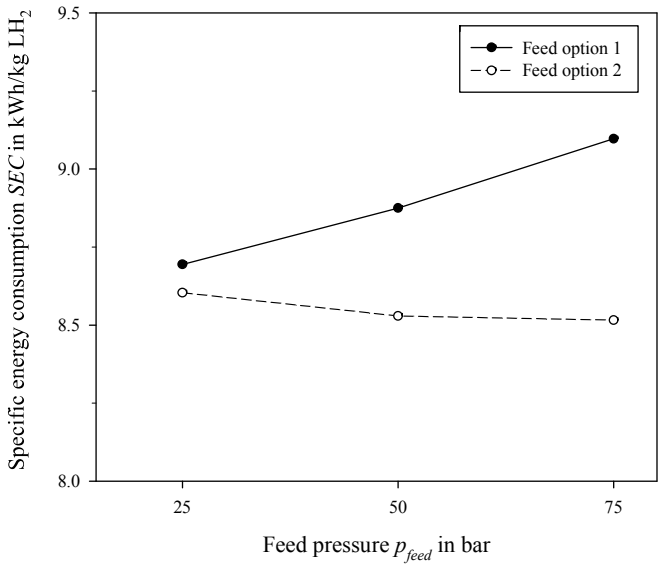

Figure 8.5: Specific energy consumption *SEC* for the 100 tpd LH_2 Hydrogen Claude Cycle with LN_2 precooling calculated as a function of feed pressure p_{feed} with the feed option 1 and 2

For feed option 2, two JT turbines in series are required for the simulation case with $p_{feed} = 75\,\text{bar}$. Compared to the feed option 1, all simulation cases with feed option 2 result in lower *SEC* and *SLC*. The large-scale hydrogen liquefaction processes in this work are thus designed with feed option 2. Compared to the base simulation case with $p_{feed} = 25\,\text{bar}$, the *SEC* calculated with $p_{feed} = 75\,\text{bar}$ decreases by about 1%. However, for $p_{feed} = 75\,\text{bar}$, the CAPEX required for the additional feed compressor and feed turbines result in higher *SLC* and is thus economically not favorable.

Ortho- to para-hydrogen conversion

The catalytic ortho- to para-hydrogen conversion has a major impact on the minimum specific work w_{ideal} for an ideal hydrogen liquefaction process and on the actual specific energy consumption *SEC*. The higher the final mole fraction of para-hydrogen $y_{p,final}$ required in the LH_2 product, the higher the minimum specific work w_{ideal} for an ideal hydrogen liquefaction process. Theoretically, the thermodynamic efficiency of the hydrogen liquefaction process is higher when the catalytic ortho- to para-hydrogen conversion is started at higher temperatures T. Compared to a single catalytic ortho- to para-hydrogen conversion carried out at $p_{LH_2} = 2\,\text{bar}$ and $T_{LH_2} = 22.9\,\text{K}$, an about 25% lower minimum specific work w_{ideal} is required for an ideal hydrogen liquefaction process with a continuous catalytic ortho- to para-hydrogen conversion at equilibrium [Cardella et al. 2015b]. The temperature T at which the catalytic ortho- to para-hydrogen conversion is started is practically constrained by the adsorption temperature $T_{ads} \leq 100\,\text{K}$. To avoid the risk of a degradation of the catalyst, the catalyst is used only downstream of the cryogenic adsorbers.

The hydrogen feed stream cooling and catalytic ortho- to para-hydrogen conversion in a plate-fin heat exchanger (PFHX) was investigated for feed pressures $p_{feed} = 25\,\text{bar}$ and $p_{feed} = 75\,\text{bar}$ [Donaubauer 2015, Cardella et al. 2015b].

At the inlet of the first PFHX, the difference between the equilibrium mole fraction of para-hydrogen $y_{p,in}^{eq}$ and the actual mole fraction of para-hydrogen $y_{p,in}$ is reduced by installing upstream adiabatic or isothermal ortho- to para-hydrogen reactor vessels downstream of the cryogenic adsorber vessels AD-01. A simplified schematic drawing of a hydrogen liquefaction process with a catalyst-filled adiabatic ortho- to para-hydrogen reactor vessel OP-01 is shown in Figure 8.6. As shown in Figure 8.6, a continuous catalytic ortho- to para-hydrogen conversion in PFHX is considered downstream of the ortho- to para-hydrogen reactor vessel OP-01.

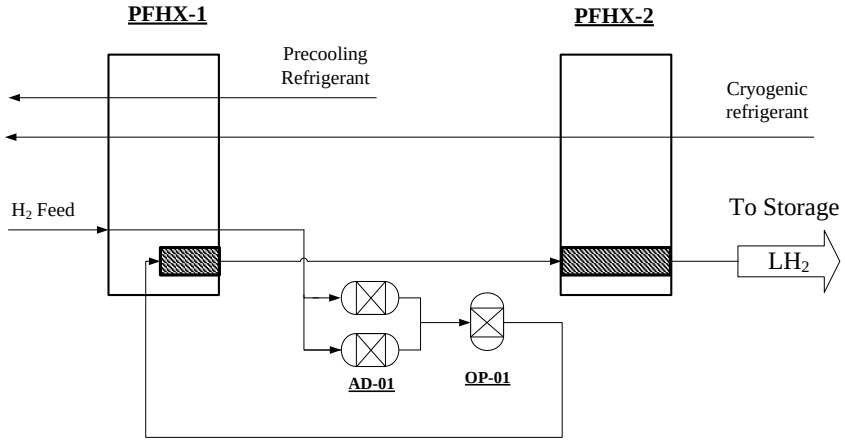

Figure 8.6: Simplified schematic drawing of a hydrogen liquefaction process with a catalyst-filled ortho- to para-hydrogen reactor vessel OP-01 downstream of the cryogenic adsorber vessels AD-01

The cooling and catalytic ortho- to para-hydrogen conversion of the 100 tpd LH_2 hydrogen feed stream inside the PFHX is calculated with the model of Donaubauer 2015. The ortho- to para-hydrogen reactor vessels, placed in the hydrogen feed stream downstream of the adsorber vessels AD-01, reduce both the volume of catalyst V_{cat} required in the PFHX and the PFHX size by nearly 15% [Donaubauer 2015, Cardella et al. 2015b, Donaubauer et al. 2018].

In Figure 8.7 the calculated ortho- to para-hydrogen conversion factor η_{conv} for the hydrogen feed stream cooling and catalytic ortho- to para-hydrogen conversion between the temperatures 85 K and 31 K is plotted [Cardella et al. 2017a]. A high ortho- to para-hydrogen conversion factor η_{conv} reflects an efficient ortho- to para-hydrogen conversion in the PFHX close to the equilibrium mole fraction of para-hydrogen y_p^{eq}. However, a high $\eta_{conv} > 0.9$ requires substantially higher catalyst volumes V_{cat} and larger PFHX volumes V_{PFHX} that are limited by the maximum feasible PFHX block size and coldbox size. In the PFHX at the cold end of the hydrogen liquefier, at temperatures below about 35 K, the equilibrium curve shown in Figure 3.8 becomes flatter. In this

temperature range the actual mole fraction of para-hydrogen y_p calculated in the PFHX can approach the equilibrium fraction of para-hydrogen y_p^{eq} more easily [Lipman et al. 1963, Cardella et al. 2015b, Donaubauer et al. 2018].

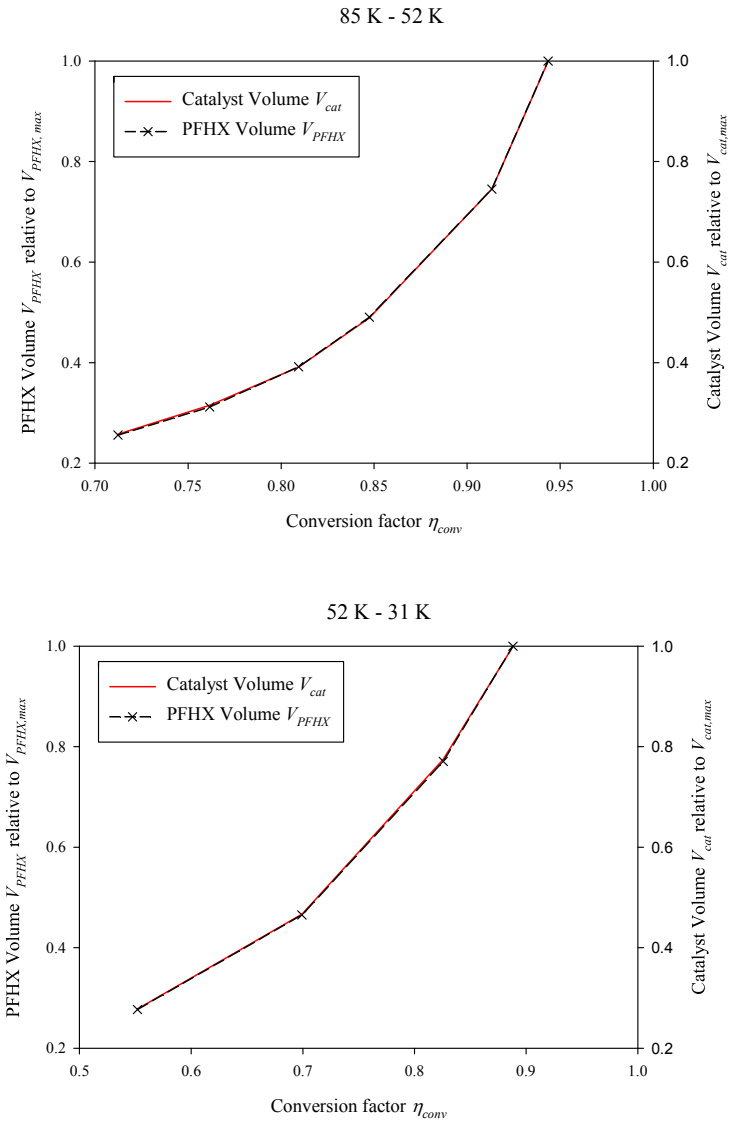

Figure 8.7: PFHX volume V_{PFHX} and catalyst volume V_{conv} calculated as a function of the ortho- to para-hydrogen conversion factor η_{conv} with the kinetic model of Donaubauer 2015 for the hydrogen feed stream cooling and catalytic ortho- to para-hydrogen conversion between the temperatures $T = 85\,\mathrm{K}$ and $T = 31\,\mathrm{K}$ [Cardella et al. 2017a]

8.3.2 Investigation of the cryogenic refrigeration cycle

The refrigerant fluids available for the cryogenic refrigeration cycle of hydrogen liquefaction processes are limited to hydrogen H_2, helium He and neon Ne or a mixture of

these fluids. Hydrogen is the preferred refrigerant for the cryogenic refrigeration cycle because hydrogen is available at the hydrogen liquefier plant site at low cost at around 2 €/kg H_2 [Ball & Wietschel 2009] and can be filled directly from the hydrogen feed stream. Neon and helium are inert gases while the flammability of hydrogen requires additional safety measures and costs to reduce the risk of explosions. Special materials are required for hydrogen because of the risk of material deterioration and embrittlement. However, compared to hydrogen, helium and neon need to be imported to the hydrogen liquefier plant site and are substantially more expensive. In particular, neon is expensive and scarce because the worldwide supply is limited. The specific refrigerant costs c_{rfr} for pure neon of up to 100-200 €/kg Ne are by two order-of-magnitudes higher than for hydrogen and by a factor of up to 20 higher than for helium [Quack et al. 2015].

Compared to helium and neon, hydrogen has superior heat transfer properties and is the most efficient refrigerant for the cryogenic refrigeration cycle. This can be explained by the higher thermal conductivity λ and the higher specific isobaric heat capacity c_p of hydrogen [Kloeppel et al. 2017]. For the hydrogen refrigerant in the cryogenic refrigeration cycle, the variation in the specific isobaric heat capacity c_p with temperature T and pressure p follows a similar pattern to the hydrogen feed stream. The warm and cold composite curves between the hydrogen feed stream and the hydrogen refrigerant in the plate-fin heat exchanger (PFHX) can thus be matched with small temperature differences ΔT. Compared to helium and neon, the isentropic exponent κ of hydrogen is also lower. This results in lower compressor discharge temperatures T_{out} and a more efficient compression.

Liquid hydrogen (LH_2) as refrigerant has a high molar enthalpy of evaporation $\Delta\bar{H}_V$ and can be evaporated with high heat transfer coefficients U at the cold end of the PFHX of the Hydrogen Claude Cycle. In constrast, helium refrigerant in the Helium Brayton Cycle is in gaseous form and can not be evaporated. The triple point temperature T_{trp} of neon is above the normal boiling temperature T_{sat} of hydrogen. Pure neon or fluid mixtures with neon can not be used for the full liquefaction and subcooling of hydrogen for the LH_2 product storage temperature $T_{LH_2} \leq 22.8\,\mathrm{K}$ defined in Table 8.2.

Compression and expansion

The main challenge for the large-scale cryogenic refrigeration cycle is the design of the compressors and turbines. Compared to hydrogen, the higher molar mass $\bar{M}$ and lower velocity of sound a_0 of helium and neon help to achieve higher turbine expansion pressure ratios π_{TU} and reduce the number of turbines.

The maximum expansion pressure ratio π_{TU} in a turbine stage calculated as a function of the inlet turbine temperature T_{in} for a maximum impeller wheel tip velocity $u_{2,max} = 500\,\mathrm{m/s}$ is plotted in Figure 8.8. The feasible turbine expansion pressure ratio π_{TU} increases with lower turbine inlet temperatures T_{in}. Additionally, the velocity of sound a_0 in the refrigerant fluid decreases for lower T_{in}. Higher turbine inlet temperatures T_{in} in the cryogenic refrigeration cycle may require additional turbine strings with a higher number of turbines in series.

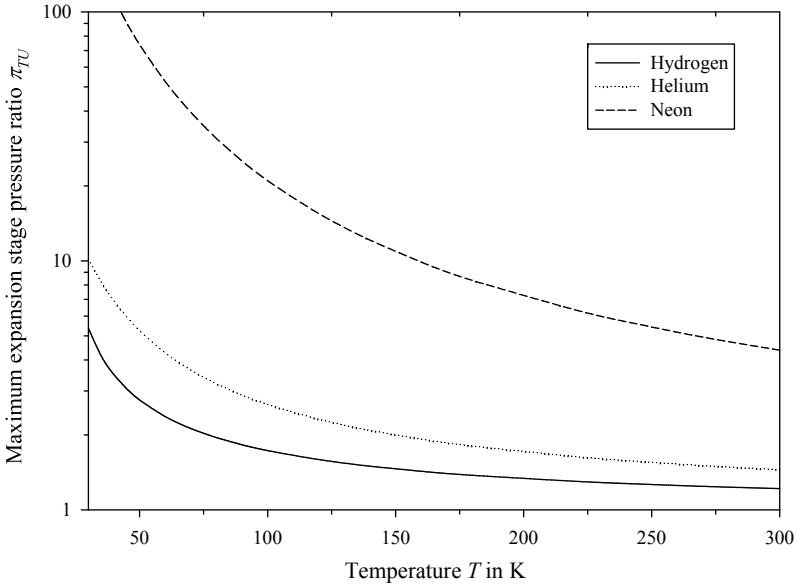

Figure 8.8: Maximum expansion pressure ratio π_{TU} in a turbine stage as a function of the inlet turbine temperature T_{in} for a maximum impeller wheel tip velocity $u_{2,max} = 500\,\mathrm{m/s}$

The main drawback of hydrogen and helium refrigerants is the compression because of the limited size of reciprocating piston compressors. The low molar mass of hydrogen $\bar{M}_{\mathrm{H_2}}$ and helium $\bar{M}_{\mathrm{He}}$ is technically challenging for the compression in turbo compressors.

A plot of the turbo compressor optimal wheel tip velocity $u_{2,opt}$ calculated for different fluids as a function of the compression stage pressure ratio π_{TC} is shown in Figure 8.9. As described in Chapter 6, the assumed maximum impeller wheel tip velocity $u_{2,max} = 500\,\mathrm{m/s}$ limits the maximum feasible compression pressure ratio in turbo compressors to approximately $\pi_{TC,max} \leq 1.1$ per stage for hydrogen. For the total compression pressure ratio $\pi_{TC} \approx 5$ typically implemented in a Hydrogen Claude Cycle, about $N_{TC} = 18$ turbo compressor stages are required divided in at least three turbo compressors in series ($N_{TC} > N_{TC,max} = 8$). The molar mass of helium $\bar{M}_{\mathrm{He}}$ is only slightly higher than the molar mass of hydrogen $\bar{M}_{\mathrm{H_2}}$ and the maximum feasible compression pressure ratio is limited to about $\pi_{TC,max} \leq 1.25$ per stage for helium. The development of affordable high-speed turbo compressors with maximum impeller wheel tip velocities $u_{2,max} > 600\,\mathrm{m/s}$ may enable the design of a cost-optimized Hydrogen Claude Cycle or a Helium Brayton Cycle with turbo compressors in the future. However, these high-speed turbo compressors are not available yet and are not considered for the process development.

The restrictions in the current design of reciprocating piston compressors and turbo compressors can be partially overcome by the use of neon. The high molar mass $\bar{M}_{\mathrm{Ne}}$ and the low triple point temperature $T_{trp} = 24.56\,\mathrm{K}$ of neon make neon a viable option for using turbo compressors in the cryogenic refrigeration cycle. Compared to hydrogen and helium, neon or fluid mixtures with neon have a higher molar mass $\bar{M}$ and can

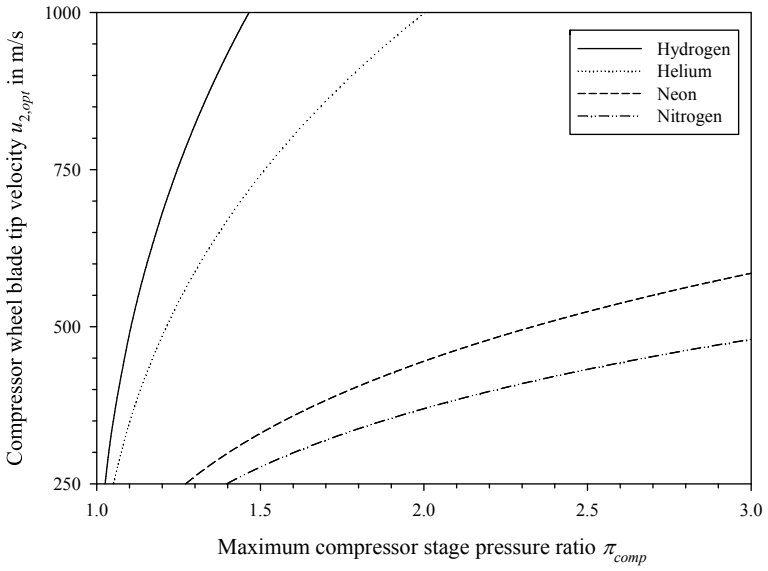

Figure 8.9: Optimal wheel tip velocity $u_{2,opt}$ calculated at ambient temperature T_{amb} as a function of the turbo compression stage pressure ratio π_{TC}

achieve higher compression pressure ratios π_{TC} per stage. However, compared to helium and hydrogen, neon has inferior heat transfer properties [Kloeppel et al. 2017].

As described in Chapter 4, Neon and Helium-Neon Mixture Brayton Cycles are proposed as cryogenic refrigeration cycles for large-scale hydrogen liquefaction in literature. Compared to the Hydrogen Claude Cycle, efficient Helium and Neon Brayton Cycles typically require higher expansion and compression pressure ratios. Compared to hydrogen, the fluid mixture of helium with neon (He-Ne mixture) combines two less efficient and more expensive refrigerants. The high specific refrigerant costs c_{rfr} for helium and neon are included in the specific liquefaction costs SLC as CAPEX for the initial refrigerant inventories C_{ivt} and as OPEX for the refrigerant make-up costs $C_{OPEX,rfr}$. The continuous helium and neon refrigerant leakage losses need to be minimized. Compressors with conventional shaft sealing for pure neon or fluid mixtures with neon would result in extremely high $C_{OPEX,rfr}$ that are economically not viable. As proposed in the IDEALHY process concept [Berstad et al. 2013], single-shaft hermetically-sealed turbo compressors can be used. However, single-shaft hermetically-sealed turbo compressors are generally more expensive, reach lower compression pressure ratios π_{TC} and lower efficiencies compared to multi-shaft turbo compressors [Cardella et al. 2017c].

A novel fluid mixture of hydrogen with neon (H_2-Ne mixture) is proposed in this work for a H_2-Ne Mixture Brayton Cycle with turbo compressors. The H_2-Ne mixture combines the inexpensive and efficient hydrogen refrigerant with the high molar mass of neon $\bar{M}_{\mathrm{Ne}}$. As for the He-Ne mixture proposed by Quack 2002, the H_2-Ne mixture increases the molar mass $\bar{M}$ of the refrigerant. Besides hermetically-sealed turbo compressors, the

herein proposed H_2-Ne mixture in the H_2-Ne Mixture Brayton Cycle allows to use also conventional turbo compressors with dry gas seals.

Single cryogenic refrigeration cycles

Based on the previous considerations, single and dual cryogenic refrigeration cycles are investigated for large-scale hydrogen liquefaction. The Hydrogen Claude Cycle and the Helium Brayton Cycle are possible single cryogenic refrigeration cycles. Due to the comparatively high triple point temperature T_{trp} of neon, single cryogenic refrigeration cycles containing neon are not considered.

The Hydrogen Claude Cycle is more efficient than the Helium Brayton Cycle and is thus chosen as preferred single cryogenic refrigeration cycle over a Helium Brayton Cycle and a Helium-Hydrogen Mixture Brayton Cycle. Moreover at the present state-of-the-art, helium compressors do not offer substantial advantages over hydrogen compressors for large-scale hydrogen liquefaction.

Figure 8.10 shows the herein implemented Hydrogen Claude Cycle. The Hydrogen Claude Cycle design is optimized to reduce the temperature differences ΔT in the plate-fin heat exchangers (PFHX). At the cold end, the Joule-Thomson (JT) part of the Hydrogen Claude Cycle is designed with a JT turbine upstream of the final JT valve.

The Brayton part of the Hydrogen Claude Cycle is investigated with two or three turbine strings and with turbine energy recovery with turbine-generator units. A higher number of turbine strings is thermodynamically efficient because the refrigeration can be provided at different temperature levels and can reduce the temperature differences ΔT in the PFHX. A higher number of turbine strings reduces the refrigerant mass flow rate $\dot{m}$ and the turbine power P_{TU} per turbine string but increases the total number of turbines and costs in the Hydrogen Claude Cycle. Additionally, the turbine energy recovery technology is expensive and the total number of turbines in the Hydrogen Claude Cycle is thus minimized. A process configuration with two turbine strings benefits larger cost-optimized turbine expanders with turbine energy recovery. Three or more turbine strings benefit smaller gas bearing turbines that are limited in size.

Simulation results for the Hydrogen Claude Cycle yielded a negligible difference of below 1% in the calculated specific liquefaction costs SLC between the configuration with two or three turbine strings. In the base simulation cases, the cryogenic refrigeration cycle is designed with two turbine strings.

In the conventional Hydrogen Claude Cycle in built hydrogen liquefiers, a high-pressure (HP) level between $p_{HP} = 20 - 22\,\text{bar}$ and a medium pressure (MP) level between $p_{MP} = 3 - 5\,\text{bar}$ were designed [Gross et al. 1994, Bracha & Decker 2008]. A simple up-scaling of the conventional Hydrogen Claude Cycle of the built 5.5 tpd LH_2 hydrogen liquefier in Leuna [Bracha & Decker 2008] to 100 tpd LH_2 leads to very large compressor inlet volumetric flows $\dot{V}_{in} > 75000\,\text{m}^3/\text{h}$ for the H_2 MP-COMP-2 compressor. Such compressor inlet volumetric flows $\dot{V}_{in}$ are challenging because the

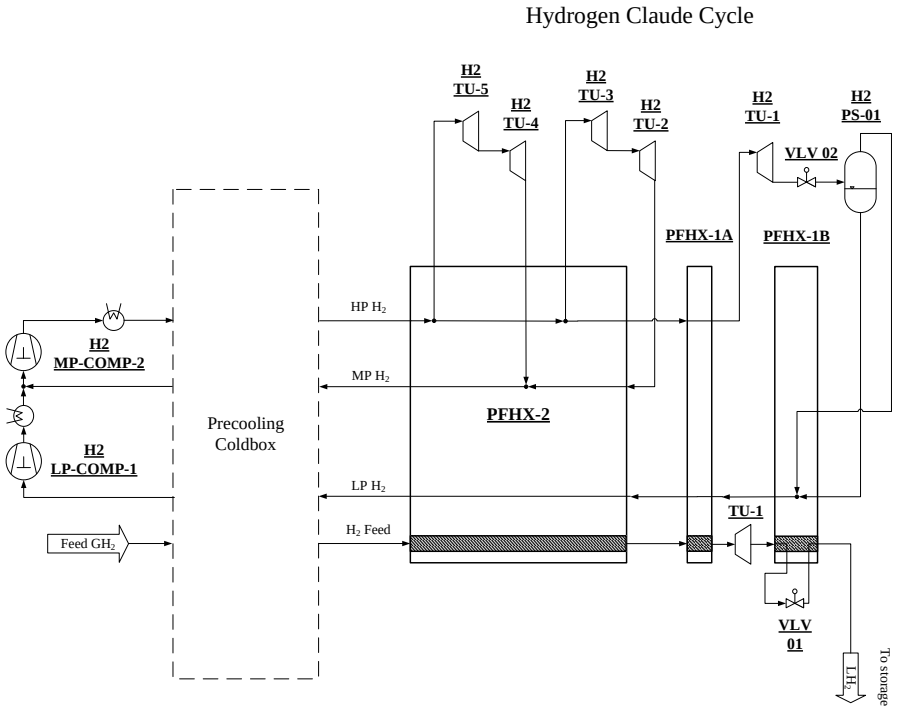

Figure 8.10: Process flow diagram of the Hydrogen Claude Cycle as single cryogenic refrigeration cycle

design requires more than two ($z > 2$) large hydrogen reciprocating piston compressors in parallel configuration.

In this work, the limited size of the reciprocating piston compressors for the 100 tpd LH_2 large-scale hydrogen liquefaction is overcome by optimizing the process design of the Hydrogen Claude Cycle. At the inlet of the hydrogen compressors, hydrogen behaves nearly as an ideal gas, The mass density ϱ of hydrogen increases linearly with higher compressor inlet pressures p_{in} while the specific volume v in m^3/kg of hydrogen decreases. The process design is optimized by substantially increasing the MP level p_{MP} and the HP level p_{HP} in the Hydrogen Claude Cycle. The higher pressures p_{MP} and p_{HP} decrease the compressor inlet volumetric flow $\dot{V}_{in}$. The total pressure ratio in the Hydrogen Claude Cycle is designed with $p_{HP}/p_{MP} \geq 4$. The maximum MP level is limited to pressures $p_{MP,max} \leq 13\,\text{bar}$. The optimized HP level is increased well above the standard pressure of about $p_{HP} \approx 20\,\text{bar}$ and is limited to pressures $p_{HP,max} \leq 80\,\text{bar}$.

The herein designed Hydrogen Claude Cycle for 100 tpd LH_2 is calculated in the hydrogen liquefier process simulator with different MP p_{HP} and HP levels p_{HP} with the total pressure ratio of about $p_{HP}/p_{MP} \approx 4$. In Figure 8.11 the calculated H_2 MP-COMP-2 compressor inlet volumetric flow $\dot{V}_{in}$ is plotted as a function of the HP level p_{HP}. Compared to the conventional HP level $p_{HP} = 20\,\text{bar}$, the calculated H_2 MP-COMP-2 compressor inlet volumetric flow $\dot{V}_{in}$ in the Hydrogen Claude Cycle decreases by up to 60% with higher MP and HP levels. The calculated specific energy

consumption *SEC* and specific liquefaction costs *SLC* at the higher MP and HP levels are also lower.

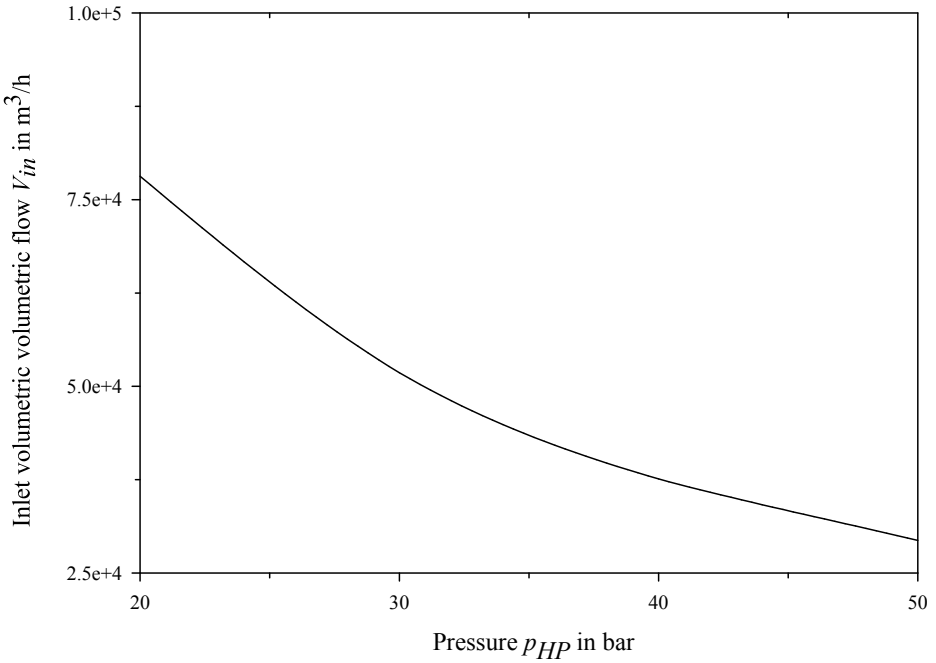

Figure 8.11: H_2 MP-COMP-2 compressor inlet volumetric flow $\dot{V}_{in}$ calculated for 100 tpd LH_2 at different pressure levels in the Hydrogen Claude Cycle

In this work, a HP Hydrogen Claude Cycle for up to 100 tpd LH_2 is thus developed and optimized. The state-of-the-art hydrogen reciprocating piston compressors with a maximum compressor volumetric flow $\dot{V}_{in,max} = 18000\,\mathrm{m^3/h}$ per compressor and up to two ($z = 2$) compressors in parallel configuration are designed for the HP Hydrogen Claude Cycle. To further reduce the H_2 MP-COMP-2 compressor inlet volumetric flow $\dot{V}_{in}$ and the specific energy consumption *SEC*, the total pressure ratio is increased to $p_{HP}/p_{MP} > 4$.

Dual cryogenic refrigeration cycles

A dual cryogenic refrigeration cycle is developed to design a Brayton Cycle with neon or fluid mixtures comprising neon as refrigerant with a turbo compressor as main compressor. For the hydrogen liquefier cooling below the precooling temperature T_{PC}, the dual cryogenic refrigeration cycles are designed with two distinct refrigeration cycles in cascade. A process flow diagram of the developed dual cryogenic refrigeration cycle is shown in Figure 8.12.

For the first cryogenic refrigeration cycle, a Neon Brayton Cycle and a Hydrogen-Neon (H_2-Ne) Mixture Brayton Cycle are investigated. The Neon Brayton Cycle and the H_2-Ne Mixture Brayton Cycle are designed with one multi-stage turbo compressor. A higher neon mole fraction y_{Ne} in the H_2-Ne Mixture Brayton Cycle reduces the number of required turbo compressor stages N_{TC} but increases the specific energy

consumption *SEC* and the neon refrigerant inventory. At the present state-of-the-art, an economical trade-off between a low *SEC* and a viable turbo compressor designs with $N_{TC} \leq 6$ turbo compressor stages is found with a hydrogen mole fraction between approximately $y_{\mathrm{H_2}} = 0.5\text{-}0.7$.

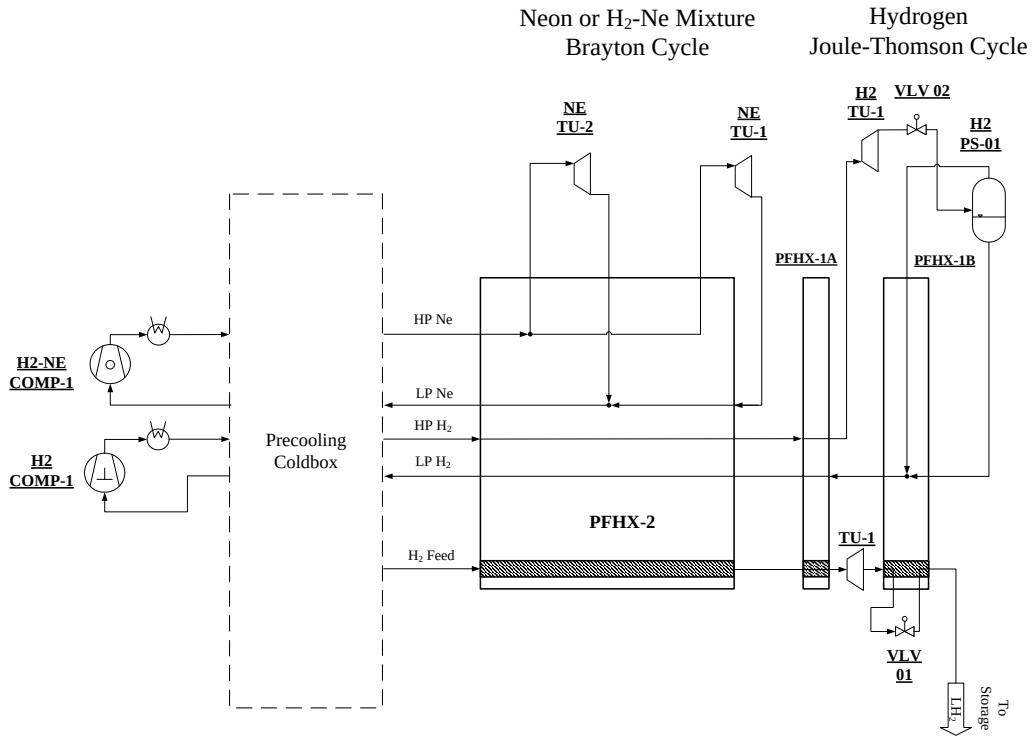

Figure 8.12: Process flow diagram of the dual cryogenic refrigeration cycle with Neon or H_2-Ne Mixture Brayton Cycle

The second cryogenic refrigeration cycle is used to provide the refrigeration power for the final cooling and liquefaction of the hydrogen feed stream. For the second cryogenic refrigeration cycle, a Hydrogen Joule-Thomson Cycle (H_2 JT Cycle) and a Helium Brayton Cycle are investigated. The Helium Brayton Cycle is designed without the JT valve VLV 02 and phase separator PS-01 shown in Figure 8.12 because the helium refrigerant remains gaseous. To minimize the risk of neon solidification in the first cryogenic refrigeration cycle, the cut-off temperature between the cryogenic refrigeration cycles is set above the normal boiling point temperature T_{sat} of neon and below the critical temperature T_{crit} of hydrogen.

The Neon Brayton Cycle and the H_2-Ne Mixture Brayton Cycle are thus calculated in the hydrogen liquefier process simulator model with the H_2 JT Cycle as the second cryogenic refrigeration cycle. Compared to the H_2 JT Cycle, the simulation case with the Helium Brayton Cycle yields a higher specific energy consumption *SEC*. The simulation cases for the H_2-Ne Mixture Brayton Cycle are calculated with a variation in the hydrogen mole fraction between $y_{\mathrm{H_2}} = 0.5\text{-}0.7$. The calculated *SEC* decreases

at higher y_{H_2} while the difference in the specific liquefaction costs SLC is small and less than 1%. The simulation case with the Neon Brayton Cycle in the first cryogenic refrigeration cycle yield up to 7% higher SEC compared to the process simulations with the H_2-Ne Mixture Brayton Cycle.

8.3.3 Investigation of the hydrogen precooling

As described in Chapter 4, different hydrogen precooling processes with either pure fluids or with fluid mixtures can be implemented for large-scale hydrogen liquefaction.

Liquid nitrogen (LN_2) is the conventional hydrogen liquefier precooling. Liquid nitrogen is inexpensive and has a high molar enthalpy of evaporation $\Delta\bar{H}_V$ which is used to evaporate LN_2 with high heat transfer coefficients U at a nearly constant precooling temperature $T_{PC} = 80\,\mathrm{K}$. For large-scale hydrogen liquefaction, the LN_2 precooling is inefficient and the LN_2 supply becomes uneconomical.

A hydrogen liquefaction process without precooling is calculated for different liquefaction capacities in the hydrogen liquefier process simulator model with a Hydrogen Claude Cycle. The LN_2 precooling is replaced by an additional turbine string in the Hydrogen Claude Cycle. A hydrogen liquefaction process without precooling is relevant only for small hydrogen liquefiers in locations where a LN_2 supply is not available or economically not viable and where the specific electricity costs c_{el} are very low, e.g. below 0.05 €/kWh. The specific energy consumption SEC and the specific liquefaction costs SLC calculated for the hydrogen liquefaction process without precooling are higher compared to the process with LN_2 precooling. A large-scale hydrogen liquefaction process without precooling can not reach the combined SEC and SLC targets defined in this work.

Compared to the conventional LN_2 precooling, a major reduction in the specific energy consumption SEC and the specific liquefaction costs SLC can be achieved with closed-loop precooling cycle processes. However, the additional CAPEX that can be invested economically for improved precooling cycle processes is limited. Therefore, different precooling processes for large-scale hydrogen liquefaction are investigated within this section.

Nitrogen Expander Cycle

Nitrogen Expander Cycles are inexpensive and are widely used in industrial cryogenic processes for precooling temperatures down to about $T_{PC} = 80\,\mathrm{K}$. The nitrogen refrigerant make-up costs are low: the specific refrigeration costs c_{rfr} for nitrogen are by over one order-of-magnitude lower than for hydrogen. As indicated by Kohler et al. 2014, the operational flexibility of Nitrogen Expander Cycles is high and the part-load capability is wide. In this work, a Single Nitrogen Expander Claude Cycle (Single N_2 Cycle) and a Dual Nitrogen Expander Brayton Cycle (Dual N_2 Cycle) are investigated.

The Single N_2 Cycle shown in Figure 8.13 is designed with one nitrogen turbine expander N2 TU-1 and a Joule-Thomson (JT) valve VLV-1. At the outlet of the JT valve VLV-1, the nitrogen refrigerant is expanded into the two-phase region. The Dual N_2 Cycle shown in Figure 8.14 is designed with two nitrogen turbine expanders N2 TU-1 and N2 TU-2. The Dual N_2 Cycle design is similar to the Nitrogen Expander Cycles implemented in LNG plants [Kohler et al. 2014]. The Dual N_2 Cycle is designed with a second nitrogen turbine that is operated in the gas phase and replaces the JT valve VLV-1 in the Single N_2 Cycle. Therefore, the capital expenses (CAPEX) for the Dual N_2 Cycle are higher but the total turbine power P_{TU} that is recovered is also higher. For turbine energy recovery, the nitrogen turbines are designed with turbine-generator units. Alternatively, also turbine-compressor units can be implemented.

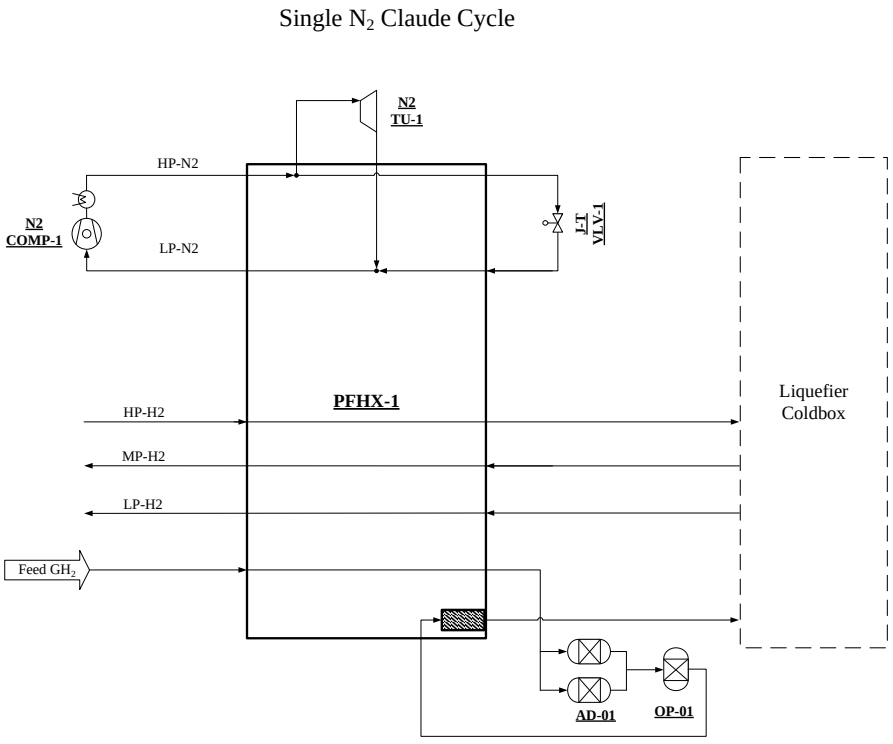

Figure 8.13: Process flow diagram of the Single Nitrogen Expander Claude Cycle

Compared to the Linde-2010 process concept, both the Single N_2 Cycle and the Dual N_2 Cycle are both designed with only one turbo compressor with up to $N_{TC} = 4$ compressor stages and inter-cooling. For the compressor sealing system, nitrogen dry-gas seals are assumed. The nitrogen refrigerant make-up as well as the nitrogen required as seal and purge gas is stored in a LN_2 storage tank [Kohler et al. 2014].

The Single N_2 Cycle and the Dual N_2 Cycle are investigated in the hydrogen liquefier process simulator model with the Hydrogen Claude Cycle and for different liquefaction capacities between $25 - 100\,\text{tpd}$ LH_2. To evaluate the influence of the precooling temperature T_{PC} on the hydrogen liquefaction process, the Dual N_2 Cycle is calculated

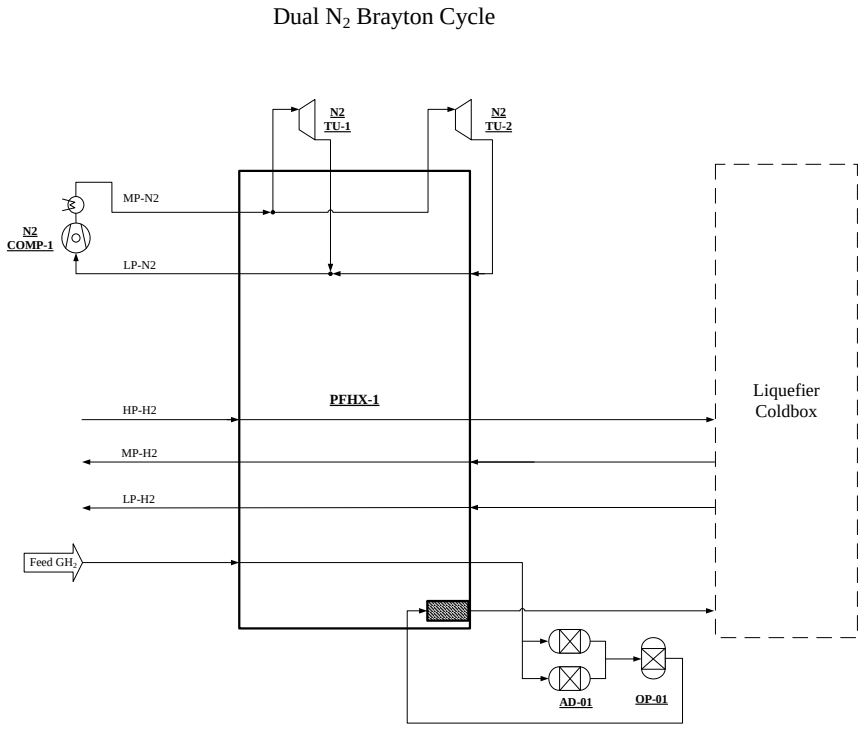

Figure 8.14: Process flow diagram of the Dual Nitrogen Expander Brayton Cycle

with precooling temperatures between $T_{PC} = 80 - 100\,\mathrm{K}$. The lowest specific energy consumption SEC is calculated with $T_{PC} = 100\,\mathrm{K}$. Additionally, the higher precooling temperature T_{PC} decreases the N_2 COMP-1 compressor inlet volumetric flow rate $\dot{V}_{in}$ because the low-pressure (LP) level of the Nitrogen Expander Cycle can be increased. The Single N_2 Cycle and the Dual N_2 Cycle are thus calculated with $T_{PC} = 100\,\mathrm{K}$. The specific energy consumption calculated with the Dual N_2 Cycle is in the range $SEC = 6.5 - 7.5\,\mathrm{kWh/kg\ LH_2}$ and is lower compared to the Single N_2 Cycle.

Mixed-refrigerant Joule-Thomson Cycle

Mixed-refrigerant Joule-Thomson Cycle (MRC) processes with fluid mixtures of nitrogen with hydrocarbons and precooling temperatures of about $T_{PC} = 120\,\mathrm{K}$ are state-of-the-art in natural gas liquefaction processes. The advantage of MRC is that the fluid mixtures evaporate and condensate over a wider temperature range compared to pure nitrogen refrigerant [Khan & Lee 2013] and MRC require a lower specific energy consumption compared to Nitrogen Expander Cycles [Kohler et al. 2014]. Compared to Nitrogen Expander Cycles, the total number of rotating equipment in MRC is lower but the number of vessels and storage tanks is higher. The plate-fin heat exchanger (PFHX) design for MRC is more complex because of the potential technical risks related to flow maldistribution and thermal stresses [Alekseev 2016]. Additionally, the MRC operation and control is more complex compared to Nitrogen Expander Cycles [Kohler et al. 2014].

Different MRC processes and fluid mixtures are investigated in the hydrogen liquefier process simulator model. The MRC fluid mixture composition is optimized to reduce the temperature differences ΔT between the cold and warm composite curves inside the PFHX. Compared to natural gas liquefaction plants, the MRC fluid mixture components are typically not available at the hydrogen liquefier site and need to be imported for refrigerant make-up. Therefore, to minimize the gas management complexity and the refrigerant make-up costs, only four MRC fluid mixture components are optimized in this work. Furthermore, the process optimization with more than four MRC fluid mixture components does not yield a significant improvement in the specific energy consumption *SEC*.

Table 8.6 lists the quaternary MRC fluid mixture compositions used for the MRC process optimization. The quaternary fluid mixtures in Table 8.6 differ in the high boiling refrigerant component. For each simulation case, the MRC fluid mixture composition is optimized in the hydrogen liquefier process simulator with the refrigerant composition mole fractions y_i as optimization variables.

Table 8.6: Refrigerant composition of the quaternary fluid mixtures used for the MRC precooling optimization for large-scale hydrogen liquefaction processes

Mix-1	Mix-2	Mix- 3
N_2	N_2	N_2
CH_4	CH_4	CH_4
C_2H_6	C_2H_6	C_2H_6
i-C_4H_{10}	i-C_5H_{12}	C_3H_8

The specific energy consumption *SEC* calculated in the simulation cases with the optimized fluid mixture Mix-1 is only slightly lower compared to the optimized fluid mixture Mix-2 and between $2-4\%$ lower compared to the optimized fluid mixture Mix-3. The difference in the calculated specific liquefaction costs *SLC* between the optimized fluid mixtures is small.

The mixture melting point temperature $T_{melt,mix}$ at which the MRC fluid mixture solidifies is estimated with the methods described in Section 3.3.4. A temperature offset of about 5 K is added as safety margin on the estimated $T_{melt,mix}$. Additionally, the assumed lowest MRC temperature is limited to $T_{MRC,min} \geq 91\,\mathrm{K}$, which is above the triple point temperature T_{trp} of C_2H_6 and CH_4. To decrease $T_{melt,mix}$, the refrigerant component mole fraction y_i of the fluid with the highest triple point temperature T_{trp} is limited by the optimization constraint $y_{max} = 0.10$ in the hydrogen liquefier process simulator model.

The MRC process developed for large-scale hydrogen liquefaction in this work are based on industrial MRC processes for small-scale natural gas liquefaction such as the enhanced PRICO® process by Black&Veatch and the LIMUM® process by Linde AG [Khan & Lee 2013, Kohler et al. 2014].

Figure 8.15 illustrates two MRC process options implemented and simulated for large-scale hydrogen liquefaction. The MRC process option 1 is a simple Joule-Thomson (JT) Cycle. The MRC process option 2 with phase separator is more complex and is similar to a MRC process proposed for small-scale natural gas liquefaction plants [Cao et al. 2006]. The advantage of the MRC process option 2 is that only a small molar fraction y_i of the highest boiling refrigerant component reaches the lowest MRC temperature T_{min}. This configuration reduces the risk of solidification for the refrigerant components with the higher triple point temperature T_{trp}. The differences in the calculated specific energy consumption SEC and specific liquefaction costs SLC between the MRC process option 1 and 2 are small.

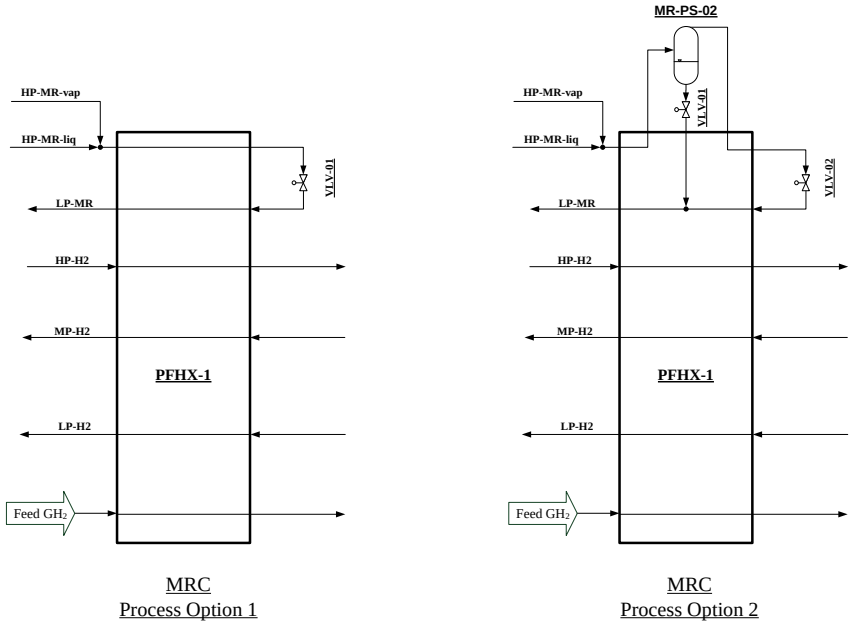

Figure 8.15: Process flow diagram of the MRC process option 1 and 2 for large-scale hydrogen liquefaction

Figure 8.16 illustrates the MRC process used for the hydrogen liquefaction process simulation. Downstream of the MR-COMP-1 compressor after-cooler, the high-pressure (HP) HP MR stream is routed through the discharge phase separator MR-PS-02 and is separated into the liquid HP-MR-liq stream and the vapour HP-MR-vap stream. The HP-MR-liq stream and the HP-MR-vap stream are precooled in PFHX-1 and expanded to the low-pressure (LP) level in the JT valves VLV-01 and VLV-02 at two different precooling temperatures $T_{PC,1}$ and $T_{PC,2}$. The expanded LP MR streams are mixed either at the temperature level $T_{PC,1}$ or at the warm end of PFHX-1.

The MRC compression process design and simulation is comparable to industrial MRC processes like PRICO™ and LIMUM® with a turbo compressor with inter-stage cooling and dry-gas seals to minimize the refrigerant make-up costs $C_{OPEX,rfr}$ [Kohler et al. 2014]. In addition to the LN_2 storage tank, a MR make-up system with three storage vessels is required for the hydrocarbons in MRC fluid mixture.

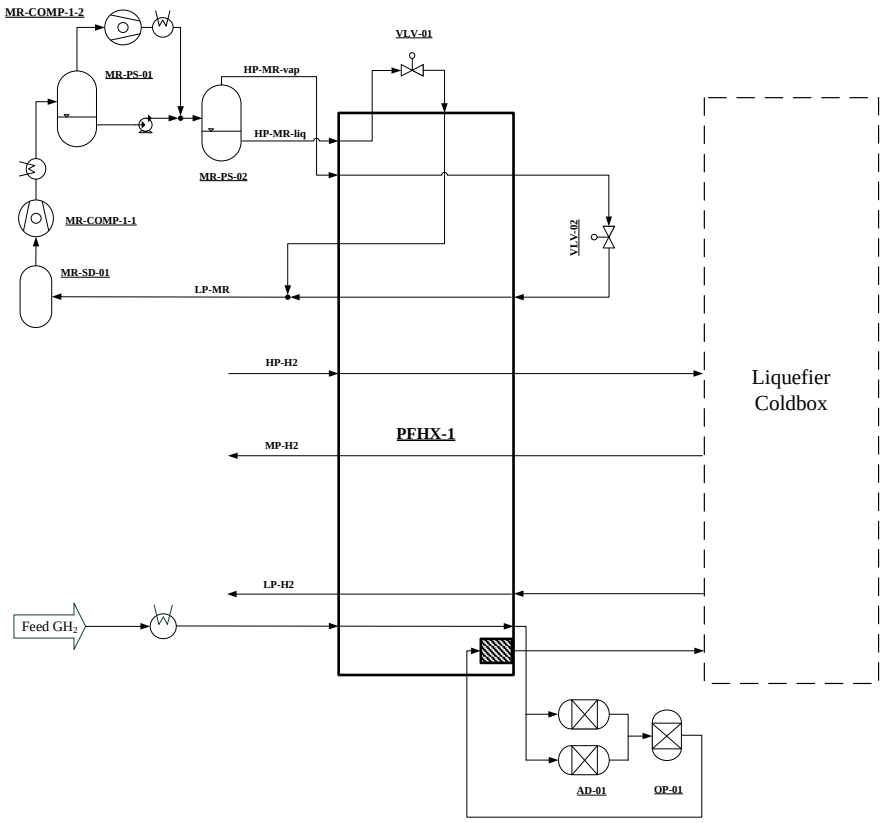

Figure 8.16: Process flow diagram of the MRC implemented for large-scale hydrogen liquefaction [Cardella et al. 2017d]

Compared to MRC processes for natural gas liquefaction, the MRC process for hydrogen precooling is designed for lower precooling temperatures $T_{PC} \leq 110\,\mathrm{K}$. A lower precooling temperature T_{PC} is beneficial because this shifts the refrigeration power to the precooling cycle and leads to lower turbine inlet temperatures T_{in} in the cryogenic refrigeration cycle. The optimization of the 100 tpd LH_2 hydrogen liquefaction process with MRC at different precooling temperatures between $T_{PC} = 90 - 110\,\mathrm{K}$ indicated that the minimum SEC is calculated between $T_{PC} = 95 - 105\,\mathrm{K}$ [Cardella et al. 2017b]. The base MRC simulation cases are calculated with fluid mixture Mix-1 and a MRC precooling temperature $T_{PC} = 100\,\mathrm{K}$. The specific energy consumption calculated for the large-scale hydrogen liquefaction with Hydrogen Claude Cycle and MRC precooling process reaches $SEC \approx 6.0\,\mathrm{kWh/kg\ LH_2}$.

Mixed-refrigerant Expander Cycle

A further precooling process design for large-scale hydrogen liquefaction is implemented by combining the Nitrogen Expander Cycles with the Mixed-refrigerant Joule-Thomson Cycle (MRC). As proposed for small-scale LNG processes [Cao et al. 2006], the Single Nitrogen Expander Claude Cycle (Single N_2 Cycle) shown in Figure 8.13 is modified to a Mixed-refrigerant Expander Cycle with a binary fluid mixture composed of nitrogen

with methane (Single N_2-CH_4 Cycle). However, the specific energy consumption *SEC* calculated for the large-scale hydrogen liquefaction with Single N_2-CH_4 Cycle is higher compared to the MRC precooling processes.

Also the MRC process in Figure 8.16 can be designed as Mixed-refrigerant Expander Cycle by replacing the two JT valves VLV 01 and VLV 02 with liquid turbine expanders [Cryostar n.d.(b), Berstad et al. 2010]. Compared to the MRC process with JT valves, the liquid turbine expanders further reduce the specific energy consumption by up to 2% to about $SEC = 5.8\,\text{kWh/kg}$ LH_2. However, no improvement in the specific liquefaction costs *SLC* is achieved with the liquid turbine expanders because their isentropic efficiency η_{is} is relatively low and additional CAPEX is required.

8.4 Developed process concepts

The process-economic investigations carried out for the crogenic refrigeration cycle result in the development of two novel process concepts for large-scale hydrogen liquefaction. Hydrogen is chosen as principal refrigerant in both process concepts. The precooling process investigation indicates that the Mixed-refrigerant Joule-Thomson Cycle (MRC) achieves the lowest specific energy consumption *SEC*. The developed process concepts are thus designed with MRC precooling.

8.4.1 Process concept A: HP Hydrogen Claude Cycle with MRC

The process concept A for large-scale hydrogen liquefaction is designed with the high-pressure (HP) Hydrogen Claude Cycle (HP-H_2 Claude Cycle) and the Mixed-refrigerant Joule-Thomson Cycle (MRC). The process flow diagram of the process concept A is illustrated in Figure 8.17 [Cardella et al. 2017d].

The HP-H_2 Claude Cycle of process concept A is the modification to the conventional H_2 Claude Cycle. Compared to the conventional H_2 Claude Cycle, the HP-H_2 Claude cycle of the process concept A is designed and optimized to operate at higher pressure levels with a HP level $p_{HP} \geq 40\,\text{bar}$ and a MP level $p_{MP} \geq 8\,\text{bar}$. The HP-$H_2$ Claude Cycle process design reduces the compressor inlet volumetric flow rate $\dot{V}_{in}$ to use state-of-the-art hydrogen compressors and turbine-expanders for large-scale hydrogen liquefaction up to approximately 100 tpd LH_2. The H_2 LP-COMP-1 compressor and the H_2 MP-COMP-2 compressor are designed as dry-running hydrogen reciprocating piston compressors with up to three stages and inter-stage cooling. For a liquefaction capacity of 100 tpd LH_2, the larger H_2 MP-COMP-2 compressor is designed with two compressor units running in parallel.

As an alternative to the reciprocating piston compressors, high-speed hydrogen turbo compressors with impeller wheel tip velocities $u_2 > 500\,\text{m/s}$ may be employed in the future. The Brayton part of the HP-H_2 Claude Cycle is designed with either two or three turbine strings with the option of turbine energy recovery via a turbo-generator. The

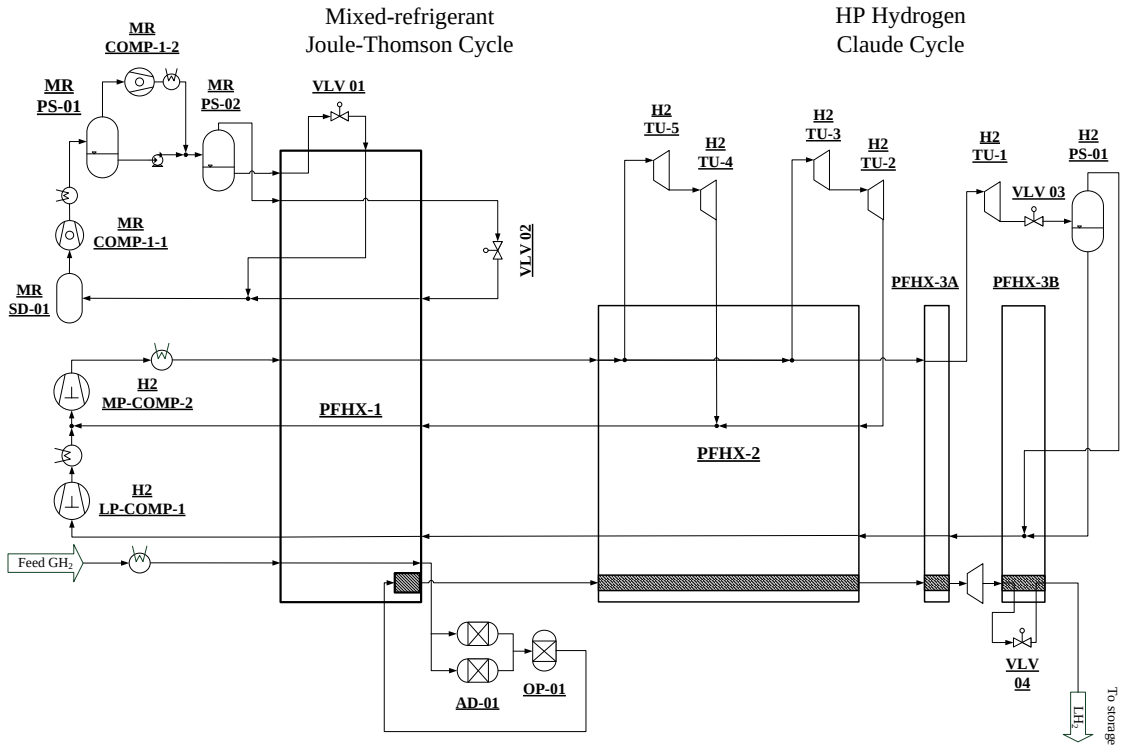

Figure 8.17: Process flow diagram of the process concept A: the high-pressure (HP) Hydrogen Claude Cycle with Mixed-refrigerant Joule-Thomson cycle (MRC) precooling [Cardella et al. 2017d]

hydrogen turbine expanders with a turbine power below approximately $P_{TU} \leq 150\,\text{kW}$ are designed with gas bearings while the larger turbine expanders are designed with oil or magnetic bearings.

8.4.2 Process concept B: Dual Hydrogen-Neon Cycle with MRC

The process concept B is the Dual Hydrogen-Neon (H_2-Ne) Mixture Brayton Cycle with Mixed-refrigerant Joule-Thomson Cycle (MRC). The process flow diagram of the process concept B is illustrated in Figure 8.18 [Cardella et al. 2017d].

The developed process concept B is designed with two separate cryogenic refrigeration cycles in a cascade and with MRC precooling. The H_2-Ne Mixture Brayton Cycle is designed with two or three turbine strings and the option of turbine energy recovery. A higher hydrogen mole fraction y_{H_2} increases the efficiency of the hydrogen liquefaction process but is restricted by the feasible impeller wheel tip velocity $u_{2,max}$ of the turbo compressor H2-NE COMP-1. The H_2-Ne mixture composition is designed with a hydrogen mole fraction between $y_{H_2} = 0.5\text{-}0.7$ that enables the compression in a state-of-the-art turbo compressor with $N_{TC} = 6$ impeller stages. In the base simulation cases, the H_2-Ne mixture composition is calculated with $y_{H_2} = 0.5$. Future high-speed

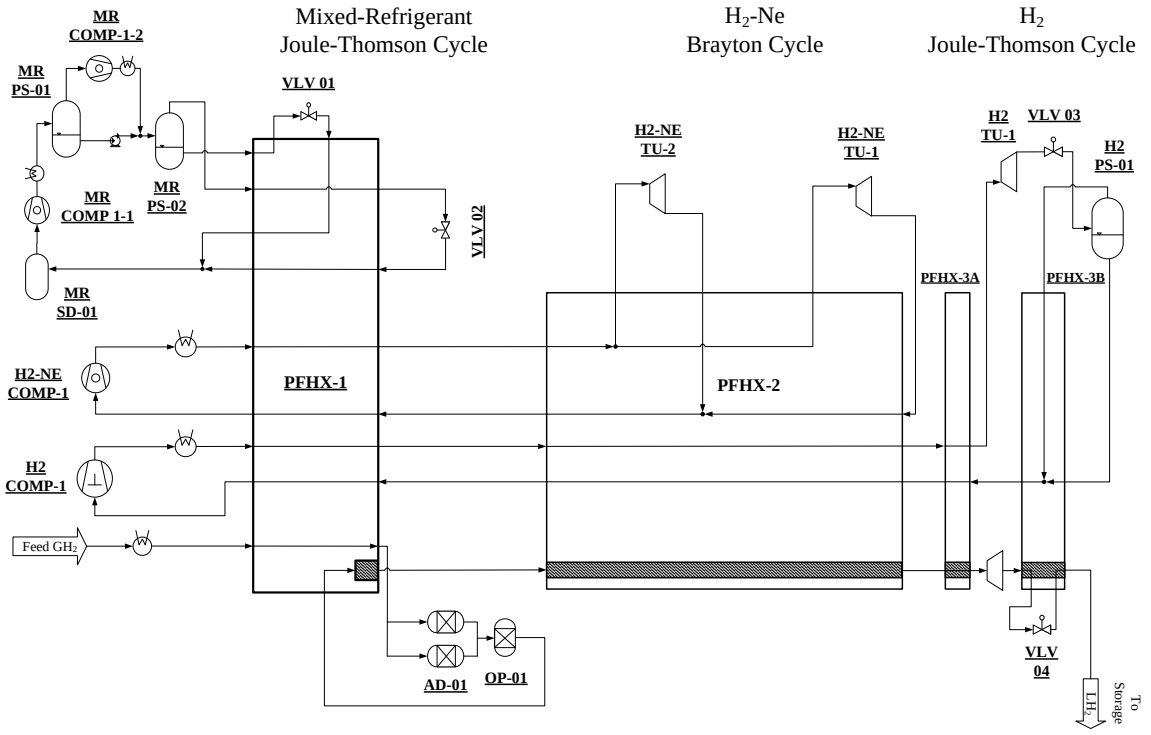

Figure 8.18: Process flow diagram of the process concept B: the Hydrogen-Neon Mixture Brayton Cycle and the Hydrogen Joule-Thomson Cycle with Mixed-refrigerant Joule-Thomson cycle (MRC) precooling [Cardella et al. 2017d]

turbo compressors may allow to maximize the hydrogen mole fraction $y_{H_2} \geq 0.9$ for the He-Ne mixture. The continuous leakage losses of neon in the turbo compressor are minimized with double dry-gas seals. As an alternative, also hermetically-sealed turbo compressors can be used.

To provide the final refrigeration power for the hydrogen feed stream liquefaction and subcooling, the H_2 Joule-Thomson Cycle with pure hydrogen is designed. The H_2 Joule-Thomson Cycle is operated with the hydrogen reciprocating piston compressor H_2 COMP-1 at moderate HP levels up to $p_{HP} = 25\,\text{bar}$.

8.5 Process optimization

The developed process concepts are optimized in the hydrogen liquefier process simulator model to select the optimal process solution for large-scale hydrogen liquefaction. The process optimization cases are simulated with the basis of design defined in Section 8.1.

As described in Table 8.7, the process concepts are simulated with the specific energy consumption *SEC* (energy-optimized EO case) and the specific liquefaction costs *SLC* (cost-optimized CO case) as objective functions $f(x)$ of optimization.

Table 8.7: Objective function $f(x)$ for the process optimization [Cardella et al. 2017d]

Case	Objective function $f(x)$	Feed pressure p_{feed}
EO-1	SEC	$25 - 80\,\text{bar}$
EO-2	SEC	$25\,\text{bar}$
CO-2	SLC	$25\,\text{bar}$

The inlet feed pressure p_{feed} is defined as an optimization variable in the hydrogen liquefier process simulation. The energy-optimized (EO) simulation cases are further distinguished in simulation cases that are carried out with the optimization of the inlet feed pressure $p_{feed} = 25 - 80\,\text{bar}$ (EO-1) and simulation cases that are carried out with the fixed inlet feed pressure $p_{feed} = 25\,\text{bar}$ (EO-2).

For the specific electricity costs c_{el} defined in Table 8.2, the cost-optimized (CO) simulation cases with the fixed inlet feed pressure $p_{feed} = 25\,\text{bar}$ (CO-2) shows lower SLC compared to simulation cases with a variable inlet feed pressure $p_{feed} = 25 - 80\,\text{bar}$. To minimize the SLC calculated in the hydrogen liquefier process simulator model, the optimizer keeps $p_{feed} = 25\,\text{bar}$ to avoid additional compressor costs $C_{comp,RC}$. The capital expenses (CAPEX) added for a hydrogen reciprocating piston compressor for the compression from 25 bar to 80 bar result in an economically less feasible solution. Therefore, the cost-optimized simulation cases are simulated only with a fixed inlet feed pressure $p_{feed} = 25\,\text{bar}$ (CO-2).

In the hydrogen liquefier process simulator, the low-pressure (LP) level p_{LP}, medium-pressure (MP) level p_{MP} and the high-pressure (HP) level p_{HP} are defined as optimization variables in both the precooling and cryogenic refrigeration cycles. Also temperatures T and heat exchanger temperature differences ΔT are defined as optimization variables. The minimum temperature difference $\Delta T_{min} = 0.5{-}2.5\,\text{K}$ and the maximum temperature difference $\Delta T_{max} = 25\,\text{K}$ between the warm and the cold streams are set as optimization constraints for each heat exchanger unit operation. The optimizer in the energy-optimized EO-1 and EO-2 simulation cases minimizes the heat exchanger ΔT_{min} to the defined lower optimization constraint. Small heat exchanger ΔT_{min} lead to lower SEC but require larger plate-fin heat exchangers (PFHX) with higher $CAPEX$. The optimization constraints on the heat exchanger minimum temperature difference ΔT_{min} avoid a temperature cross between the warm and cold streams and ensure that the ratio between cold and warm temperature is $T_{cold}/T_{warm} < 0.99$ in all calculated heat exchangers.

The sum of the calculated total heat exchanger $(U \cdot A)_{sim}$ value, the product of the overall heat transfer coefficient U and the total heat exchanger surface area A, is set as optimization constraint with $(U \cdot A)_{PC,max}$ for the precooling coldbox and $(U \cdot A)_{liq,max}$ for the liquefier coldbox. The compressor inlet volumetric flow rate $\dot{V}_{in}$ of the compressor unit operation with the highest volumetric flow rate is set as optimization constraint $\dot{V}_{in,max}$.

The optimization variables and constraints defined for the 100 tpd LH_2 simulation cases of the process concepts A and B are listed in the Tables A.2, A.3 and A.4 in the Appendix A.

8.5.1 Reference process optimization

The reference 5 tpd LH_2 process is optimized in the hydrogen liquefier process simulator model in UniSim Design® and is used as basis for process concept evaluations. The improvements in the Hydrogen Claude Cycle described in Section 8.3.2 are applied to the reference 5 tpd LH_2 process with LN_2 precooling. Additionally, the hydrogen reciprocating piston compressors are simulated with up to three stages with inter-stage cooling.

As shown in the plot in Figure 8.19, the heat exchanger temperature differences ΔT in the cost-optimized CO-2 simulation cases are reduced in comparison with the non-optimized reference 5 tpd LH_2 process calculated in Section 8.2.1. The cost-optimized CO-2 simulation thus reduces inefficiencies in the hydrogen liquefaction process. The simple improvements in the process design and the cost-optimized CO-2 simulation yields a 8% decrease in the calculated specific energy consumption from about $SEC = 9.9\,\mathrm{kWh/kg}$ to $SEC = 9.1\,\mathrm{kWh/kg}$ LH_2. The specific liquefaction costs $SLC_{5\mathrm{tpd}}$ calculated for the optimized referenced 5 tpd LH_2 process (CO-2) are nearly identical to the SLC calculated for the non-opztimized reference 5 tpd LH_2 process.

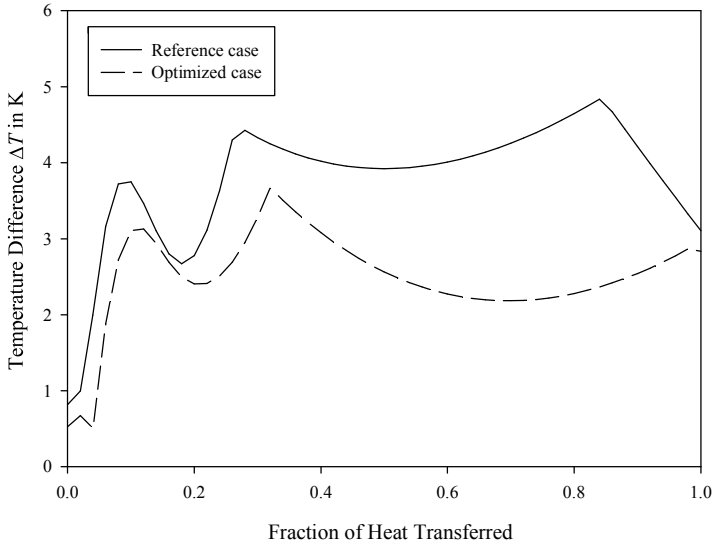

Figure 8.19: Heat exchanger composite curves with the temperature difference ΔT between the cold and warm streams for the non-optimized and the optimized reference process with LN_2 precooling (CO-2) [Cardella et al. 2017d]

8.5.2 Optimization of process concepts A and B

In order to find the optimal process solution for different boundary conditions, a process optimization is carried out in the hydrogen liquefier process simulator model for the developed large-scale hydrogen liquefaction process concepts A and B.

Influence of the objective function

The process concepts A and B are calculated in energy-optimized (EO-1 and EO-2) and cost-optimized (CO-2) simulation cases. The process concepts are simulated with a Mixed-refrigerant Joule-Thomson Cycle (MRC) precooling temperature $T_{PC} = 100\,\mathrm{K}$. The optimization results for the specific energy consumption *SEC* and the specific liquefaction costs *SLC* of the simulated 100 tpd LH_2 hydrogen liquefaction process concepts A and B are plotted in Figure 8.20 [Cardella et al. 2017d].

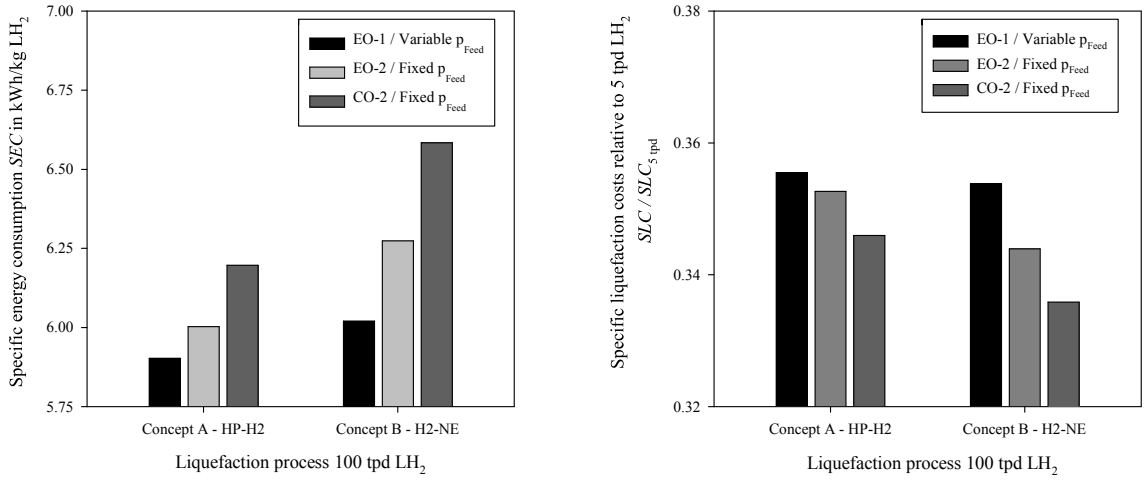

Figure 8.20: Optimization results for the specific energy consumption *SEC* (left plot) and the specific liquefaction costs *SLC* relative to the reference 5 tpd LH_2 process $SLC_{5\mathrm{tpd}}$ (right plot) calculated for the 100 tpd LH_2 process concepts A and B with MRC [Cardella et al. 2017d]

As illustrated in the left bar chart in Figure 8.20, the lowest specific energy consumption *SEC* is calculated in the energy-optimized simulation cases with the inlet feed gas pressure p_{feed} as optimization variable (EO-1). In all the simulation cases, the *SEC* of the optimized process concept A with HP-H_2 Claude Cycle is lower compared to the process concept B with Dual H_2-Ne Cycle. For process concept A in the EO-1 simulation case, the *SEC* is optimized to $SEC = 5.9\,\mathrm{kWh/kg\ LH_2}$. For process concept B in the EO-1 simulation case, the specific energy consumption is optimized to $SEC = 6.0\,\mathrm{kWh/kg\ LH_2}$. In the EO-1 and the EO-2 simulation cases, the optimizer increases the inlet feed gas pressure to the defined upper limit of $p_{feed} = 80\,\mathrm{bar}$. The hydrogen liquefier process simulator model adds a two-stage reciprocating piston compressor as unit operation with the compressor costs $C_{comp,RC}$ in the hydrogen feed stream. In the EO-1 simulation cases, the calculated total heat exchanger $(U \cdot A)_{sim}$ value reaches the defined upper

limit for the optimization constraint $(U \cdot A)_{max}$ which represents the heat exchanger size.

The simulation cases that are optimized with the fixed inlet feed pressure $p_{feed} = 25\,\text{bar}$ (EO-2 and CO-2) without the hydrogen feed compressor unit operation results in a higher *SEC* but lower specific liquefaction costs *SLC*. For process concept A, the *SEC* calculated in the EO-2 simulation case increases by about 2% to $SEC = 6.0\,\text{kWh/kg LH}_2$ compared to the EO-1 simulation case. For process concept B, the specific energy consumption $SEC = 6.3\,\text{kWh/kg LH}_2$ calculated in the EO-2 simulation case is approximately 4% higher compared to the EO-1 simulation case. The negative impact of the lower inlet feed pressure $p_{feed} = 25\,\text{bar}$ on the *SEC* is higher for process concept B.

In the cost-optimized (CO-2) simulation cases, the optimizer manipulates the optimization variables of the process concepts A and B to minimize the specific liquefaction costs *SLC*. To reduce the plate-fin heat exchanger (PFHX) size and costs C_{PFHX}, the optimizer in the CO-2 simulation cases selects larger heat exchanger temperature differences ΔT. Compared to the EO-1 simulation cases, the specific energy consumption in the CO-2 simulation cases increases by approximately 5% to $SEC = 6.2\,\text{kWh/kg}$ for process concept A and by approximately 9% to $SEC = 6.6\,\text{kWh/kg LH}_2$ for process concept B. The lower *SEC* of the process concept A can be explained by the higher efficiency of hydrogen as a refrigerant compared to the fluid mixture of hydrogen with neon in process concept B. Additionally, at the simulated hydrogen liquefaction capacity, the isentropic efficiency η_{is} assumed in the hydrogen liquefier process simulator model for the hydrogen reciprocating piston compressors is higher compared to the isentropic efficiency $\eta_{is,TC}$ of the H_2-Ne turbo compressor.

The specific liquefaction costs *SLC* calculated relative to the reference 5 tpd LH_2 process $SLC_{5\text{tpd}}$ are illustrated in the right bar chart in Figure 8.20. Compared to the EO-1 simulation cases, the CO-2 simulation cases achieve a *SLC* reduction by 3% for process concept A and by 5% for process concept B. For 100 tpd LH_2, the specific liquefaction costs *SLC* calculated with process concept B with the Dual H_2-Ne Cycle are approximately 3% lower compared to the process concept A with the HP-H_2 Claude Cycle. The cost difference is mainly due to the improved economies of scale for process concept B with the H_2-Ne turbo compressor. However, the *SLC* for process concept B are highly dependent on the assumed yearly neon refrigerant make-up costs $C_{rfr,\text{Ne}}$.

For the further optimization of the process concepts A and B, only the EO-2 and the CO-2 simulation cases are considered. The 100 tpd LH_2 CO-2 simulation cases are used as base simulation cases.

Influence of the liquefaction capacity

To evaluate the impact of the hydrogen liquefaction capacity on the performance of large-scale hydrogen liquefaction processes, the developed process concepts A and B are simulated also for 50 tpd LH_2.

As shown in the Table 8.8, process concept A reaches the target specific energy consumption $SEC = 6\,\text{kWh/kg LH}_2$ defined within this work. Compared to the specific liquefaction costs $SLC_{5\text{tpd}}$ calculated for the reference 5 tpd LH_2 process, the SLC calculated in the CO-2 simulation cases are reduced by nearly 60% for 50 tpd LH_2 and by more than 65% for 100 tpd LH_2 CO-2 simulation cases.

Table 8.8: Specific energy consumption SEC calculated for the process concept A and the process concept B for the liquefaction capacities of 50 tpd and 100 tpd LH_2 with the energy-optimized EO-2 and the cost-optimized CO-2 simulation cases

Case	50 tpd LH_2		100 tpd LH_2	
SEC in kWh/kg	EO-2	CO-2	EO-2	CO-2
Concept A	5.99	6.29	6.00	6.20
Concept B $\left(y_{H_2} = 0.5\right)$	6.33	6.85	6.27	6.58

The SEC calculated in the 50 tpd LH_2 energy-optimized EO-2 simulation cases are comparable to the respective SEC calculated for 100 tpd LH_2. The SEC calculated in the 50 tpd LH_2 cost-optimized CO-2 simulation cases are higher: $SEC = 6.29\,\text{kWh/kg LH}_2$ for process concept A and $SEC = 6.85\,\text{kWh/kg LH}_2$ for process concept B. This is mainly due to the lower compressor and turbine isentropic efficiencies η_{is} assumed in the hydrogen liquefier process simulator model for lower inlet volumetric flows $\dot{V}_{in}$.

The specific liquefaction costs SLC calculated for the CO2 simulation cases relative to the $SLC_{5\text{tpd}}$ of the reference 5 tpd LH_2 process are plotted in Table 8.9 for the process concept A and the process concept B $\left(y_{H_2} = 0.5\right)$.

Table 8.9: Specific liquefaction costs SLC relative to $SLC_{5\text{tpd}}$ calculated for the process concept A and the process concept B $\left(y_{H_2} = 0.5\right)$ for the liquefaction capacities of 50 tpd and 100 tpd LH_2 in the cost-optimized CO-2 simulation cases

Case	50 tpd LH_2	100 tpd LH_2
Ratio $SLC/SLC_{5\text{tpd}}$	CO-2	CO-2
Concept A	0.408	0.346
Concept B (Leak 1)	0.421	0.336
Concept B (Leak 2)	0.442	0.346

In contrast to the 100 tpd LH_2 simulation cases, the specific liquefaction costs SLC optimized for process concept A in the 50 tpd LH_2 are approximately 3% lower compared to process concept B. For process concept B, the total neon refrigerant loss rate through leakage is assumed with $\dot{V}_{loss,1} = 1.5\,\text{Nm}^3/\text{h}$ (Leak 1). High neon refrigerant loss rates through leakage $\dot{V}_{loss}$ decrease the economic viability of process concept B relative to process concept A. To investigate the impact on the specific liquefaction costs SLC, a sensitivity in the $\dot{V}_{loss}$ is considered by assuming a higher neon refrigerant loss

rate $\dot{V}_{loss,2} = 3.0\,\mathrm{Nm^3/h}$ (Leak 2). The higher $\dot{V}_{loss,2}$ increases the *SLC* calculated in the 100 tpd LH_2 CO-2 simulation cases by approximately 3%. The impact of the higher $\dot{V}_{loss,2}$ on the 50 tpd LH_2 is higher: the *SLC* increase by approximately 5%. A hermetic zero-leakage plant design for the neon refrigerant further reduces the *SLC* of process concept B relative to process concept A.

Influence of the neon concentration

The H_2-Ne Mixture Brayton Cycle of process concept B is optimized with the hydrogen mole fraction between y_{H_2} = 0.5-0.7. The *SEC* calculated for process concept B in the 100 tpd LH_2 EO-2 simulation cases are listed in Table 8.10 as a function of the hydrogen mole fraction y_{H_2}. For validation, the Brayton Cycle in the process concept B is optimized also with pure neon ($y_{H_2} = 0$) and pure hydrogen ($y_{H_2} = 1.0$). In all simulation cases, the *SEC* decreases at higher hydrogen mole fractions y_{H_2}.

Table 8.10: Specific energy consumption *SEC* calculated for the energy-optimized EO-2 simulation cases of the 100 tpd hydrogen liquefaction process concept B at different hydrogen mole fractions y_{H_2} in the H_2-Ne cycle

y_{H_2}	*SEC* in kWh/kg
0.0	6.59
0.5	6.27
0.7	6.15
1.0	6.03

Influence of the electricity costs

A sensitivity analysis for the specific electricity costs c_{el} between 0.05-0.10 €/kWh is carried out for the 100 tpd LH_2 large-scale hydrogen liquefaction process concepts A and B. The specific energy consumption *SEC* calculated for the cost-optimized CO-2 simulation cases as a function of c_{el} is plotted in Figure 8.21.

The specific energy consumption *SEC* decreases in the CO-2 simulation cases with higher specific electricity costs c_{el}. This can be explained by the fact that the variable operating expenses (OPEX) $C_{OPEX,var}$ in the hydrogen liquefier cost estimation model increase at higher electricity costs c_{el}. The impact of the *SEC* on the specific liquefaction costs *SLC* is higher at higher c_{el}. In order to minimize the objective function *SLC* at higher c_{el}, the optimizer manipulates the optimization variables to further decrease the *SEC*. The optimizer reduces the temperature differences ΔT in the heat exchanger unit operations of the hydrogen liquefier process simulator model.

In Figure 8.22 the specific liquefaction costs *SLC* calculated for the 100 tpd LH_2 process concept A is plotted as a function of the specific electricity costs c_{el} in the CO-2 simulation cases. At higher c_{el}, the economic viability of the more efficient process

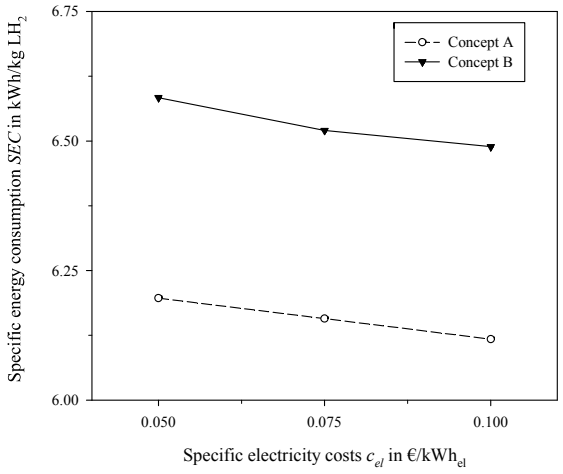

Figure 8.21: Specific energy consumption *SEC* of the 100 tpd LH_2 CO-2 simulation cases calculated for the process concepts A and B as a function of the specific electricity costs c_{el} [Cardella et al. 2017d]

concept A improves relative to the process concept B.

Influence of turbine energy recovery

The turbine energy recovery via turbine-generator units is assumed in the simulation cases with a turbine power $P_{TU} \geq 50\,\text{kW}$. The influence of the turbine energy recovery on the specific energy consumption *SEC* is investigated in the 100 tpd LH_2 cost-optimized CO-2 simulation cases. As shown in Table 8.11, the total hydrogen turbine power P_{TU} increases for larger liquefaction capacities. Also the difference in the specific energy consumption *SEC* between the hydrogen liquefaction processes calculated with and without turbine energy recovery increases for larger liquefaction capacities.

For process concept A, the *SEC* calculated without turbine energy recovery is approximately 5.9% higher. For process concept B, the *SEC* calculated without turbine energy recovery increases by approximately 5.2% from $SEC = 6.58\,\text{kWh/kg LH}_2$ to $SEC = 6.92\,\text{kWh/kg LH}_2$. The costs assumed for turbine energy recovery are included in the turbine costs within the hydrogen liquefier process simulator model. The impact of the turbine energy recovery on the specific liquefaction costs *SLC* is investigated in Chapter 9 for the final conceptual process design.

8.5.3 Precooling optimization with the HP-Hydrogen Claude Cycle

The results of process optimization indicate process concept A with the HP-H_2 Claude Cycle and Mixed-refrigerant Joule-Thomson Cycle (MRC) as optimal solution for the large-scale hydrogen liquefaction. The optimal precooling process is dependent on the liquefaction capacity as well as on boundary conditions such as the plant location, the utility costs and requirements from the plant operator.

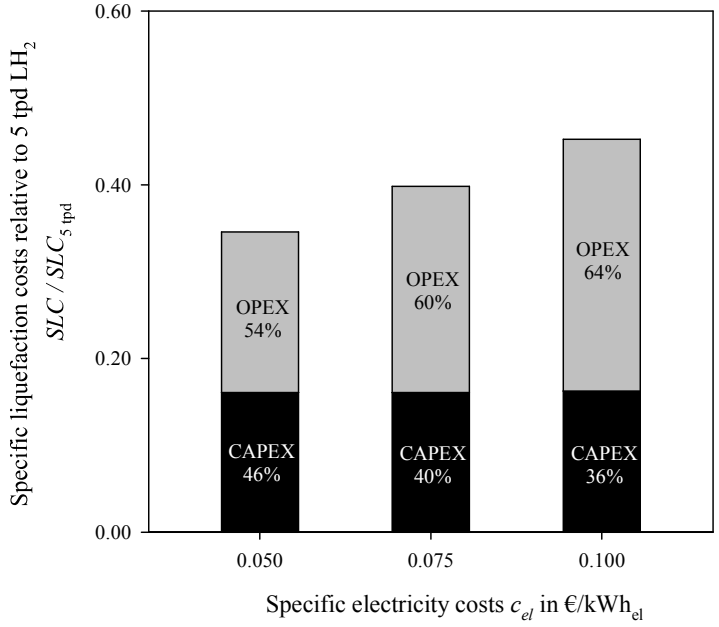

Figure 8.22: Specific liquefaction costs SLC relative to the reference 5 tpd LH_2 process $SLC_{5\text{tpd}}$ of the 100 tpd LH_2 CO-2 process concept A as a function of the specific electricity costs c_{el} [Cardella et al. 2017d]

Table 8.11: Difference in the specific energy consumption ΔSEC and the specific liquefaction costs ΔSLC calculated with and without turbine energy recovery for the CO-2 process concept A between $25 - 100$ tpd LH_2 at $c_{el} = 0.05$ €/kWh

Capacity	P_{TU}	ΔSEC	ΔSLC
tpd LH_2	kW	-	-
25	425	5.0%	0.0%
50	889	5.4%	0.4%
100	1894	5.9%	0.8%

In this section, the HP-H_2 Claude Cycle is optimized in the hydrogen liquefier process simulator model with the precooling processes investigated in Section 8.3.3. For a consistent comparison, the precooling cycles are simulated with the precooling temperature $T_{PC} = 100$ K. The LN_2 precooling is simulated with $T_{PC} = 80$ K.

Precooling process optimization for 100 tpd LH_2

The heat exchanger composite curves calculated in the 100 tpd CO-2 simulation cases for the hydrogen liquefaction process with LN_2 precooling and with the Dual N_2 Cycle are plotted in Figure 8.23. In the left plot, the evaporation of LN_2 precooling at a constant temperature T leads to a large maximum heat exchanger temperature difference ΔT_{max} near to $T_{PC} = 80$ K, which indicates substantial inefficiencies in the hydrogen precooling

process. The process optimization for the Dual N_2 Cycle leads to smaller heat exchanger temperature differences ΔT.

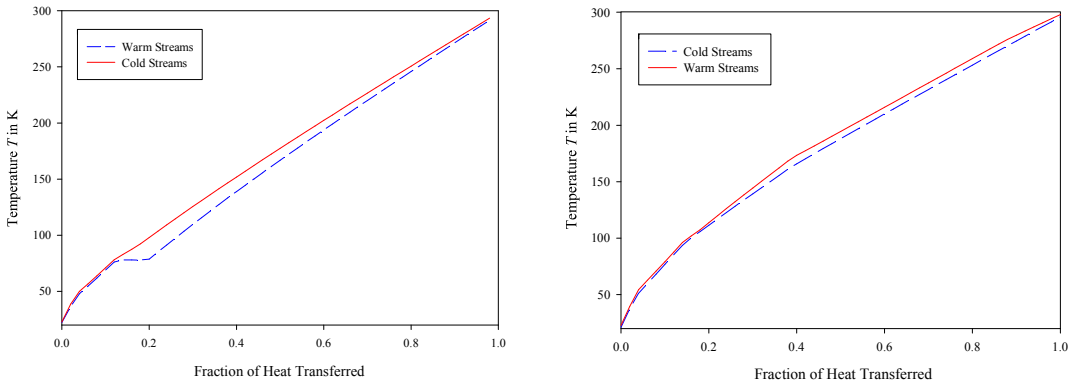

Figure 8.23: Heat exchanger composite curves calculated in the 100 tpd CO-2 simulation cases as a function of the fractional heat that is transferred in the hydrogen liquefaction process with LN_2 (left plot) and with Dual N_2 Cycle precooling (right plot)

The plot in Figure 8.24 shows the calculated heat exchanger composite curves for the cold and warm streams in the cost-optimized (CO-2) simulation cases with MRC. Compared to the CO-2 simulation cases with LN_2, the ΔT_{max} with MRC is calculated closer to ambient temperature T_{amb}, indicating a thermodynamically more efficient process. The flatter temperature regions in the MRC composite curves can be explained by the evaporation and the condensation of the refrigerant components [Cao et al. 2006].

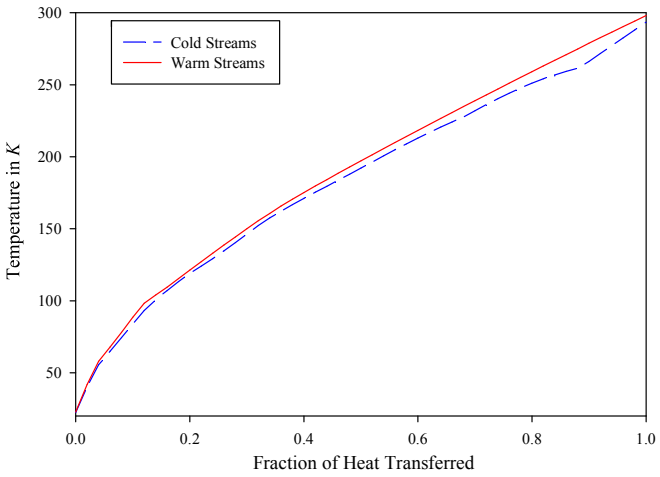

Figure 8.24: Heat exchanger composite curves calculated in the 100 tpd CO-2 simulation cases as a function of the fractional heat that is transferred in the hydrogen liquefaction process with MRC precooling [Cardella et al. 2017d]

The plot in Figure 8.25 shows the heat exchanger temperature differences ΔT between warm and cold streams calculated for the hydrogen liquefaction processes with LN_2, Dual N_2 Cycle and the MRC precooling. Compared to LN_2, the process optimization

for the Dual N_2 Cycle and the MRC precooling result in smaller ΔT, indicating a more efficient cooling process and lower specific energy consumption *SEC*.

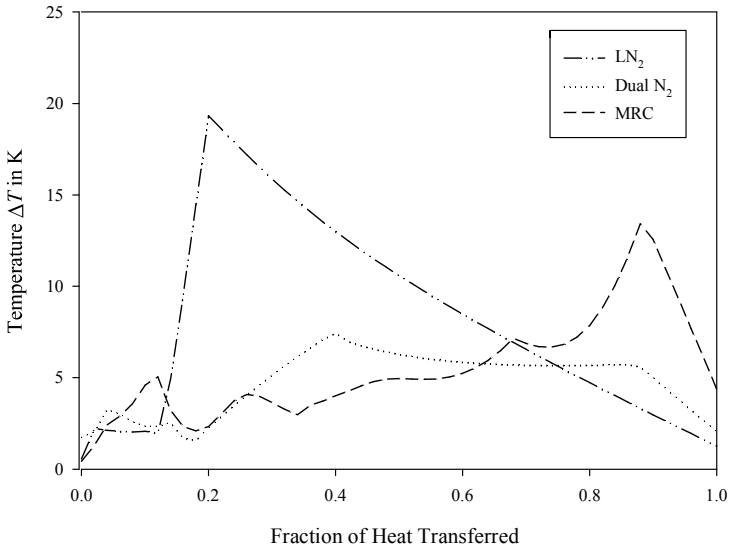

Figure 8.25: Heat exchanger temperature difference ΔT between the warm and cold composite curves calculated in the 100 tpd CO-2 simulation cases as a function of the fractional heat that is transferred in the hydrogen liquefaction process with LN_2, Dual N_2 Cycle and MRC precooling [Cardella et al. 2017d]

The process optimization results for the 100 tpd LH_2 hydrogen liquefaction processes calculated in CO-2 simulation cases with HP Hydrogen Claude Cycle and different precooling processes are summarized in Table 8.12.

Table 8.12: HP Hydrogen Claude Cycle calculated in the 100 tpd LH_2 CO-2 simulation cases for different precooling processes

Case	*SEC*	Ratio $(U \cdot A)_{sim}/(U \cdot A)_{LN_2}$	Ratio SLC/SLC_{5tpd}
	kWh/kg	-	-
LN_2	8.01	1.00	0.393
Single N_2	7.06	1.04	0.354
Single N_2-CH_4	6.81	1.28	0.359
Dual N_2	6.70	1.24	0.350
MRC	6.20	1.42	0.346

Compared to the process with LN_2 precooling, the closed-loop precooling cycles achieve a substantial improvement in the specific energy consumption *SEC* and specific liquefaction costs *SLC*. For the Nitrogen Expander Cycles, a $SEC = 7.06$ kWh/kg LH_2 is calculated with the Single N_2 Cycle and a $SEC = 6.70$ kWh/kg LH_2 with the Dual N_2 Cycle. Although the CAPEX for the Single N_2 Cycle is lower, the *SLC* calculated for the more

efficient Dual N_2 Cycle are lower. The Single N_2-CH_4 Cycle is optimized with a nitrogen mole fraction $y_{N_2} = 0.49$ and results in a $SEC = 6.81\,\text{kWh/kg LH}_2$. The process optimization with MRC achieve the lowest *SEC* and the lowest *SLC* for 100 tpd LH_2.

Influence of the liquefaction capacity

The large-scale hydrogen liquefaction process with HP-H_2 Claude Cycle is optimized with LN_2, Dual N_2 Cycle and MRC precooling for different hydrogen liquefaction capacities between $25 - 100$ tpd LH_2. The process optimization results for the calculated specific energy consumption *SEC* are shown in the left plot (EO-2 simulation cases) and in the right plot (CO-2 simulation cases) of Figure 8.26.

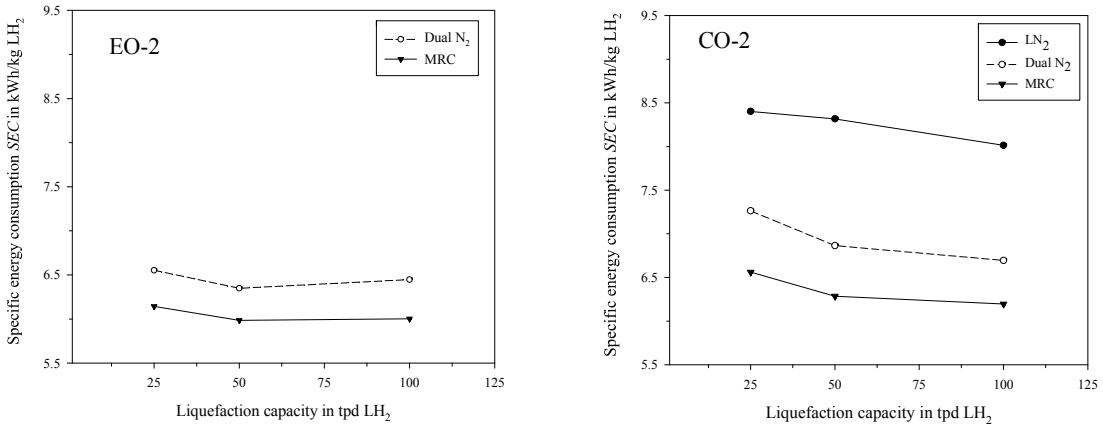

Figure 8.26: Specific energy consumption *SEC* calculated in the energy-optimized EO-2 (left plot) and the cost-optimized CO-2 (right plot) simulation cases for different precooling processes with the HP-H_2 Claude Cycle as a function of liquefaction capacity [Cardella et al. 2017d]

The specific energy consumption *SEC* calculated in the EO-2 simulation cases are lower compared to the *SEC* calculated in the CO-2 simulation cases. In all simulation cases, the lowest *SEC* is calculated with MRC precooling. The *SEC* for the hydrogen liquefaction process with MRC precooling is calculated between 6% and 10% lower compared to the *SEC* calculated with the Dual N_2 Cycle and up to 24% lower compared to the *SEC* calculated with the LN_2 precooling. In the EO-2 simulation cases, the *SEC* calculated for 50 tpd LH_2 is lower compared to the 100 tpd LH_2 case. To minimize the *SEC* in the 100 tpd LH_2 EO-2 simulation cases, the upper limit for the optimization constraint $(U \cdot A)_{max}$ is reached and cannot be increased by the optimizer.

The specific liquefaction costs *SLC* calculated in the CO-2 simulation cases for different precooling processes are plotted in Figure 8.27 as a function of the liquefaction capacity. Relative to the specific liquefaction costs of the reference 5 tpd LH_2 process $SLC_{5\text{tpd}}$, the *SLC* calculated in the 25 tpd LH_2 CO-2 simulation cases are reduced by nearly 50%. The lowest *SLC* for the 25 tpd LH_2 CO-2 simulation cases are calculated with the Dual N_2 Cycle. Relative to $SLC_{5\text{tpd}}$, the *SLC* calculated in the CO-2 simulation cases with MRC precooling are reduced by nearly 60% for 50 tpd LH_2 and by nearly

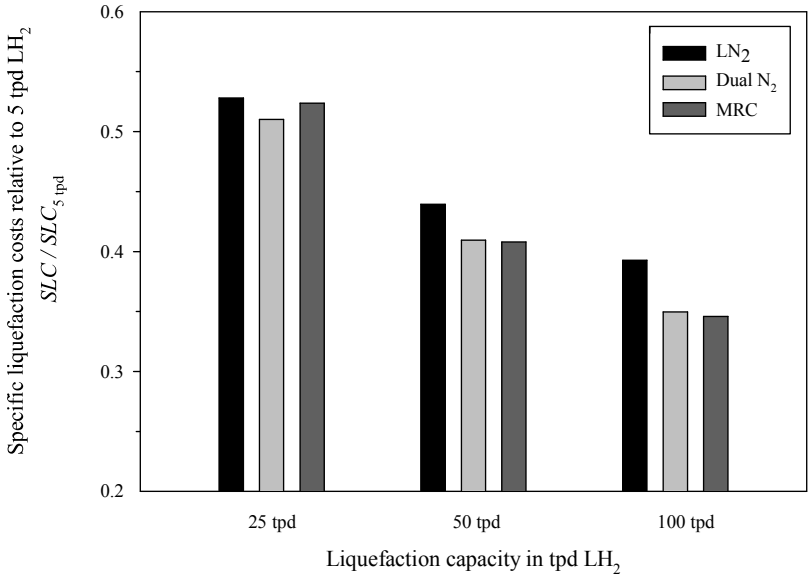

Figure 8.27: Specific liquefaction costs SLC relative to the reference 5 tpd LH_2 process $SLC_{5\text{tpd}}$ calculated in the cost-optimized CO-2 simulation cases for different precooling processes with the HP-H_2 Claude Cycle as a function of liquefaction capacity [Cardella et al. 2017d]

67% for 100 tpd LH_2. For the 50 tpd LH_2 and the 100 tpd LH_2 CO-2 simulation cases, the lowest SLC are calculated with the MRC precooling process.

Influence of the electricity costs

In Figure 8.28 the specific liquefaction costs SLC calculated in the 100 tpd LH_2 cost-optimized CO-2 simulation cases are plotted as a function of the specific electricity costs c_{el} for the HP-H_2 Claude Cycle with MRC and Dual N_2 Cycle.

For $c_{el} = 0.05$ €/kWh, the SLC optimized with MRC are 1% lower than calculated with the Dual N_2 Cycle. Due to the lower specific energy consumption SEC of the hydrogen liquefaction process with MRC, the difference in the calculated SLC between the simulation cases with MRC and Dual N_2 Cycle increases for higher c_{el}.

8.6 Final process evaluation

The minimum specific liquefaction costs SLC calculated in the cost-optimized CO-2 simulation cases as a function of the liquefaction capacity are plotted in Figure 8.29.

The capacity scale-up from the reference 5 tpd LH_2 process to 25 tpd LH_2 leads to a substantial reduction in the SLC by nearly 50%. The liquefaction capacity scale-up from 25 tpd to 50 tpd and 100 tpd LH_2 result in a weaker decrease in the SLC. For

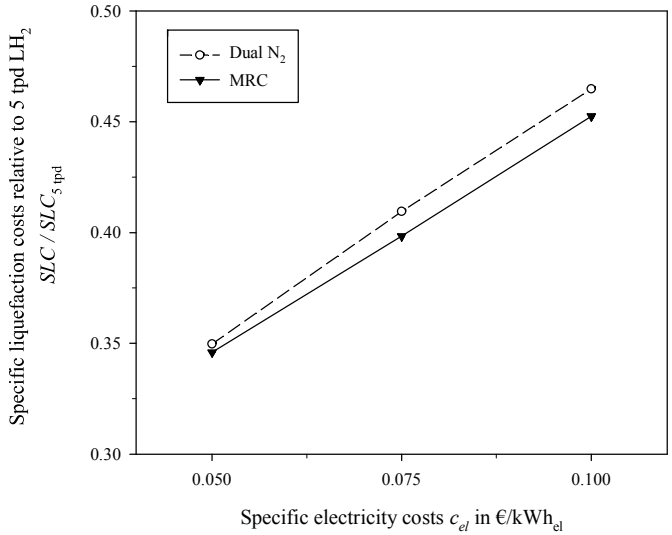

Figure 8.28: Specific liquefaction costs *SLC* relative to the reference 5 tpd LH_2 process SLC_{5tpd} calculated in the 100 tpd LH_2 CO-2 simulation cases for the HP-H_2 Claude Cycle with MRC and Dual N_2 Cycle as a function of the specific electricity costs c_{el} [Cardella et al. 2017d]

50 tpd LH_2, the lowest *SLC* are calculated with process concept A, the HP-H_2 Claude Cycle with MRC precooling. For 100 tpd LH_2, the lowest *SLC* are calculated with process concept B, the Dual H_2-Ne Cycle with MRC precooling. Compared to process concept B, process concept A achieves a lower specific energy consumption *SEC* in all simulation cases.

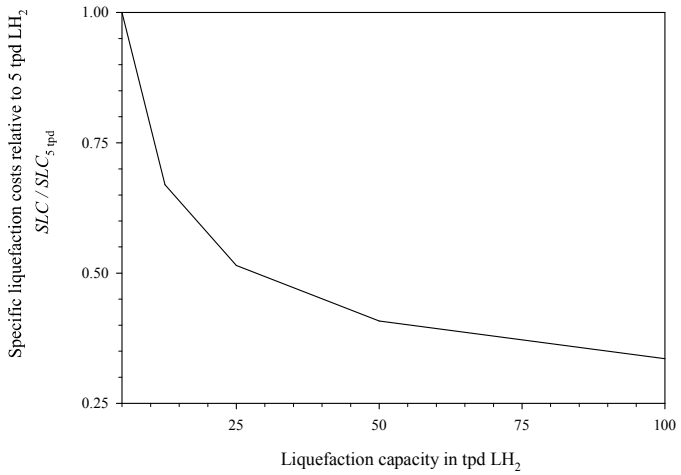

Figure 8.29: Specific liquefaction costs *SLC* relative to the reference 5 tpd LH_2 process SLC_{5tpd} calculated in the cost-optimized CO-2 simulation cases for different process concepts as a function of liquefaction capacity

The results of process optimization and process evaluation for the developed large-scale hydrogen liquefaction processes are summarized in Figure 8.30 and Table 8.13.

Table 8.13: Large-scale hydrogen liquefaction process concept evaluation and selection

Criteria	State-of-the-art	Medium-term	Long-term
Capacity	≤ 25 tpd	≤ 100 tpd	≥ 100 tpd
Cryogenic refrigeration	H_2	H_2	H_2-Ne, H_2 or He
Compressor	Piston	Piston	Turbo
Precooling	LN_2 or N_2 Cycle	N_2 Cycle or MRC	MRC

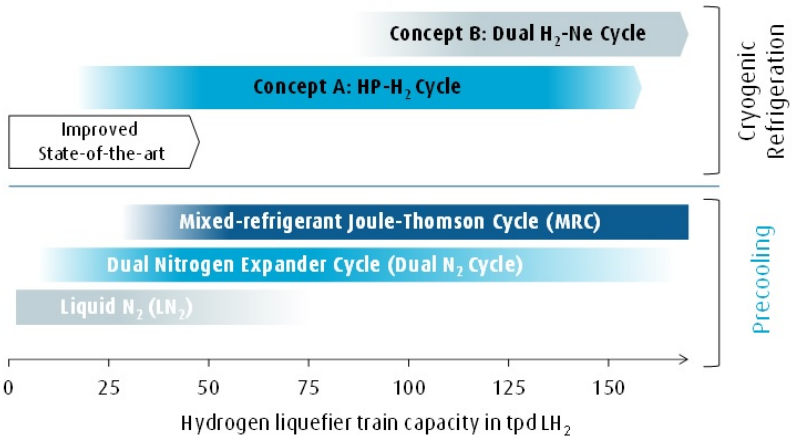

Figure 8.30: Overview summarizing the results of the process optimization and evaluation of large-scale hydrogen liquefaction processes as a function of the liquefaction capacity [Cardella et al. 2017d]

In order to evaluate the technical risks and the maturity for the large-scale hydrogen liquefaction process concepts A and B, a technological risk assessment is carried out. The technological risk assessment for process concepts A and B is summarized in Table 8.14. The large-scale hydrogen liquefaction process concepts A and B require further technical development and detailed engineering. Compared to the state-of-the-art hydrogen liquefiers, the turbine expander design in the cryogenic refrigeration cycle require technical adjustments that can be implemented in the short-term. As described in Section 4.3, gas bearing turbines need to be adapted to the larger turbine capacities required for large-scale hydrogen liquefaction up to 50 tpd LH_2 [Cardella et al. 2017c].

As an alternative, large oil bearing turbines and magnetic bearing turbines are available but may need to be adapted to the cryogenic refrigeration cycle design and operating conditions. The turbine energy recovery is only an optional feature to reduce the specific energy consumption *SEC*. The turbine energy recovery technology is novel to the cryogenic refrigeration cycle of hydrogen liquefiers and needs to be transferred to hydrogen liquefiers. The MRC precooling processes are state-of-the-art for natural gas liquefaction but the herein developed MRC process is novel to industrial hydrogen liquefiers.

Table 8.14: Technical risk assessment (TRA) for the developed large-scale hydrogen liquefaction process concepts A and B

Technical Risk Assessment	Process Concept A	Process Concept B
Technical uncertainties	Low	Medium
Technical Risk	Low	Medium
Technically qualified	Yes	No

The process concept A has a high technical maturity, low complexity and is considered as technically qualified after a detailed plant design is carried out. The developed HP Hydrogen Claude Cycle can be designed based on a state-of-the-art Hydrogen Claude Cycle. The MRC precooling technology can be transferred from natural gas liquefaction plants. Compared to process concept A, the technical maturity of process concept B is lower because it requires technical development and qualification before implementation. The H_2-Ne refrigerant mixture in process concept B is novel. Accurate fundamental equations of state for binary cryogenic fluid mixtures of neon with hydrogen and helium are still in the development phase and require testing as well as validation prior to the use in industrial hydrogen liquefiers. The operation with H_2-Ne mixture in the cryogenic refrigeration cycle is a novelty for industrial hydrogen liquefiers which increases the uncertainties in the plant design, operation and control complexity. Moreover, the potential neon refrigerant losses in process concept B are connected with higher economic risks.

Based on the process-economic evaluations and the technological risk assessment carried out in this chapter, the process concept A is selected as preferred large-scale hydrogen liquefaction process for liquefaction capacities up to 100 tpd LH_2.

9 Final conceptual process design

The process concept A, the high-pressure (HP) Hydrogen Claude Cycle (HP-H_2 Claude Cycle) with Mixed-refrigerant Joule-Thomson Cycle (MRC) precooling, is selected as preferred large-scale hydrogen liquefaction process.

In this final chapter, the process concept A is further elaborated and optimized for a liquefaction capacity of 100 tpd LH_2. The estimation accuracy for the specific energy consumption *SEC* and specific liquefaction costs *SLC* in the hydrogen liquefier process simulator model is increased with the input of actual equipment performance and cost data from industrial manufacturers.

Part of this Chapter are included in Cardella et al. 2017a.

9.1 Equipment design for process concept A

Based on the results of the cost-optimized CO-2 process concept A, a preliminary equipment design is carried out for the compressors, the turbine expanders and the plate-fin heat exchangers (PFXH) in process concept A. The preliminary equipment sizing correlations described in Chapter 6 are used and are validated with more detailed design calculations carried out by industrial manufacturers.

9.1.1 Compressors

The hydrogen and MRC compressor process data calculated in the hydrogen liquefier process simulator model for the 100 tpd LH_2 process concept A are given in Table 9.1. The hydrogen reciprocating piston compressors H_2 LP-COMP-1 and H_2 MP-COMP-1 are the largest electrical consumers with the respective power consumption calculated in the hydrogen liquefier process simulator model. These hydrogen reciprocating piston compressors are available on the market and are supplied by different companies, as for instance: Burkhart Compression, Borsig ZM and General Electric. The H_2 LP-COMP-1 and H_2 MP-COMP-1 compressors are designed as double-acting dry-running piston compressors. The H_2 MP-COMP-1 compressor is designed with two identical compressor units running in parallel configuration.

The H_2 LP-COMP-1 and H_2 MP-COMP-1 compressors can be designed with only $N_{RC} = 2$ stages with inter-cooling. The difference in the compressor power consumption P_{comp} between a design with $N_{RC} = 2$ and $N_{RC} = 3$ compressor stages with inter-cooling is below 3%. The H_2 LP-COMP-1 compressor is designed with two cylinders per stage and the H_2 MP-COMP-1 compressor is designed with three cylinders per stage with a piston diameter $D_{pist} = 0.8\,\text{m} < D_{pist,max}$ and a piston rod diameter $D_{rod} < D_{rod,max} = 0.15\,\text{m}$.

Table 9.1: Hydrogen and MRC compressors calculated in the hydrogen liquefier process simulator model for the 100 tpd LH_2 process concept A with the original model assumptions for the compressor unit operations

Gas compressors	H_2 LP-COMP	H_2 MP-COMP	MRC-COMP
Compressor volumetric flow	9273 m^3/h	32942 m^3/h	21145 m^3/h
Inlet temperature T_{in}	295 K	295 K	295 K
Inlet pressure p_{in}	1.4 bar	8.1 bar	2.5 bar
Outlet pressure p_{out}	8.2 bar	50.3 bar	50.4 bar
Power consumption $P_{comp,el}$	0.9 MW	19.2 MW	5.9 MW

For the H_2 LP-COMP-1 and H_2 MP-COMP-1 compressors, the compressor power consumption calculated with the original model assumptions for the compressor unit operation results in a total compressor power consumption $P_{comp,el} = 20.1\,\text{MW}$. Compared to the original model assumptions for the compressor unit operation in the hydrogen liquefier process simulator model, the total compressor power consumptions estimated from actual performance data given by industrial manufacturers is about 5% lower with $P_{comp,el} = 19.1\,\text{MW}$.

The MRC compressor for the fluid mixture Mix-1 is designed as a multi-stage and multi-shaft integrally-geared turbo compressor with dry gas seals. The fluid mixture at the outlet of the compressor inter-coolers condensates and is separated in a downstream phase separator. These MRC turbo compressors are available on the market and are supplied by several companies, as for instance: MAN Turbo, Atlas Copco, and General Electric. Compared to the original model assumptions for the compressor unit operation, the actual power consumption P_{comp} of the MRC turbo compressor given by industrial manufacturers is expected to be lower.

9.1.2 Hydrogen Turbines

The Joule-Thomson (JT) turbine at the cold end of the hydrogen feed stream and the JT turbine H_2 TU-1 in the HP-H_2 Claude Cycle are state-of-the-art gas bearing turbines with a turbine power of $P_{TU} = 20\,\text{kW}$ and $P_{TU} = 15\,\text{kW}$, respectively. The gas bearing turbine design is validated with the turbine design of the industrial manufacturer Linde Kryotechnik.

The HP-H_2 Claude Cycle is designed with two and with three hydrogen turbine strings. The actual costs for the hydrogen turbine energy recovery from manufacturers is higher than originally assumed in the hydrogen liquefier process simulator model. The design with three turbine strings requires slightly smaller turbine powers P_{TU} because of the lower refrigerant mass flow rate $\dot{m}_{rfr}$ required per turbine string. Therefore, the HP-H_2 Claude Cycle design with two turbine strings with fewer but larger turbines is more cost efficient. For the expansion pressure ratio of about

$\pi_{TU} \approx 6$, the warmer hydrogen turbine string is designed with three turbine stages while the colder turbine strings are designed with only two turbine stages. The hydrogen turbines in the HP-H_2 Claude Cycle achieve high isentropic efficiencies up to $\eta_{is} = 0.88$. The two turbines H_2 TU-2 and H_2 TU-3 in the colder turbine string are designed with a turbine power between $P_{TU} = 200 - 300\,\text{kW}$ while the three turbines H_2 TU-6, H_2 TU-7 and H_2 TU-8 in the warmer turbine string are designed with a turbine power between $P_{TU} = 200 - 450\,\text{kW}$. The turbines with turbine energy recovery can be designed with large oil or magnetic bearing turbines for turbine wheel diameters between approximately $D_{wheel} = 100 - 200\,\text{mm}$ and for turbine rotational speeds $n_{TU} \leq 60000\,\text{rpm}$.

At present, the turbine energy recovery is regarded as an optional add-on to further decrease the specific energy consumption *SEC* of the hydrogen liquefaction process. If turbine energy recovery is not implemented, a turbine design with smaller gas bearing turbines is more economical. If these turbines are designed with smaller gas bearing turbines, up to three gas bearing turbines in parallel with turbine wheel diameters $D_{wheel} > 50\,\text{mm}$ and turbine rotational speeds $n_{TU} \leq 100000\,\text{rpm}$ are required.

9.1.3 Plate-fin heat exchangers

The aluminium brazed plate-fin heat exchangers (PFHX) of the industrial manufacturer Linde AG are used as a reference for the dimensioning. For the 100 tpd LH_2 process concept A, the maximum operating temperature is limited to $p_{max} < 55\,\text{bar}$ and a design pressure of $p_{ds} = 63\,\text{bar}$ can be chosen. In the final conceptual process design, no ortho- to para-hydrogen conversion catalyst is included in the precooling PFHX. The total PFHX volume V_{PFHX} required for the precooling PFHX-1 is estimated from the calculated $(U \cdot A)_{PC}$ value to about $V_{PFHX,1} = 50\,\text{m}^3$ and is distributed in two parallel PFHX with geometrical dimensions close to the maximum PFHX dimensions of $l \times ht \times wt = 8.2 \times 2.5 \times 1.5\text{m}$ per core [Linde AG n.d.]. The feasibility of the PFHX-1 design is validated with the industrial manufacturer and the actual PFHX costs C_{PFHX} are lower than calculated in the original hydrogen liquefier process simulator model.

The total volume for the PFHX in the liquefier coldbox is estimated from the calculated $(U \cdot A)_{liq}$ value to below $V_{PFHX} = 30\,\text{m}^3$. The PFHX in the liquefier coldbox can be implemented with the maximum feasible geometrical dimensions $l \times ht \times wt = 8.2 \times 2.5 \times 1.5\text{m}$ per core [Linde AG n.d.] in one or in two smaller PFHX in parallel. An additional smaller PFHX block is required for PFHX-3. However, a detailed PFHX design considering the ortho- to para-hydrogen conversion and catalyst volume is required for the sizing of PFHX-2 and PFHX-3.

9.1.4 Ortho- to para-hydrogen conversion

The hydrogen liquefier process simulator model is based on the calculation with equilibrium-hydrogen. In reality, the ortho- to para-hydrogen conversion at equilibrium is not achieved in PFHX-2 and PFHX-3. The final design of process concept A proposes the combination of stepwise adiabatic reactor vessels and continuous catalytic conversion in PFHX, as shown in Figure 9.1. The hydrogen feed stream is designed with adiabatic ortho- to para-hydrogen reactor vessels placed downstream of the cryogenic adsorber vessels. The plate-fin heat exchangers PFHX-2 and PFHX-3 in the liquefier coldbox are filled with catalyst for the catalytic ortho- to para-hydrogen conversion near to the equilibrium. To reduce the difference between the actual mole fraction of para-hydrogen y_p and the equilibrium mole fraction of para-hydrogen y_p^{eq} at the inlet of PFHX-2, the first adiabatic reactor vessel OP-1 is used. This configuration reduces the catalyst volume V_{cat} required in the PFHX-2 [Cardella et al. 2015b].

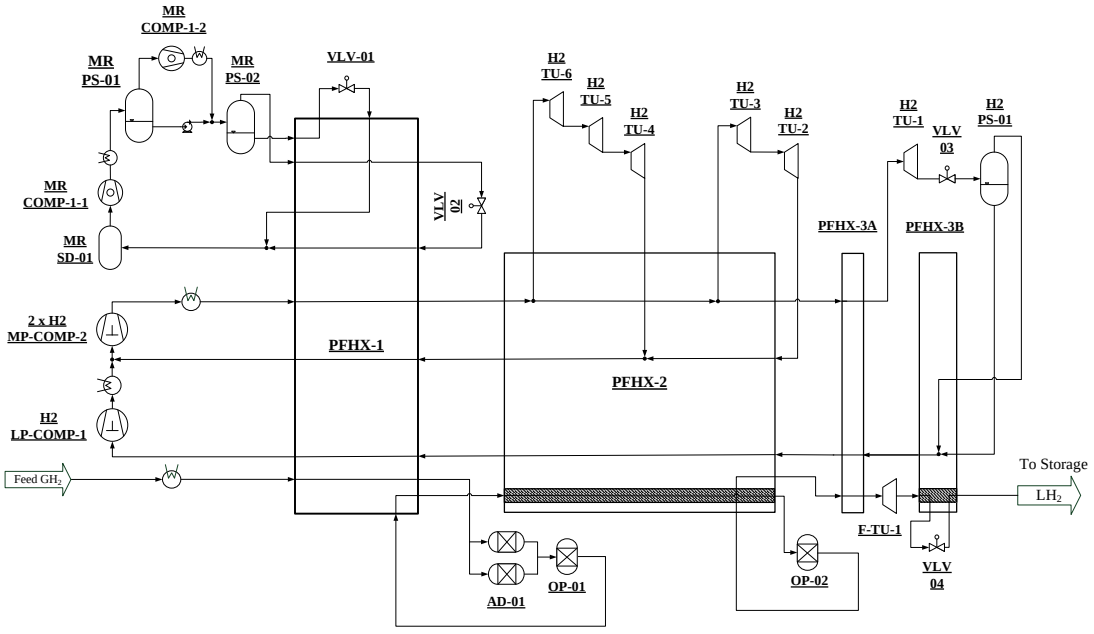

Figure 9.1: Process flow diagram for the final design of process concept A

The design of the PFHX and reactor vessels with the prediction of the catalytic ortho- to para-hydrogen conversion is carried out with the kinetic ortho- to para-hydrogen conversion model for plate-fin heat exchangers developed by Donaubauer 2015 and Donaubauer et al. 2018 in Matlab®. The catalytic ortho- to para-hydrogen conversion in PFHX-2 and PFHX-3 is designed in order to ensure that the maximum geometrical dimensions of the PFHX are within the feasible limits. To limit the volume of catalyst V_{cat} and the PFHX volume V_{PFHX} required for the catalytic ortho- to para-hydrogen conversion in PFHX-2 and PFHX-3, a ortho- to para-hydrogen conversion factor between about $\eta_{conv} = 0.75 - 0.85$ is chosen. In the adiabatic reactor vessels $\eta_{conv} > 0.9$ is achieved. At the outlet of the adiabatic reactor vessels OP-1, the mole

fraction of para-hydrogen is calculated to approximately $y_p = 0.4$. At the outlet of PFHX-2, $y_p = 0.9$ is calculated.

The second adiabatic reactor vessel OP-2 is placed downstream of PFHX-2 to balance out the incomplete conversion in PFHX-2. At the outlet of OP-2, $y_p = 0.96$ is calculated. The final mole fraction of para-hydrogen $y_{p,final} \geq 0.98$ is achieved with the catalytic conversion in PFHX-3 as the hydrogen is finally cooled and liquefied at the nearly constant temperature.

9.2 Final process optimization

A final process optimization is carried out for the 100 tpd LH_2 hydrogen liquefaction process concept A illustrated in Figure 8.17. The cost-optimized CO-2 simulation cases are calculated in the hydrogen liquefier process simulator with the precooling temperature $T_{PC} = 100\,\mathrm{K}$ and the fixed inlet feed pressure $p_{feed} = 25\,\mathrm{bar}$. Compared to the process optimization carried out in Chapter 8, a multi-objective optimization is carried out with the specific liquefaction costs SLC as objective function $f(x)$ and the maximum specific energy consumption SEC_{max} defined as additional optimization constraint. Based on the findings made in Chapter 8, $SEC_{max} = 6.10 - 6.30\,\mathrm{kWh/kg}$ LH_2 is used as optimization constraint.

For the final process optimization, the optimization variables and constraints are refined to match the design of industrial process equipment available on the market. The optimization variables for the pressure p and temperature T levels in the HP-H_2 Claude Cycle and in the MRC are further restricted. To limit the design pressure p_{ds} of plate-fin heat exchangers (PFHX), the high-pressure (HP) levels are limited to $p_{HP,max} = 50\,\mathrm{bar}$. The maximum compressor inlet volumetric flow $\dot{V}_{in,max}$ for the MP H_2 compressor is reduced even further to design more compact compressors. The product of the heat exchanger heat transfer coeffient U and the heat transfer surface A is further limited to a maximum value $(U \cdot A)_{max,PC}$ for the precooling part and $(U \cdot A)_{max,liq}$ for the liquefier part of the hydrogen liquefaction process. The optimization variables and constraints adopted for the final process optimization are listed in Tables 9.2 and 9.3.

At lower values for the maximum specific energy consumption SEC_{max}, the optimizer finds a solution with smaller heat exchanger $(U \cdot A)_{sim}$. The multi-objective process optimization with the MRC fluid mixture Mix-3 satisfied all optimization constraints for $SEC_{max} \geq 6.30\,\mathrm{kWh/kg}$ LH_2 while the optimizer cannot satisfy all optimization constraints for $SEC_{max} < 6.30\,\mathrm{kWh/kg}$ because larger than defined heat exchangers are required. The multi-objective process optimization with the MRC fluid mixture Mix-1 satisfies all optimization constraints even for $SEC_{max} = 6.10\,\mathrm{kWh/kg}$ LH_2. The minimum MRC temperature with the MRC fluid mixture Mix-1 is $T_{MRC,min} > 96\,\mathrm{K}$.

Based on the final multi-objective process optimization, the process concept A is re-calculated without optimization by inserting actual equipment performance and cost data that are validated with industrial manufacturers. Compared to the original

Table 9.2: Optimization variables for the final process concept A

Optimization variables	Lower bound	Upper bound	Calculated
p_{feed}	25 bar	80 bar	25 bar
$p_{HP,MRC}$	25 bar	50 bar	50 bar
$p_{MP,MRC}$	15 bar	25 bar	25 bar
$p_{LP,MRC}$	1.5 bar	6.0 bar	2.9 bar
$T_{MRC,int}$	150 K	200 K	163.5 K
y_{N_2}	0.1	0.3	0.14
y_{CH_4}	0.2	0.35	0.30
$y_{i-C_4H_{10}}$	0.15	0.3	0.25
p_{HP,H_2}	40 bar	50 bar	49.9 bar
p_{MP,H_2}	8 bar	10 bar	8.3 bar
T_{ce}	28 K	32 K	29.8 K
ΔT_1	2.0 K	10 K	2.6 K
$\Delta T_{2\text{-}1}$	2.5 K	6.0 K	2.7 K
$\Delta T_{2\text{-}2}$	4.0 K	6.0 K	4.3 K

model assumptions for the unit operations, the actual power consumption P_{comp} of the hydrogen reciprocating piston compressors is input into the hydrogen liquefier process simulator model. For the MRC turbo compressor, the more conservative power consumption P_{comp} estimated from the original model assumptions is used. The originally assumed turbine isentropic efficiencies η_{is} match well with turbine performance data from industrial manufacturers and are not modified. The turbine energy recovery efficiency is increased from the originally assumed $\eta_{recov} = 0.8$ to $\eta_{recov} = 0.9$. The actual hydrogen reciprocating piston compressor costs $C_{comp,RC}$ and the MRC turbo compressor costs $C_{comp,TC}$ are lower than calculated in the hydrogen liquefier cost model while the turbine costs C_{TU} with turbine energy recovery are higher.

The final results for the 100 tpd LH_2 process concept A calculated with the original hydrogen liquefier process simulator model assumptions and with manufacturer data are summarized in Table 9.4. Relative to the specific liquefaction costs of the reference 5 tpd process $SLC_{5\text{tpd}}$, the SLC calculated for the 100 tpd process concept A are reduced by about 65%. The specific energy consumption SEC calculated without turbine energy recovery is nearly 7% higher than the SEC calculated with turbine energy recovery. The specific liquefaction costs SLC calculated with manufacturer data without turbine energy recovery are about 7% lower than the SLC calculated with turbine energy recovery and are below 1 €/kg LH_2.

The SEC calculated for the 100 tpd LH_2 process concept A with manufacturer data is less conservative than the SEC calculated with the original model assumptions. However, the uncertainties and simplifications in the hydrogen liquefier process simulator model

Table 9.3: Optimization constraints for the final process concept A

Optimization constraints	Limit	Calculated
SEC_{max}	6.10 kWh/kg LH_2	6.10 kWh/kg LH_2
$y_{N_2,min,VLV\text{-}2}$	0.2	0.2
$y_{i-C_4H_{10},max,VLV\text{-}2}$	0.1	0.1
$\Delta T_{min,1\text{-}1}$	2 K	2.0 K
$\Delta T_{min,1\text{-}2}$	2 K	3.0 K
$\Delta T_{min,VLV\text{-}1}$	2 K	3.9 K
$\Delta T_{min,VLV\text{-}2}$	2 K	3.5 K
$\Delta T_{min,2\text{-}1}$	0.5 K	0.5 K
$\Delta T_{min,2\text{-}2}$	1.0 K	1.5 K
$\Delta T_{min,2\text{-}3}$	1.0 K	3.9 K
$\Delta T_{min,3}$	0.5 K	0.5 K
$\Delta T_{max,1\text{-}1}$	25 K	3.9 K
$\Delta T_{max,1\text{-}2}$	25 K	11.2 K
$\Delta T_{max,2\text{-}1}$	15 K	2.8 K
$\Delta T_{max,2\text{-}2}$	15 K	4.3 K
$\Delta T_{max,2\text{-}3}$	15 K	4.3 K
$LMTD_{max,1\text{-}1}$	6 K	2.8 K
$LMTD_{max,1\text{-}2}$	6 K	5.1 K
$(U \cdot A)_{max,PC}$	6.9×10^3 kJ/(K · s)	6.9×10^3 kJ/(K · s)
$(U \cdot A)_{max,liq}$	2.1×10^3 kJ/(K · s)	2.1×10^3 kJ/(K · s)
$\dot{V}_{H_2,in,max}$	36000 m^3/h	32942 m^3/h
$T_{TU\text{-}6,in,max}$	99 K	99 K

justify the original more conservative model assumptions. To further increase the estimation accuracy for the *SEC* and *SLC*, a detailed plant engineering is required.

Table 9.4: Final results for the 100 tpd LH_2 process concept A calculated in the multi-objective CO-2 simulation ($SEC_{max} = 6.10$ kWh/kg) with the original model assumptions and with available manufacturer data

Case	Original Model	Manufacturer Data
with turbine energy recovery		
SEC in kWh/kg LH_2	6.10	5.80
$SLC/SLC_{5\text{tpd}}$	0.349	0.349
without turbine energy recovery		
SEC in kWh/kg LH_2	6.45	6.20
$SLC/SLC_{5\text{tpd}}$	0.352	0.324

10 Summary and outlook

The aim of this work is the development of thermodynamic efficient large-scale hydrogen liquefaction processes that are optimized in the specific liquefaction costs *SLC* and can be implemented within the next 5 years. In order to evaluate the technical and economic viability, a novel process development approach is implemented within this work.

The hydrogen liquefaction processes in this work are modelled and simulated in the hydrogen liquefier spreadsheet model in MICROSOFT EXCEL® and in the hydrogen liquefier process simulator model in UNISIM DESIGN®. To find an optimal balance between the plant capital expenses and the operating expenses, a detailed hydrogen liquefier cost estimation model is implemented in this work. The implemented hydrogen liquefier process simulation and cost estimation models are used for the development and optimization of hydrogen liquefaction processes. A mathematical optimization method available in MATLAB® from literature is coupled to the hydrogen liquefier process simulator for the process optimization with both specific energy consumption *SEC* and specific liquefaction costs *SLC* as objective functions. The process optimization is carried out for different hydrogen liquefaction process configurations and capacities as well as with sensitivities in key cost parameters such as the electricity costs.

State-of-the-art built hydrogen liquefiers and existing process concepts are investigated to detect the areas of potential improvements in the hydrogen liquefaction process. For the development of novel process concepts, process-economic investigations of the hydrogen liquefier subsystems and the main process equipment are carried out. A particular attention is given to the technical feasibility of compressors, turbine expanders as well as the plate-fin heat exchangers and the catalytic ortho- to para-hydrogen conversion. The results of process development and optimization show that the optimal process concept for large-scale hydrogen liquefaction is mainly dependent on the liquefaction capacity and boundary conditions such as the plant location, the electricity costs and the refrigerant costs. The process-economic investigations and the process optimization results indicate hydrogen or a fluid mixture composed of hydrogen and neon as suitable refrigerants for the cryogenic refrigeration cycle of large-scale hydrogen liquefaction processes in the short- to medium-term. The Mixed-refrigerant Joule-Thomson Cycle and the Dual Nitrogen Expander Cycle are promising precooling cycle designs.

The results of process optimization show that the specific liquefaction costs *SLC* substantially decrease with the scale-up of the hydrogen liquefaction capacity. In particular from the reference 5 tpd to 25 tpd LH_2, the specific liquefaction costs *SLC* are reduced with an improved process design and with process optimization by nearly 50%. The capacity scale-up to 25 tpd LH_2 can be implemented in the short-term with state-of-the-art hydrogen liquefier technology. The up-scaling of the liquefaction capacity from 25 tpd to 50 tpd or 100 tpd LH_2 results in a further but weaker decrease in the specific liquefaction costs *SLC*. Depending on the specific electricity costs and

refrigerant costs, the simple liquid nitrogen precooling results to be the cost effective precooling design for liquefaction capacities up to approximately 15 tpd LH_2. The Dual Nitrogen Expander Cycle results to be the cost effective precooling design for liquefaction capacities between approximately 15 tpd and 50 tpd LH_2. The process concepts with Mixed-refrigerant Joule-Thomson Cycle precooling achieve the lowest specific energy consumption *SEC* in all simulation cases. For liquefaction capacities near to 50 tpd LH_2 or higher, the process concepts with Mixed-refrigerant Joule-Thomson Cycle precooling achieve also the lowest specific liquefaction costs *SLC*.

In this work two novel process concepts are presented as process solutions for economically viable large-scale hydrogen liquefaction. The process concept A is designed with a high pressure Hydrogen Claude Cycle. The process concept B is designed with two cryogenic refrigeration cycles: a Hydrogen-Neon Mixture Brayton Cycle and a Hydrogen Joule-Thomson Cycle. Turbine energy recovery is considered with turbine-generator units. At present, the turbine energy recovery in the cryogenic refrigeration cycle is economically not convenient. Both process concept A and B are designed with Mixed-refrigerant Joule-Thomson Cycle precooling with a fluid mixture composed of nitrogen and hydrocarbons. The optimization results for the large-scale process concepts A and B indicate a substantial reduction in the calculated specific liquefaction costs *SLC*. For the two 100 tpd LH_2 process concepts, a specific energy consumption *SEC* between approximately $5.8 - 6.6$ kWh/kg LH_2 is calculated in energy-optimized and cost-optimized simulation cases. The process concept A is calculated with the lowest specific energy consumption *SEC* in all simulated cases. Compared to the state-of-the-art built hydrogen liquefiers, the specific energy consumption *SEC* calculated with the process optimization methods is improved by up to about 40 %.

For the developed large-scale hydrogen liquefaction process concepts, a technological risk assessment was carried out. The Mixed-refrigerant Joule-Thomson Cycle precooling is novel for low-temperature hydrogen precooling. For the scale-up of the turbine expanders and, optionally, for the turbine energy recovery in the cryogenic refrigeration cycle, a technological development is required. Compared to the process concept B, the process concept A has a higher level of technical maturity and can be implemented in the medium-term with lower technical risks. The hydrogen-neon mixture in process concept B is novel. Accurate thermodynamic fundamental equations of state for fluid mixtures of neon with helium and hydrogen were not available at the time of writing. These fluid mixtures require a comprehensive testing and validation before the use in industrial hydrogen liquefiers. In addition, a process and equipment design comprising neon refrigerant needs to minimize the losses of expensive neon. The process concept B thus requires a longer-term technical development before implementation.

The process concept A is thus chosen as optimal process solution for liquefaction capacities of up to 100 tpd LH_2. The process concept A is further cost-optimized with a multi-objective optimization and further elaborated with actual industrial equipment designs. In comparison to the state-of-the-art 5 tpd LH_2 process, the final process concept reduces the specific liquefaction costs *SLC* by nearly 68%. The specific energy consumption *SEC* is calculated to about 6.1 kWh/kg LH_2 with and 6.5 kWh/kg LH_2

without turbine energy recovery. By inserting actual equipment performance data, the calculated specific energy consumption *SEC* is reduced to about 5.8 kWh/kg LH_2 with and 6.5 kWh/kg LH_2 without turbine energy recovery. The results of process development and optimization in this work show that the up-scaling of the hydrogen liquefaction process can decrease both the specific liquefaction costs *SLC* and the specific energy consumption *SEC*. Specific liquefaction costs *SLC* below 1 €/kg are feasible with the large-scale hydrogen liquefaction process concepts presented in this work. The total costs for hydrogen delivery can be reduced substantially with liquid hydrogen.

Further work is required to turn the process concept into a final plant design that is ready for construction. The specific liquefaction costs *SLC* can be reduced further by using surplus liquefied natural gas or liquid nitrogen for precooling. Chiller units can further improve the specific energy consumption *SEC*. The development of affordable high-speed turbo compressors for the Hydrogen Claude Cycle or a Helium Brayton Cycle may, in the long-term, optimize the specific liquefaction costs *SLC* even further.

For a detailed plant engineering, further work can be done to improve the modelling and the simulation of hydrogen liquefaction processes. The accurate thermodynamic property estimation for the hydrogen allotropes at all ortho- and para-hydrogen mixture compositions is currently under development and was not available in the process simulator used in this work. A detailed dimensioning of the plate-fin heat exchangers with ortho- to para-hydrogen catalyst is required prior to implementation. A current limitation of the implemented hydrogen liquefier process simulation model is the assumption of equilibrium-hydrogen for the catalytic ortho- to para-hydrogen conversion. The ortho- to para-hydrogen conversion in plate-fin heat exchangers and reactor vessels is calculated outside the process simulator environment in a kinetic model in MATLAB®. An improvement to hydrogen liquefier process simulation can be achieved by coupling the accurate kinetic ortho- to para-hydrogen conversion model with the process simulator model and optimization methods. In this way, the process simulation can be optimized with the kinetic ortho- to para-hydrogen conversion model.

A Appendix

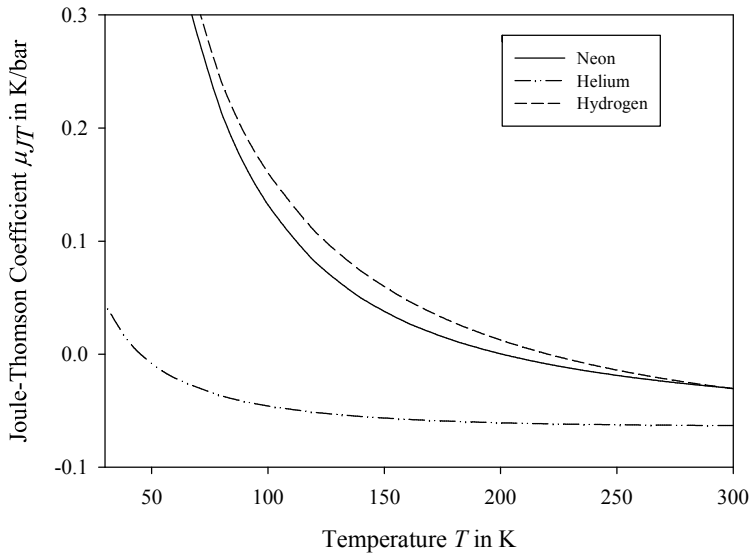

Figure A.1: Joule-Thomson (JT) coefficient μ_{JT} for helium, hydrogen and neon as a function of temperature T at 1 bar, calculated with REFPROP [Lemmon et al. 2013]

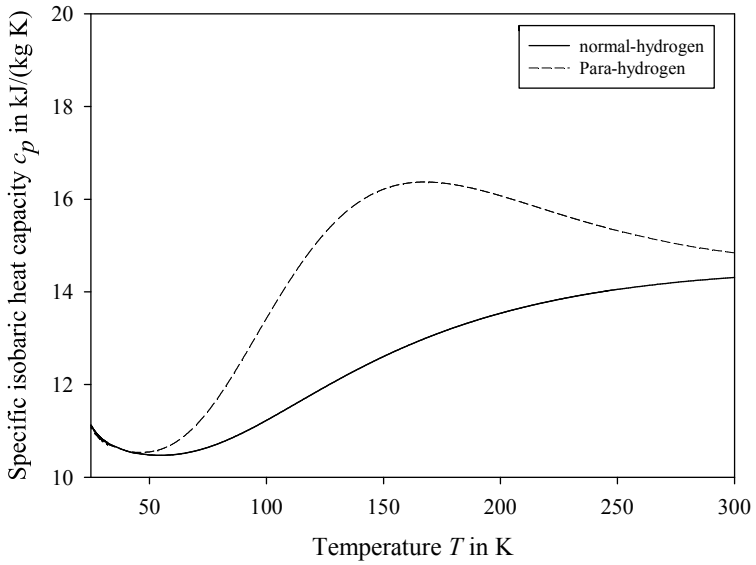

Figure A.2: Specific isobaric heat capacity c_p of normal- and para-hydrogen as a function of temperature T at 1 bar, computed with REFPROP [Lemmon et al. 2013]

Table A.1: Relevant physical properties of cryogenic fluids with a triple point temperature $T_{trp} > 54$ K, as given in REFPROP [Lemmon et al. 2013]

Fluid	Molar mass	Critical point		Triple point	NBP, 1.01 bar
	$\bar{M}$ in kg/kmol	T_{crit} in K	p_{crit} in bar	T_{trp} in K	T_{sat} in K
Nitrogen	28.01	126.19	33.96	63.15	77.36
Argon	39.95	150.69	48.63	83.81	87.30
Propane	44.10	369.89	42.51	85.53	231.04
Ethane	30.07	305.32	48.72	90.37	184.57
Methane	16.04	190.56	45.99	90.69	111.67
Ethylene	28.05	282.35	50.42	103.99	169.38
i-Pentane	72.15	460.35	33.78	112.65	300.60
i-Butane	58.12	407.81	36.29	113.73	261.07
n-Butane	58.12	425.13	37.96	134.90	272.66
n-Pentane	72.15	469.70	33.70	143.47	309.21

Table A.2: Optimization variables for the 100 tpd LH_2 process concept A

Optimization variables	Lower bound	Upper bound
p_{feed}	25 bar	80 bar
$p_{HP,MRC}$	25 bar	65 bar
$p_{MP,MRC}$	12 bar	25 bar
$p_{LP,MRC}$	1.5 bar	6.0 bar
$T_{MRC,int}$	120 K	200 K
y_{N_2}	0.1	0.3
y_{CH_4}	0.2	0.4
$y_{i-C_4H_{10}}$	0.1	0.3
p_{HP,H_2}	30 bar	80 bar
p_{MP,H_2}	6 bar	12.7 bar
p_{LP,H_2}	1.2 bar	1.8 bar
T_{ce}	28 K	33 K
ΔT_1	2.0 K	10 K
$\Delta T_{2\text{-}1}$	1.5 K	6.0 K
$\Delta T_{2\text{-}2}$	4.5 K	10 K

Table A.3: Optimization variables for the 100 tpd LH_2 process concept B

Optimization variables	Lower bound	Higher bound
p_{feed}	25 bar	80 bar
$p_{HP,MRC}$	25 bar	65 bar
$p_{MP,MRC}$	12 bar	30 bar
$p_{LP,MRC}$	1.5 bar	6.0 bar
$T_{MRC,int}$	120 K	200 K
y_{N_2}	0.1	0.3
y_{CH_4}	0.2	0.4
$y_{i-C_4H_{10}}$	0.15	0.3
$p_{HP,H_2\text{-}Ne}$	$4 \cdot p_{LP,H_2\text{-}Ne}$	$10 \cdot p_{LP,H_2\text{-}Ne}$
$T_{LP,H_2\text{-}Ne}$	26 K	35 K
p_{HP,H_2}	13 bar	25 bar
p_{LP,H_2}	1.2 bar	1.75 bar
T_{ce}	26 K	35 K
ΔT_1	2 K	15 K
$\Delta T_{2\text{-}1}$	1 K	8 K
$\Delta T_{2\text{-}2}$	1 K	10 K

Table A.4: Optimization constraints for the 100 tpd LH_2 process concepts A and B

Constraint	Limits concept A	Limits concept B
$y_{i-C_4H_{10}}$	0.1	0.1
$\Delta T_{min,1\text{-}1}$	2 K	2 K
$\Delta T_{min,1\text{-}2}$	2 K	2 K
$\Delta T_{min,VLV\text{-}1}$	2 K	2 K
$\Delta T_{min,VLV\text{-}2}$	2 K	2 K
$\Delta T_{min,2\text{-}1}$	0.5 K	0.5 K
$\Delta T_{min,2\text{-}2}$	1 K	1 K
$\Delta T_{min,2\text{-}3}$	1.2 K	1.2 K
$\Delta T_{min,3}$	0.5 K	0.5 K
$\Delta T_{max,1\text{-}1}$	25 K	25 K
$\Delta T_{max,1\text{-}2}$	25 K	25 K
$\Delta T_{max,2\text{-}1}$	15 K	15 K
$\Delta T_{max,2\text{-}2}$	15 K	15 K
$\Delta T_{max,2\text{-}3}$	15 K	15 K
$LMTD_{max,1\text{-}1}$	6 K	6 K
$LMTD_{max,1\text{-}2}$	6 K	6 K
$(U \cdot A)_{max,PC}$	8.3×10^3 kJ/(K · s)	8.3×10^3 kJ/(K · s)
$(U \cdot A)_{max,liq}$	2.8×10^3	2.8×10^3 kJ/(K · s)
$\dot{V}_{H_2,in,max}$	38000 m^3/h	-
$\dot{V}_{H_2\text{-}Ne,in,max}$	-	200000 m^3/h

Bibliography

Aceves et al. 2010
Aceves, S. M.; Espinosa-Loza, F.; Ledesma-Orozco, E.; Ross, T. O.; Weisberg, A. H.; Brunner, T. C.; Kircher, O.: *High-density automotive hydrogen storage with cryogenic capable pressure vessels*. In: International Journal of Hydrogen Energy 35.3 (2010), pp. 1219–1226.

Alabdulkarem et al. 2011
Alabdulkarem, A.; Mortazavi, A.; Hwang, Y.; Radermacher, R.; Rogers, P.: *Optimization of propane pre-cooled mixed refrigerant LNG plant*. In: Applied Thermal Engineering 31.6 (2011), pp. 1091–1098.

Alekseev 2014
Alekseev, A.: *Basics of Low-temperature Refrigeration*. In: Contribution to the CAS-CERN Accelerator School: Superconductivity for Accelerators arXiv:1501.07392 (2014). Erice, Italy, 24 April - 4 May 2013, 29 p. doi: 10.5170/CERN-2014-005.111. url: http://cds.cern.ch/record/1974048.

Alekseev 2015
Alekseev, A.: *Grundlagen der Kälteerzeugung und industrielle Tieftemperaturanlagen*. Vorlesungsskript SS2015, Technische Universität München. 2015.

Alekseev 2016
Alekseev, A.: "Hydrogen Liquefaction". In: Hydrogen Science and Engineering : Materials, Processes, Systems and Technology. Wiley-VCH Verlag GmbH & Co. KGaA, 2016, pp. 733–762. isbn: 9783527674268.

ALPEMA 2000
ALPEMA, B. A. P.-F. H. E. M. A.: *The standards of the brazed aluminium plate-fin heat exchanger manufacturers' association*. Standards. ALPEMA, 2000.

AmsterCHEM 2010
AmsterCHEM: *REFPROP CAPE-OPEN Version 1.1 interface*. Software. 2010.

Arp et al. 1999
Arp, V.; McCarty, R.; Fox, J.: *CRYODATA INC. Users Guide to GASPAK*. http://www.htess.com/gaspak.htm. 1999.

Baehr & Kabelac 2012
Baehr, H.; Kabelac, S.: *Thermodynamik. Grundlagen und technische Anwendungen*. 15th ed. Springer-Verlag Berlin Heidelberg, 2012. doi: 10.1007/978-3-642-24161-1.

Baehr & Stephan 2004
Baehr, H. D.; Stephan, K.: *Wärme-und Stoffübertragung*. Heidelberg: Springer-Verlag, 2004.

Baker & Shaner 1978
Baker, C.; Shaner, R.: *A Study of the Effiency of Hydrogen Liquefaction*. In: International Journal of Hydrogen Energy 3.3 (1978), pp. 321–334.

Balje 1981
Balje, O.: *Turbomachines - A guide to design, selection, and theory*. John Wiley & Sons, 1981.

Ball & Wietschel 2009
Ball, M.; Wietschel, M.: *The hydrogen economy: opportunities and challenges*. Cambridge University Press, 2009.

Barrick et al. 1965
Barrick, P.; Brown, L.; Hutchinson, H.; Cruse, R.: *Improved Ferric Oxide Gel Catalysts For Ortho-Parahydrogen Conversion*. In: Advances in Cyrogenic Engineering 10 (1965), pp. 181–189.

Barron 1985
Barron, R.: *Cryogenic systems*. Clarendon Press, 1985.

Bathen & Breitbach 2001
Bathen, D.; Breitbach, M.: *Adsorptionstechnik*. 1st ed. Springer-Verlag, 2001. doi: 10.1007/978-3-642-18235-8.

Belloni et al. 2008
Belloni, A.; Ahner, C.; Häring, H.-W.: *Industrial gases processing*. John Wiley & Sons, 2008.

Berstad et al. 2009
Berstad, D.; Stang, J.; Neksa, P.: *Comparison criteria for large-scale hydrogen liquefaction processes*. In: International journal of hydrogen energy 34.3 (2009), pp. 1560–1568.

Berstad et al. 2010
Berstad, D.; Stang, J.; Neksa, P.: *Large-scale hydrogen liquefier utilising mixed-refrigerant pre-cooling*. In: International journal of hydrogen energy 35.10 (2010), pp. 4512–4523.

Berstad et al. 2013
Berstad, D.; Walnum, H.; Neksa, P.; Decker, L.; Elliott, A.; Quack, H.: *Schedule for Demonstration Plant Including Options for Location*. Grant Agreement Number 278177. Integrated design for demonstration of efficient liquefaction of hydrogen (IDEALHY), July 2013.

Bischoff & Decker 2010
Bischoff, S.; Decker, L.: *First Operating Results of a Dynamic Gas Bearing Turbine in an Industrial Hydrogen Liquefier*. In: Advances in Cryogenic Engineering, AIP Conference Proceedings. 1218. 1. AIP. 2010, pp. 887–894.

Bloch & Geitner 2006
Bloch, H.; Geitner, F.: *Maximizing Machinery Uptime*. 5. Gulf Professional Publishing, 2006.

Bloch & Godse 2006
Bloch, H.; Godse, A.: *Compressors and modern process applications*. John Wiley & Sons, 2006. doi: 10.1002/0470047208.

Bloch & Soares 2001
Bloch, H.; Soares, C.: *Turboexpanders and process applications*. Gulf Professional Publishing, 2001.

Bonhoeffer & Harteck 1929
Bonhoeffer, K. F.; Harteck, P.: *Experimente über para-und orthowasserstoff*. In: Naturwissenschaften 17.11 (1929), pp. 182–182.

Bracha & Decker 2008
Bracha, M.; Decker, L.: *Grosstechnische Wasserstoffverfluessigung in Leuna*. In: Deutsche Kaelte-Klima-Tagung 2008. 2008.

Bracha et al. 1994
Bracha, M.; Lorenz, G.; Patzelt, A.; Wanner, M.: *Large-scale hydrogen liquefaction in Germany*. In: International journal of hydrogen energy 19.1 (1994), pp. 53–59.

Bromaghim et al. 2010
Bromaghim, G.; Gibeault, K.; Serfass, J.; Serfass, P.; Wagner, E.: *Hydrogen and fuel cells: the US market report*. In: National Hydrogen Association. 22. 2010.

Brouwer et al. 1970
Brouwer, J.; Van Den Meijdenberg, C.; Beenakker, J.: *Specific heat of the liquid mixtures of neon and hydrogen isotopes in the phase-separation region: I. The system Ne-H2*. In: Physica 50.1 (1970), pp. 93–124.

Burkhardt Compression 2015
Burkhardt Compression, a.: *Reciprocating compressors*. Online. 2015. URL: https://www.burckhardtcompression.com/wp-content/uploads/2015/11/150903BCReciprocatingCompressorsENWeb.pdf.

Buyanov 1960
Buyanov, R.: *A Study of Orthohydrogen-Parahydrogen Conversion under Solid Catalysts: I to III*. In: Kinetics and Catalysis 1.2-4 (1960), pp. 280–285.

Campbell 2014
Campbell, J.: *Gas Conditioning and Processing, Volume 2: The Equipment Modules*. Ed. by R. Hubbard ; K. Snow-McGregor. 9th ed. Oklahoma: Campbell Petroleum Series, 2014.

Cao et al. 2006
Cao, W. ; Lu, X. ; Lin, W. ; Gu, A.: *Parameter comparison of two small-scale natural gas liquefaction processes in skid-mounted packages*. In: Applied Thermal Engineering 26.8 (2006), pp. 898–904.

Cardella et al. 2015a
Cardella, U. ; Decker, L. ; Klein, H.: *Wirtschaftlich umsetzbare Wasserstoff Grossverfluessiger*. In: Deutsche Kaelte-Klima-Tagung 2015. AA I. 02. Nov. 2015.

Cardella et al. 2017a
Cardella, U. ; Decker, L. ; Klein, H.: *Aspects of hydrogen liquefier scale-up - Process and equipment design*. In: Proceedings of the 14th Cryogenics 2017 IIR International Conference. 056. www.iifiir.org. Dresden, Germany, 2017. DOI: 10.18462/iir.cryo.2017.0056. URL: www.iifiir.org.

Cardella et al. 2017b
Cardella, U. ; Decker, L. ; Klein, H.: *Economically viable large-scale hydrogen liquefaction*. In: Materials Science and Engineering. Proceedings of the 26th International Cryogenic Engineering Conference and International Cryogenic Materials Conference. 171. IOP Conference Series. 2017, p. 012013. DOI: 10.1088/1757-899X/171/1/012013.

Cardella et al. 2017c
Cardella, U. ; Decker, L. ; Klein, H.: *Roadmap to economically viable hydrogen liquefaction*. In: International Journal of Hydrogen Energy 42 (19 2017), pp. 13329–13338. ISSN: 0360-3199. DOI: 10.1016/j.ijhydene.2017.01.068.

Cardella et al. 2017d
Cardella, U.; Decker, L.; Sundberg J Jand Klein, H.: *Process optimization for large-scale hydrogen liquefaction*. In: International Journal of Hydrogen Energy 42 (17 2017), pp. 12339–12354. issn: 0360-3199. doi: 10.1016/j.ijhydene.2017.03.167.

Cardella et al. 2015b
Cardella, U.; Donaubauer; Decker, L.; Klein, H.: *Katalytische Ortho-Para Wasserstoff Umwandlung in Plattenwaermetauscher*. In: Annual Meeting of the Deutscher Kaelte und Klimatechnischer Verein 2015. AA I. 03. Dresden, Nov. 2015.

Casey et al. 2013
Casey, M.; Kraehenbuhl, D.; Zwyssig, C.: *The Design of Ultra-High-Speed Miniature Centrifugal Compressors*. In: Proc. 10th European Conference on Turbomachinery, Fluid Dynamics and Thermodynamics, Lappeenranta, Finland. 2013.

Chemical Engineering n.d.
Chemical Engineering, a.: *Chemical Engineering Plant Cost Index*. url: http://www.chemengonline.com/pci-home.

Couper 2003
Couper, J. R.: *Process engineering economics*. CRC Press, 2003.

Cretegny et al. 2003
Cretegny, D.; Schonfeld, H.; Decker, L.; Lohlein, K.: *Efficiency Improvement of Small Gas Bearing Turbines- Impact on Standard Helium Liquefier Performance*. In: Advances in Cryogenic Engineering: Transactions of the Cryogenic Engineering Conference, AIP Conference Proceedings; Volume 49 A 710 (2003), pp. 272–278. doi: 10.1063/1.1774692.

Cryostar n.d.(a)
Cryostar: *Turbo expander with compressor brake TC*. online. Data Sheet. Zone Industrielle F-68220 Hésingue France. url: http://www.cryostar.com/pdf/datasheet/en/tc.pdf.

Cryostar n.d.(b)
Cryostar: *Turbo-expanders for cold production and energy recovery*. online. Data Sheet. Zone Industrielle F-68220 Hésingue France. url: http://www.cryostar.com/pdf/dnl-zone/Cryostar-process-machinery.pdf.

Dauber 2011
Dauber, F.: *Einfluss von Stoffdatenmodellen auf die Simulation von Prozessen mit verfluessigtem Erdgas (LNG)*. PhD thesis. Ruhr-Universität Bochum, 2011.

Dewar 1898
Dewar, J.: *Liquid hydrogen*. In: Science (1898), pp. 3–6.

Di Bella & Osborne 2014
Di Bella, F.; Osborne, C.: *Development of a Centrifugal Hydrogen Pipeline Gas Compressor*. Online. 2014 DOE Hydrogen Program Merit ReviewProject ID: PD017. June 2014. URL: https://www.hydrogen.energy.gov/pdfs/review14/pd017dibella2014o.pdf.

Dixon & Hall 2013
Dixon, S.; Hall, C.: *Fluid mechanics and thermodynamics of turbomachinery*. Butterworth-Heinemann, 2013.

Donaubauer 2015
Donaubauer, P.: *Plate-Fin Heat Exchanger Model for the Ortho-Para Conversion in Industrial Hydrogen Liquefiers*. MA thesis. Technischen Universitaet Muenchen, Apr. 2015.

Donaubauer et al. 2018
Donaubauer, P.; Cardella, U.; Decker, L.; Klein, H.: *Kinetics and Heat Exchanger Design for Catalytic Ortho- to Para-Hydrogen Conversion during Liquefaction*. In: Manuscript accepted for publication in Chemical Engineering and Technology (2018).

Drnevich 2003
Drnevich, R.: *Hydrogen delivery-liquefaction and compression, Strategic Intiatives for Hydrogen Delivery*. Workshop. May 2003.

Eifler et al. 2009
Eifler, W.; Schlücker, E.; Spicher, U.; Will, G.: *Küttner Kolbenmaschinen: Kolbenpumpen, Kolbenverdichter, Brennkraftmaschinen*. 7th ed. Springer-Verlag, 2009. DOI: 10.1007/9783834893024.

EIGA 2010
EIGA, E. I. G. A.: *Indirect CO 2 emissions compensation: Benchmark proposal for Air Separation Plants*. Position Paper PP-33. Dec. 2010. URL: https://www.eiga.eu/index.php?id=294&tx%5C_abdownloads%5C_pi1%5Baction%5D=getviewclickeddownload&tx%5C_abdownloads%5C_pi1%5Buid%5D=1614&no%5C_cache=1.

Essler 2013
Essler, J.: *Physikalische und Technische Aspekte der Ortho-Para-Umwandlung von Wasserstoff*. PhD thesis. Technische Universität Dresden, 2013.

Farkas 1935
Farkas, A.: *Orthohydrogen, parahydrogen and heavy hydrogen.* In: Cambridge University Press (1935).

Farkas & Sachsse 1933
Farkas, L.; Sachsse, H.: *Ueber die Homogene Katalyse der Para-Ortho Wasserstoffumwandlung unter Einwirkung Paramagnetische Molekuele. I.* In: Zeitschrift fuer Physikalische Chemie, Abteilung B - Chemie der Elementarprozesse Aufbau der Materie 23 (1933), pp. 1–18.

FCH2JU 2014
FCH2JU: *Multi - Annual Work Plan 2014 - 2020.* Fuel cells and hydrogen joint undertaking (FCH JU), June 2014.

Fischer 2008
Fischer, C.: *Vergleich von Kaeltekreislaeufen fuer schwimmende Erdgasverfluessigungsanlagen.* MA thesis. Technische Universitaet Braunschweig, Apr. 2008.

Flynn 2004
Flynn, T.: *Cryogenic engineering.* CRC Press, 2004.

Froeschle & Kederer 2010
Froeschle, P.; Kederer, T.: *Planung zum Aufbau einer flächendeckenden Wasserstoff Tankstellen Infrastruktur in Deutschland.* Report. 2010.

Fukano et al. 2000
Fukano, T.; Yamashita, N.; Ohira, K.: *A Study of the Large Hydrogen Liquefaction Process.* In: Journal of High Pressure Institute of Japan 38.5 (2000), pp. 298–305.

Gallarda 2001
Gallarda, J.: *Liquefaction de L'Hydrogene.* Ed. Techniques Ingenieur, 2001.

Gardiner 2009
Gardiner, M.: *Energy requirements for hydrogen gas compression and liquefaction as related to vehicle storage needs.* DOE Hydrogen and Fuel Cells Program, July 2009.

Gaumer et al. 1988
Gaumer, L.; Winters, J.; Arthur, R.: "Hydrogen liquefaction using a dense fluid expander and neon as a precoolant refrigerant". US4765813A. Aug. 1988.

General Electric 2005a
General Electric, a.: *General Electric Oil and Gas: Centrifugal and Axial Compressors.* online. Dec. 2005.

General Electric 2005b
General Electric, a.: *Reciprocating Compressors*. online. 2005. URL: http://site.ge-energy.com/businesses/ge%5C_oilandgas/en/literature/en/downloads/reciprocatingcompressors.pdf.

General Electric n.d.
General Electric, a.: *Turboexpanders*. online. Accessed 27.04.2017. URL: http://site.ge-energy.com/businesses/ge%5C_oilandgas/en/prod%5C_serv/prod/turboexpanders/en/index.htm.

Gonen 2011
Gonen, T.: *Electrical Machines with MATLAB®*. CRC Press, 2011.

Grave et al. 2015
Grave, K.; Hazrat, M.; Boeve, S.; Blücher, F. von; Bourgault, C.; Breitschopf, B.; Friedrichsen, N.; Arens, M.; Aydemir, A.; Pudlik, M.: *Electricity Costs of Energy Intensive Industries An International Comparison*. In: German Ministry of Economic Affairs and Energy (2015).

Gross et al. 1994
Gross, R.; Otto, W.; Patzelt, A.; Wanner, M.: *Liquid hydrogen for Europe–the Linde plant at Ingolstadt*. In: Linde-Reports on science and technology 54 (1994), pp. 37–43.

Grote & Feldhusen 2007
Grote, K.-H.; Feldhusen, J.: *Dubbel: Taschenbuch für den Maschinenbau*. Springer-Verlag, 2007.

Guthrie 1969
Guthrie, K.: *Data and techniques for preliminary capital cost estimating*. In: Chemical Engineering 76.6 (1969), p. 114.

H2 Mobility 2010
H2 Mobility, a.: *70MPa Hydrogen Refuelling Station Standardization Functional Description of Station Modules*. H2 Mobility, June 2010.

H2 Mobility 2015
H2 Mobility, a.: *H2 Mobility*. Online. 2015. URL: http://h2-mobility.de/.

Haeussinger et al. 2000a
Haeussinger, P.; Lohmueller, R.; Watson, A.: *Hydrogen, 2. Production*. In: *Ullmann's Encyclopedia of Industrial Chemistry*. Wiley-VCH Verlag GmbH & Co. KGaA, 2000. DOI: 10.1002/14356007.a13_297.

Haeussinger et al. 2000b
Haeussinger, P.; Lohmueller, R.; Watson, A.: *Hydrogen, 3. Purification*. In: *Ullmann's Encyclopedia of Industrial Chemistry*. Wiley-VCH Verlag GmbH & Co. KGaA, 2000. Chap. 3. doi: 10.1002/14356007.o13_o04.

Hausen & Linde 1985
Hausen, H.; Linde, H.: *Tieftemperaturtechnik: Erzeugung sehr tiefer Temperaturen, Gasverfluessigung und Zerlegung von Gasgemischen*. 2nd ed. Springer Berlin Heidelberg, 1985. doi: 10.1007/978-3-662-10553-5.

Heck & Barrick 1966
Heck, C.; Barrick, P.: "Liquid-Vapor Phase Equilibria of the Neon-Normal Hydrogen System". In: Advances in Cryogenic Engineering: Proceedings of the 1965 Cryogenic Engineering Conference Rice University Houston, Texas August 23–25, 1965. Ed. by K. D. Timmerhaus. Boston, MA: Springer US, 1966, pp. 349–355. isbn: 978-1-4757-0522-5.

Hood & Grilly 1952
Hood, C.; Grilly, E.: *A Hydrogen Liquefier Using Neon as an Intermediate*. In: Review of Scientific Instruments 23.7 (1952), pp. 357–361. doi: http://dx.doi.org/10.1063/1.1746276.

Hust & Stewart 1965
Hust, J.; Stewart, R.: *A Compilation of the Property Differences of Ortho and Para Hydrogen or Mixtures of Ortho and Para Hydrogen*. 1965.

Hutchinson 1966
Hutchinson, H.: *Analysis of Catalytic Ortho-Parahydrogen Reaction Mechanisms*. Ph.D. Thesis. University of Colorado, 1966.

IDEALHY 2011
IDEALHY: *Integrated design for efficient advanced liquefaction of hydrogen (IDEALHY)*. Online. http://www.idealhy.eu/. 2011. url: http://www.idealhy.eu/.

IDEALHY 2012
IDEALHY: *Report on Technology Overview and Barriers to Energy- and Cost-Efficient Large Scale Hydrogen Liquefaction*. FCH JU FP7-JTI. IDEALHY Consortium, 2012.

Ilisca 1992
Ilisca, E.: *Ortho-para Conversion of Hydrogen Molecules Physisorbed on Surfaces*. In: Progress in Surface science 41.3 (1992), pp. 217–335. doi: 10.1016/0079-6816(92)90019-E.

Iwamoto 1996
Iwamoto, K.: *Theoretical Calculation of the Large Hydrogen Liquefaction Process.* In: Proceedings of the 16th International Cryogenic Engineering Conference (1996). Elsevier Ltd.

Jacobsen et al. 1997
Jacobsen, R. T. ; Penoncello, S. G. ; Lemmon, E. W.: *Thermodynamic properties of cryogenic fluids.* Springer Science & Business Media, 1997.

Jumonville 2010
Jumonville, J.: *Tutorial on cryogenic turboexpanders.* In: Proceedings of the 39th Turbomachinery Symposium. 2010.

Katti et al. 1986
Katti, R. ; Jacobsen, R. ; Stewart, R. ; Jahangiri, M.: *Thermodynamic properties of neon for temperatures from the triple point to 700 K at pressures to 700 MPa.* In: *Advances in cryogenic engineering.* Springer, 1986, pp. 1189–1197.

Kerry 2007
Kerry, F.: *Industrial gas handbook: gas separation and purification.* CRC Press, 2007.

Khan & Lee 2013
Khan, M. ; Lee, M.: *Design optimization of single mixed refrigerant natural gas liquefaction process using the particle swarm paradigm with nonlinear constraints.* In: Energy 49 (2013), pp. 146–155.

Kloeppel et al. 2017
Kloeppel, S. ; Dittmar, N. ; Haberstroh, C. ; Quack, H.: *Mixed refrigerant cycle with neon, hydrogen, and helium for cooling sc power transmission lines.* In: IOP Conference Series: Materials Science and Engineering. 171. 1. IOP Publishing. 2017, p. 012019.

Kohler et al. 2014
Kohler, T. ; Bruentrup, M. ; Key, R. ; Edvardsson, T.: *Choose the best refrigeration technology for small-scale LNG production.* In: Hydrocarbon Processing, January (2014), pp. 45–52.

Krasae-in 2013
Krasae-in, S.: *Efficient Hydrogen Liquefaction Processes.* PhD thesis. Norges teknisk-naturvitenskapelige universitet (NTNU), 2013.

Krasae-in et al. 2010
Krasae-in, S.; Stang, J.; Neksa, P.: *Development of large-scale hydrogen liquefaction processes from 1898 to 2009.* In: International journal of hydrogen energy 35.10 (2010), pp. 4524–4533. doi: 10.1016/j.ijhydene.2010.02.109.

Kuendig et al. 2006
Kuendig, A.; Loehlein, K.; Kramer, G.; Huijsmans, J.: *Large scale hydrogen liquefaction in combination with LNG re-gasification.* In: Proceedings of the 16th World Hydrogen Energy Conference 2006, Lyon, France. Curran Associates, Inc. Red Hook, NY, USA. 2006, pp. 3326–3333.

Kunz et al. 2007
Kunz, O.; Klimeck, R.; Wagner, W.; Jaeschke, M.: *The GERG-2004 Wide-Range Equation of State for Natural Gases and Other Mixtures.* Düsseldorf, 2007: GERG Technical Monograph, 2007.

Kunz & Wagner 2012
Kunz, O.; Wagner, W.: *The GERG-2008 wide-range equation of state for natural gases and other mixtures: an expansion of GERG-2004.* In: Journal of chemical & engineering data 57.11 (2012), pp. 3032–3091.

Langguth 2015
Langguth, H.: *Kapitalmarktorientiertes Wertmanagement: Unternehmensbewertung, Unternehmenssteuerung und Berichterstattung.* Vahlen, 2015.

Lauermann et al. 2013
Lauermann, G.; Haeussinger, P.; Lohmueller, R.; Watson, A.: *Hydrogen, 1. Properties and Occurrence.* In: *Ullmann's Encyclopedia of Industrial Chemistry.* Wiley-VCH Verlag GmbH & Co. KGaA, 2013. Chap. 1.

Le Duigou et al. 2013
Le Duigou, A.; Quéméré, M.-M.; Marion, P.; Menanteau, P.; Decarre, S.; Sinegre, L.; Nadau, L.; Rastetter, A.; Cuni, A.; Mulard, P.: *Hydrogen pathways in France: results of the HyFrance3 project.* In: Energy policy 62 (2013), pp. 1562–1569.

Le Roy et al. 1990
Le Roy, R.; Chapman, S.; McCourt, F.: *Accurate Thermodynamic Properties of the Six Isotopomers of Diatomic Hydrogen.* In: Journal of Physical Chemistry 94.2 (1990), pp. 923–929. doi: 10.1021/j100365a077.

Leachman et al. 2007
Leachman, J. W.; Jacobsen, R. T.; Penoncello, S. G.; Huber, M. L.: *Current Status of Transport Properties of Hydrogen*. In: International Journal of Thermophysics 28.3 (2007), pp. 773–795. doi: 10.1007/s10765-007-0229-4.

Leachman et al. 2009
Leachman, J.; Jacobsen, R.; Penoncello, S.; Lemmon, E.: *Fundamental equations of state for parahydrogen, normal hydrogen, and orthohydrogen*. In: Journal of Physical and Chemical Reference Data 38.3 (2009), pp. 721–748.

Leachman & Richardson 2012
Leachman, J.; Richardson, I.: *Thermophysical Properties of Hydrogen and Deuterium at all Ortho-Para Compositions*. In: Proceedings of the 12th IIR International Conference on Cryogenics 2012 ID067 (2012).

Leachman et al. 2017
Leachman, J.; Jacobsen, R. T.; Penoncello, S.; Lemmon, E.: *Thermodynamic properties of cryogenic fluids*. In: (2017).

Lemmon et al. 2013
Lemmon, W.; Huber, M.; McLinden, M.: *NIST Standard Reference Database 23: Reference Fluid Thermodynamic and Transport Properties-REFPROP, Version 9.1*. Standard Reference Data Program. Gaithersburg, MD: National Institute of Standards and Technology, 2013.

Leon 2008
Leon, A.: *Hydrogen technology: mobile and portable applications*. Springer Science & Business Media, 2008. doi: 10.1007/978-3-540-69925-5.

Linde AG n.d.
Linde AG, a.: *Aluminium Plate-Fin Heat Exchangers*. Online. url: http://www.linde-engineering.com.

Lipman et al. 1963
Lipman, M.; Cheung, H.; Roberts, O.: *Continuous Conversion Hydrogen Liquefaction*. In: Chemical Engineering Progress 59.8 (1963), pp. 49–54.

MAN n.d.
MAN, a.: *RG Integrally geared compressors*. online. url: http://turbomachinery.man.eu/docs/librariesprovider4/Turbomachinery%5C_doc/rg-integrally-geared-compressors.pdf?sfvrsn=8.

Matsuda & Nagami 1997
Matsuda, H.; Nagami, M.: *Study of large hydrogen liquefaction process*. In: WE-NET: summary of annual reports 8.3 (1997), pp. 175–175. URL: http://www.enaa.or.jp/WE-NET/ronbun/1997/e5/sanso1997.html.

Maytal & Pfotenhauer 2012
Maytal, B.-Z.; Pfotenhauer, J. M.: *Miniature Joule-Thomson cryocooling: principles and practice*. Springer Science & Business Media, 2012.

McCoy & Douglass 2014
McCoy, G.; Douglass, J.: *Premium Efficiency Motor Selection and Application Guide*. In: US Department of Energy's Office of Energy Efficiency and Renewable Energy (2014).

Milenko et al. 1997
Milenko, Y.; Sibileva, R.; Strzhemechny, M.: *Natural Ortho-Para Conversion Rate in Liquid and Gaseous Hydrogen*. In: Journal of Low Temperature Physics 107.1-2 (1997), pp. 77–92.

Ohira 2004
Ohira, K.: *A Summary of Liquid Hydrogen and Cryogenic Technologies in Japans WE-NET Project*. In: Advances in cryogenic engineering: Transactions of the Cryogenic Engineering Conference CEC. 710. 1. AIP Publishing. 2004, pp. 27–34.

Ohlig 2014
Ohlig, K.: *Engineering, Procurement, and Commissioning of the new helium liquefaction facility for Gazprom in Orenburg*. Presentation at the ICEC/ICMC 2014 Conference. Presentation. July 2014. URL: https://indico.cern.ch/event/244641/contributions/1563458/.

Ohlig & Bischoff 2012
Ohlig, K.; Bischoff, S.: *Dynamic gas bearing turbine technology in hydrogen plants*. In: Advances in Cryogenic Engineering: Transactions of the Cryogenic Engineering Conference,AIP Conference Proceedings 1434 (2012), pp. 814–819. DOI: 10.1063/1.4706994.

Ohlig & Decker 2013
Ohlig, K.; Decker, L.: *Hydrogen Liquefaction*. In: *Ullmann's Encyclopedia of Industrial Chemistry*. Ed. by F. Ullmann. Wiley-VCH Verlag GmbH & Co. KGaA, 2013. DOI: 10.1002/14356007.o13_o05.pub2.

Ohlig & Decker 2014
Ohlig, K. ; Decker, L.: *The latest developments and outlook for hydrogen liquefaction technology*. In: AIP Conference Proceedings. 1573. 1. AIP. 2014, pp. 1311–1317. doi: 10.1063/1.4860858.

Peng & Robinson 1976
Peng, D. ; Robinson, D.: *A new two-constant equation of state*. In: Industrial & Engineering Chemistry Fundamentals 15.1 (1976), pp. 59–64.

Peters et al. 1991
Peters, M. ; Timmerhaus, K. ; West, R.: *Plant design and economics for chemical engineers*. 4th ed. McGraw-Hill New York, 1991.

Polifke & Kopitz 2005
Polifke, W. ; Kopitz, J.: *Wärmeübertragung*. In: Grundlagen, analytische und numerische Methoden (2005).

Poling et al. 2001
Poling, B. ; Prausnitz, J. ; O'connell, J.: *The properties of gases and liquids*. 5th ed. Mcgraw-hill New York, 2001. doi: DOI:10.1036/0070116822.

Quack 2001
Quack, H.: *Die Schluesselrolle der Kryotechnik in der Wasserstoff-Energiewirtschaft: Herausforderungen des 21. Jahrhunderts in der aktuellen Forschung*. In: Wissenschaftliche Zeitschrift der Technischen Universitaet Dresden 50.5-6 (2001), pp. 112–117.

Quack 2002
Quack, H.: *Conceptual design of a high efficiency large capacity hydrogen liquefier*. In: Advances in Cryogenic Engineering: Proceedings of the Cryogenic Engineering Conference. 613. 1. AIP Publishing. 2002, pp. 255–263.

Quack et al. 2015
Quack, H. ; Haberstroh, C. ; Seemann, I. ; Klaus, M.: *Nelium, a Refrigerant with High Potential for the Temperature Range between 27 and 70 K*. In: Physics Procedia 67 (2015), pp. 176–182.

Richardson et al. 2015
Richardson, I. ; Blackham, T. ; Leachman, J. ; Lemmon, E.: *Helium-Hydrogen pressure-density-temperature-x measurements and equation of state*. In: Cryogenic Engineering Conference June 28 - July 2 2015. C3OrC-01. https://indico.cern.ch/event/344330/contributions/806698/attachments/677864/931328/C3OrC-01-Richardson.pdf. Tucson, Arizona, USA, 2015.

Robinson 1995
Robinson, L.: *Phase Equilibria in Cryogenic Mixtures: Part II*. In: *Cryocoolers 8*. Springer, 1995, pp. 559–567.

Roder 1984
Roder, H. M.: *Thermal Conductivity of Parahydrogen*. In: Journal of Chemical and Engineering Data 29.4 (1984), pp. 382–386. doi: 10.1021/je00038a005.

Serio et al. 2015
Serio, L. ; Bremer, J. ; Claudet, S. ; Delikaris, D. ; Ferlin, G. ; Pezzetti, M. ; Pirotte, O. ; Tavian, L. ; Wagner, U.: *CERN experience and strategy for the maintenance of cryogenic plants and distribution systems*. In: IOP Conference Series: Materials Science and Engineering. 101. 1. IOP Publishing. 2015, p. 012140.

Seume & Mailach 2014
Seume, J. ; Mailach, R.: *Grundlagen der Stroemungsmaschinen*. In: *Dubbel*. Springer, 2014, pp. 1250–1277.

Shigekiyo 2015
Shigekiyo, H.: *International Workshop on Liquefied Hydrogen Technology*. Workshop. Japan Ship Technology Research Association, Mar. 2015.

Shimko & Gardiner 2008
Shimko, M. ; Gardiner, M.: *Innovative hydrogen liquefaction cycle*. website. 2008. url: https://www.hydrogen.energy.gov/pdfs/progress08/iii%5C_7%5C_shimko.pdf.

Sinnott 1993
Sinnott, R.: *Chemical engineering design: SI Edition*. 2nd ed. Elsevier, 1993.

Soave 1972
Soave, G. a.: *Equilibrium constants from a modified Redlich-Kwong equation of state*. In: Chemical Engineering Science 27.6 (1972), pp. 1197–1203.

Span et al. 2000
Span, R. ; Lemmon, E. ; Jacobsen, R. ; Wagner, W. ; Yokozeki, A.: *A reference equation of state for the thermodynamic properties of nitrogen for temperatures from 63.151 to 1000 K and pressures to 2200 MPa*. In: Journal of Physical and Chemical Reference Data 29.6 (2000), pp. 1361–1433.

Staats 2008
Staats, W.: *Analysis of a supercritical hydrogen liquefaction cycle*. MA thesis. Massachusets Institute of Technology, 2008.

Stang et al. 2006
Stang, J.; Neksa, P.; Brendeng, E.: *On the design of an efficient hydrogen liquefaction process*. In: World Hydrogen Energy Conference 38.43 (June 2006).

Stephan et al. 2007
Stephan, P.; Schaber, K.; Stephan, K.; Mayinger, F.: *Thermodynamik. Grundlagen und technische Anwendungen. Band 1 Einstoffsysteme*. 19. Auflage. Springer Vieweg, 2007. doi: 10.1007/978-3-642-30098-1.

Stolten 2016
Stolten, D.: *Hydrogen Science and Engineering: Materials, Processes, Systems and Technology, 2 Volume Set*. 1. John Wiley & Sons, 2016.

Stolzenburg et al. 2013
Stolzenburg, K.; Berstad, D.; Decker, L.; Elliott, A.; Haberstroh, C.; Hatto, C.; Klaus, M.; Mortimer, M.; Mubbala, R.; Mwabonje, O.; Neksa, P.; Quack, H.; Rix, J.; Seemann, I.; Walnum, H.: *Efficient Liquefaction of Hydrogen: Results of the IDEALHY Project*. Fuel Cells and Hydrogen Joint Undertaking (FCH JU), Nov. 2013.

Stolzenburg & Mubbala 2013
Stolzenburg, K.; Mubbala, R.: *Hydrogen Liquefaction Report, Whole Chain Assessment*. Dec. 2013.

Streett & Jones 1965
Streett, W.; Jones, C.: *Liquid phase separation and liquid-vapor equilibrium in the system neon-hydrogen*. In: The Journal of Chemical Physics 42.11 (1965), pp. 3989–3994.

Sundberg et al. 2017
Sundberg, J.; Rehfeldt, S.; Peschel, A.; Klein, H.: *Process Optimization of the Methanol Synthesis Using Different Local Optimization Algorithms*. In: Chemie Ingenieur Technik 89.5 (2017), pp. 675–685. doi: 10.1002/cite.201600108.

Syed et al. 1998
Syed, M.; Sherif, S.; Veziroglu, T.; Sheffield, J.: *An economical analysis of three hydrogen liquefaction systems*. In: International Journal of Hydrogen E 23.7 (1998), pp. 565–576.

Taylor et al. 1986
Taylor, J.; Alderson, J.; Kalyanam, K.; Lyle, A.; Phillips, L.: *Technical and economic assessment of methods for the storage of large quantities of hydrogen*. In: International Journal of Hydrogen Energy 11.1 (1986), pp. 5–22.

Timmerhaus & Flynn 1989
Timmerhaus, K.; Flynn, T.: *Cryogenic process engineering*. Springer US, 1989. doi: 10.1007/978-1-4684-8756-5.

UNFCC 2015
UNFCC, U. N. F. C. o. C. C.: *Paris Climate Conference (COP21)*. In: Paris Agreement. UNFCCC, Dec. 2015. url: http://unfccc.int/resource/docs/2015/cop21/eng/l09r01.pdf.

UniSim Design 2015
UniSim Design, a.: *UniSim Design R440, Honeywell International Inc.* Documentation. 2005-2015. 2015.

U.S. Department of Energy 2011
U.S. Department of Energy, a.: *Technology readiness assessment guide (DOE G 413.3-4)*. U.S. Department of Energy, Office of Management, 2011.

Valenti & Macchi 2008
Valenti, G.; Macchi, E.: *Proposal of an innovative, high-efficiency, large-scale hydrogen liquefier*. In: International journal of hydrogen energy 33.12 (2008), pp. 3116–3121.

Valenti et al. 2012
Valenti, G.; Macchi, E.; Brioschi, S.: *The influence of the thermodynamic model of equilibrium-hydrogen on the simulation of its liquefaction*. In: International journal of hydrogen energy 37.14 (2012), pp. 10779–10788.

VDI 2013
VDI: *Waermeatlas, VDI*. 11. Auflage. Springer Verlag, 2013.

Vega 2013
Vega, D.: *A New Wide Range Equation of State for Helium-4*. PhD thesis. Texas A&M University, 2013.

Venkatarathnam & Timmerhaus 2008
Venkatarathnam, G.; Timmerhaus, K.: *Cryogenic mixed refrigerant processes*. 100. Springer, 2008.

Walas 1988
Walas, S.: *Chemical Process Equipment Selection and Design*. Butterworths Pub., 1988.

Weitzel et al. 1960a
Weitzel, D.; Blake, J.; Konecnik, M.: *Flow Conversion Kinetics of Ortho and Parahydrogen*. In: Advances in Cryogenic Engineering 4 (1960), pp. 286–295.

Weitzel et al. 1960b
Weitzel, D.; Van valin, C.; Draper, J.: *Design Data for Ortho-Parahydrogen Converters*. In: Advances in Cyrogenic Engineering 3 (1960), pp. 190–196.

Whitfield & Baines 1990
Whitfield, A.; Baines, N.: *Design of radial turbomachines*. John Wiley and Sons Inc., 1990.

Wigner 1933
Wigner, E.: *Ueber die Paramagnetische Umwandlung von Para-Orthowasserstoff. III.* In: Zeitschrift fuer Physikalische Chemie, Abteilung B - Chemie der Elementarprozesse Aufbau der Materie 23 (1933), pp. 28–32.

Williams 1947
Williams, R.: *Six-tenths factor aids in approximating costs*. In: Chemical Engineering 54.12 (1947), pp. 124–125.

Woolley et al. 1948
Woolley, H. W.; Scott, R. B.; Brickwedde, F. G.: *Compilation of Thermal Properties of Hydrogen in its Various Isotopic and Ortho- Para Modifications*. In: Journal of Research of the National Bureau of Standards 41.RP1932 (1948), pp. 379–475.

Younglove 1982
Younglove, B.: *Thermophysical Properties of Fluids. I. Argon, Ethylene, Parahydrogen, Nitrogen, Nitrogen Trifluoride, and Oxygen*. In: Journal of Physical and Chemical Reference Data 11.1 (1982), pp. 1-11.

Yurum 1995
Yurum, Y.: *Hydrogen energy system: production and utilization of hydrogen and future aspects*. 295. Springer Science & Business Media, 1995.